# ENGINEERING THE MICRO-ENVIRONMENT TO CONTROL THE FATE OF MAMMALIAN CELLS

BY

PIYUSH BAJAJ

DISSERTATION

Submitted in partial fulfillment of the requirements
for the degree of Doctor of Philosophy in Bioengineering
in the Graduate College of the
University of Illinois at Urbana-Champaign, 2013

Urbana, Illinois

Doctoral Committee:

Professor Rashid Bashir, Chair
Professor K. Jimmy Hsia
Professor Hyunjoon Kong
Professor Lawrence Schook

# ABSTRACT

Bio-physical and bio-chemical factors in the local micro-environment like substrate stiffness, geometry, ligand density, and topography can have strong influences on determining the fate of cells. Mammalian cells respond to this myriad of micro-environmental cues by an interplay between actomyosin based cellular contractions and integrin mediated focal adhesions. A force balance is established between the intracellular micro-environment and the extracellular matrix. This mechanotransduction process is ultimately responsible for changes in the cytoskeletal characteristics, morphology, migration, division and gene expression of mammalian cells. The goal of this dissertation was to develop a platform to control the fate of mammalian cells by engineering the cellular micro-environment.

Beating rate, force of contraction and cytoskeletal structure of embryonic chicken cardiac myocytes was examined by varying the elasticity of the underlying substrate. Cells cultured on substrates with elasticity comparable to the native myocardium (18 kPa) exhibited the highest beating rate during the first few days of culture. Higher percentage of mature focal adhesions were seen on cells on stiffer substrates (50 kPa or greater), while only small punctate focal adhesions could be noticed on soft substrates (1 kPa). As a result, cells on the soft substrate only showed non-aligned sarcomeric striations. However, cells on the substrate which mimicked the stiffness of the native myocardium showed highly aligned sarcomeric striations, hallmark of a striated muscle cell. In addition, quantitative analysis was performed to provide a bio-physical basis for understanding the affect of substrate elasticity on cell-cell interactions in cardiac tissue.

Next, geometrical cues of the substrate were used to modulate the process of myogenesis on the murine derived muscle cell line (C2C12). By using micro-contact printing, three different protein geometries, linear, circular, and hybrid (linear and circular) were patterned on the surface of petri dishes.

Hybrid 30° geometry showed the highest fusion and maturation indices for C2C12 cells. Myotubes on the hybrid 30° were highly aligned and showed the best response to an electrical pulse stimulation. It was verified that these differences in the myogenic parameters could not be attributed to the differences in density of cells on the different geometrical structures. The different morphologies of protein micro-patterns changed the cellular tractional stresses and cytoskeletal organization leading to the differences in myogenesis on the different patterns.

A new class of $sp^2$-hybridized carbon based allotrope, graphene, was then investigated as a potential biomaterial for muscle tissue engineering. C2C12 skeletal muscle myoblasts showed a very high degree of myogenic potential on graphene. Also, being an organic material, graphene could also provide a similar micro-environment as the native extracellular matrix in terms of its chemical composition and physical structure. Thus graphene could potentially be used for the development of artificial synthetic muscle scaffolds.

Finally, different cues of geometry and stiffness were combined in a three dimensional poly ethylene glycol diacrylate hydrogel to truly mimic the native tissue. Stereolithography apparatus enabled modulating the stiffness of the substrate by controlling the degree of polymerization of the different polymers. Dielectrophoresis helped in controlling the spatial location of cells in these polymers. Thus by integrating stereolithography with dielectrophoresis, mouse embryonic stem cells were patterned and encapsulated in three dimensional hydrogels of physiologically relevant stiffnesses. The cells showed very high viability for both the aligned and the non-aligned samples. Since, embryoid body formation is the precursor to the differentiation of mouse embryonic stem cells, both the viability and alignment of embryoid bodies was verified in the hydrogels as well. Also, some preliminary results are presented that show the differentiation of mESCs.

It is extremely important to independently control multiple cues simultaneously in a three-dimensional architecture to control the fate of cells. Cells in our body do not respond to one environmental cue at a time. Rather they simultaneously experience multiple cues like stiffness, geometry, topography, etc. and respond to them accordingly. This work first looked at different environmental cues in two-dimensions and then combined them in three-dimensional cultures to fully mimic the native *in vivo* tissue. This novel platform could thus open new doors in stem cell biology and enable

applications in tissue engineering, regenerative medicine, and drug discovery/screening.

*I dedicate this thesis to my mom, dad, and my wife, for their love and support. I love you all dearly.*

# ACKNOWLEDGMENTS

Finishing the PhD has definitely been the most challenging aspect of my academic life and numerous people have contributed in its successful completion. There have been a lot of great and some bad days during this journey and I will cherish these memories throughout my life. I have made some great friends some of which are very dear to me. I believe this PhD has not only improved my knowledge but also helped in the development of my character, which I believe is the true meaning of a good education. It was a great privilege spending close to five years in the Department of Bioengineering at the University of Illinois - Urbana Champaign.

First and foremost, I would like to thank my advisor Dr. Rashid Bashir for his tremendous support and guidance. I could not have asked for a better advisor for my graduate studies. Dr. Bashir allowed me to explore my own ideas and gave me an opportunity to be independent. As a result of this, I was able to explore areas which I was really interested in and this greatly enhanced the PhD experience. In addition, he actively encouraged me to collaborate with others and to participate in conferences. This has helped both in my professional and personal growth. He has been inspirational, supportive, patient, kind, and a great mentor. I will forever be indebted to him.

I would also like to thank my other committee members - Dr. Jimmy Hsia, Dr. Hyunjoon Kong, and Dr. Lawrence Schook for their guidance throughout my PhD. I have collaborated with all of them/their students at some point or other during my PhD and it is only with their help and support that I was able to successfully complete my PhD. In addition, I would also like to thank Dr. Jianjun Cheng, Dr. Taher Saif, and Dr. Fei Wang for their help during my PhD.

I would like to thank both past and present members of the Bashir lab for helping me during different projects and making my stay in the Bashir lab

so wonderful. In particular, I would like to thank Dr. Bobby Reddy, Jr., for being such a great friend. This PhD would have been much harder without his friendship and words of encouragement. Also, other members like Dr. Yi-Shao Liu, Dr. Larry Millet, Dr. Kidong Park, Mitchell Collens, Carlos Duarte, Daniel Marchwiany, and Eric Salm have made this PhD experience a more memorable one.

I would also like to thank some of my other friends not directly related to Bashir group - Dr. Matthias Kasten, Enrique Carrion, Joseph Gaonzalez, Steven Letourneau, Andrey Serov for always being there for me and making this PhD experience more fun.

All of this work was carried out at the Micro and Nanotechnology Laboratory (MNTL). Therefore, I would like to thank all the staff of MNTL for making this an amazing environment to work in. I would also like to thank Dr. Mayandi Sivaguru (Shiv) at the Institute of Genomic Biology (IGB) for helping me tremendously with confocal imaging.

None of this work would have been possible without the help of the funding agencies. Therefore, I would also like to thank my funding agencies - Army Telemedicine and Advanced Technology Research Center (ARMY TATRC), U.S. Army Medical Research & Materiel Command (USAMRMC), and National Science Foundation Science and Technology Center on Emergent Behaviors of Integrated Cellular Systems (EBICS).

In the end and probably the most important, I would like to thank my mom and dad for their unconditional love and support throughout my life. I could not have done this PhD or for that matter anything in my life without their help and guidance. Thank you very much for being the best parents in the world!

# TABLE OF CONTENTS

# CHAPTER 1

# INTRODUCTION

The demand for organ transplantation has rapidly increased over the past few decades. However, there is a huge crisis in meeting this additional demand. Currently, the transplantation of vital organs like kidney, heart, liver, and lung is the only treatment for their end-stage failure. Every day, about 79 people receive some sort of organ transplant [1]. However, each day an average of 18 people die waiting for an organ transplant because of their shortage [1]. Currently, in the US alone, there are over 116,537 people waiting for an organ transplant [1]. Even after organ transplantation, rejection by the immune system remains a central issue [2]. One way around the problem of organ transplantation is to grow tissues/organs *de novo* using stem cells in the lab.

Tissue engineering and cellular therapies in combination with therapeutic development have the potential to revolutionize modern medicine and significantly impact human health globally [3]. The translation of basic biomedical research into a drug that could impact and improve human health is a very intricate process and it requires a series of complex steps starting from: target discovery, target validation, assay development, screening and hits to leads, lead optimization, development, clinical trials and introduction in the market [4]. As a result of this tedious but necessary process, the average length of time from target discovery to approval of a drug currently averages 12-15 years [5]. Fewer than 5% of all compounds that are screened enter pre-clinical development and only 2% of these candidates enter clinical setting [5]. Of all the drugs that make it to the Phase I trials, around 80% fail during development [5]. Currently, animal models are used for drug testing and therapeutic validation. This process is very time consuming, costly and many times does not accurately predict the efficacy of the drug in humans [4, 6]. As a result of this, the compounds that are cleared in Phase I trials, sometimes fail in Phase II or Phase III trials [4]. Therefore, the cost of a successful drug ac-

counting for all failures is in excess of $1 billion [7, 8]. Therefore, there exists a need to test the drug on entities which have a much closer representation to humans and show a closer approximation of the native function [6, 9].

Pluripotent stem cells (PSCs) might hold the promise to shorten the screening process for drugs by providing an alternate pipeline and for growing new tissues/organs [4]. Differentiated PSCs will be better at testing the efficacy of drugs for human because of their physiological relevancy and rich biological utility. PSCs have the capacity to differentiate into a variety of cells of the three primary germ layers ectoderm, mesoderm, and endoderm [10, 11, 12, 13]. Thus from a single and potentially limitless starting source, most of the cells types in the body that could be affected by drugs could be tested [14]. However, directing their differentiation into the desired cell type with a high purity still remains a grand challenge [15, 16, 17]. It is becoming increasing clear that the cellular micro-environment plays a big role in influencing the fate decisions of these stem cells [18, 19]. Within each of these niches, cells are presented with a myriad of biological, chemical and mechanical cues which exert a variety of complex signals to collectively influence the two hallmark properties of mammalian cells [20, 21]. However, it is often very difficult to simultaneously mimic the bio-chemical and the bio-physical cues of the natural niche in an engineered three dimensional micro-environment. This presents a major bottleneck in reconstructing the native niche and differentiating stem cells.

This work focuses on systematically breaking down the micro-environmental cues of stiffness, geometry, and topography to individually study their influence on a variety of mammalian cells and thereby controlling their fate. Finally, all these cues are combined together in the same hydrogel construct to build a robust platform which can be used for controlling the fate of a variety of cells including embryonic stem cells in three dimensions. Chapter 2 will focus on the background of micro-environmental cues and its importance in controlling the fate of mammalian cells. Some of the key relevant literature to date on the importance of micro-environmental cues will be addressed. Also, the grounds for using differentiated cells/tissues for drug screening and tissue engineering applications will be established. Next, Chapter 3 will show how the elasticity (stiffness) of the substrate can be used to alter both the morphological and cytoskeletal structure of embryonic cardiac cells. Chapter 4 will use micro-contact printing ($\mu$CP) to constraint C2C12 muscle

cells in specified geometries and study the influence of geometrical cues on the process of myogenesis. Chapter 5 will introduce a new class of carbon based organic material, graphene, for tissue engineering applications. This chapter will also show the influence of graphene on the differentiation of C2C12 muscle cells. Chapter 6 will then combine the different cues of stiffness and geometry together in three dimensional (3D) hydrogel constructs. Using two different technologies of dielectrophoresis (DEP) and stereolithography (SL), 3D hydrogel constructs with physiologically relevant stiffnesses and micro-scale geometry will be fabricated. These constructs will also show the micro-scale patterning of embryonic stem cells (ESCs), C2C12 muscle cells, mouse embryoid bodies (mEBs) and hence truly mimic the *in vivo* native micro-environment. Chapter 7 will present some preliminary data on the differentiation of ESCs using these micro-environmental cues in 3D hydrogel constructs. Finally, chapter 8 will conclude this dissertation and present some ideas for taking this work to the next step.

# CHAPTER 2

# BACKGROUND AND LITERATURE REVIEW

In this chapter, the relevant background information about tissue engineering and regenerative medicine will be presented in section 2.1. Since, tissue engineering is such an enormous field; the focus of this chapter will be mostly on muscle tissue engineering both cardiac and skeletal muscle. In section 2.2 some of the key recent work that has shown the importance of the cellular micro-environment (stiffness, geometry, topography, roughness, and dimensionality) in controlling the fate of cells in both two dimensional (2D) and 3D scaffolds will be highlighted.

## 2.1 Background

Currently, in the US alone, there are over 116,537 people waiting for an organ transplant [1]. However, each day an average of 18 people die waiting for an organ transplant [1]. These deaths are solely due to the fact there are more people on the waiting list then there are available organs. Currently, the transplantation of vital organs like kidney, heart, liver, and lung is the only treatment for their end-stage failure. People waiting for a kidney transplant have to wait many years hooked up to a dialysis machine before finally getting a new organ. In the case of heart, patients spend months or even years on end in a hospital bed waiting for a new heart. Furthermore, if one is above $\sim$75 years or so and suffering from some type of cardiovascular disease (CVD), one might never receive a new heart. Any hearts that are donated might go to a younger patient. But what if a new heart can be grown from your own body cells? Then as long as one is fit enough to undergo surgery, he/she would be able to get a new heart which would be as healthy as one had when they were young. This technology is termed as organogenesis, *de novo* growth of organs.

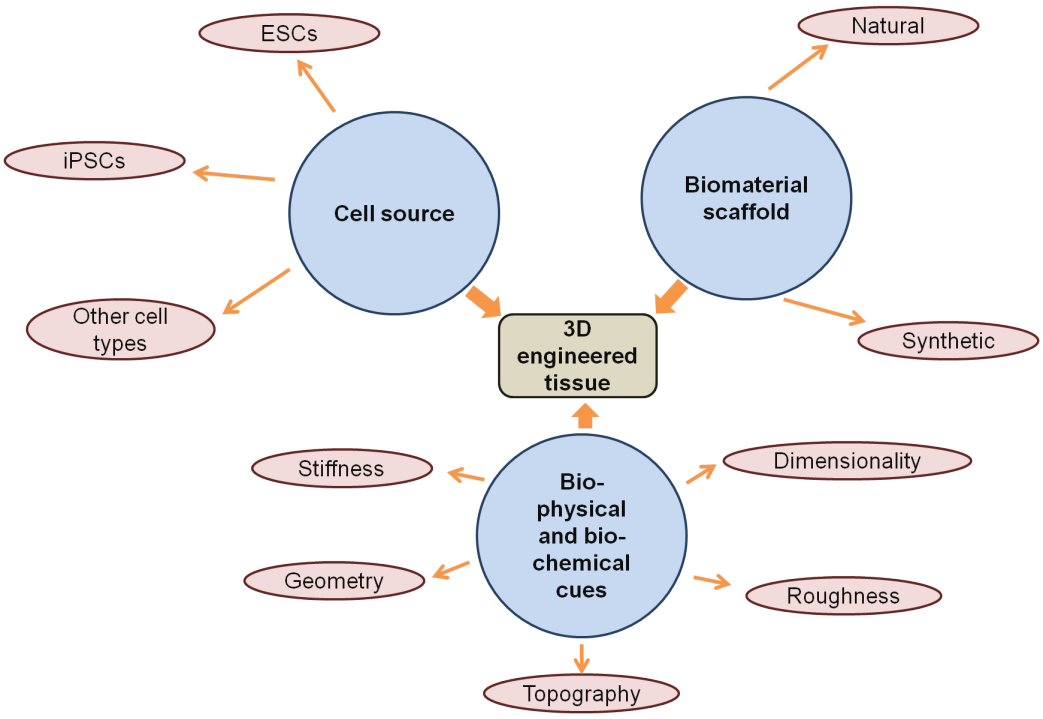


Figure 2.1: Tissue engineering triad consisting of cells, biomaterial, and bio-physical/bio-chemical cues for fabricating a 3D tissue engineering construct and its various components.

### 2.1.1 What is tissue engineering?

Tissue engineering was first defined by Drs. Langer and Vacanti as "an interdisciplinary field that applies the principles of engineering and biology towards the development of functional substitutes for damaged tissues [22]."Technologies like organogenesis, tissue engineering and regenerative medicine have a significant overlap. These are relatively new fields where living cells, bio-compatible materials, and bio-physical/bio-chemical cues are combined together to create tissue-like structures (Figure 2.1) [23]. Each of these (cell source, bio-materials, and cues) presents their own set of challenges and optimization of each parameter is required to fabricate a fully functional 3D tissue construct. Ideally, one would like to have ESCs or induced pluripotent stem cells (iPSCs) encapsulated in a 3D biocompatible, bio-degradable material which provides these cells with the same set of physical, chemical, and biological cues as seen in a growing embryo. ESCs are pluripotent stem cells and therefore able to differentiate into multiple cell types of the three primary germ layers - ectoderm, mesoderm, and endoderm [3]. Therefore, any tissue

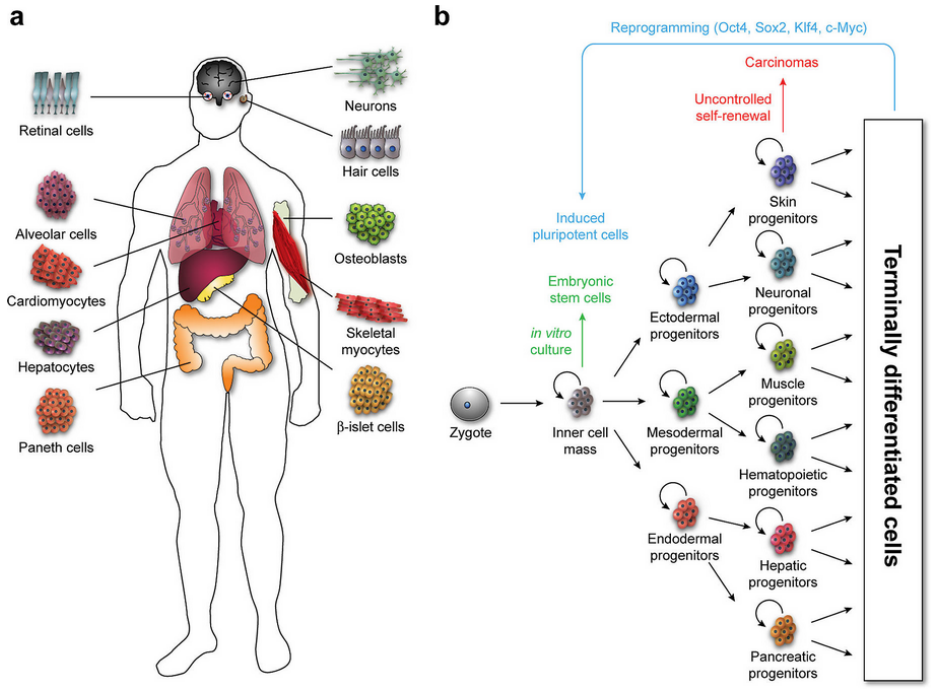


Figure 2.2: (A)Specialized cells of the human body. (B) Self-renewal and differentiation potential of ESCs and iPSCs. Image taken from [25].

of the body can be theoretically derived from these pluripotent stem cells. iPSCs are a type of pluripotent stem cells which are derived from somatic cells by a forced expression of a set of four genes - Oct3/4, Sox2, Klf4, and c-Myc [24]. Figure 2.2 shows the specialized cell types in the human body and schematic representation of self-renewal and differentiation of ESCs and iPSCs.[25] Bio-materials can be natural (hyaluronic acid, collagen, etc.) or synthetic (poly (lactic-co-glycolic acid) (PLGA), poly (ethylene glycol) di-acrylate (PEGDA), etc.) and should be bio-compatible, bio-degradable and match the physical properties of the tissue that is being fabricated [26]. In addition, in order for the scaffold to be clinically and commercially viable, it should be easily fabricated by a manufacturing technology that allows for its batch production. In terms of the cues, the scaffold should be able to mimic the micro-environment of the native tissue being fabricated in terms of stiffness, geometry, and topography. Capturing all these cues to differentiate cells in a 3D bio-compatible, bio-degradable material is therefore a very challenging task and to date there have been no reports to develop complex organs like heart, lungs, and kidneys *de novo* [27].

### 2.1.2 Examples of tissue engineered constructs

Significant progress has been made in the field of tissue engineering since the coining of this term in 1987 [23]. Researchers have tried 3D tissue engineered constructs for a variety of tissues/organs like - heart [28], lungs [29], cartilage [30], bone [31], skin [32], etc. An example of a tissue engineered construct for each of the germ layers, ectoderm (skin), mesoderm (heart), and endoderm (lung) is presented below.

Tissue engineered skin:

Skin is the largest organ of the body and critical to the survival of the organism by providing a barrier between the intra and extra cellular environment. Every year about 450,000 people receive medical treatment for burn injuries in the US and about 3,500 of these people die due to severe burns [33]. Engineered skin substitutes can provide critical medical treatments to the burn victims. To date, this is the only organ for which commercially available products are available [34]. Both autografts and allografts are available, however, for an autograft it may take upto 3 weeks before it can be implanted back on to the patient. Allografts are available off the shelf and have to the cryopreserved and banked. The type of product to be used depends on the extent of injury. The basic idea is to incorporate fibroblasts and keratinocytes in a bio-compatible material to mimic the multi-layered nature of skin. Lee et al., used a 3D bio-printer to systematically pattern multiple layers of collagen, fibroblasts, and keratinocytes resulting in two distinct layers of inner fibroblasts and outer keratinocytes in the cell hydrogel composite [35]. Both the fibroblasts and keratinocytes were highly proliferative in this collagen based hydrogel. Figure 2.3A shows their schematic of layer-by-layer printing and figure 2.3B shows a confocal stack of this multi-layered skin construct. Commercially available skin grafts like Karoskin, Apligraf, OrCel, PolyActive, and TissueTech can also be used to treat wound injuries [34].

Tissue engineered heart:

CVD are the leading cause of death worldwide and currently around 22 million individuals live with a possibility of heart failure [36, 28]. Therefore, a

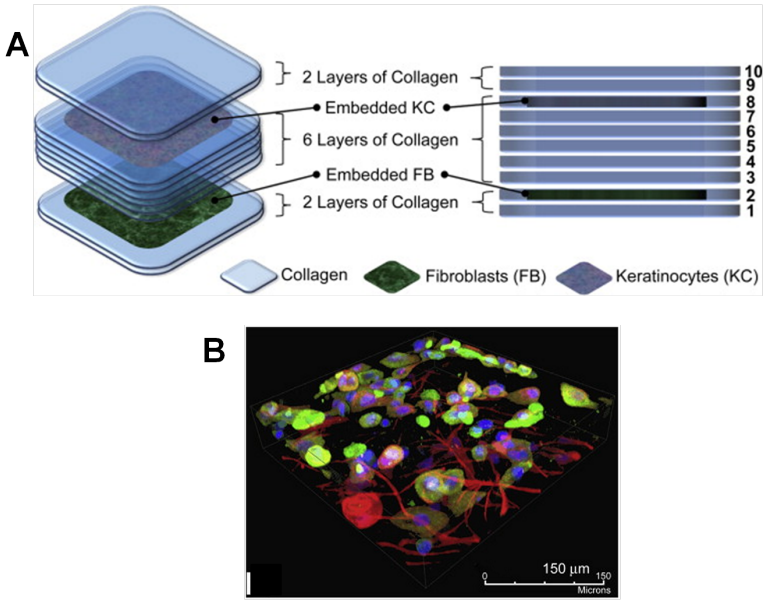


Figure 2.3: (A) Layer-by-layer printing of fibroblasts and keratinocytes using a 3D bio-printer. (B) Confocal stack of the multi-layered skin. Image taken from [35].

bio-artificial heart can be an alternative to transplantation and will benefit a very large population. Otto et al., fabricated a bio-artificial heart using nature's platform [28]. They decellularized a cadaveric heart using sodium dodecyl sulphate (SDS) for 12 hours using antegrade coronary perfusion shown in figure 2.4A. This lead to removal of cells, DNA, and intracellular structural proteins leaving behind only collagen I, III, laminin and fibronectin in the decellularized heart matrix. As a result, the fiber composition and orientation of the myocardial extra-cellular matrix (ECM) was preserved. This served as the "nature's scaffold" on which neonatal cardiac and endothelial cells were seeded. First, they showed that the perfused 2D culture showed tissue formation and maturation to a higher degree versus the control. As early as 4 days in the culture, contracting cellular patches were seen and lead to synchronized tissue rings by day 9. Next, whole-heart experiments were done where the decellularized heart was mounted on a bioreactor and seeded with freshly isolated neonatal cardiac cells shown in figure 2.4B. Sterile cell culture conditions were maintained to simulate systolic and diastolic medium flow through pulsatile heart perfusion. In addition to maintaining physiological pressures, they also provided electrical stimulation through epicardial leads to simulate the contraction of heart muscle. They maintained these

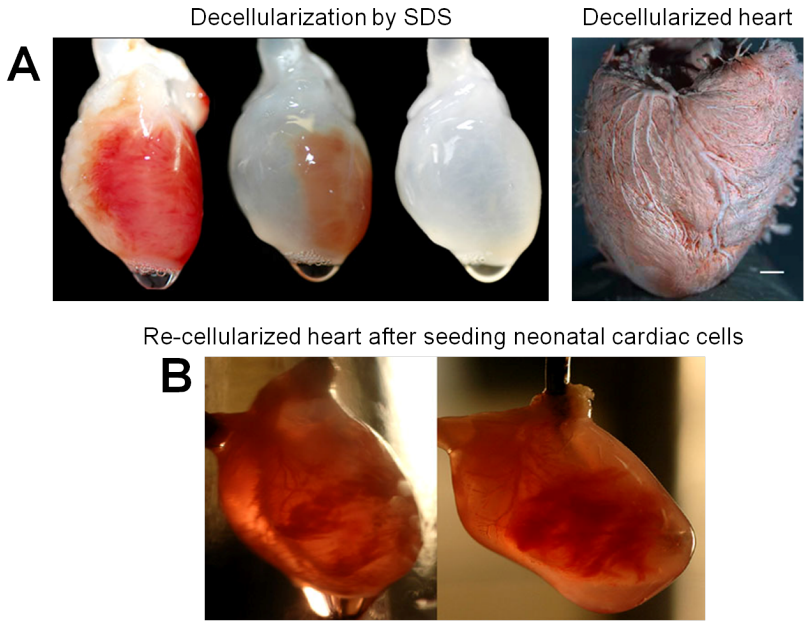


Figure 2.4: (A) The process of decellularization of heart using SDS and the decellularized heart. Scale bar = 1 mm (B) Recellularized heart after seeding it with neonatal cardiac cells. Images taken from [28].

constructs under these conditions for upto 28 days. As early as 8 days in the culture, increase in left ventricular pressure (LVP) was seen and repolarizations could be recorded. These bio-artificial hearts were able to generate forces equivalent to 2% of adult and 25% of a 16-week fetal heart. Even though very small forces were generated by these bio-artificial hearts, this study did meet three important milestones of tissue engineering:

- Engineered a construct to provide an architecture for cell attachment.
- Populated that construct with the appropriate cell type and composition.
- Showed construct maturation with appropriate function.

This study showed the importance of the cellular micro-environemnt in maintaining cell function. Since, nature's own ECM was used, the material properties were highly controlled which enabled the cells to proliferate and perform their function of beating as early as 8 days in the bio-reactor culture. Even though this study did not show *de novo* organ development, it showed an engineered 3D heart tissue which was able to perform some of the ba-

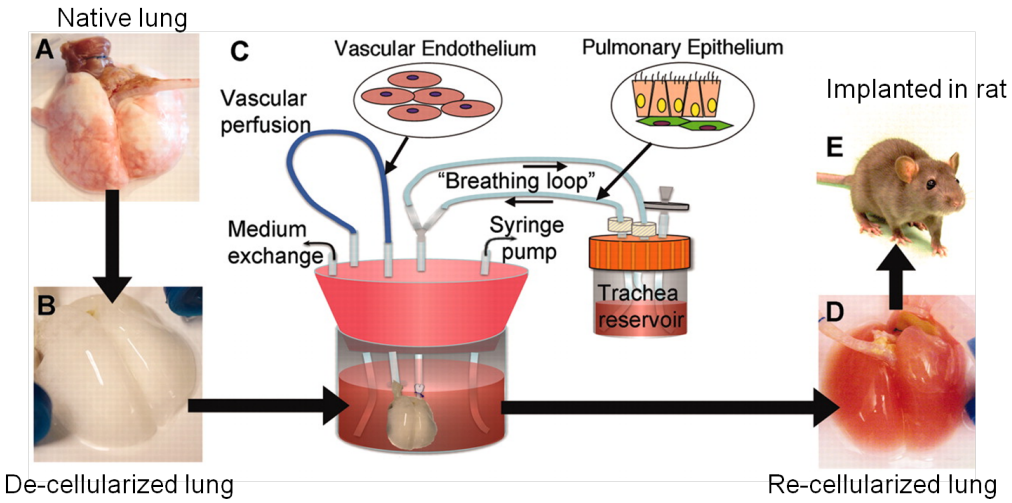


Figure 2.5: Schematic for lung tissue engineering. Image taken from [29].

sic functions and maintained synchronous contractions for upto 28 days in culture.

Tissue engineered lung:

Lung diseases account for over 400,000 deaths in the US alone [37]. Adult lung has little to no regenerative capacity and therefore lung transplant is the only option for patients with end-stage lung failure. However, given the huge deficiency of transplanted organ, a tissue engineered lung would be extremely beneficial. Decellularization was used by Petersen et al. for regenerating the lung tissue [29]. Using a zwitterionic based detergent, they decellularized the lung tissue to remove all the cellular constituents but retaining the micro-architecture. After this, they repopulated this ECM with mixed populations of neonatal rat lung epithelial cells and vascular endothelial cells in correct anatomic locations by using a perfusion based bioreactor system. The bioreactor also enabled to enhance the viability and differentiation of the lung epithelium. Finally, to check the functionality of the engineered lung, it was implanted back in the rodent and the lung participated in gas exchange for short periods of time. Figure 2.5 summarizes their approach. This study again highlights the importance of the cellular micro-environment in controlling the differentiation of cells. Since, nature's own ECM was used, the physical, chemical, and biological properties of the ECM matched to the na-

tive tissue and therefore the lung epithelial cells were able to differentiate and function efficiently.

### 2.1.3 Tissue engineering triad for heart

In addition to developing an entire organ (for example: heart, lungs, kidneys, etc.), 3D tissue engineering can be used to make tissue constructs that can re-establish the structure and function of the injured organ. This will be extremely beneficial especially in the case of myocardial infarction where interruption of blood supply resulting from a blocked coronary artery leads to the death of heart cells [38]. The whole idea here again would be to provide the cells - the actual "tissue engineer" highly controlled 3D micro-environment which would allow cell differentiation and functional assembly. Specifically, for cardiac regeneration, some of the key requirements would be a cell source, ideally human, establishment of a cardiac specific ECM, coupling between the cells to provide an electromechanical feedback loop, and functional vascularization [38]. The choice of cell source is central to any tissue engineered organ as cells drive regeneration based on the set of cues received by them from the micro-environment. Since, mature cardiac myocytes have very limited capacity to divide, it is very important to choose a cell source that can re-establish the myocardial structure and function at multiple hierarchical levels [38, 39]. The most obvious choice is the use of ESCs as the cell source for cardiac regeneration. Various reports have shown the differentiation of ESCs to cardiac progenitors [40, 41, 42, 43]. With the recent advances of the iPSC technology, these cells also emerge as a viable source for cardiac regeneration [44, 45]. An added advantage of iPSCs would be the immune tolerance, since, they would be derived by an autologous source. Other preferred cell choices should also have this autologous requirement to prevent immune rejection. Bone marrow derived adult stem cells, adipose derived stem cells, adult skeletal myoblasts, and resident cardiac stem cells can all be used as a cell source for cardiac regeneration [38].

It would only be possible to differentiate the above mentioned cells to cardiac specific cells by providing them the right environmental cues. Thus the choice of biomaterial is of utmost importance. Ideally, a biomaterial should be chosen which can mimic the properties of the cardiac matrix in terms

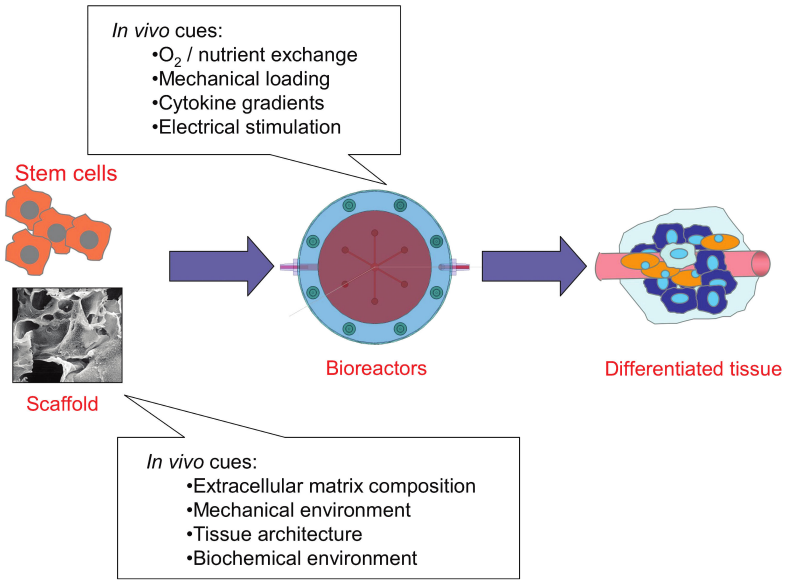


Figure 2.6: The basic method for 3D stem cell based culture for 3D cardiac tissue engineering. Image taken from [38].

of its physical composition, chemical, structural, and mechanical properties [38]. The biomaterial should allow the cells to proliferate and differentiate and could be natural, synthetic or a combination of both. It would however be easier to control the physical, chemical and structural properties of a synthetic matrix. Either natural or synthetic, it will be important for the scaffold to capture the entire milieu of the native cardiac ECM and should be able to degrade the matrix and replace it with its own matrix [38]. The matrix should have an elasticity close to that of the muscle (8 - 17 kPa) and should have an ideal geometry as well which would allow the cells to match the hierarchical structure of the cardiac muscle [38, 46]. Also, the scaffold should allow for vascularization as the thickness of tissue increases because the diffusion of factors would be limited to the first 200 $\mu$m of the scaffold [47]. *In vitro* use of a bioreactor can be useful for enhancing the diffusion of nutrients through the scaffold/tissue construct. Figure 2.6 summarizes the basic strategy for a 3D stem cell culture for cardiac tissue engineering.

### 2.1.4 Strategies for 3D tissue engineering

There are four basic type of scaffolding approaches in tissue engineering [48]:

- Pre-made porous scaffolds

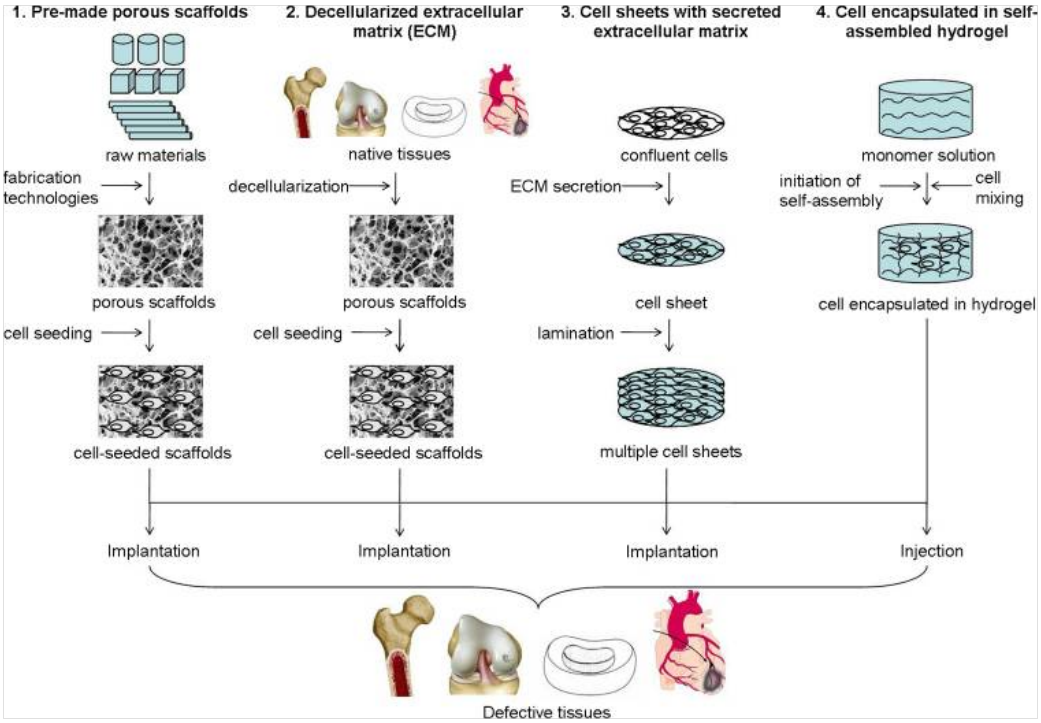


Figure 2.7: Schematic showing the scaffolding approaches in tissue engineering. Image taken from [48].

- Decellularization
- Cell sheet stacking
- Cells encapsulated in a hydrogel

Figure 2.7 shows these four basic strategies for tissue engineering. Each of these strategies have their own set of advantages and disadvantages and use different bio-material (natural or synthetic) as the starting source. Furthermore, each of these scaffolding techniques have different fabricating or processing technology. This review will briefly talk about each of these techniques [48].

Pre-made porous scaffolds for cell seeding:

Using pre-made porous scaffolds allows for the most diversified choices of biomaterials and fabrication technology as the cells are seeded after the scaffolds are completed. The scaffolds seeded with the cells can be incubated under

cell culture conditions with specific growth factors and finally can be implanted in the host tissue. However, this is very time consuming and leads to inhomogeneous cell distribution. This fabrication modality could be applied to both soft as well as load bearing hard tissues.

Decellularized extracellular matrix for cell seeding:

This leads to the most nature-simulating scaffolds as it uses nature's own ECM. The scaffold mimics the physical, chemical and biological properties of the native tissue and therefore allows for very high degree of cell proliferation and differentiation. However, a source donor is required which makes the technology not commercially viable because of the huge shortage of donors. Furthermore, since the raw materials are allogenic or xenogenic, immune rejection can be a big problem in case of incomplete decellularization. This scaffolding strategy can be applied for tissues which have a high degree of ECM like heart, lungs, etc.

3D cell stacking:

Generally, most of the cell culture is done on 2D cell culture plates. However, a 3D tissue is required for re-establishing the structure and function of an injured organ. Various techniques have been applied for creation of 3D tissue constructs. Shimizu et al., proposed stacking of 2D cell sheets on top of each other to create a 3D sheet [49]. By using thermo-responsive polymers like Poly(N-isopropylacrylamide) (PNIPAAm), they were able to extract intact cell sheets without disrupting the cellular gap junctions and other cell surface proteins. By stacking these individual 2D sheets on top of each other they were able to obtain 3D sheets. Electrical communication between the sheets was verified by layering two sheets on top of one another and recording their spontaneous action potentials. However, multiple laminations are needed for making a thick construct. Since, no other material is involved, this strategy is extremely bio-compatible. It can be applied for tissues which have a high degree of cell density like epithelial and endothelial tissues.

Cells encapsulated in self-assembled hydrogels:

This strategy allows for the most efficient functioning of cells as there is intimate cell and bio-material interactions. It allows for the cells to use their "tissue engineering" abilities to remodel the matrix based on their own needs. However, being in hydrogel, this scaffolding strategy can only be used to make soft tissues. Hard load bearing tissues like bone cannot be repaired using this technique. However, it allows the use of both natural and synthetic bio-materials. It also allows for multi-cell and multi-material encapsulation during the fabrication of scaffold. Researchers have used this technology widely just by itself or in combination with other techniques to allow for mimicking the native tissue function. For example, Jeong et al., used this scaffolding strategy to create "living" micro-vascular stamps that allows for the release of multiple angiogenic growth factors and subsequently creates neo-vessels with the same pattern as that engraved in the stamp [50]. Another example was that of combining soft-lithography with hydrogel fabrication to create highly aligned, differentiated skeletal muscle constructs by Bursac et al [51, 52]. They combined cell laden fibrin hydrogel with polydimethylsiloxane (PDMS) molds containing an array of elongated posts. The cell laden fibrin hydrogel compacted around the PDMS posts resulting into a highly porous network which composed of densely packed, aligned and highly differentiated myofibers. The differentiated myofibers expressed myogenin, showed cross-striations, and spontaneous contractions indicators of a functional 3D tissue. Figure 2.8A shows the PDMS posts and the fibrin/cell hydrogel being seeded on the posts. After 2 weeks in culture, fibrin gel contracts around the posts and thus the hydrogel takes the form of a criss cross mesh. Fluorescent images in figure 2.8B show the striations and the distribution of nuclei in the hydrogel. In order to create a fully functional 3D tissue a combination of these strategies would be needed to meet the needs of the native tissue.

### 2.1.5 Drug discovery/screening with tissue engineered construct

In addition to repairing an injured organ, an engineered 3D tissue can also serve as a novel tool for drug discovery and screening. The development of new drugs is very costly and time consuming especially during the early stages

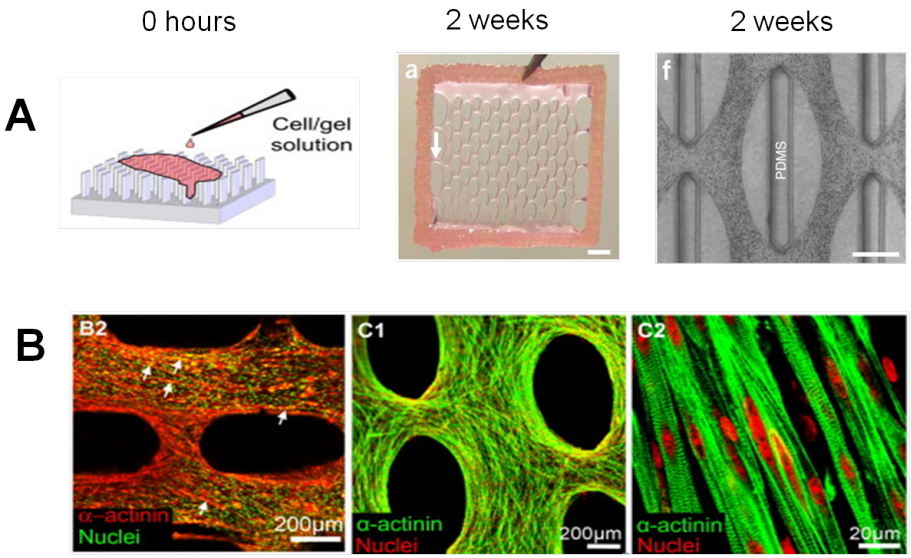


Figure 2.8: (A) Schematic of the PDMS posts with the cell-fibrin cell being seeded on it. Next image shows a 14 × 14 mm fibrin gel after two weeks, scale bar = 2mm. The last image in (A) is a phase-contrast image of cells in fibrin gel around the post, scale bar = 500 $\mu$m. (B) Fluorsencet images showing the distribution and differentiation of skeletal muscle cells in the fibrin gel. Images taken from [51, 52].

of research and development where *in vitro* models are required to screen the activity and toxicity of thousands of compounds [14, 53]. Generally, animal models or highly proliferative immortalized cancerous cell lines are used for testing of compound libraries. However, they do not necessarily provide the effect of the compound on normal human cells or the specific cell type under normal conditions [14]. Since, ESCs can provide a close approximation of the native function of cells, previous studies have suggested using them as a screening platform to identify low molecular weight compounds and for drug screening [17, 53, 54, 55]. These small molecules thus discovered can then be used to affect endogenous stem cell populations and repair damaged tissues. Both primary (high-throughput screening (HTS)) and secondary screening can be performed using these stem cells [53]. A recent HTS of a library of 2.4 million compounds using an mESCs indentified novel chemical "hits" for $\alpha$-amino-3-hydroxyl-5-methyl-4-isoxazolepropionate-subtype glutamate receptors and characterized the structure-function relationships of compounds and receptors [56]. Another study screened 1040 compounds using a human ESC (hESC) colony based assay [57]. This study was an image-based,

high-content assay to screen compounds that affect the survival and pluripotency of hESCs. Several steroids that promoted the differentiation of the hESCs were identified and the anti-hypertensive drug, pinacidil, was shown to affect the survival of hESCs. Before a drug enters mechanistic study, the compounds assayed by primary screens can be further confirmed by a series of more functional secondary assays like the structure-activity relationship and the pharmacokinetic properties on the stem cells [58, 59]. In addition to screening these small molecules as only drugs for the treatment of degenerative diseases, they can also be used to lower the oncogenic potential of iPSCs and increase their programming efficiency [53]. These iPSCs could then be used as an additional cell line that can be used in conjunction with ESCs as they contain the genetic information of the patients and reflect their physiological and pathological conditions. The iPSCs could also be generated from patients with specific disease traits, thereby allowing for more relevant drug screens and the idea of personalized medicine could be possible [14]. The small molecules identified can also affect the fate of the hESCs themselves as shown by Barbaric et al [57]. hESCs could also been used for toxicology analysis [60, 61]. The ReProGlo assay allowed for screening of several test chemicals and embryo toxicants like retinoic acid (RA) and lithium chloride that induced the inhibition of ESC differentiation [53].

## 2.2 Literature review

In the last section, the field of tissue engineering was briefly discussed. Also, some of the strategies that are currently used to make 3D scaffolds were highlighted. This section will present a review of some micro-environmental cues that control the fate of the cells for fabricating these 3D tissues. As cells are the actual "tissue engineers" they need to be presented with cues that mimics the native *in vivo* cues. These cues can be thought of as the raw materials and conditions required by the cells to build a 3D tissue architecture. First, the process of mechanotransduction will be briefly explained as this is responsible for translating the physical cues of the environment to a biological signal inside the cell. Next, the importance of five different cues stiffness, geometry, topography, roughness, and dimensionality will be highlighted. This is not an exhaustive list of the cues experienced by the

cells. Many other cues like electrical signals, growth factors (soluble and attached), cellular density, etc. also play an important role in determining the final state of the cell. However, this review will only focus on these five cues as these have been widely used in the literature for controlling the fate of cells.

### 2.2.1 Mechanotransduction

Cells sense their physical surroundings through the process of mechanotransduction and respond by changes in adjusting their gene expression, differentiation, proliferation, apoptosis, migration, and extra-cellular organization [62]. Mechanotransduction is the translation of mechanical forces to biochemical signals by activation of a variety of different signaling pathways and changes in intracellular calcium concentration [62]. Thus this mechanosensitive feedback is of critical importance for organogenesis and homeostasis. It is ubiquitously found in nature and is present from the most primitive to the most complex organisms. For example, skeletal muscles respond to exercise by hypertrophy, vascular smooth muscle cells maintain a constant blood pressure by constricting or dilating the blood vessels, the displacement of the stereocilia in the inner ear allows hearing, etc. [62]. In all these and many other day-to-day activities, the cells in the body are responding to a variety of physical forces by the process of mechanotransduction. Most of the cells in the body have stretch-activated ion-channels that respond directly to these forces or this force sensing can also be done by the family of GTPases. Figure 2.9 shows the molecules involved in cell in the translation of forces from the ECM to the nucleus [62]. Focal adhesions (FAs) which are made of transmembrane integrin receptors along with vinculin, talin connect the ECM to the actin filaments. Depending on the affinity of the integrin receptors to the scaffold/ECM complex, its configuration changes. This change is cascaded to the nucleus through actin filaments, intermediate filaments, and microtubules *via* nesprin and plectin. These nesprins then bind to SUN1, SUN2 and nuclear lamins. Finally, nuclear lamins can bind to DNA and thus the signal from the ECM gets propagated all the way to the nucleus [62]. FA formation is the beginning of this elaborate mechanosensitive feedback cycle and dictates the functional response of a cell to mechanical aspects of the

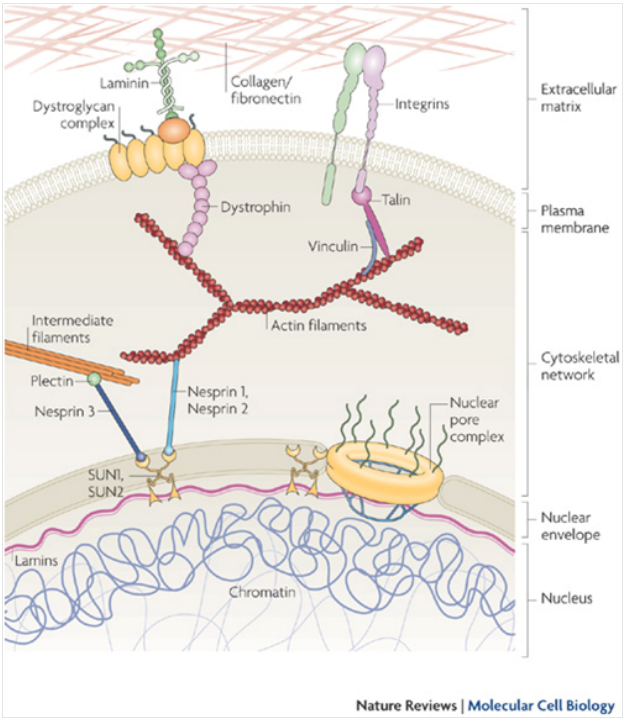


Figure 2.9: Force transmission between the ECM and the nucleus. Image taken from [62].

scaffold.

In cardiac cells and skeletal muscle cells, mechanotransduction plays a huge role in determining the fate of the cell as these cells are constantly responding to mechanical forces of stretching/contracting and fluid shear. Specifically, in cardiac cells, the stretch activated ion-channels located in the phospholipid bilayer act as efficient mechanosensors even in the absence of ligands. These sensors activate multiple cellular pathways like the Ras/Rho and mitogen-activated protein kinase (MAPK) that leads to calcium/calcineurin mediated signaling and micro RNAs [62, 63]. This leads to the expression of genes which are involved in the hypertrophy of muscles and causes increase in the length and width of myocytes. Thus this mechanosensitive feedback loop allows the heart to remodel its surrounding ECM which is also referred as cardiac re-modeling [62]. Figure 2.10 shows the process of mechanotransduction and the complex signaling cascade involved [62].

Figure 2.11 shows the process of stretching, migration and proliferation of a cell and the key intracellular proteins involved [64]. This process of cell stretch/migration is the first response of the cell after it is seeded on the

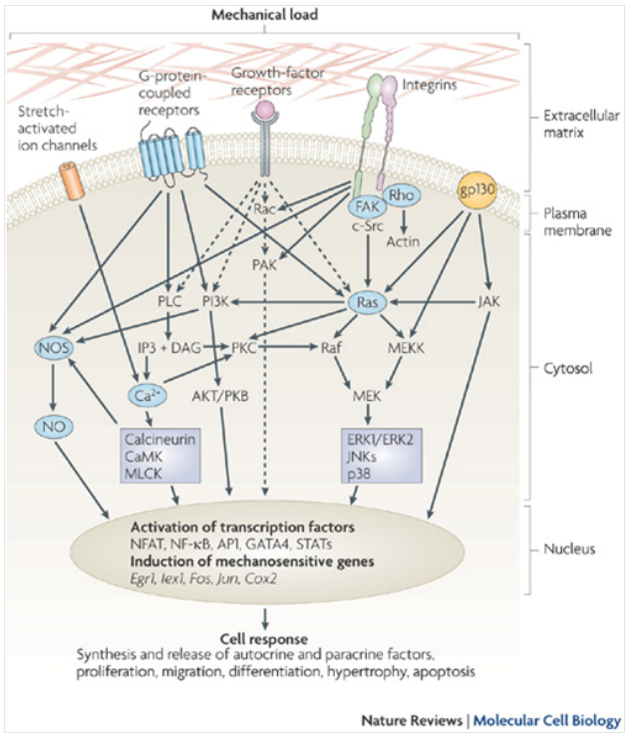


Figure 2.10: Mechanotransduction and signaling cascade in a cardiac cell. Image taken from [62]

surface and is heavily governed by mechanotransduction. First, the cell settles on the surface of the scaffold and starts sensing its surroundings by the filopodia. If the cues from the surroundings are positive, vinculin is recruited to form focal complexes at the leading edge of the cell. Until this point, there are low-affinity interactions of vinculin with talin which keeps vinculin at the leading edge of the cell for its association with actin. Only by linking with actin, vinculin gets activated and turns from a low-affinity interaction to a high-affinity association [64]. This leads to a conformational change of integrins in the FAs and leads to the formation of larger FAs and activation of the focal adhesion kinase (FAK). This also leads to the activation of the Ras/Rho family of GTPases like cdc42. From here onwards, many other downstream signaling pathways like MAPK, Janus-activated kinase (JAK), and the signal transducer and activator of transcription (STAT) gets activated. These lead to the activation of mechanosensitive genes in the nucleus which causes the cell to either spread or retract back [64]. The force generation in the cell happens by the movement of the myosin motor on the actin filaments which allows the stabilization of the FAs and results into cell stretching. Therefore,

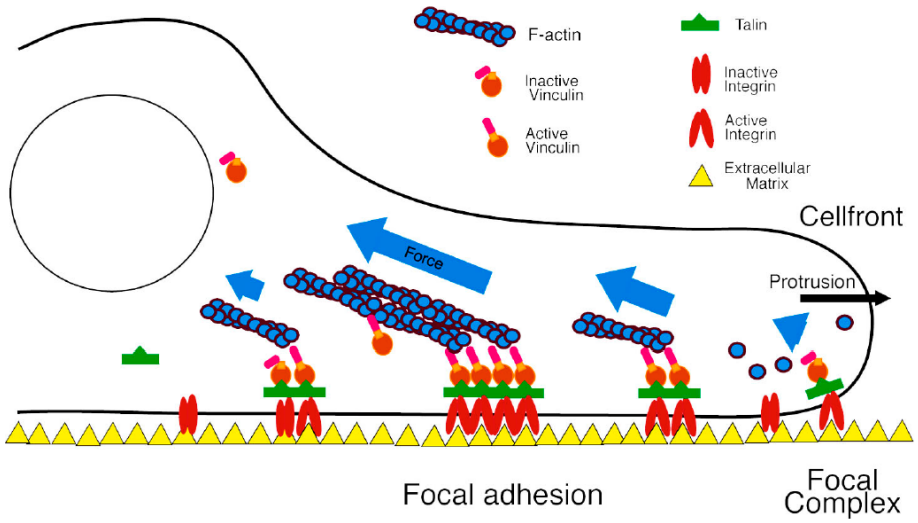


Figure 2.11: Schematic showing the model of a cell stretching on a substrate. Image taken from [64].

on very soft substrates, very little to no cell spreading happens as there is not enough force produced by the myosin motors to stabilize the FAs leading to their disassembly. However, on rigid substrates, myosin motors are easily able to walk on the actin filaments by the stiff nature of the substrate allowing for larger and stable FAs causing the cell to spread. A very simple way to look at this phenomenon is by looking at the force balance established by a cell on the different substrates. On stiff substrates, the cells are able to support a force balance by pulling on the substrate and the substrate resisting. The soft substrate however, does not resist this pull leading to the disassembly of the FAs and thus leaving the vinculin in a low-binding affinity with talin. This does not allow the activation of any of the downstream signaling pathways of the cell which are responsible for migration and proliferation but instead it might activate the apoptotic pathway causing cell death. Thus presence of isometeric tension (prestress) at a number of different levels allows this entire process of mechanotransduction which in turn dictates the fate of the cell on a given scaffold or substrate [65]. The next few sections will show how altering the properties of the scaffold changes this process of mechanotransduction and thus cellular functions like migration, proliferation, differentiation, apoptosis, and cytoskeletal organization.

### 2.2.2 Stiffness

In order to understand the function of the cells like movement, migration, and cytokinesis it is important to investigate the mechanical properties of the cell [66, 67]. Mechanically, a cell acts both as a force and a stiffness sensor. An example of a force sensor is a hair cell which translates the mechanical pressure on the stereocilia to an electrical impulse which is picked up by the nerves in the brain. This is a passive response as no work is done and the cell merely responds to a force [67]. On the other hand, as a stress sensor (durosensor) the cell is constantly applying a stress (force per unit area) and measuring the strain (deformation). The cell then computes this stress strain ratio in order to evaluate the elasticity (stiffness) of the substrate [67]. The application of the stress on the surface is done by the molecular motors of the cell, actin and myosin. There is a constant feedback cycle and the up/down regulation of mechanosensory genes depends on the output of this stress-strain assay. Most of the cells, but not all respond to the stiffness of the substrate by modulating their initial stress and strain input. Generally, cells prefer the stiffness of their native tissue from which they were extracted or are being differentiated. That is neurons grow and spread better on soft matrices, myotubes prefer intermediate stiffness substrate while bone cells show best characteristics on rigid substrates [68, 69].

Although the exact mechanism of how the cell senses the stiffness of the substrate is unknown, research has shown that the molecular motors of the cell generate tension at the cell-substrate interface which is sensed by the cells durosensor [67]. This induces a change in some transmembrane proteins (possibly integrins) which then activates a cascade of signaling pathways [67]. Some of the proteins mentioned in sub-section 2.2.1 are then responsible for transmitting these signals to the nucleus which up/down regulates a series of genes that allow the cell to spread, migrate, differentiate, etc. on that substrate. Myosin is the leading candidate for the stress-strain generator in the cell and this tension generated by myosin gets passed on through actin filaments to flexible protiens like talin, vinculin, and other clutch proteins [70]. This causes a conformational change to the transmembrane proteins like integrins which link the cell to the ECM [67]. Figure 2.12A shows the cellular components involved in sensing the stiffness of the substrate and Figure 2.12B, C shows the schematic of a cell on a soft and rigid substrate

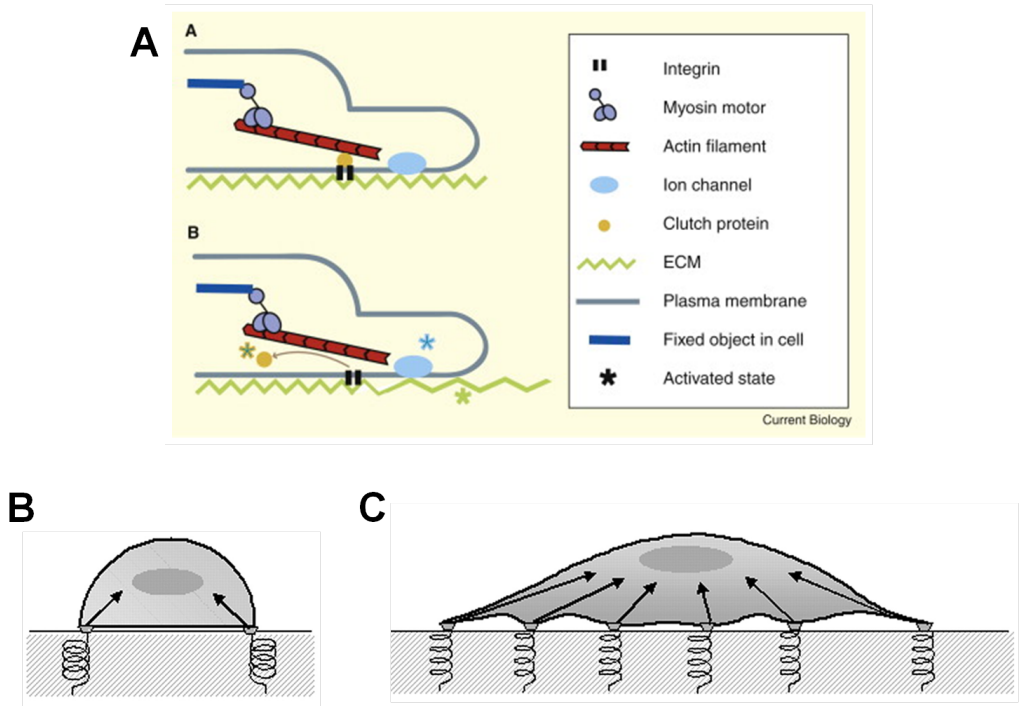


Figure 2.12: (A) Cellular components involved in stiffness sensing of the substrate. Schematic of a cell on a (B) Soft substrate. (C) Stiff substrate. Images taken from [67, 71].

respectively. When a cell pulls on the substrate with a force $P$, it displaces the substrate by a distance $x$. This force is equal and opposite of the force $F = -kx$. On a soft gel, the cell is easily able to pull the surface because of smaller $k$ as shown in figure 2.12B. However, for a stiff substrate shown in figure 2.12C, which has a larger $k$, a larger force is required to displace the matrix which leads to cell spreading and higher/bigger FAs to support this larger force [67, 71].

One of the earliest reported studies on understanding the cells' response to soft substrates was done by Harris et al., by seeding fibroblasts on thin silicone rubber, collagen matrix and looking at the wrinkling of the underlying substratum by the cells tractional forces [72, 73]. These studies were the first to show that as the cells spread on the surface, they slowly pull on it and thousands of cells moving on the soft substrata produced a striking degree of distortion and wrinkling of these soft substrates. Later, work done by Drs. Pelham and Wang showed that mammalian cells are highly responsive to the stiffness of the underlying substrate [74, 75]. They used a synthetic hydrogel which has polyacrylamide (PA) as the base polymer with bis-acrylamide as

the cross-linker to obtain substrates with a wide range of elasticity from few Pascals to tens of kilo Pascals thereby mimicking the range of physiological stiffnesses. Using this synthetic hydrogel, they showed that fibroblasts modulate their cytoskeletal organization depending on the stiffness of the substrate. Fibroblasts show increased motility and lower spreading on flexible substrates than compared with cells on rigid substrates. Furthermore, cells on the soft flexible substrates showed irregularly shaped FAs which were very dynamic while those on the stiff substrates had a normal morphology and higher stability. These studies for the first time demonstrated that cells survey their surroundings. The need to understand the intracellular changes as the cells explore their environment and the associated signaling pathways, developed the field of mechanobiology.

Many studies have been published since then which investigated the effect of substrate stiffness on a variety of different cell types like neurons [76], skin [77], muscle [78], mesenchymal stem cells (MSCs) [68], ESCs [79], fibroblasts and endothelial cells [80], cardiac cells [81, 46, 82], etc. by using this synthetic PA hydrogel. Some of these studies are discussed below. Engler et al., showed that the fusion of myocytes into myotubes is independent of the stiffness of the underlying substrate. However, the actomyosin striations, hallmark of a skeletal muscle only emerges on substrates with stiffness typical of a normal muscle (E $\sim$ 12 kPa) shown in figure 2.13A [78]. In addition, they showed that when myotubes are grown on top of a layer of glass-attached myotubes, the top layer of myotubes show striations (figure 2.13B). However, when the same myotubes are grown on the softer fibroblasts no striations are visible (figure 2.13C). This study clearly showed the importance of substrate stiffness in determining the fate of cells, in this case, the differentiation of myoblasts to myotubes. As actomyosin striations are the functional units of the muscle cells, the stiffness of the underlying substrate can determine the functionality of the cells.

Yeung et al., investigated the morphology and cytoskeletal organization of fibroblasts, endothelial cells, and neutrophils by culturing them on PA gel substrates with stiffness ranging from very soft (2 Pa) to stiff (55 kPa) [80]. On the soft substrates, ($<$ 3 kPa) fibroblasts show no stress fibers (actin filaments) and do not show much spreading. As the stiffness of the substrate increases past 3 kPa, there is an abrupt increase in the cell area. This could possibly be because the stiffness of a fibroblast is in the range of 2-5 kPa

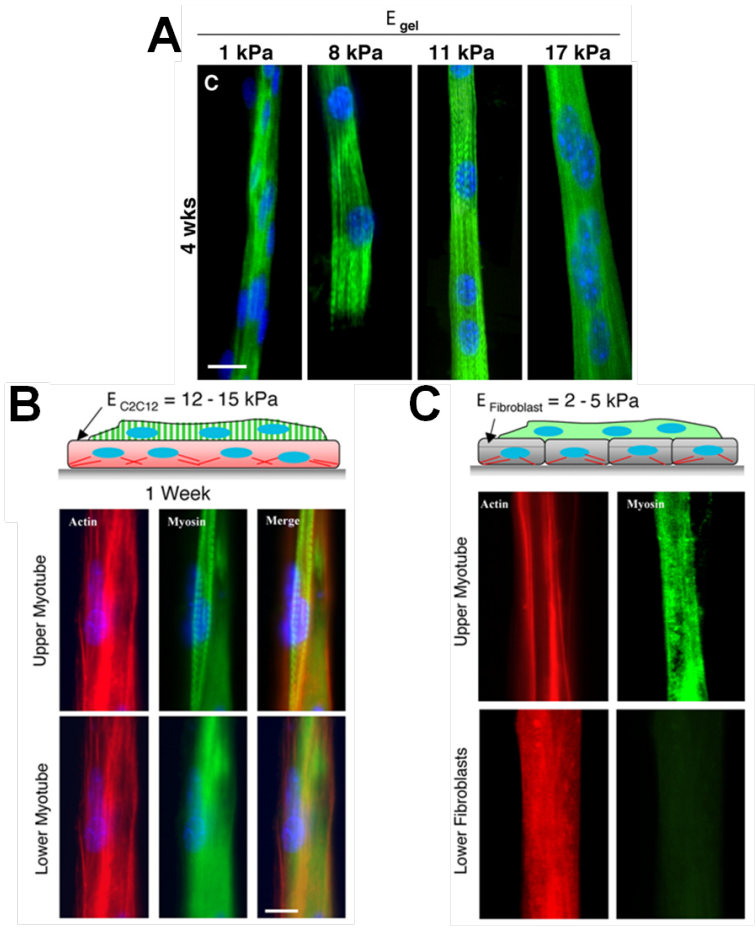


Figure 2.13: Effect of substrate stiffness on the myoblasts. (A) Myotube striation is dependent on the stiffness of the underlying substrate. (B) Myotube underlayers provide optimal stiffness for myotube striation. (C) Fibroblast underlayers are too soft for myotube striation. Images taken from [78].

[78]. However, when these fibroblasts are allowed to make cell-cell contacts, even on the soft substrate, these cells show good spreading indicating that cell-cell contact overrides cell-substrate contact.

A very interesting study done by Lo et al.,showed that cell movement is guided by the rigidity of the underlying substrate [83]. By plating NIH/3T3 fibroblasts on PA gel substrates which had a transition in the rigidity, they showed that cells from the soft side could easily migrate to the stiff side of the gel while simultaneously increasing their area on the stiff side. This directed movement of cells from the soft to the stiff side was termed as "durotaxis" or "mechanotaxis". However, the reverse of this phenomenon was not true. Cells which were present on the stiff side of the gel turned

around or retracted as they reached the boundary and never crossed the boundary to go to the soft side of the gel. As cell migration or movement plays a critical role in many physiological processes like wound healing, immune response, and tissue morphogenesis this study highlighted the importance of substrate rigidity in controlling cell locomotion.

Seminal work done by Discher et al., showed that MSCs showed extreme sensitivity to the stiffness of the underlying substrate [68]. When cultured on soft matrices (0.1-1 kPa) which mimicked the stiffness of the brain tissue ($\sim E_{brain}$ = 0.1-1 kPa), majority of the MSCs adhered, spread and showed filopodia rich morphology similar to that of a neuron. When the same cells were cultured on intermediate stiffness substrates (8-17 kPa) which mimics the stiffness of striated muscle ($\sim E_{muscle}$ = 8-17 kPa), MSCs showed a spindle shaped morphology similar to C2C12 skeletal myoblasts. Finally, by seeded these cells on rigid substrates (25-40 kPa) which is in the range of bone tissue ($\sim E_{bone}$ = 25-40 kPa), the MSCs yielded in polygonal morphology similar to osteoblasts. Figure 2.14 shows the morphology of MSCs on the different stiffness PA substrates. Micro-array profiling of these MSCs on the different substrates confirmed that cells on the soft substrates showed highest neurogenic markers, on the intermediate stiffness substrate showed highest myogenic markers while on the most rigid substrates showed highest concentrations of ostogenic markers. This matrix stiffness based cell lineage specification is based on the ability of the cells to pull on the substrates. By blocking the cellular mechanosensors (non-muscle myosin II) by blebbistatin, they showed that the stiffness based linage specification of the cell was lost. Similar studies done on ESCs also showed that stiffer substrates increased the osteogenic differentiation of ESCs compared to the softer ones [79].

Cardiac cells also show a strong dependence for the stiffness of the substrate on which they are cultured. Cardiac myocytes cultured on soft substrates showed lowest excitation threshold but increased troponin I staining. However, the force of contraction, cell elongation and cell density was reduced. Those cultured on stiffness which matched the stiffness of the native myocardium showed reasonable excitation threshold, high contractile force and well-developed striations [82].

The above mentioned studies have used PA hydrogels to modulate the stiffness of the substrate. Other hydrogel based systems both synthetic and natural like thiolated hyaluronic acid (HA) [84], collagen I [85], PDMS [86],

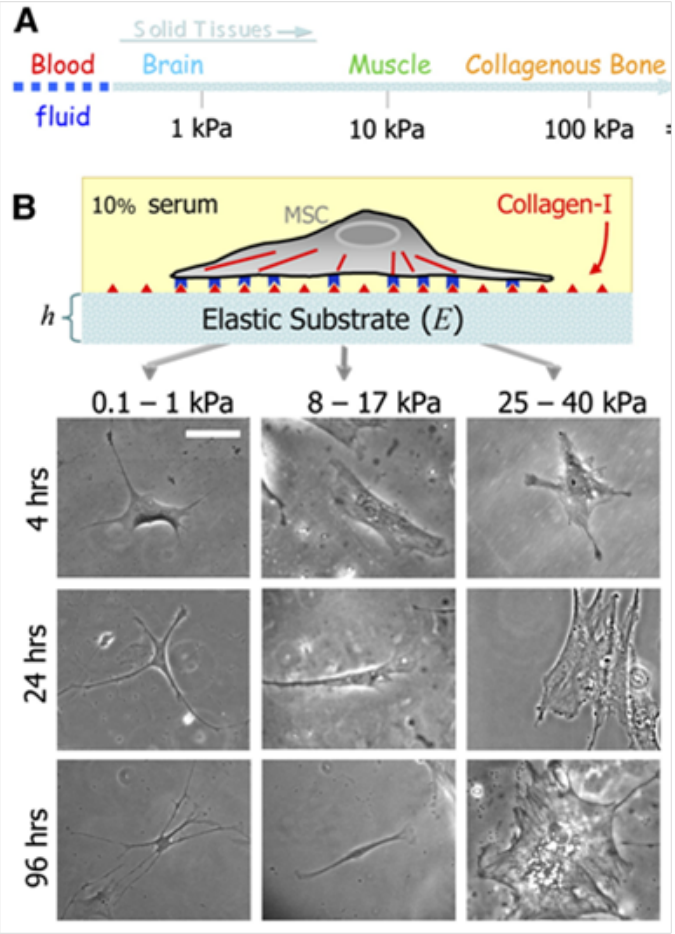


Figure 2.14: Stiffness of the substrate determines the fate of naive MSCs. Image taken from [68].

poly (ethylene glycol) diacrylate (PEGDA) [87], gelatin [88], and Poly(methyl methacrylate) (PMMA) [89] have also been used to obtain substrates with varying elasticity in both 2D and 3D cultures. The basic principle of tuning the elasticity of the substrate relies on changing the cross-linking density of the polymer by increasing or decreasing its concentration [90]. However, altering the cross-linking density not only alters substrate rigidity but also changes other material properties like porosity, surface chemistry, binding properties of ligands, etc [91, 92]. Recently, it was shown by Kumar et al., that the fate of the cell is more affected by the physical properties of the substrate than its composition [93]. In order to circumvent the problem of changing the physical properties of the substrate while changing stiffness, Fu et al., designed a clever experiment where the polymer concentration (PDMS) was kept constant to create micro-posts of varied heights to tune

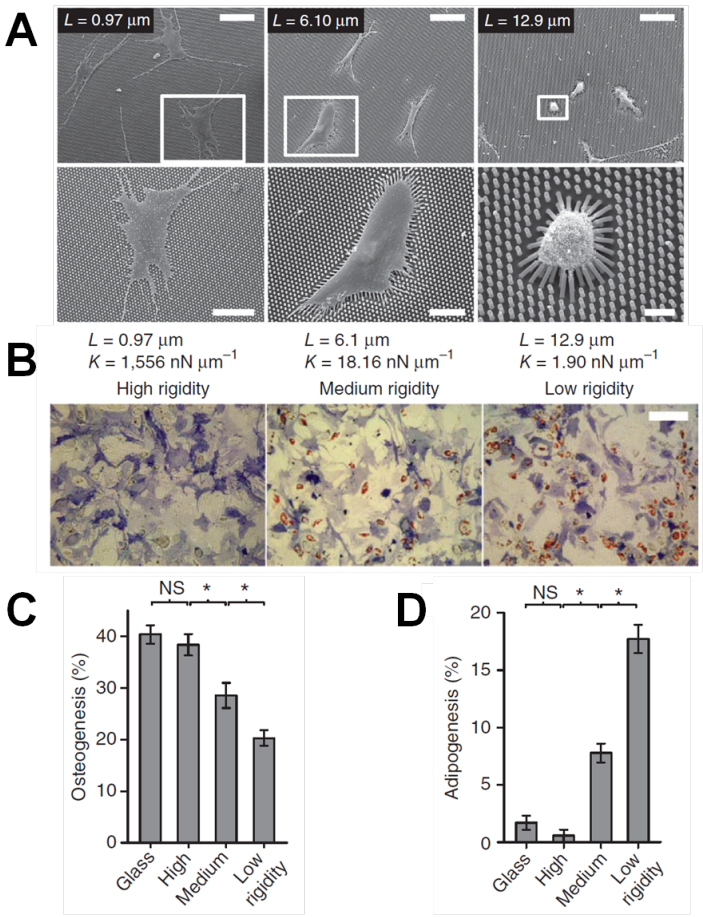


Figure 2.15: Micro-molded elastomeric posts to engineer substrate stiffness. (A) Scanning electron micrographs of hMSCs plated on elastomeric pillars of different heights. (B) Bright-filed images showing hMSCs stained for alkaline phosphatase (blue) and lipid droplets (red). Quantification of (C) Osteogenesis and (D) Adipogenesis. Images taken from [86].

the elasticity of the substrate [86]. Based on classical cantilever mechanics, they showed that a longer post would be more flexible and hence mimic a soft substrate shown in figure 2.15A. A shorter post would be more rigid and hence similar to a stiff substrate. They showed that human MSCs showed osteogenic differentiation when cultured on the rigid posts while adipogenic differentiation was seen on the flexible posts (figures 2.15B, C and D). The presence of micro-posts allowed the researchers to attribute the displacement of the micro-posts directly to the FAs thus allowing tractional force mapping of cells simultaneously with their differentiation. A strong correlation was observed between the traction forces and the lineage specification of hMSCs.

hMSCs that underwent osteogenic differentiation showed much higher traction forces than the control while the ones that became adipocytes showed lower forces than the control. Thus by using the micro-posts and reading the tractional profile of cells on the different substrates, the researchers were able to attribute the differentiation potential of cells to the tractional forces. To confirm their findings, they treated the cells with Y-27632 which is a reversible Rho-kinase inhibitor (ROCK signaling pathway) for upto 1 day. These treatments decreased the osteogenic potential of hMSCs proving the role of tractional forces and hence substrate elasticity in determining the fate of hMSCs.

All these studies clearly show the importance of stiffness in determining the mechanical properties of the cell and provide an opportunity to control and manipulate the fate of mammalian cells. As elasticity of the substrate plays such a pivotal role in cell locomotion, wound healing, immune response, and differentiation, this micro-environmental cue needs to be carefully studied and optimized with different cell lines in order to realize the idea of a fully functional 3D tissue construct.

### 2.2.3 Geometry

Cells are highly complex machines with defined shapes and geometry. This geometry and structure of the cell is critical for its functioning and gives rise to tissue morphogenesis [94]. Geometry is of critical importance in developmental biology and embryogenesis as irrespective of the organism's size, the size of the different parts of the body remains constant [95, 96]. In addition, geometry also creates gradients and polarity of soluble factors which in turn defines tissue functions like migration, cell fate determination, junction formation, organ development, and regulates the homeostasis of cells [95, 97]. Furthermore, geometry also plays a big role in the scaling laws for the cell and the position of internal structures like mitochondria, nucleus, ribosomes, etc [94]. Mitotic spindle which determines cell division, is directly related to the geometry of the cell [94]. Therefore, by altering the geometry of the cell, the spindle size would be rescaled proportionately thereby altering the division of the cell into two daughter cells [94].

The shape, morphology, and geometry of the cell arises from its physical

surroundings by establishing a mechanical equilibrium at the adhesion sites [98]. Therefore, controlling the physical surroundings by tuning the adhesion sites for the cells can be used to control the fate of the cell. The physical mechanism for this goes back to the same idea as described in sub-section 2.2.1 where by altering the cellular geometry (constricting it in defined spaces or modulating its adhesion sites), the characteristics of FAs (number, area, maturity, etc.) and spreading area of the cells change thus changing the intracellular signaling pathways and altering cell fate. This phenomenon is supported by the findings that endothelial cells were able to survive and spread on large beads ($> 100$ $\mu$m) but die within 10 hours when cultured on smaller beads (4.5 $\mu$m) [99, 100]. Since, the early 1990s, efforts have been on the way to control the geometry of the cells by engineering the substrate. One of the earliest and most successful attempts to date was made by the Whitesides group at Harvard where Dr. Whitesides and his colleagues introduced a new technology termed as "soft lithography" which could be used to pattern self-assembled monolayers (SAMs) of alkanethiol on gold substrates [101, 102]. This technology shares its roots with the micro-fabrication technology which is used for manufacturing of semi-conductor devices. Using the same set of principles, a master is created with a photoresist on silicon wafer. This master can then be used to make a PDMS negative of the master which can be used for coating thin SAMs (ECM protiens) on a variety of substrates. This process is termed as micro-contact printing ($\mu$CP). Similar processes like replica molding and hot-embossing can also be used to fabricate substrates with specified geometries.

One of the earliest reports of controlling the geometry of cells by $\mu$CP was reported by Chen et al [103]. In their seminal work, they showed that the life and death of human and bovine capillary endothelial cells (ECs) can be controlled by modulating their spreading area. ECs cultured on smaller fibronectin squares (5 $\mu$m - 10 $\mu$m) showed a high rate of apoptosis. However, apoptosis progressively decreased when the fibronectin island size was increased from 75 to 3000 $\mu m^2$. At the same time, the rate of DNA synthesis increased as the cells were able to spread on a larger area. Figure 2.16A shows the cells on the different fibronectin islands and figure 2.16B shows the rate of apoptosis and DNA synthesis on the different size islands [103].

Another study by McBeath et al., showed that the shape of the cell can be used to control the fate decisions of hMSCs to adipocytes or osteoblasts [104].

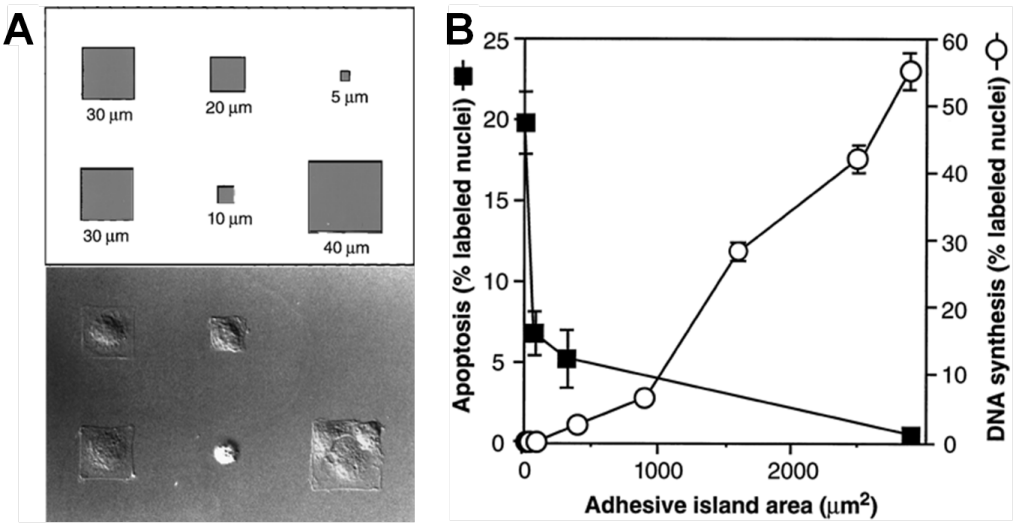


Figure 2.16: Geometric control of cell life and death. (A) Fibronectin islands of different sizes. (B) Apoptotic and DNA synthesis index. Images taken from [103].

hMSCs that were cultured on large fibronectin islands (10000 $\mu$m$^2$) showed osteogenic differentiation while those cultured on smaller islands (1024 $\mu$m$^2$) showed adipogenic differentiation. Figure 2.17A shows hMSCs on different size fibronectin islands after 1 week. It can be seen that the cells in 50:50 induction media showed a strong preference to different lineages depending on the island size. Figure 2.17B shows the quantification of differentiation index for the cells on the different islands while figure 2.17C verifies that micro-patterning did not affect the viability of hMSCs. To confirm the role of cytoskeletal tension in lineage specification of hMSCs, the researchers cul-

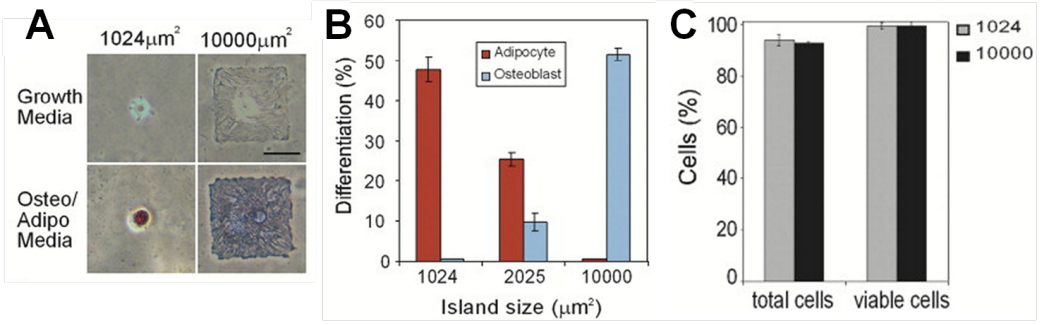


Figure 2.17: (A) hMSCs after 1 week on different size fibronectin islands. (B) Quantification of differentiation for the hMSCs on the different islands. Images taken from [104].

tured the cells in cytochalasin D (disrupts actin filaments) and observed that disrupting actin lead to an increase in adipogenesis while decreasing osteogenesis. Since, cytochalasin D inhibits actin polymerization, treatment of cells with it made the cells rounded. Therefore, the cultures were treated with Y-27632 (Rho kinase inhibitor) which inhibits myosin-generated cytoskeletal tension. As a result of this, the cells still remained spread but it decreased the cytoskeletal tension by inhibiting non-muscle myosin II. The cells again showed higher differentiation to adipogenic lineage which was verified by the formation of lipid droplets in the Y-27632 treated samples. At the same time, their osteogenic differentiation capability was reduced. This suggests that lineage specification of hMSCs was the result of intracellular actomyosin based cytoskeletal tension. When the cells are seeded on larger fibronectin islands, they are able to spread and produce critical tension that turns on/up-regulates the osteogenic genes and thereby differentiating the cells to osteogenic lineage. On smaller islands, not enough cytoskeletal tension is produced and the cells become adipocytes. This study clearly demonstrates the role of geometry in determining the fate decisions of hMSCs.

A study done by Gallant et al., showed that the adhesion strength, integrin binding, vinculin and talin recruitment was a function of the cellular adhesive area [105]. Adhesion strength exponentially increased with the bound integrins and vinculin contributed 30% of the adhesion strength. However, above a threshold area, both the adhesion strength and FA assembly reached saturation. This shows that as long as that critical area is met to generate enough cytoskeletal tension, the cells will be able to up-regulate the mechanosensory genes and control their migration, contractility, and gene expression.

Nelson et al., showed that even in the same micro-patterned structure but in different regions, the cells will experience different levels of tractional stresses and this will correlate to their growth [106]. Regions with high tractional stresses showed higher cellular growth. Based on the same set of idea, Ruiz et al., and Kilian et al., showed that regions of the structure which had high tractional stresses (edges) showed osteogenic differentiation of hMSCs while the center of the same structure showed adipogenic differentiation [107, 108]. Kilian et al., patterned two different structures flower shaped and star shaped fibronectin islands on glass. They showed that the flower shaped structure showed smaller cytoskeletal tension (evidenced by smaller myosin II staining) and therefore hMSCs on these structures became adipocytes.

Stress fibers dominate at the acute corners between the petals. However, on the star shaped structure, high level of myosin II staining was seen which corresponded to higher cytoskeletal tension. On average, hMSCs on this structure showed osteogenic differentiation. Figures 2.18A, B, C, D show the immunofluorescent heat maps of actin (A, B) and vinculin (C, D) on the flower and star shaped structure which clearly show higher concentrations of vinculin at the edges of the star compared to the flower. Figure 2.18E shows the quantification of differentiation on the different shapes [108]. It can be seen that the higher cytoskeletal tension makes the hMSCs on the star to differentiate to osteoblasts while the hMSCs on the flower become adipocytes. Ruiz et al., showed that on different geometries, hMSCs at the edges differentiate to osteogenic lineage (presence of blue colored alkaline phosphatase) while those at the center differentiate to adipogenic lineage (presence of red colored lipid droplets) as shown in figure 2.18F, G, H, I [107]. They also divided the circular region shown in figure 2.18J into a number of different concentric regions and showed that the hMSCs at the center become adipocytes (zone 1) while those at the edges of the circle become osteoblasts (zone 4) as seen in figure 2.18K [107]. Both the researchers used cytoskeletal disrupting agents like Y-27632, cytochalasin D, nocodazole, and blebbistatin to confirm the role of non-muscle myosin in this differentiation process.

Lee et al., used $\mu$CP to control the colony size of human ESCs (hESCs) [16]. They showed that in the presence of bone morphogenic protein 2 (BMP-2) and activin A, hESCs in large colonies (1200 $\mu$m diameter circle) gave rise to mesoderm while smaller colonies (200 $\mu$m diameter circle) differentiated to endoderm showed in figure 2.19A. The relative expression of T-Bry and KDR (mesoderm specific genes) were up-regulated in larger diameter circles while smaller circular islands showed higher expression levels of Sox17, GSC, and Cer1 (endoderm specific genes) shown in figure 2.19B. A similar study done by Hwang et al., showed that larger embryoid bodies (EBs) promoted cardiogenesis (450 $\mu$m in diameter) while smaller EBs (150 $\mu$m in diameter) showed endothelial differentiation of mESCs (figure 2.19C) [109]. Figure 2.19D shows the number of beating colonies per square centimeter and it can be seen that as the colony size increases, the number of beating colonies also increases. Furthermore, higher expression levels of early markers of cardiac differentiation were seen in larger colonies than smaller ones. On the other hand, smaller colonies showed higher expression levels of endothelial differ-

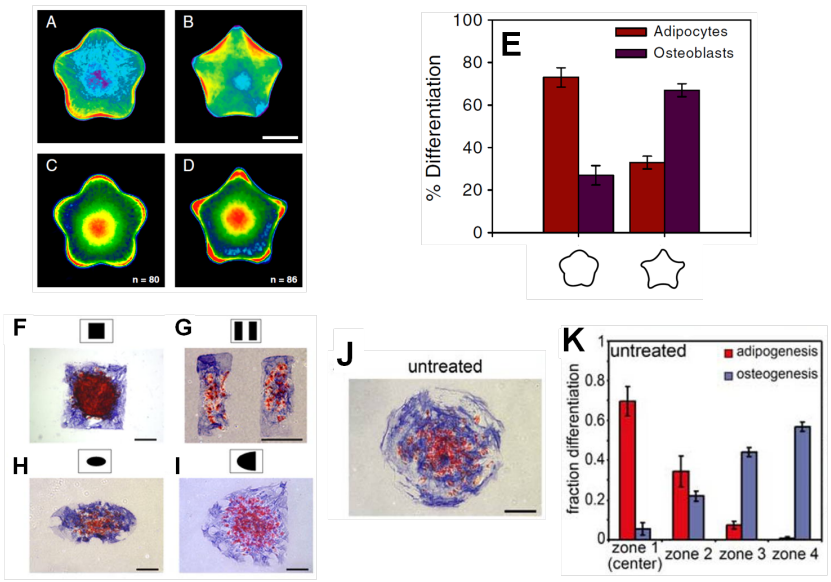


Figure 2.18: Geometric control of hMSC differentiation. Immunofluorescent heat maps of hMSCs on flower and star shaped islands (A, B) actin and (C, D) vinculin. (E) Quantification of differentiation on the flower and star shaped fibronectin islands. Geometrical shapes like (F) square (G) rectangle (H) ellipse (I) half-ellipse (J) circle showing hMSCs in the center region differentiating to adipocytes while those at the edges becoming osteoblasts. (K) Quantification of differentiation for (J). Images taken from [107, 108].

entiation (figure 2.19E). They confirmed that differential expression levels of WNT signaling, specifically WNT5a and WNT11, causes this size based differentiation of mESCs.

In addition to controlling fate of mammalian cells by using geometrical cues, it can also be used to modulate cell motility, migration, and alignment, all of which could be used to enhance the functionality of a 3D engineered tissue construct [110, 111, 112, 113]. Kushiro et al., patterned different types of patterns, (tear-drop, square, and yin-yang) to understand the directional bias of MCF-10A epithelial cells. Figure 2.20 shows the directional bias of epithelial cells. It can be seen that most of the cells migrate from the blunt end to the tip as seen for both the teardrop(figure 2.20A) and the yin-yang (figure 2.20G). They confirmed that these directional biases were the result of Rac1, a small GTPase which is involved in lamellipodial extensions. Suppression of Rac1 significantly reduced this directional bias in the cells. Mahmud et al., used asymmetric "ratchet' micro-geometries to create cell polarizations and thereby control the motility of cells. In addition, different

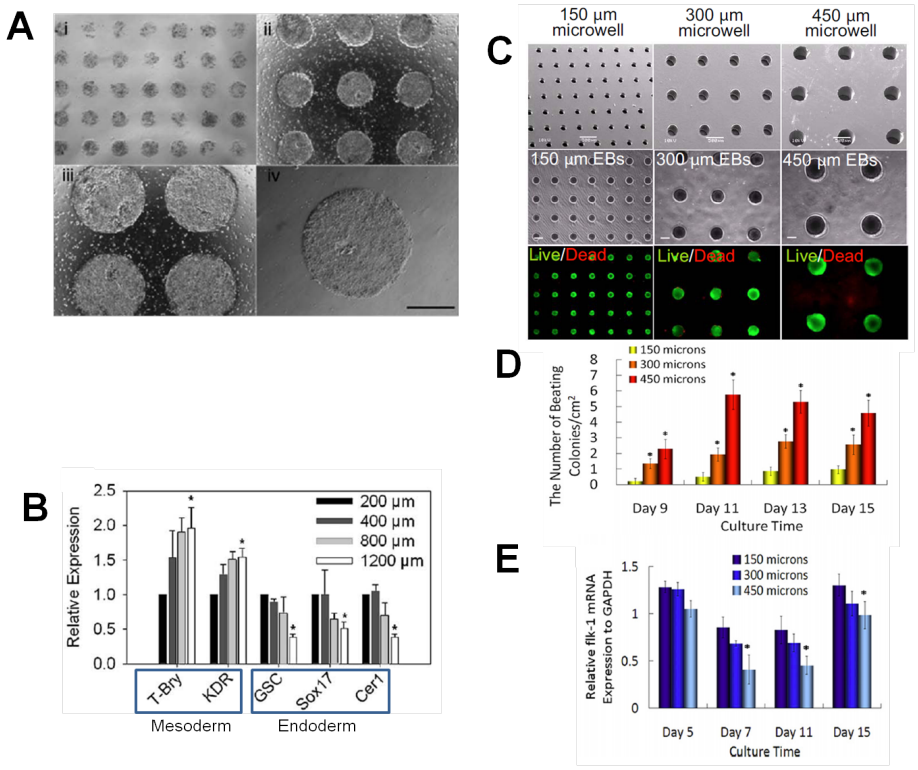


Figure 2.19: Size based differentiation of ESCs. (A) hESCs seeded on different size Matrigel islands. (B) Smaller islands showed higher expression levels for endoderm while larger islands promoted mesodermic differentiation of hESCs. (C) mEBs formed in different size hydrogel wells. (D) Larger EBs show higher number of beating colonies. (E) mRNA expression levels showing smaller colonies promotes endothelial differentiation of mEBs. Images taken from [16, 109].

types of cells showed different migration patterns. Cimetta et al., used $\mu$CP to create arrays of cardiac and skeletal muscle fibers on PA hydrogels (figure 2.20I) [112]. Flaibani et al., used $\mu$CP to enhance the differentiation of muscle precursor cells (figure 2.20J) [113].

Recently, Bidan et al., used geometry as a factor to optimize tissue growth [98]. They cultured MC3T3-E1 pre-osteoblasts in thick hydroxyapatite plates containing pores with square or cross-shaped sections. First, they simulated the growth rate in the different shapes and their simulations predicted that higher initial growth rates would be seen in pores which were non-convex (cross, star) compared to convex (square) pore sections (figure 2.21A, B). Next, experimentally they showed that overall tissue deposition was indeed twice as fast in the large cross-shaped pores than in large square-shaped

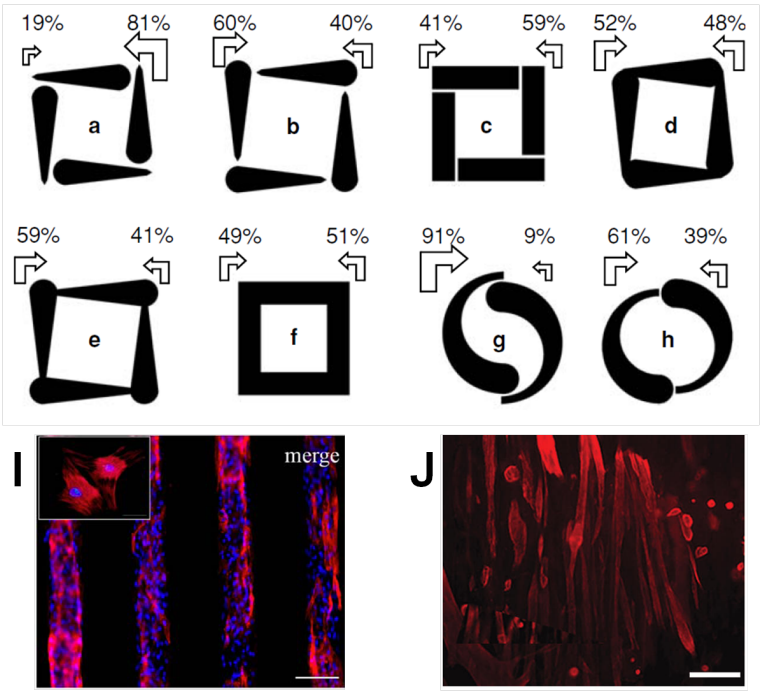


Figure 2.20: (A-H)Directional basis of epithelial cells on different patterns. (I) Array of cardiomyocytes on PA gel stained for troponin I. (J) Troponin expression in muscle precursor cell showing a high degree of alignment. Images taken from [110, 112, 113].

pores (figure 2.21C, D) [98]. Thus optimizing the shape of the pore may improve the in growth of bone tissue which would be useful for orthopedic tissue engineering.

Geometrical cues can alter the fate of mammalian cells, influence migration of cells and control their functionality by changing their attachment dynamics and cytoskeletal tension. Thus optimizing the geometry of the scaffold to optimize cellular growth and functionality is extremely important for fabricating a 3D engineered tissue.

### 2.2.4 Topography and roughness

The impact of surface topography and roughness is a very important physical cue as they influence cell migration, adhesion, alignment, proliferation, differentiation, adhesion and cytoskeletal organization [114]. Specifically, nanoscale/microscale topography can strongly influence cellular behavior as cells in the native tissue are constantly in contact with the nano/micro scale

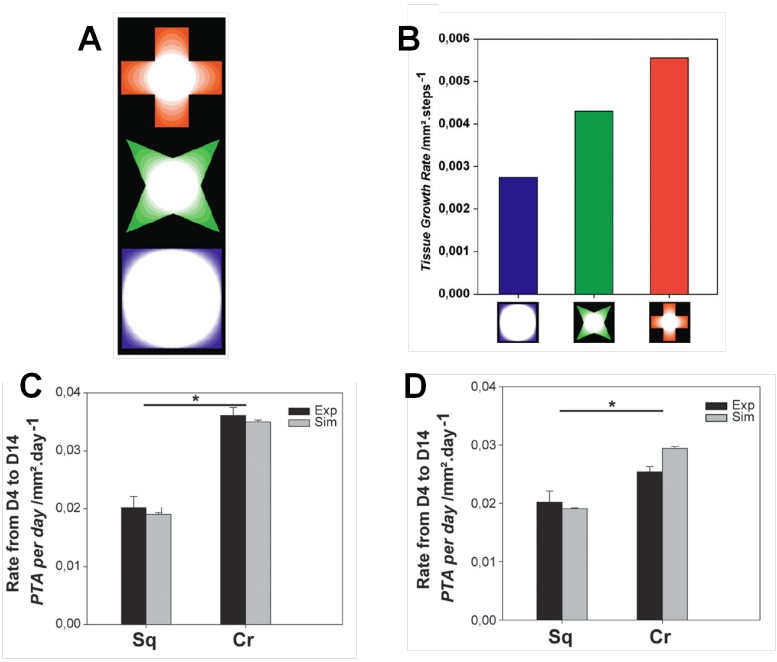


Figure 2.21: (A) The computational simulation of different shapes used for tissue growth. (B) Predicted rate of tissue growth in the different shapes. Rate of tissue growth on the different shapes (C) Large pores (D) Medium pores. Images taken from [98].

features of the ECM. For example, collagen molecules are about 300 nm long and 1.5 nm wide [115]. These collagen molecules can then form fibrils which can be micrometers in length [116]. Cells use these collagen fibrils as ropes and migrate on it through a phenomenon called contact guidance. Contact guidance plays a very important role in cellular migration, wound healing, and immune response [117, 118, 119]. Roughness at the nanoscale is important as it increases the area of contact between the cells and the surface [120]. Cells sensing of surface roughness is called haptotaxis, this phenomenon is known to trigger cytoskeletal re-organization and promote adhesion [120, 121, 122, 123].

A variety of different methods have been used to modulate the surface topography for instance using grooves/ridges [124], by grinding the substrate with absrasives [125], by using UV-lithography to micro-pattern glass [126], two-photon polymerization [127], capillary force lithography [128], etc. Suitable substrate for this includes a wide range of engineering materials like polymers (PDMS, PMMA, PEGDA), silicon oxide, and metals [125, 126, 129]. Generally, metals like platinum, stainless steel, titanium, etc. are used for

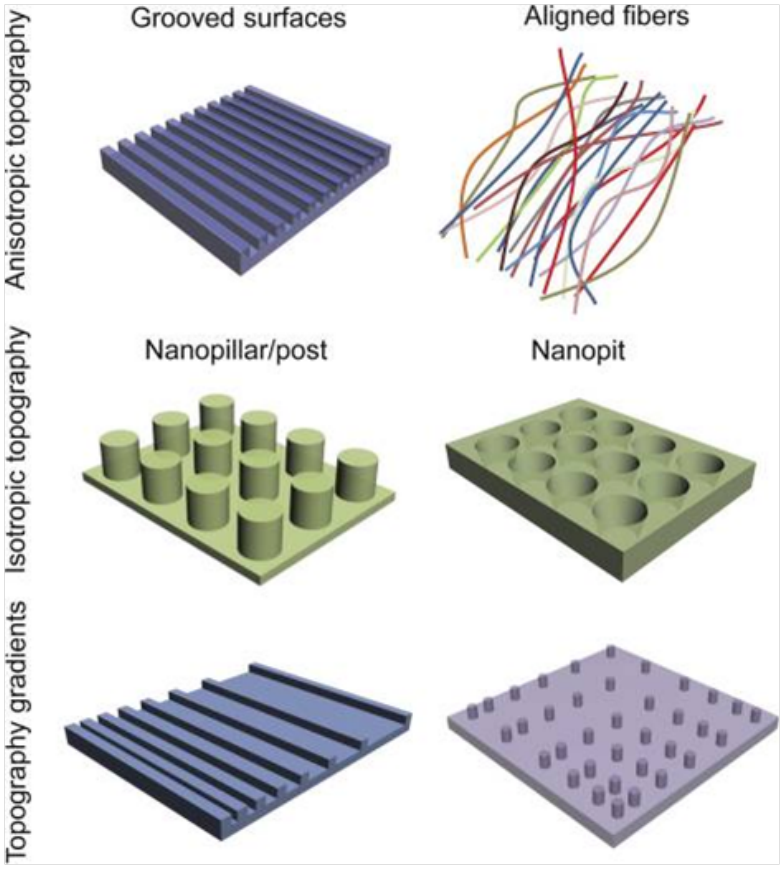


Figure 2.22: Different types of nanotopographies used to modulate cell function. Image taken from [130].

engineering implants for bones and other hard tissues while polymers are used for the tissue engineering of soft tissues.

Figure 2.22 shows three representative nanotopography geometries like nano-grooves/ridges, nanopost arrays, nanopit arrays which are commonly used for modulating the functions of the cell like migration, differentiation, alignment, etc [130]. Anisotropic topographies as the name suggests depend on the direction and provide cues along a single axis. Isotropic topographies on the other hand provide cues uniformly in all the axes. Gradient topographies provides cues through gradual changes in physical features [130].

Teixeir et al., fabricated nono/micro scale structures on silicon oxide to study the attachment, spreading, and migratory characteristics of human corneal epithelial cells [131]. They found that the cells followed the contact cues of the substrate, thereby aligning and elongating along the patterns and grooves of the substrates with feature dimensions as small as 70 nm.

However, cells on the smooth surface mostly remain round and did not show any elongation or spreading (figures 2.23A, B). In addition, FAs which are the sensory organs of the cells were dependent on the ridges of the underlying substrate. On the 70 nm ridge substrates (figures 2.23C), the FAs were much smaller and narrower compared to the FAs formed on the larger ridge widths (figures 2.23D). However, on all patterned substrates, stress fibers and FAs were aligned along the features of the substrate. Cells cultured on smooth silicon oxide surface formed FAs with no preferred orientation (figures 2.23E). The distribution of filopodia and lamellipodia was affected by the topography of the substrate. Figure 2.23F shows the filopodia aligning along the grooves of the 400 nm pitch substrate. As the pitch size increased (4000 nm pitch), even the lamellipodia were able to enter the groove of the substrate and adhere to the floor (figures 2.23G, H). As cell alignment creates polarization, these nanotopographies can be extremely useful for optimizing the behavior and functions of epithelial cells like detection of sensation, secretion, transport, etc. Another reason other than contact guidance for the elongation of cells could be because of the roughness of the substrate. It has previously been shown that bare silicon oxide substrate is very smooth with an average root mean square roughness of only 0.4 nm [132]. The presence of these ridges significantly increases the surface area available for attachment and thus helps in spreading of cells.

Number of studies have been done to modulate the alignment and differentiation of C2C12 skeletal myoblasts by using nano/micro topography and roughness [124, 125, 126, 133, 134, 135]. Wang et al., used e-beam lithography and dry etching to form grooves and ridges in silicon and showed that groove depth was influential in controlling the morphology, proliferation, and differentiation of C2C12 skeletal myoblasts than groove width [124]. Shimizu et al., sand paper to grind iron blocks in one direction and molded PDMS with that. They showed that for rougher substrates, C2C12 cells showed alignment while alignment was seen for flat or smoother substrates [125]. Yamamoto et al., used UV-lithography to etch glass and showed that C2C12 cells get neatly aligned in the ridges of the glass and show both MyoD negative cells in the latter stages of differentiation [126]. Altomare el al., used silicon wafers with different groove widths to solvent cast bio-degradable poly-L-lactide/trimethylene carbonate copolymer (PLLA-TMC) [133]. They showed that micro-grooved surfaces were able to influence myotube formation

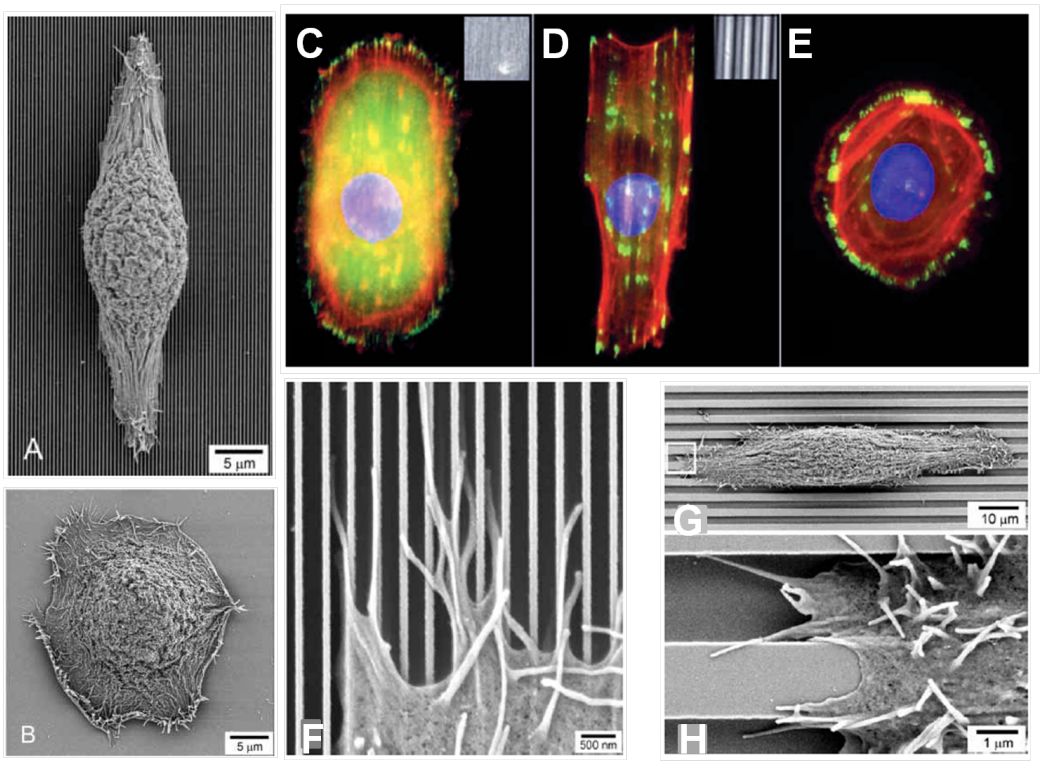


Figure 2.23: Scanning electron micrograpahs (SEM) of epithelial cells on (A) 70 nm ridge with a 400 nm pitch. (B) Smooth silicon oxide surface. Cells stained for actin (red), vinculin (green) and nucleus (blue) on (C) 70 nm ride with a 400 nm pitch (D) 1900 nm ridge with a 4000 nm pitch (E) Smooth silicon oxide. SEM of the cross-section of the cells on (F) 400 nm pitch (G) 4000 nm pitch (H) Zoomed of (G). Images taken from [131].

and alignment and grooves of 2.5 and 1 $\mu$m depth with 50 and 25 $\mu$m width presented the highest differentiation and alignment of C2C12 myotubes. Recently, Wang et al., combined both chemical and topographical cues to study the development of C2C12 myotubes [135]. Arginine-glycine-aspartic acid (RGD) and amine (-$NH_2$) conjugation was done on the polystyrene (PS) substrates (both grooved and flat) to study the differentiation of C2C12 cells. In general, the grooved surfaces showed slightly higher differentiation than flat surfaces. Moreover, the RGD modified showed the highest differentiation of C2C12 cells and best alignment (figure 2.24A,B). In addition, the amount of FA protein intensity was highest on the PS-RGD followed by PS-$NH_2$ while the bare PS showed the lowest vinculin intensity. This study coupled two cues (1) surface chemisty and (2) nanotopography to study the differentiation of myotubes and showed that substrates modified with RGD

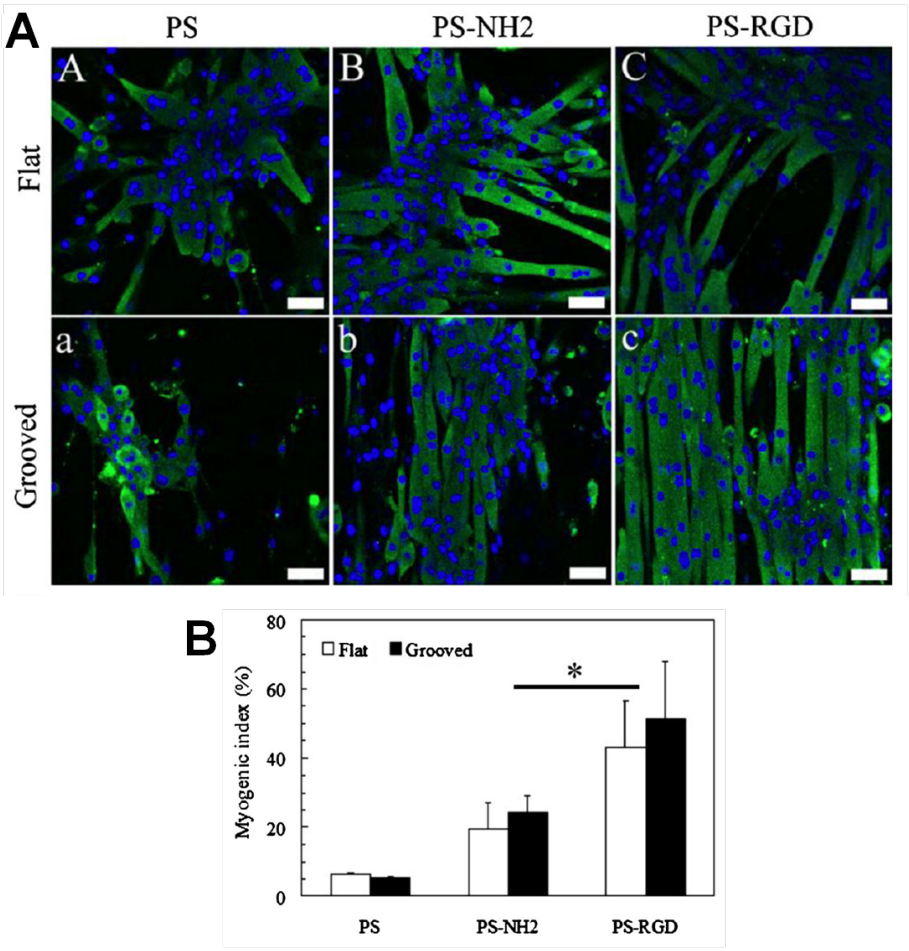


Figure 2.24: (A) Myosin heavy chain staining for C2C12 cells on the different types of substrates. (B) Quantification of the myogenic differentiation index on these substrates. Images taken from [135].

and which presented a nanotopography to C2C12 cells showed the highest differentiation [135].

Topography and roughness have been widely used to control the fate of ESCs, MSCs, neural stem cells, and hematopoietic stem cells by modulating their attachment dynamics [136, 137, 138, 139, 140]. Chen et al., seeded hESCs on glass substrates with different roughness (hence different topography) and investigated cell morphology, adhesion, proliferation, and self-renewal capabilities of these cells [136]. Substrates with three different roughness (1, 70, and 150 nm) were generated by using a combination of photo-lithography and reactive ion etching (RIE). The initial roughness of unprocessed glass wafer was 1 nm which also served as the control or smooth

substrate. The glass with roughness, 150 nm, was designated as the nanorough substrate. Interestingly, a highly branched, filopodia rich structure was seen on the smooth glass surface while only few short extensions were seen on the nanorough glass as seen in figure 2.25A. Interestingly, after 48 hours of adhesion, un-differentiated hESCs selectively adhered to the smooth islands and retained their "stemness" while spontaneously differentiating hESCs showed no adhesion preference. In addition, hESCs proliferated much more quickly with a doubling time of only 41 hours while it took almost 77 hours for doubling of cells on the nanorough glass (figure 2.25C). hESCs on the smooth glass showed vinculin-containing FAs only on the periphery of the of the undifferentiated (OCT3/4+) hESCs but randomly distributed throughout the area of the differentiated (OCT3/4-) hESCs. However, on the nanorough glass both the un-differenitated and differentiated hESCs showed randomly distributed punctate FAs (figure 2.25B). Interestingly, number of FAs per cell were more for the nanorough glass for both the OCT3/4+ and OCT3/4- cells (figure 2.25D). In order to better understand the phenomenon of haptotaxis, they seeded NIH/3T3 fibroblasts on these smooth and nanorough glass surfaces. Unlike hESCs, fibroblasts preferred the nanorough substrate over the smooth glass surface seen in figure 2.25E. The adhesion selectivity of fibroblasts to the nanorough substrates was over 90% (figure 2.25F). Taken together this study showed that un-differentiated hESCs prefer smooth over nanorough surfaces and retain their "stemness" on the smooth surfaces. Contrary to that, fibroblasts preferred nanorough substrates over smooth substrates.

Oh et al., used titanium oxide nanotubes to seed hMSCs and study its behavior. It was found that smaller nanotubes ($\sim$30 nm diameter) allowed adhesion of cells but did not allow much cell spreading or osteogenic differentiation. In contrast, hMSCs on larger nanotubes ($\sim$ 70-100 nm diameter) allowed extensive cell spreading and elongation. On flat titanium oxide surfaces, the hMSCs appeared more round and lacked filopodia extensions. The flat surfaces showed the least cell spreading while increasing the diameter of the nanotubes progressively increased hMSC spreading as well possibly by increasing the roughness of the substrate (figure 2.26A). As a result of elongation and spreading of hMSCs on the larger diameter nanotubes, the relative transcript level for osteogenic markers like osteopontin (OPN), osteocalcin (OCN) and alkaline phosphatase (ALP) were higher on the larger diameter nanotubes as seen in figure 2.26B.

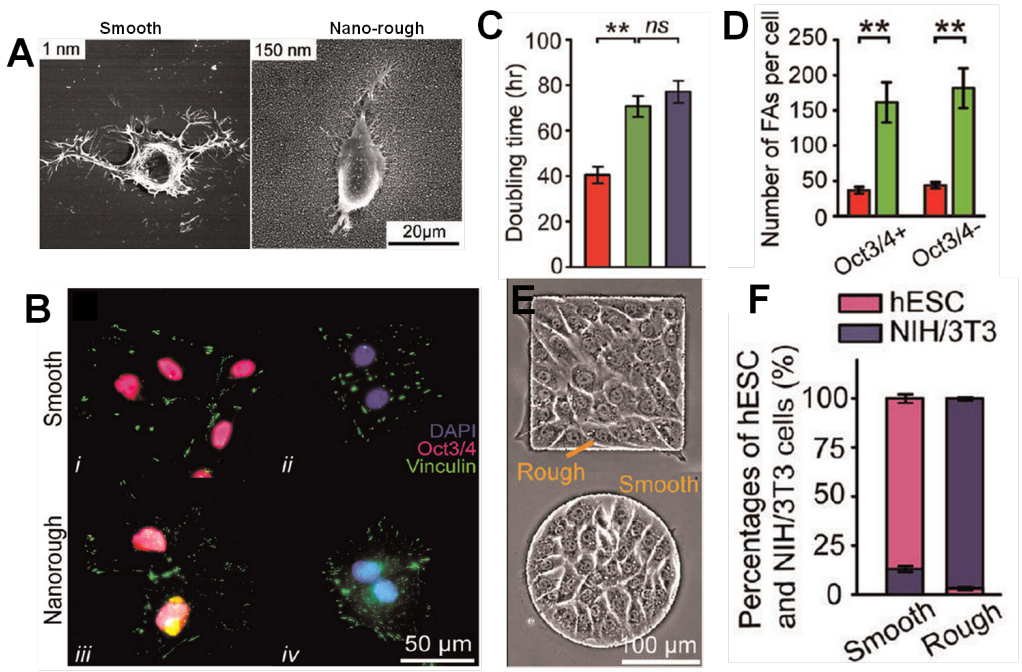


Figure 2.25: (A) hESC on smooth and nanorough glass surface. (B) Vinculin and OCT3/4 staining on the nanorough and smooth surfaces for hESCs. (C) Doubling time of hESCs on the smooth and nanorough substrate. (D) Number of FAs per cell on the smooth and nanorough substrate. Red bar is smooth surface; green bar corresponds to a surface with roughness of 70 nm while blue bar corresponds to 150 nm rough surface. (E) Fibroblast attachment on the smooth and nanorough substrates. Fibroblasts prefer nanorough over smooth surfaces. (F) Adhesion rate of fibroblasts on the different substrates. Images taken from [136].

A number of studies have been done by many different research groups to understand the interaction of different cell types with nano/micro pillar topography [141, 142, 143, 144]. Turner et al., fabricated nanopillars and nanowells on silicon wafers by standard photolithographic techniques and seeded LRM55 astroglial cells to study their interactions with pillars [141]. Cells seeded on the nanowells were mostly round and showed poor attachment. On the other hand, cells appeared more spread on the pillars. Over 70% of the cells adherence preference to the pillars versus the smooth surface. Actin and vinculin distribution was very different for the cells on the different surfaces. Since, cells did not spread much on the smooth surface, diffuse vinculin immunoreactivity was seen around the nuclei (figure 2.27A). Contrary to that, cells on the nanopillars exhibited well organized actin struc-

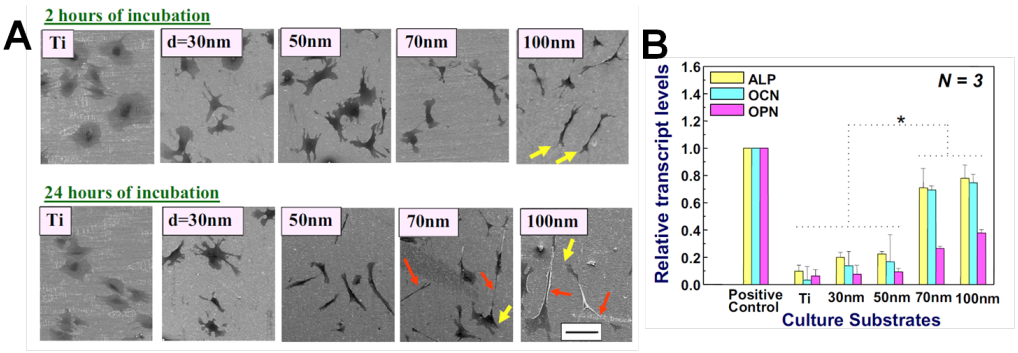


Figure 2.26: (A) SEMs of hMSCs on different types of titanium oxide substrates. Red arrows indicate extraordinary cell elongation while yellow arrows show lamellipodial extensions. (B) Relative transcripts levels of common osteogenic markers after 14 days on the different substrates. Images taken from [138].

tures and dense vinculin patches were visible on the pillars as seen in figure 2.27B. Xie et al., used e-beam to fabricate arrays of 150 nm diameter, 1 $\mu$m high platinum nano-pillars directly on top of multi-electrode arrays to pin down neurons in a non-invasive manner in order to record its electrical activity [142]. They showed that indeed the nanopillars were able to slow down the mobility of neurites from 57.8 $\mu$m on a flat surface to 3.9 $\mu$m on the nanopillars over 5 days. In addition, the growth pattern of the cells did not differ significantly from that grown on a flat surface. Figure 2.27C shows an SEM of neuron-nanopillar interaction. Both these studies can have applications in neural tissue engineering and designing better neural prosthesis. Ghibaudo et al., grew fibroblasts on PDMS micro-pillars of different dimensions [143]. Cells grown on pillars with height 10 $\mu$m height, 5 $\mu$m diameter and 5 $\mu$m spacing showed very long cellular protrusions (figure 2.27D) while those grown on pillars with height 2 $\mu$m height, 5 $\mu$m diameter and 5 $\mu$m spacing had morphology similar to that on a flat surface.

The reason for such different cell behavior on different pillar geometries is because these pillars potentially alter the clustering of integrins. This changes/delays the development of FAs which in turn changes the cytoskeleton organization of the cell. The end result being the cells' behavior on that substrate changes. Figure 2.28 shows a schematic of a cell perception of different surfaces [145].

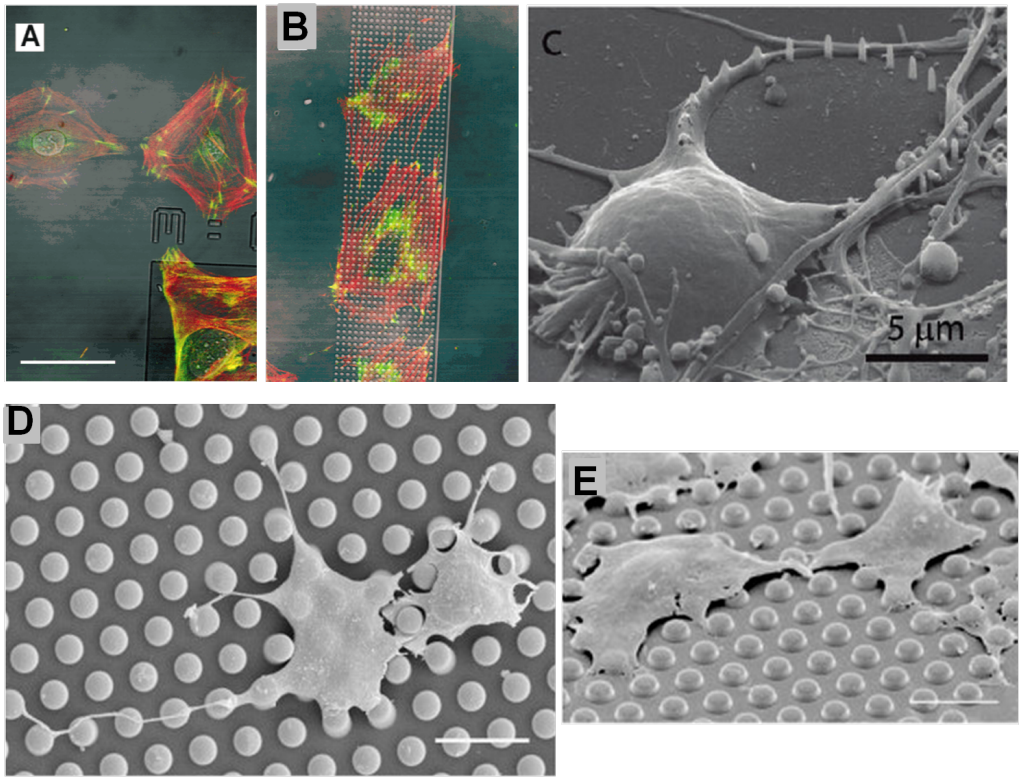


Figure 2.27: Growth of cells on nanopillars.(A) Astroglial cell grown on flat surface. (B) Astroglial cell grown on nanopillars of width 1.25 $\mu$m and gap 1.5 $\mu$m. Scale bar = 50 $\mu$m. Red is actin, green shows vinculin and blue shows the nuclei. (C) Nanopillars pinning down the neurites of embryonic cortical neurons. Fibroblasts grown on (D) Pillars with height 10 $\mu$m height, 5 $\mu$m diameter and 5 $\mu$m. (E) Pillars with height 2 $\mu$m height, 5 $\mu$m diameter and 5 $\mu$m spacing. Scale bar = 20 $\mu$m. Images taken from [141, 142, 143].

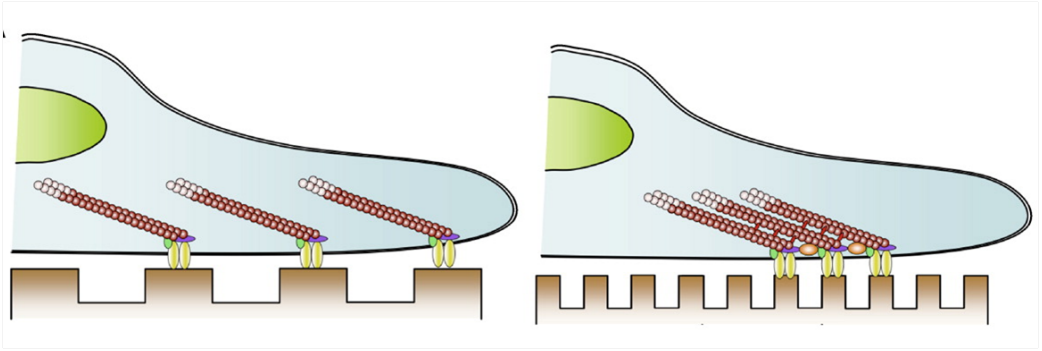

Figure 2.28: Cells' perception of different pillar geometries. Images taken from [145].

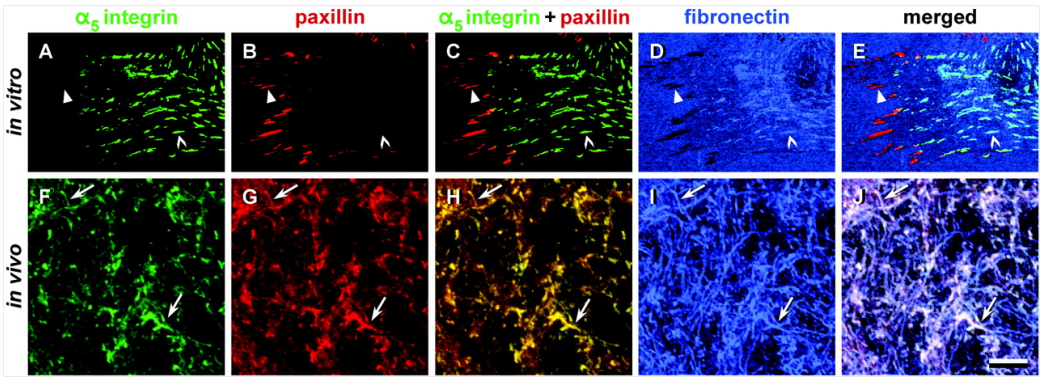


Figure 2.29: Immunofluorescent images of ECM molecules (A-E) *(*In vitro)-2D substrates (F-J) *(*In vivo)-3D substrates. Scale bar = 5 $\mu$m. Image taken from [146].

### 2.2.5 Dimensionality

Cells in our bodies experience a 3D micro-environment. However, most of our understanding about the behavior of cells comes from two-dimensional (2D) cultures. Even though these 2D studies have helped us to understand a lot of fundamental questions about basic cell biology, there exists a need to bridge the gap between 2D and 3D cultures in order to fully understand the functionality of the cells and to truly mimic the *in vivo* cellular environment. Previous studies have already shown that cells behave very differently in 3D versus 2D cultures [146, 147, 148, 149, 150, 151]. Cukierman et al., compared the growth of fibroblasts on 2D versus 3D cultures. Figure 2.29A-E shows immunofluorescence staining of an NIH/3T3 fibroblast *in vitro* on a 2D fibronectin coated cover slip. Figure 2.29F-J shows the transverse craniofacial cryostat section of a mouse embryo (*in vivo*)[146]. It can be seen that the morphologies of the ECM molecules and their co-localization is very different in 2D versus 3D cultures. In 2D cultures, FAs contain integrin $\alpha_5\beta_3$ and other proteins like vinculin, paxillin, and FAK. However, they are present separately. In 3D cultures, paxillin and $\alpha_5$ integrin co-localize (figure 2.29C, H). Fibronectin localizes to fibrillar structures and it can be seen in figure 2.29J that there is a substantial overlap of all three molecules. In 2D cultures, the co-localization between these molecules is not seen. Furthermore, relative to a 2D substrate, 3D cultures show enhanced biological activities and less of an integrin usage [146]. Bissell group demonstrated that human breast cancer cell lines can be reverted back to morphologically normal phe-

notype by integrin blocking in 3D cultures and this reversal was never seen in traditional 2D cultures [147, 148]. Increased viability of human hepatoma cell line HepG2 is seen in 3D over 2D cultures [149]. Hepatocytes grown in 3D show enhanced drug metabolism activities than their counterparts in 2D [150]. MSCs show higher attachment, proliferation, and differentiation to osteogenic lineage when cultured in 3D over 2D cultures [151]. These are just few examples showing the importance of 3D micro-environment in controlling the organization of mammalian cells.

Hydrogels are becoming increasingly popular to construct a 3D cellular micro-environment to study the properties of mammalian cells and for tissue engineering [152, 153]. Hydrogels are just repeating chains of polymers which have been linked together by a cross-linker. Depending on the concentration of the cross-linker and the pre-polymer, hydrogels can adapt a number of different physical properties. Also, since hydrogels are hydrophilic, they can absorb large quantities of water and thus can mimic the properties of *in vivo* soft tissues. Hydrogels can be used in a variety of biomedical applications such as drug delivery, wound management and tissue engineering [154, 155, 156, 157]. Many studies have used different techniques like solvent casting [158], freeze drying [159], gas foaming [160], electrospinning [161], and SL [87] for constructing the complex 3D architecture found in the body using hydrogels. Beyond the architectural aspects of the native ECM, the scaffold will also need to provide spatio-temporal cues to guide tissue morphogenesis [162].Therefore, integration of multiple technologies or fabrication modalities would be needed to provide the cells with the right set of cues to guide their function in this 3D matrix.

In addition, many of the current techniques could actually be translated to the fabrication of 3D constructs which would recapitulate some of the cues that were discussed above. Figure 2.30 shows a schematic of these proposed translations. Aligned cells on geometrically or topographically patterned substrates could be rolled into a tube to create micro-vessels. These micro-vessels could then be cultured in fibrin gels or other type of hydrogels to retain their 3D dimensionality. In order to constrict the cells in confined spaces to mimic the differentiation of hMSCS to osteoblasts or adipocytes, the concentration of the pre-polymer or cross-linking density could be changed to create dense regions in hydrogel constructs. Cell-sheet engineering could also be used to stack multiple 2D sheets on top of each other to create a 3D sheet [162].

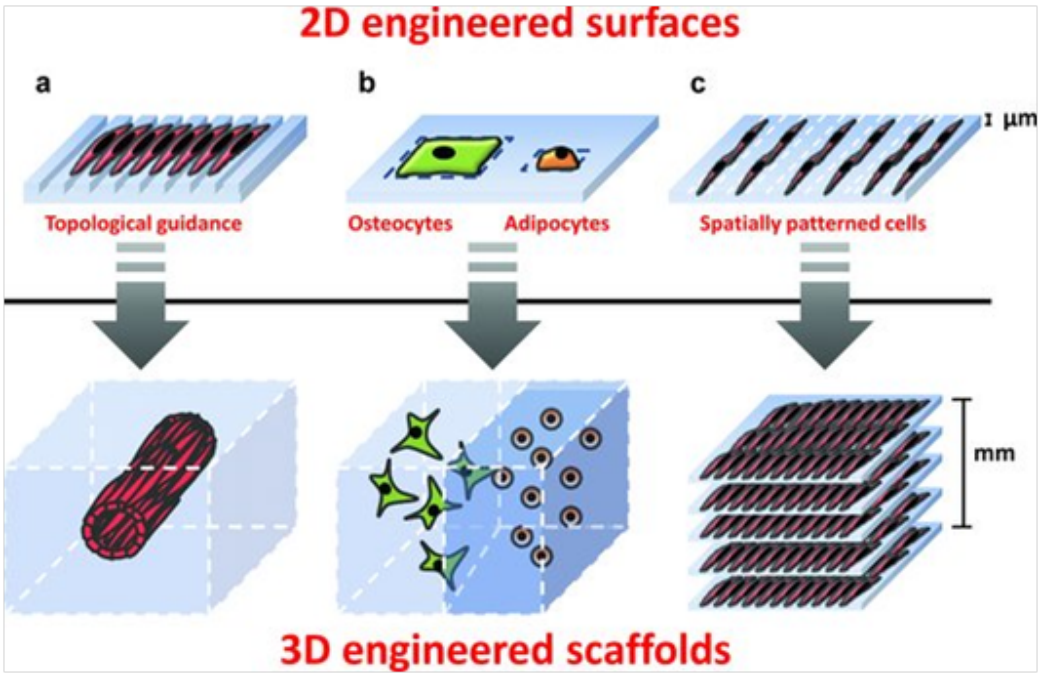


Figure 2.30: Schematic showing the translation of 2D techniques for creating 3D substrates. Image taken from [162].

This review provided a brief background about tissue engineering techniques. Then it highlighted the importance of different micro-environmental cues that need to be presented to the cells in order to control their fate in a 3D tissue construct. Here, the cues were decoupled from each other and most of the research has been done to investigate the response of cells to only cue at a time. However, *in vivo* the cells are presented with all the cues of stiffness, geometry, topography, and roughness simultaneously. Therefore, in order to realize the goal of fabricating a 3D tissue which could be used for regenerative medicine or drug discovery/screening, the cellular response to multiple cues has to be studied simultaneously. Fabrication techniques will be needed to independently control multiple cues simultaneously in a 3D architecture so that the cells' response to all these cues could be studied. Only then, it would be possible to truly mimic the *in vivo* micro-environment and control the fate of mammalian cells.

# CHAPTER 3

# INFLUENCE OF SUBSTRATE STIFFNESS ON THE PHENOTYPE OF EMBRYONIC CHICKEN CARDIAC MYOCYTES

## 3.1 Introduction

This chapter will describe the influence of substrate stiffness on the beating rate, force of contraction and cytoskeletal structure of embryonic chicken cardiac myocytes (ECCMs). These cells were cultured on PA hydrogels of three different stiffnesses 1 kPa, 18 kPa, and 50 kPa to mimic the stiffness of brain, muscle, and bone tissue respectively. Tissue culture plates served as the control in this study. In addition, a quantitative evaluation for understanding the effect of substrate stiffness on mechanical communication between distant cells in cardiac tissue is also presented.

Section 3.2 will describe the material and method section of this chapter. This will include the fabrication of PA hydrogels, its activation, isolation of cardiac cells, the parameters used for imaging and its processing. Section 3.3 will evaluate the beating characteristics of ECCMs on PA hydrogels of different stiffnesses. Section 3.4 will quantify the FA characteristics of ECCMs on the different hydrogels. Section 3.4.1 will point out the differences in the cytoskeletal structure of ECCMs on PA gels of different stiffnesses. Section 3.5 will show the measurement of beating force of these cells using a novel micro-electro mechanical systems (MEMS) probe. Section 3.6 will present both simulated and measured results of mechanical communication between these ECCMs *via* the hydrogel substrates. Section 3.7 will summarize the major findings of this chapter and highlight the importance of substrate elasticity for the heart (cardiac tissue) as a whole. These results have been published in [163, 164].

## 3.2 Experimental

This section of the chapter presents the experimental protocol that was followed to undertake the study.

### 3.2.1 Fabrication of activated polyacrylamide hydrogels on glass coverslips

PA gels were prepared following the protocols described by Wang et al [75]. Formation of PA gel on the glass surface is a multi-step process which involves (1) Activation of the glass coverslip (2) Preparation of PA gels (3) Activation of the PA gel and (4) Characterization of the PA gel surfaces.

Activation of glass coverslips:

The following procedure was used to activate the glass surface to allow for efficient attachment of the PA gels:

- 22×22 mm coverslips were first cleaned by sonicating them successively in pure acetone and methanol.
- These coverslips were then dried by blowing them with nitrogen gun. In order to make the surface more reactive, these coverslips were kept in a chamber of oxygen plasma for 60 seconds.
- ∼200 $\mu$L of 3-aminipropyltrimethoxysilane was pipetted on the activated side of the coverslip.
- Coverslips were then rinsed in deionized (DI) water for 15 minutes.
- These coverslips were then incubated in a solution of 0.5% gluteraldehyde in phosphate buffered saline (PBS) for 30 minutes followed by rinsing them again in DI water twice for 15 minutes each.
- At this stage the glass coverslips were activated and ready for the attachment of PA gels.

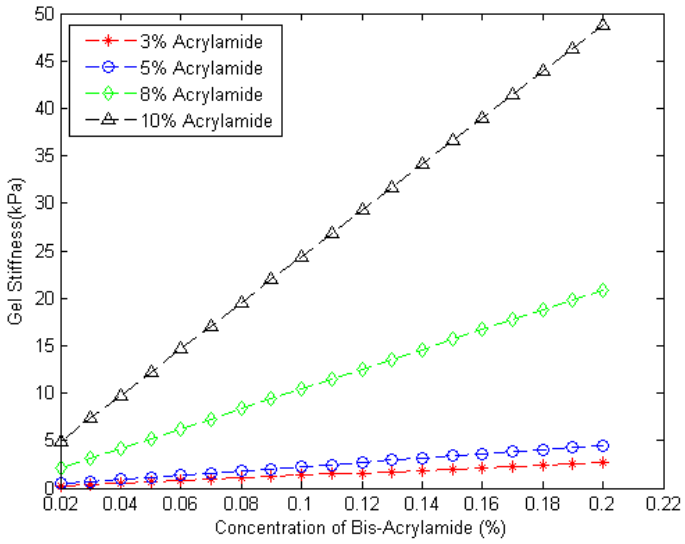


Figure 3.1: Estimation of the Young's modulus for PA gels for different concentrations of [Acry] and [Bis].

Preparation of PA hydrogels:

In order to control the mechanical properties of the PA gel equations 3.1, was used a guide [165].

$$E([Acry],[Bis]) = [Bis](a_1[Acry] + a_2[Acry]^2 + a_3[Acry]^3) \tag{3.1}$$

with $a_1$ = 0.564, $a_2$ = -4.487, and $a_3$ = 12.839. The Young's modulus ($E$) obtained from equation 3.1 is in kPa and the two concentration of bis-acrylamide ([Bis]) and acrylamide ([Acry]) are expressed as percentages. Also, it should be noted that, equation 3.1 is only valid in the range of ($3\% \leq [Acry] \leq 10\%$) and ($0.02\% \leq [Bis] \leq 0.20\%$). Figure 3.1 is obtained for different concentrations of [Acry] and [Bis]. This range of stiffness obtained from the different concentrations of [Acry] and [Bis], encompasses the entire range of physiologically relevant stiffnesses of very soft to stiff tissues [69]. Acrylamide and bis-acrylamide were mixed in 10 mM HEPES (Sigma, St. Louis, MO) at desirable concentrations to achieve very soft ($\sim$ 1 kPa) to stiff ($\sim$ 50 kPa) PA gels. To this solution, 1/200 volume of 10% ammonium persulphate and 1/2000 volume of tetramethylethylenediamine (TEMED) were added as a catalyst. Table 3.1 shows the concentrations of acrylamide and bis-acrylamide used to form the PA gels and their estimated and mea-

| [Acry] (%) | [Bis] (%) | Estimated E (kPa) | Measured E (kPa) |
|---|---|---|---|
| 3 | 0.08 | 1.06 | 1.05 ± 0.17 |
| 8 | 0.17 | 17.0583 | 18.31 ± 0.19 |
| 10 | 0.2 | 48.738 | 50.62 ± 0.92 |

Table 3.1: [Acry] and [Bis] used for preparing the PA gels of different stiffnesses.

sured stiffnesses using the atomic force microscope (AFM). The process for measuring the stiffness of the hydrogels is shown in sub-section 3.2.1. 25 $\mu$L of this solution was pipetted on to the activated glass coverslip and sandwiched by a 12 mm diameter round coverslip. To mimic a wide range of mechanical micro-environments, gels with physiologically-relevant stiffnesses were produced [69]. Soft PA gels with stiffness 1.05 ± 0.17 kPa were used to mimic mammary gland, brain, and breast tissue, which have psychological stiffness from 0.1 to 2 kPa [69]. Intermediate hard gels with stiffness 18.31 ± 0.19 kPa were used to mimic chicken embryonic myocardium, which have psychological stiffness from 9 to 20 kPa [69]. Stiff gels with stiffness 50.68 ± 0.92 kPa were used to mimic cartilage and bone [69]. TC dishes served as the control for the study (stiffness of TC $\sim$ 3 GPa). After about 30 minutes of incubation at room temperature, the top coverslip was gently removed and the gel was washed in 50 mM HEPES solution.

Activation of PA gels:

The PA gel formed here is not very conducive to the growth of cells [75]. In order to provide an adhesive surface for the growth and culture of cells, the surface of the PA gels needs to be conjugated with extracellular matrix (ECM) proteins like laminin, fibronectin, collagen - I, etc. However, these proteins will not adhere to the surface of the PA gels. Therefore, the PA gels were activated by using a photo-activatable hetero-bifunctional compound sulfosuccinimidyl-6-(4'-azido-2'-nitrophenylamino) hexanoate (sulfo-SANPAH). Sulfo-SANPAH contains a cross-linker which has an amine reactive N-hydroxysuccinimide (NHS) ester group which can react to the lysine group ($\varepsilon - NH_2$) found in a variety of ECM proteins and a photo-activatable nitrophenyl azide group which can be attached to the PA gel [75]. These PA gels were thus activated with 1 mM Sulfo-SANPAH (Thermo Scientific,

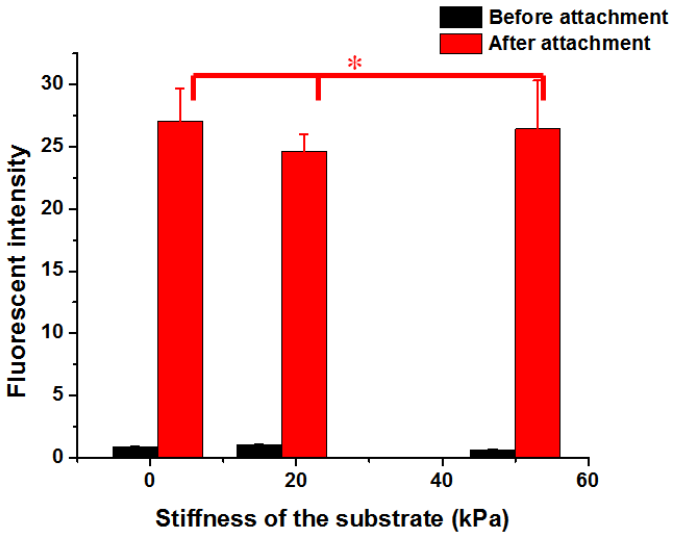


Figure 3.2: BSA attachment on the PA gels of different stiffness. The bar graphs indicate the fluorescent intensity before and after the BSA attachment. The coating concentration of BSA is independent of the substrate stiffness. Asterisks indicate statistical significance and at $p < 0.05$ the means are not statistically different. Data show is the mean ± SEM ($n = 5$).

Rockford, IL) and conjugated with 5 $\mu$g ml$^{-1}$ of laminin (Sigma, St. Louis, MO). In order to test the attachment of the protein as a function of substrate stiffness, fluorescently-tagged bovine serum albumin (BSA, Invitrogen, Carlsbad, CA) was coated on the gel. It was found that the protein concentration was independent of the stiffness as seen in figure 3.2. The coating concentration has also been shown to be independent of the stiffness of the gel with other proteins like collagen I, collagen IV, laminin, and fibronectin [166].

Characterization of PA gels:

Asylum atomic force microscope (AFM) with pre-calibrated silicon nitride tip was used to characterize the real stiffness of PA gels in phosphate buffered saline (PBS, Invitrogen, pH=7.4) solution. The spring constant of the AFM cantilever was 148.14 pN nm$^{-1}$ and it performed the indentation with a speed of 0.1 m sec$^{-1}$. Hertz theory (Equation 3.2) was used to extract the elastic modulus of the indented substrates [167].

$$Z - Z_o = d - d_o + \sqrt{\frac{k(d - d_o)}{\frac{2}{\pi}E(1 - \upsilon^2)\tan\alpha}} \tag{3.2}$$

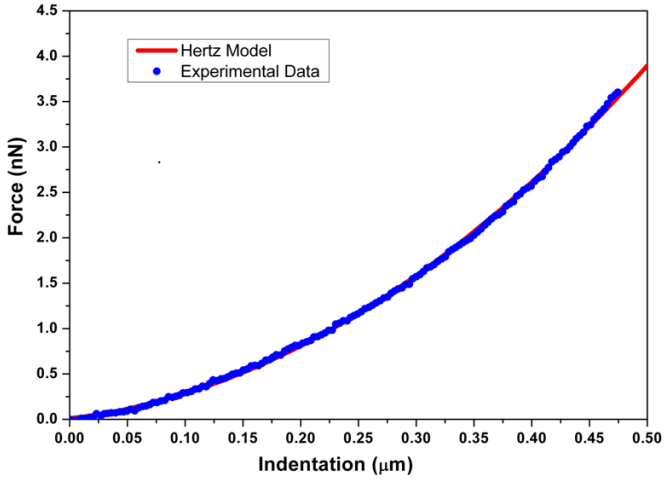


Figure 3.3: The least-square fitting of Hertz theory to experimental AFM force-indentation data.

where $k$ is the spring constant of cantilever calibrated by resonant frequency counting. $Z$ and $d$ are cantilever's base displacement and tip deflection, respectively. $Z_0$ is the piezo-controller's vertical position as the AFM tip touches the gel surface, and $d_0$ is the initial cantilever deflection prior to bending. The $\upsilon$ is the Poisson ratio of sample (0.5 for hydrated gels in the present study). $\alpha = 35°$ is the half open-angle of cantilever tip and $E$ is the elastic modulus of sample to be found. Figure 3.3 shows a representative example of force versus indentation of the substrate and the theoretical fitting curve.

### 3.2.2 Cardiac cell isolation and culture

Cardiac cells were obtained from chicken embryos during the 32-35 Hamburger Hamilton stage, which is approximately 8 days after conception [168]. After sterilizing the eggshell with 70% ethanol, the embryo was removed, placed in a petri dish containing Puck's saline, and quickly decapitated. The heart was removed, rinsed twice in PBS solution to remove the blood, and incubated in a solution containing 0.05% trypsin/PBS (Invitrogen, Carlsbad, CA) for ∼15 minutes at 37 °C. Following enzymatic digestion, the solution containing the heart was pipetted gently to dissociate the tissue. About 100,000 cells cm$^2$ were seeded on the laminin-coated substrates and cultured in minimum essential medium with alpha modification (Sigma, St. Louis,

MO), supplemented with 10% fetal bovine serum (FBS, Sigma, St. Louis, MO) and antibiotics (100 U $mL^{-1}$ penicillin and 100 $\mu$g $mL^{-1}$) (Invitrogen, Carlsbad, CA). During data acquisition, the gels and the culture dishes were kept on a heated microscope stage to maintain a temperature of 37 °C, and a tube releasing 5% $CO_2$ was kept over the dishes to maintain a physiologically relevant pH.

### 3.2.3 Immunofluorescence, imaging and image processing

Cells cultured on the PA gels and TC dishes were immunolabeled on the second and the fifth day in the study. Cells were fixed with 4% paraformaldehyde (PFA, Electron Microscopy Sciences, Hatfield, PA) for 30 minutes and then permeabilized with 0.2% Triton X-100 (Sigma, St. Louis, MO) for 15 minutes. Cells were then blocked with Image-iT FX (Invitrogen, Carlsbad, CA) for 30 minutes. They were incubated in monoclonal mouse anti-vinculin (Sigma, St. Louis, MO) at a 1:200 dilution in PBS at 4 °C overnight. These cells were permeabilized again in 0.2% Triton X-100 for 15 minutes and incubated in FITC-conjugated goat anti-mouse (BioRad Laboratories, Hercules, CA) at a 1:200 dilution in PBS at 37 °C for 2 hours. Cells were then incubated for 2 hours in 6.6 $\mu$M rhodamine-phalloidin (Invitrogen, Carlsbad, CA) and finally in 500 nM of DAPI (Invitrogen, Carlsbad, CA) for 5 minutes at 37 °C. The immunolabeled cells were mounted in ProLong gold (Invitrogen, Carlsbad, CA) antifade reagent to prevent photobleaching. The cell preparations were imaged by a Zeiss LSM 710 confocal scanning laser microscope at 40X, NA 1.4 water immersion objective.

Images were processed using ImageJ version 1.42q [169]. Area of the cell was found by first creating a maximum Z-projection from the confocal images and then thresholding it so that the entire cell area was covered. Any object smaller than 3 $\mu$m in radius was eliminated using the software to get rid of any cellular debris and then the percentage of the area covered by the cells was computed by the software. This percentage was converted to an area in square microns. In order to find the percentage of FAs, one confocal section per image was used, which is approximately 0.50 $\mu$m from the interface between the cell membrane and the coverslip. The images were thresholded and a Watershed segmentation algorithm was applied to the images to see

only the FAs [170]. ImageJ was also used to create fluorescence intensity line profiles over FAs of actin and vinculin images around different regions of the cell. The cells were found independently for computing the FA percentage.

### 3.2.4 Statistical analysis

Statistical analysis was performed using one-way ANOVA in OriginPro 8.1. Unless otherwise mentioned, the values reported are mean ± standard error of the mean (SEM) and the results were considered statistically significant when the $p$-value was less than 0.05 ($p < 0.05$).

## 3.3 Beating rate of cardiac cells

ECCMs were seeded on laminin-coated PA gel substrates of varying stiffnesses, and the beating rate of the cells was monitored as a function of time over five days. Cells were independently chosen on all the substrates and a 30 second video of the beating cells was taken every day for five days in culture. Figure 3.4A shows the variation in the average beating rate of the cardiac cells over this period. Note that the initial average beating rate varies greatly ranging from less than 20 beats per minute on the rigid TC dishes to 100 beats per minute on the 18 kPa gel. However, the average beating rate converges to a more narrow range around 60-80 beats per minute by the fifth day. Figure 3.4B shows the beating rate of the cardiac myocytes as a function of substrate stiffness after one and five days post-seeding. The 18 kPa substrate, which mimics the stiffness of the myocardium, shows the highest beating rate on the first day of culture. This beating profile on the first day can be approximated by a Gaussian curve for the stiffness of the substrate. However, by the fifth day, the beating rate of the cells converge to a narrow range of 60-80 beats per minute and no longer follows a bell curve. A plausible mechanism for this is that during the initial days when the cells are seeded on the substrate, no cell-cell interactions are possible as a confluent cell sheet is not formed. However, by second day cells started forming cell-cell junctions and a cell network was seen forming on the stiffer substrates (18 kPa, 50 kPa, and TC). Fibroblasts started proliferating between neighboring cardiac cells, which linked them together. It has been shown that the

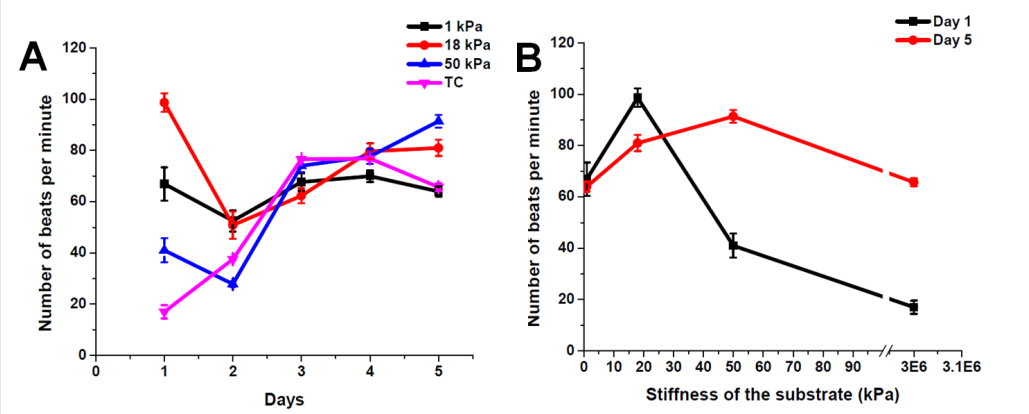


Figure 3.4: Beating rate of cardiac cells on the substrates (A) The beating rate of cardiac cells on 1 kPa, 18 kPa, 50 kPa and TC dishes as a function of time over five days. (B) The beating rate of cardiac cells as a function of stiffness on the first and the fifth day of culture. Data shown is the mean ± SEM ($n = 10$).

beating rates of cardiac cells within 300 $\mu$m can be synchronized through the fibroblast connection [171], and a similar phenomenon was observed during our experiment when two cardiac cells were connected *via* a fibroblast. It is known that fibroblasts do not extend their processes on soft substrates (1 kPa) and remain rounded [172]. So how do the cells on the soft 1 kPa gel beat around the same frequency as well? One of the reasons could be that the beating frequency of the cells reverts to a natural beating frequency that is inherent of the cell as seen in previous studies [173]. Another possible reason could be that when the cells are close to each other, the substrate itself may serve as a mechanical link between the substrates. Contraction of a cell during beating results in stretching of the nearby substrate, which in turn stretches the neighboring cells' membrane and a cascade of signaling mechanisms start in this neighboring cell. It would be interesting to see if this convergence phenomenon is still seen on the stiffer substrates when an enrichment of the cell mixture is done to limit the number of fibroblasts by pre-plating this cell mixture before seeding them on the different substrates.

## 3.4 Formation of focal adhesion complexes on polyacrylamide gels

Formation of FAs and the cytoskeletal organization of the cell were examined *via* confocal microscopy on the various substrates on the second and the fifth day. FAs are specialized sites of adhesion developed by many cells in culture. They serve as the pivots to assist the intracellular pre-stress build-up and are the sites at which cell traction are transmitted to the substrate. They link the extracellular matrix components to intracellular cytoskeleton (actin filaments) *via* integrin receptors. FAs can be thought of as a sensory organ capable of responding to a variety of diverse external features such as ligand density [174, 175], topography [144], and rigidity [176]. FAs are composed of many different types of proteins like paxillin, vinculin, and talin [177]. However, it has been proposed that vinculin depletion leads to drastic changes in the motility of cells and FA sizes [64]. Furthermore, vinculin is the most abundant FA protein [178]. Hence, the cells on these substrates were labeled with anti-vinculin antibody.

The formation of FAs is a highly orchestrated event starting from: (1) Rho-stimulated contractility, (2) the generation of isometric tension in adherent cells, (3) bundling of actin filaments, (4) aggregation of integrins, and (5) activation of the focal adhesion kinase (FAK) [179]. To produce a more visual illustration of the relative intensity of actin and vinculin, fluorescence intensities in one dimensional line profiles drawn over FAs was compared and is shown in Figure 3.5. It can be seen from the line profile that the intensity of actin and vinculin present on the soft (1 kPa) gel is very small compared to the other substrates. The cells are not able to form many FAs as there is not enough actomyosin based contractions on the soft substrate [69]. As one of the first events in the formation of FAs is reduced on the soft gel, other downstream events are also hindered and hence very few FAs form on this substrate. This is consistent with previously published results that a smaller force is required to peel off cells from soft gels compared to the rigid glass [78]. FA formation on this very soft substrate occurs by nonspecific tyrosine hyperphosphorylation [69]. On the other hand, the pixel intensity values for actin and vinculin is high on the stiff (50 kPa) gel and the rigid (TC dish) substrate. Also, there is co-localization of actin and vinculin, which leads to aggregation of integrins at the FA sites [64]. On these stiff surfaces FA

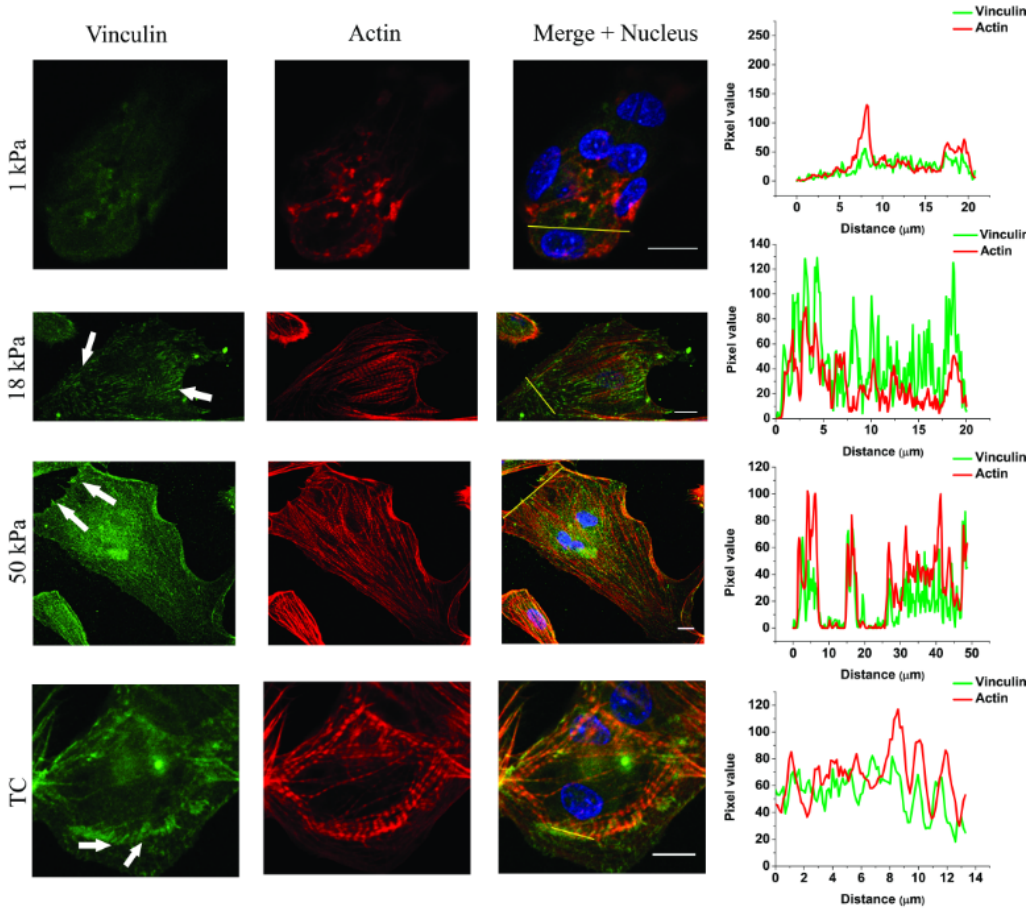


Figure 3.5: Relative fluorescent intensity of actin and vinculin for cells on the substrates. Sections of cardiac cells expressing vinculin and actin proteins on the different substrates are shown. Fluorescence intensity profiles depict the area of the line drawn in the merged images. The arrowheads show well-defined mature FAs. Scale bar: 10 $\mu$m.

development is possible by enhanced tyrosine phosphorylation on multiple FA proteins [74]. Also, a higher degree of organized cytoskeleton emerges with the increase in stiffness as seen from Figure 3.5. On the soft 1 kPa substrates, formation of tissue like aggregates can be seen and only small nascent FAs are visible. While on the other substrates, cells acquire a more spread morphology and show well defined prominent FAs of larger size.

Figure 3.6A shows a representative image of the FAs present on the cell and its corresponding area. 3.6B shows that the percentage of FA increases as a function of substrate stiffness. Both the fibroblasts and the cardiac cells show higher percentage of FAs on the rigid (TC) substrate compared to the

soft (1 kPa) PA gel and the 18 kPa gel. Small nascent FAs also referred as focal complexes (FXs) are formed on very soft 1 kPa substrates [180]. These small FAs cannot provide the necessary adhesion to propel the cell forward. As a result, these FAs quickly disassemble and the cells on the soft 1 kPa gel acquire a tissue like morphology, where a lot of cells are present in the aggregate. However, on the comparatively stiffer substrates small FAs quickly mature and form larger FAs providing the necessary traction forces for the cells to acquire a more spread morphology [74]. There is not a statistical difference in the percentage of FAs present on fibroblasts ($p = 0.49$) and cardiac cells ($p = 0.95$) for the two different days, suggesting that after the first two days, properties of FAs do not change much. This also suggests that with time, FAs change their main function from the transmission of strong propulsive forces to a more passive function of providing adhesion sites for the maintenance of a well spread cell morphology [181]. Fibroblasts were identified from cardiac cells based on the sarcomeric striation patterns seen on the cardiac cells. Figure 3.6C shows that the number of FAs per cell ($p < 0.05$) and the FA area per cell ($p < 0.05$) are much higher on the rigid (TC) substrate compared to the soft (1 kPa) gel substrate. The means of all these parameters are statistically different for the rigid and the soft gels at $p < 0.05$. FAs are the sites of attachment from the intracellular cytoskeleton *via* integrin receptors to the extracellular matrix. Formation and development of FAs require generation of isometric tension by movement of myosin II motors on the actin filaments. Since, cells on the soft substrate (1 kPa PA gel) cannot develop this isometric tension by the actomyosin contractions, very few FAs are formed on this substrate. Furthermore, the FAs that are formed on this substrate are mostly immature since aggregation of integrins is not possible on the soft substrate because of the reduced actomyosin contractions. As a result, cells on this substrate resemble tissue-like morphology where a lot of cells are present in the aggregate. On the other hand, cells on stiffer substrates are able to generate isometric tension by actomyosin contractions leading to their maturation. It should be noted that the morphology of cells on the 50 kPa PA gel is very similar to that on the rigid TC dish. Also, as seen in Figure 3.6B there is a very small increase in the percentage of FAs from the 50 kPa substrate to the TC substrate, and the graph seems to reach a steady value. This means that after a certain threshold, the stiffness of the substrate is no longer the dominant factor in the formation of FAs. Any

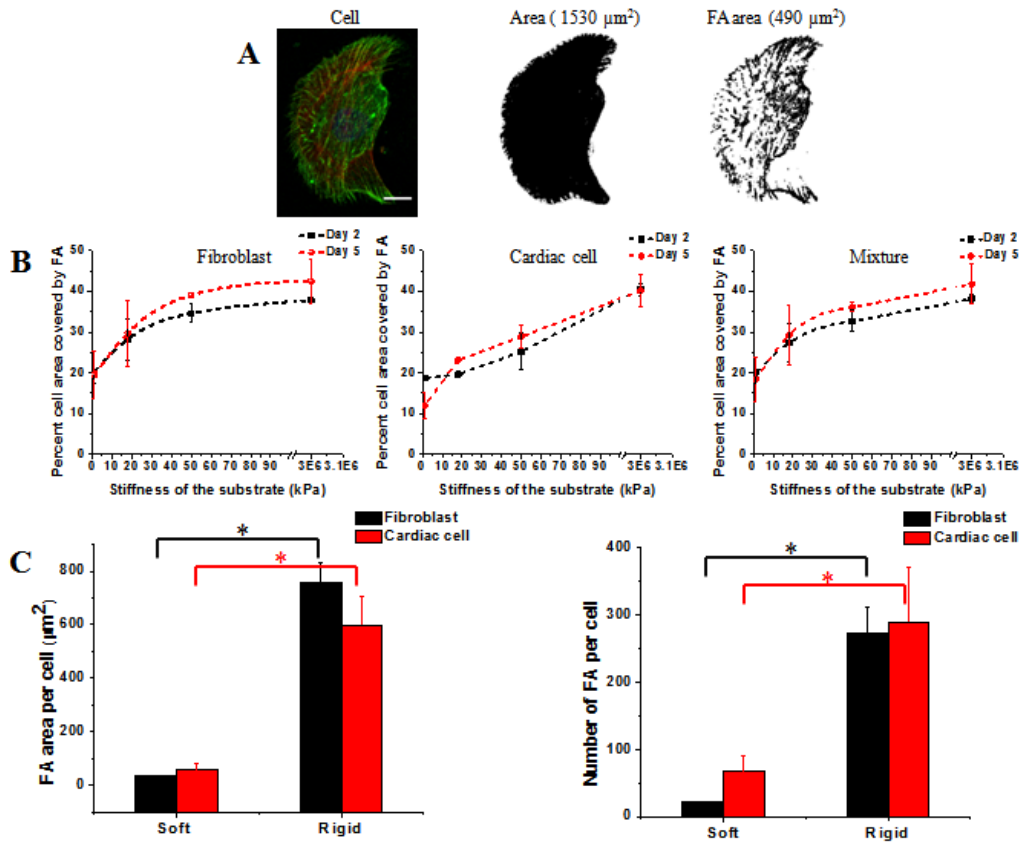


Figure 3.6: Quantification of FAs (A) The process used for quantification of FAs.(B) Quantification of FA area for fibroblasts, cardiac cells and their mixture for the 1 kPa, 18 kPa, 50 kPa PA gels and TC dishes.(C) Quantification of the number of FA/cell ($p < 0.05$) and the average FA area/cell ($p < 0.05$) for the soft (1 kPa) and the rigid (TC dish) substrates on day two. Asterisks indicate statistical significance. At $p < 0.05$, the means are statistically different. Data show is the mean ± SEM ($n = 20$). Scale bar: 10 $\mu$m.

further increase in the stiffness of the substrate after the threshold stiffness will only lead to very small changes in the overall morphology of the cells and growth of FAs. However, in order for the cells to perform their functions optimally, a stiffness matching between the cell and the substrate is desired [46].

### 3.4.1 Cytoskeletal organization of cardiac cells

Figure 3.7A shows the actin cytoskeleton on the very soft 1 kPa PA gel. It can be seen that even though there are striations visible on the cells on

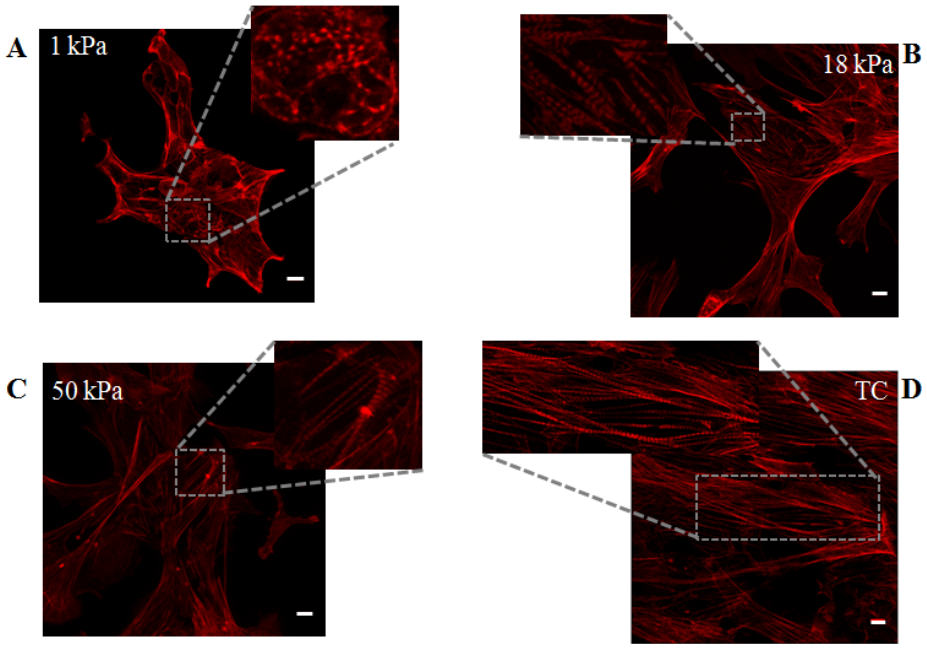


Figure 3.7: Cytoskeletal structure of the cells on the substrates. Single stack con-focal images for the cells on the (A) 1 kPa, (B) 18 kPa, (C) 50 kPa PA gels and (D) the TC dish. The insets in the figures show a zoomed view of the sarcomeric striations. Scale bar: 10 $\mu$m.

this soft gel, which is a hallmark of any striated muscle cell, these striations are not aligned as seen in the sarcomere *in vivo*. On the other hand, highly aligned sarcomeric striations are seen in Figure 3.7B, C, and D on the 18 kPa, 50 kPa PA gel and the rigid TC substrate. Previous reports have shown that optimum actomyosin striations were seen on substrates, which mimic the stiffness of the myocardium [78, 81, 82]. However, even on the rigid TC substrate we were able to see highly aligned sarcomeric patterns. This could be because cell-cell contacts might have a similar effect as cell-on-gel effect when a cellular network is formed. This was also seen in another study when endothelial cells had indistinguishable morphology on the stiff and the soft substrates when they reached confluence [80]. Also, fibroblasts which generally cannot extend their processes and remain rounded on the soft gels are seen to have a well spread morphology when cell-cell contacts are established [80]. Myofibrillogenesis involves the precise stacking of multiple linear array of units into a structured sarcomere [182]. It starts with the formation of pre-myofibrils at the periphery of spreading cardiomyocytes and get bundled into mature myofibrils over time [183]. However, since the

soft 1 kPa substrate cannot provide enough actomyosin based contractions formation of aligned sarcomeric structure is not seen on this substrate. On the other three substrates, enough tension is developed from the mature FAs that the entire process of myofibrillogenesis is possible.

## 3.5 Measurement of the contraction force of cardiac cells

A novel micro-electromechanical systems (MEMS) force sensor was used to perform a force spectroscopy on cells that were cultured on 18 kPa PA gels and TC dishes for the second and the fifth day. The fabrication process and other applications of this MEMS force sensor have been described previously [184, 185]. The resolution of the MEMS sensor was ∼0.25 nN. The MEMS force sensor has two beams, a fixed (reference) beam and a free (measurement) beam, which touches the cell cluster as seen in Figure 3.8A. The MEMS senor was kept in a solution of 70% ethanol for two hours under UV light in order to sterilize the sensor before starting the measurements. The MEMS sensor was cleaned by sterilized DI water multiple times prior to experiments in order to remove any ethanol residue or micro-physisorptions on device. To eliminate the external mechanical indentation, the forward movement of the beam was stopped right after contacting the cell body. The cyclic contraction force, $F$, was quantitatively obtained from, $F = k\Delta x$, where, $k = 48.96$ nN $\mu m^{-1}$, is the spring constant of the force sensor and $\Delta x$ is the deformation of the sensor spring. Figure 3.8B shows the phase-contrast image of the MEMS probe in contact with the 18 kPa gel, with the sensor probe contacting the cell body along direction of contraction. Figure 3.8C shows the force profile of the cardiac cell on both the 18 kPa gel and the TC substrate as a function of time on the fifth day. The duration for one contraction-relaxation cycle on both substrates was about 0.6-0.8 seconds. Figure 3.8D shows a bar graph of the force measured by the MEMS probe as a function of stiffness on both the second and fifth days. The force exerted on the MEMS sensor by the cells cultured on TC dish on the fifth day ($F = 71.30 \pm 6.38$ nN) was statistically higher than that by the cells cultured on the soft 18 kPa gel on the fifth day ($F = 30.16 \pm 3.83$ nN) at $p < 0.05$ and the same trend was seen for FAs as well. The isometric contractile stress that cardiac myocytes applied on

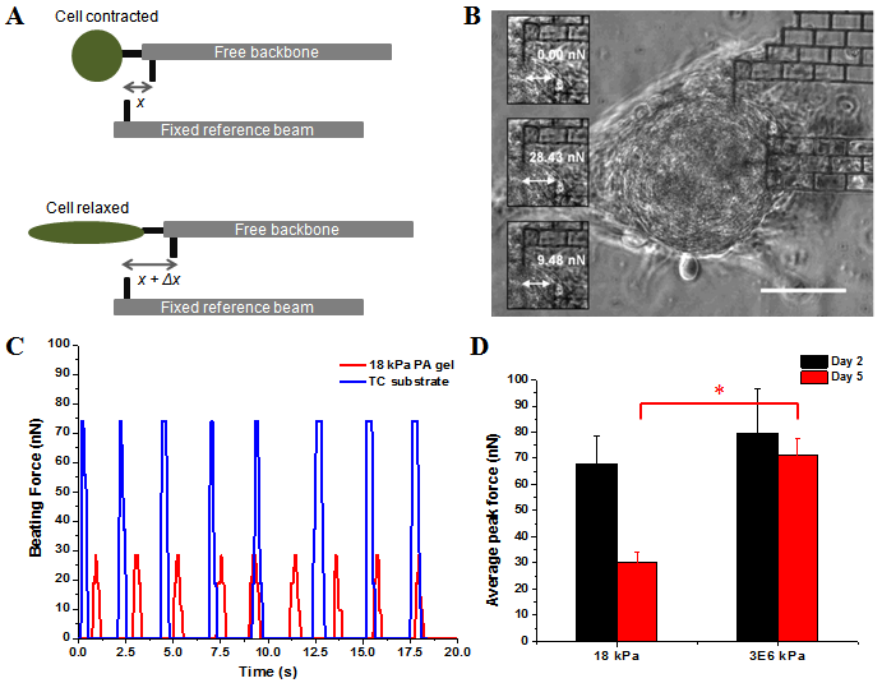


Figure 3.8: MEMS force measurement on the substrates (A) The principle of operation (B) Phase contrast image showing a cardiac cell aggregate with MEMS force sensor attaching from right side to measure the beating force during contraction-relaxation cycle. Cell is on 18 kPa gel on the fifth day of culture. (C) The force profile of the cardiac cell cluster sensed by the MEMS force sensor as a function of time on the 18 kPa PA gel and the TC dish. (D) Bar-graphs showing the average peak force exerted by the cardiac cell cluster on the 18 kPa PA gel and the TC dish on the second and the fifth day. Asterisks indicate statistical significance between the average peak force on day five between 18 kPa PA gel and TC dish (3 GPa). At $p < 0.05$, the means are statistically different. Data shown is the mean $\pm$ standard deviation (SD). ($n = 3$). Scale bar: 50 $\mu$m.

their fibroblast surrounding can be estimated by considering that the beating force measured by the force sensor is only sampled from a portion of the cell membrane (contact area of $\sim$25 m$^2$). The value of the stress on the TC dish was calculated to be 3.2 nN m$^{-2}$ while that on the 18 kPa gel was 2.7 nN m$^{-2}$ on the second day. These values are very close to the contractile stress of neonatal rat cardiac myocytes (5.5 $\pm$ 2 nN m$^{-2}$) which has been reported elsewhere [89].

The higher force on the rigid TC dish could be because of the formation of higher percentage of FA on this substrate compared to the 18 kPa gel as seen in Figure 3.6B. It should be noted that the force exerted on the MEMS sensor

might not be the total beating force of the cardiac cell cluster. Part of the force is lost in the displacement of the PA gels when the cell is contracting. Also, the size of the cluster chosen might have an important affect on the force seen by the MEMS sensor. The force seen by the MEMS probe on the rigid TC dish on day two and five was not different as seen in Figure 3.8D. Also, the percentage of FAs remained similar during this period on the TC dish as seen in Figure 3.6B. The sensor is based on the principle of Hookean mechanics, $F = k\Delta x$; therefore, if the placement of the sensor is not optimum for sensing the maximum contraction, a big difference in the force is possible. A shortcoming for the sensor is that it is dependent on the size of the cluster and the location of the sensor with respect to the cluster. If both these parameters are not optimized, an error in the force measurement is possible. While these are some of the uncertainties associated with the MEMS sensor, it can be used effectively to give a firsthand approximation for the force of a beating cardiac cell/cluster.

## 3.6 Mechanical communication between the cardiac cells

Mechanical communication between distant cardiac cells was also investigated *via* mutual stimulation of distant cardiac cells. If two distant cardiac cells communicate with each other primarily *via* paracrine interaction, the degree of stimulation will be independent of the elasticity of the substrate. However, if the primary method of communication is *via* mechanical means, then it will be highly dependent on the stiffness of the underlying substrate. To that end, cell beating patterns on two different stiffnesses soft (1 kPa) and stiff ($\sim$50 kPa) substrate were studied. Videos were taken for cells in order to locate beating pairs for both the soft and the stiff PA gel. For the soft gel 246 beating pairs were identified while for the stiff gel, 52 beating pairs were identified. Figure 3.9A shows the distributions of cell on the soft 1 kPa PA gel. Each of these beating pairs were distributed in different bins relative to their distance from the nearest neighbor as 0-5 $\mu$m, 5-10 $\mu$m, 10-20 $\mu$m, 20-30 $\mu$m, and 30-40 $\mu$m apart. Cells that did not have any neighbor within 60 $\mu$m were considered as single cells only. Figure 3.9B shows the percentage of daily beating couple on the 1 kPa gel. An exponential decay can be seen

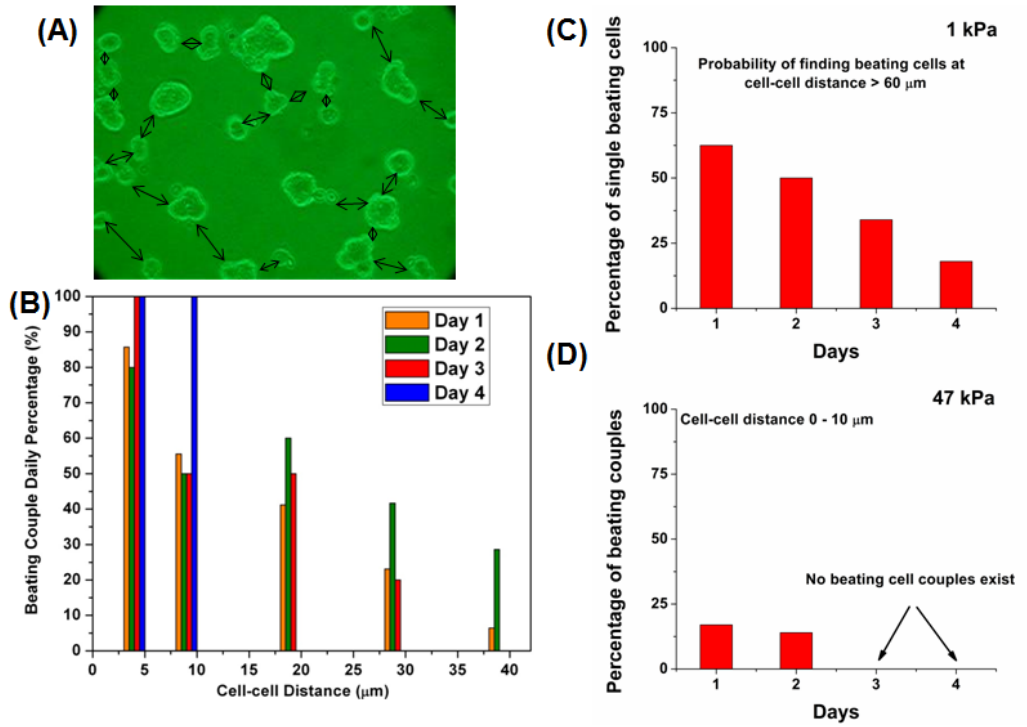


Figure 3.9: Mechanical communication between cardiac cells on PA gels of different stiffnesses. (A) Determination of cell pairs by measuring the distance between the nearest neighbors. (B) On 1 kPa gel, cell pairs are grouped by distances between neighbors, such as a group consists of pairs with partners 0-5 $\mu$m, 5-10 $\mu$m, 10-20 $\mu$m apart, etc. $n = 246$.(C) Percentages of single cells beating VS time on 1 kPa. These cells have no partners within 60 $\mu$m. (D) On 47 kPa gel, percentage of beating pairs (both cells of the pair beating) within mutual distance 0-10 $\mu$m is shown on day 1, 2, 3 and 4, respectively. $n = 52$.

for the beating couple as a function of distance especially for the first day. Cell-couples which had closer neighbors beat for a longer period of time. For example, on day 4, 100% of the pairs with partners within 0-5 $\mu$m showed beating. However, this percentage drops down to 50% as the beating pair distance is 5-10 $\mu$m apart. Single cells lack any mechanical stimulation from each other. Therefore, lower fraction of them beat over a longer time period. Figure 3.9C shows the percentage of single beating cells as a function of time on the soft 1 kPa substrate. On day 1, 2, 3, and 4, the percentages of single beating cells are 62.5%, 50%, 34% and 18% respectively.

The stiff substrate is about 50 times more rigid than the softer one. Therefore, mechanical deformation of the substrate past 10 $\mu$m was almost negli-

gible. Therefore, the beating pattern of cells only till 10 $\mu$m was studied on the stiff gel. Figure 3.9D shows that the percentage of beating-cell-couples within 0-10 $\mu$m was only 17% on day 1 and 14% on day 2, much lower than that seen on the soft, 1 kPa gel. By day 3 and 4, no beating-couples could be identified.

It is well known that there exists a mechanoelectric feedback (MEF) in cardiac cells for a variety of animals [171]. Therefore, a mechanical stimulus applied to a cardiac cell results in an action potential by the cells which caused the cells to contract (beat). This study showed that neighboring cardiac cells can stretch its neighbor by mechanically deforming the soft medium between them. Thus they can possibly stimulate each other possibly through a MEF response. Mechanical activation of single cardiac cell has also been shown in this study which further confirms the presence of a MEF loop between distant cardiac cells. To answer the question, how far a cardiac cell can see, lies in the magnitude of stretch induced by its neighbor. This in turn depends on the stiffness of the substrate. For a stiff substrate, the same amount of force would produce a smaller deformation compared to a softer substrate. Following myocardial infarction (MI), the stiffness of the tissue increases by several folds due to fibrotic rigidification [167]. Thus after an MI, the heart gradually stops beating. In human heart failure, ventricular fibrillation often results in the damaged cardiac region which is generally in the millimeter-centimeter scale. Such long cell-cell separation distance can diminish any mechanical stretching signal produced by beating cardiac cells resulting in a de-coupling cascade.

## 3.7 Conclusion

This study showed the role of stiffness of the substrate in controlling the fate of ECCMs. Cells cultured on PA substrates with elasticity comparable to that of the native myocardium (18 kPa) exhibited the highest beating rate during the first few days of culture. The initial beating rate of individual cells on all the substrates varied greatly, but began to converge within five days. Formation of FAs and cytoskeletal structure development was also investigated on substrates of different stiffnesses *via* confocal microscopy. It was found that a higher percentage of FAs formed on TC dishes compared

to the softer PA gels. Furthermore, highly aligned sarcomeric striations were clearly visible on 18 kPa, 50 kPa, and TC dish, whereas cells on 1 kPa only showed non-aligned diffused striations. The force of contraction on these substrates was measured using a MEMS force sensor, which showed that the force of contraction for the cells on TC dishes (F = 71.30 $\pm$ 6.38 nN) was significantly larger than those cultured on the 18 kPa PA gel (F = 30.16 $\pm$ 3.83 nN). This is most likely due to the formation of higher percentage of FAs on the TC dishes compared to fewer FAs on the softer gels. Also, mechanical communication between distant cardiac cells was studied on soft and stiff PA gels. As the distance between neighboring cardiac cell pair increases, the probability of them beating for a longer period of time decreases. Almost 100% beating cell pairs were found at distances of 5-10 $\mu$m for the soft substrate on day two while less than 15% were found on the stiffer substrate. The cumulative finding from this study suggests that the elasticity of the substrate plays a vital role in controlling the fate of ECCMs. These results can have a significant impact on the design of 3D cardiac tissue engineered scaffolds.

# CHAPTER 4

# GEOMETRICAL CONSTRAINTS INFLUENCE THE MYOGENESIS OF C2C12 SKELETAL MUSCLE MYOBLASTS

## 4.1 Introduction

This chapter looks at the affect of geometrical constraints on the differentiation potential of C2C12 rat skeletal muscle myoblasts. Tissue architecture in the body does not follow only linear or circular geometries. It is rather a mixture of both linear and circular elements together in the same geometry. Therefore, in this study, $\mu$CP was used to stamp fibronectin islands of three different geometries, lines of different widths, tori of different inner diameters (ID), and hybrid structures (combining linear and circular features in the same geometry) on the surface of petri dishes. For the liner geometries, the length of the line was kept constant at 2000 $\mu$m while its width was varied to 300 $\mu$m, 150 $\mu$m, 80 $\mu$m, 40 $\mu$m, and 20 $\mu$m respectively. For the tori structures, the ID was 40 $\mu$m, 100 $\mu$m and 200 $\mu$m while the outer diameter (OD) was 200 $\mu$m, 260 $\mu$m and 360 $\mu$m respectively. The linear portion of the hybrid structure was kept constant at 100 $\mu$m while changing the arc angle from 30°, 60°, and 90° for the circular portion. This resulted in hybrid 30°, hybrid 60°, and hybrid 90° structures. On each of these geometries, the differentiation parameters of fusion index, maturation index, alignment, and response to electrical pulse stimulation (EPS) was quantified for the C2C12 skeletal myoblasts. The use of micro-patterning techniques helped to decouple the geometrical (mechanical) cues experienced by the cells *in vitro* which otherwise are uncontrolled under classic cell culture conditions.

Section 4.2 will outline the protocol for $\mu$CP fibronectin on the surface of petri dishes. It will also discuss the protocol for imaging, image processing and electrical pulse stimulation (EPS) employed in this study. Section 4.3 will summarize the finite element modeling (FEM) of the three different geometries used for generating the stress maps of the cell micro-islands. Section

4.4 will quantify the fusion and maturation indices of C2C12 myoblasts on the different geometries. Section 4.5 will show the alignment of myotubes of C2C12 cells on the different micro-patterns. Section 4.6 will evaluate the actuation potential of mature C2C12 myotubes in response to an electric field. Section 4.7 will investigate the reason for differences in the myogenic potential of these cells on the different geometries. Section 4.8 will summarize the major findings of this chapter. These results have been published in [186].

## 4.2 Experimental

Micro-patterning techniques have enabled researchers to print organic molecules on substrates thereby regulating the location and shape of cells on them. These techniques have been widely used to mimic the complex 3D *in vivo* tissue architecture and have enabled to gain deeper understanding about the physiological micro-environment experienced by the cells. This section will present the protocols used in this study.

### 4.2.1 Fabrication of micro-patterned substrates

Figure 4.1 shows a schematic overview of the entire $\mu$CP process. SU-8 (Micro Chem, Newton, MA) masters were created on a silicon wafer by using standard photolithography. The master was first silanized by dimethyl (3,3,3-trifluoropropyl) silane (Sigma, St. Louis, MO) and PDMS stamps were replicated from the master by casting Sylgard 184 (Dow Corning, Midland, MI) on the silicon wafer. Micro-patterned substrates were prepared by stamping the PDMS on 35 mm Falcon polystyrene petri dishes (BD Biosciences, Bedford, MA). The PDMS stamp was coated with 50 mg $ml^{-1}$ of fibronectin (Sigma, St. Louis, MO) and incubated for 30 minutes prior to stamping them on the petri dishes. The stamps were then dried with nitrogen and kept in conformal contact with the substrate for 20 minutes in an incubator. After stamping the protein, the substrate was blocked with 2% Pluronic F-127 (Sigma, St. Louis, MO) to render all unpatterned regions non-adhesive to the cells. The substrate was rinsed three times with PBS prior to cell seeding. Approximately, 75,000 cells were seeded on each substrate and observed for nine days resulting in an initial cell seeding of 7,800

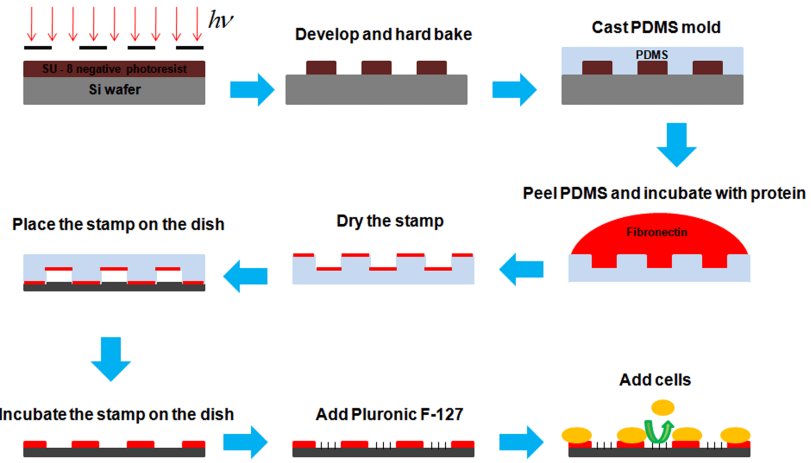


Figure 4.1: Schematic showing the preparation of the micro-patterned substrates.

cells per $cm^2$ for the 35 mm petri dish.

Three different geometries - linear, circular, and hybrid (linear and circular in the same structure) were patterned on the surface of the petri dishes which also as served as a control. Figure 4.2 shows the cells on different types of geometries after 24 hours of culture in the growth media. Skeletal myogenesis is a highly orchestrated terminal differentiation process in which the proliferating mono-nucleated myoblasts differentiate and fuse to form multi-nucleated myotubes. In this chapter, the influence of 2D geometrical cues on the differentiation of C2C12 myotubes was investigated. C2C12 myoblasts were patterned on fibronectin islands using $\mu$CP. The cells conform uniformly to the protein micro-islands and form a confluent monolayer by the end of 24 hours. However, cells on the smallest torus patterns (torus ID 40 $\mu$m) blend over the central hole to form a circle rather than a torus. This effect was inversely related to the ID and was lessened for increasing ID's from 40 $\mu$m to 200 $\mu$m.

### 4.2.2 Culture of C2C12 cells

The murine-derived muscle cell line (C2C12) was purchased from American Type Culture Collection (ATCC, Manassas, VA). The cells were cultured in Dulbecco's modified Eagle's medium (DMEM, Mediatech, Manassas, VA) supplemented with 10% FBS (growth medium, GM). To induce

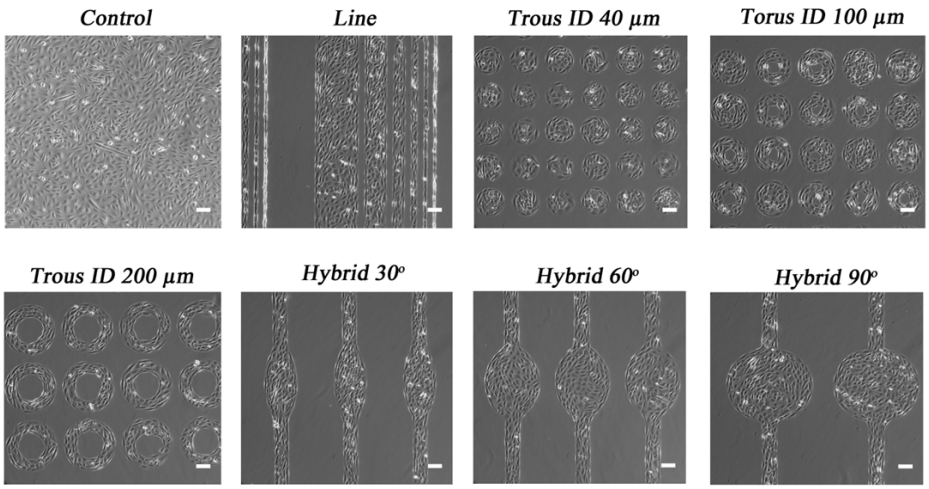


Figure 4.2: Phase contrast images of the different micro-patterned cell islands. Scale bar = 100 $\mu$m.

the differentiation of myoblasts into myotubes, C2C12 cells at 80-90% confluence were shifted to DMEM supplemented with 2% horse serum (Lonza Inc., Williamsport, PA) (differentiation medium, DM) and the medium was replaced every other day. All the time points in the figures refer to cells being present in the DM.

### 4.2.3 Immunofluorescence microscopy and quantitative analysis of myotubes

Differentiated C2C12 cells were fixed with 4% PFA for 20 minutes and permeabilized with 0.2% Triton X-100 (Sigma, St. Louis, MO) for 10 minutes. The cells were blocked with 1% bovine serum albumin (BSA, Thomas Scientific, Swedesboro, NJ) solution for 30 minutes in PBS. All the previous steps were performed at room temperature. The cells were incubated with MF-20 (anti - myosin heavy chain (MHC), Developmental Studies Hybridoma Bank (DSHB), University of Iowa, IA) overnight at 4 °C followed by incubation with fluorescein isothiocyanate (FITC) conjugated anti-mouse IgG (Invitrogen, Carlsbad, CA) and DAPI (Invitrogen, Carlsbad, CA) in dark at 37 °C. The stained cells were imaged with a fluorescent microscope (IX81, Olympus, Center Valley, PA) and the images were quantified using ImageJ. The images obtained from the MHC and DAPI signals were pseudo-colored green and blue respectively.

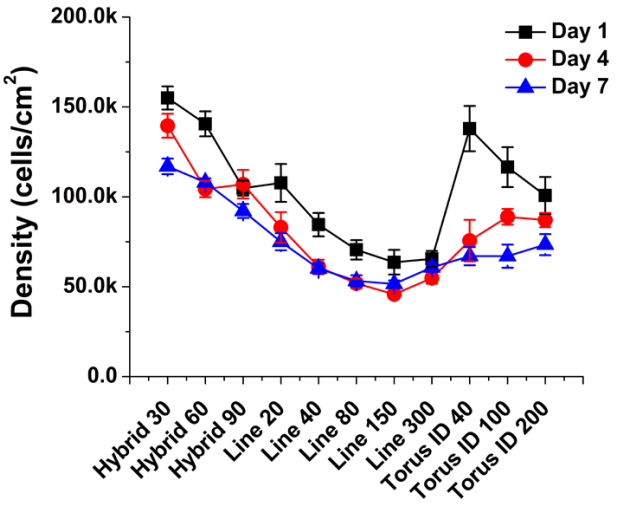


Figure 4.3: Density of the C2C12 cells as a function of time on the different micro-patterns.

### 4.2.4 Calculation of fusion index, maturation index and density for the myotubes

Fusion index was calculated as the ratio of nuclei number in myocytes with two or more nuclei versus the total number of nuclei [187]. The maturation index was defined as myotubes having five or more nuclei [187]. Edges and regions which did not show good stamping or cell adhesion were not used for analysis. Cell density was calculated by dividing the number of cells in each pattern (counting the nuclei) by the area of the pattern. Figure 4.3 shows the cell seeding density on the different geometries over seven days. Two petri dishes for each of the eight different patterns were used. At least five patterns on each dish were used for quantitative analysis. The sample size is also been mentioned in the figure legends. Table 4.1 shows the area of the different patterns used in the study.

### 4.2.5 Electrical stimulation of myotubes

The contraction of myotubes was achieved by stimulating the cells with a pulse train using a custom-built electrical setup. Figure 4.4 shows the setup used for the contraction studies. Platinum electrodes (diameter = 0.762 mm) spaced 1.2 cm apart were connected to the custom built setup and an Agilent waveform generator (Santa Clara, CA) was used for generating the pulses.

| Pattern Type | Area ($\mu$m$^2$) |
|---|---|
| Hybrid 30° | 195,000 |
| Hybrid 60° | 251,600 |
| Hybrid 90° | 346,300 |
| Line 300 $\mu$m | 600,000 |
| Line 150 $\mu$m | 300,000 |
| Line 80 $\mu$m | 160,000 |
| Line 40 $\mu$m | 80,000 |
| Line 20 $\mu$m | 40,000 |
| Torus ID 200 $\mu$m | 70,300 |
| Torus ID 100 $\mu$m | 45,239 |
| Torus ID 40 $\mu$m | 30,159 |

Table 4.1: Area of the protein micro-islands

To minimize electrolysis, a 220 F capacitor (C) was connected in series to the circuit so that the resultant signal is produced with alternating polarity [188]. The Nyquist criterion, which states that the sampling frequency must be at least twice the highest frequency contained in the signal, was maintained during all video image acquisition. The resistance of the petri dish with 1.5 ml of differentiation media ($R_{media}$) was calculated to be 475 Ω. The reactance at 1 Hz was calculated to be 725 Ω. Therefore, the net impedance of the equivalent circuit was calculated to be 865 Ω where the current leads the voltage by 56.71°. The impedance of the circuit at 1 Hz was calculated by assuming a RC circuit in series with the previously noted values for Rmedia and C. The time constant ($\tau$) of the circuit was about 105 ms and the intensity of current in the circuit was calculated to be 15.5 mA. The resistance of the Petri dish with differentiation media was calculated using the relation $\tau = R_{media}C$. The value of $\tau$ was obtained from the oscilloscope as one $\tau$ corresponds to the voltage dropping to 36.8% of the original (source) voltage. To actuate and measure myotube displacement, an electrical field pulse (amplitude 20 V, duration 50 ms and frequency 1 Hz) was applied to the culture.

### 4.2.6 Analysis of alignment and cellular displacement

The alignment of myotubes in the micro-patterned cell islands was quantified using a two-dimensional fast Fourier transform (FFT). The two-dimensional

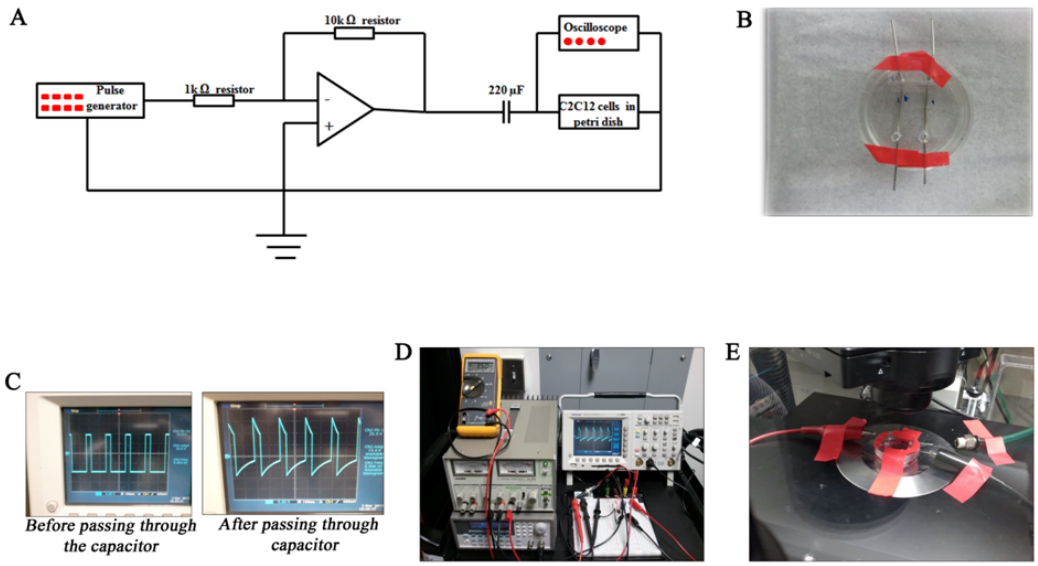


Figure 4.4: Setup for stimulating the contraction of C2C12 myotubes. (A) Circuit diagram of the electrical pulse stimulation (EPS) setup. (B) Lid with platinum (Pt) electrodes embedded on it.(C) The generation of bipolar pulses from a monopolar pulse. This phenomenon helped to minimize the electrolysis of the medium. (D) The entire setup for EPS (E) EPS in action on a petri dish.

FFT function converts the information in an image from a "real" space into a mathematically defined "frequency" space which can then be used to look at the rate of change of pixel intensity across the entire image. The resulting FFT output image contains pixels that are arranged in a pattern that reflects the degree of alignment in the original image. The low frequency pixels which also represent the background and the overall shape of the image are placed at the center. The high frequency pixels which represent edges, finer not repeated details and noise in the image are dispersed in a symmetrical pattern about the origin towards the periphery. These pixel intensities are summed along the radius for each angle of the circular projection and plotted against the corresponding angle of acquisition to produce a two-dimensional FFT alignment plot The height and the overall shape of the peaks represent the degree of alignment of cells in the original image. A high and narrow peak indicates a more uniform degree of alignment while a broad peak indicates that more than one axis of alignment may be present. A completely random alignment is shown by no discernible peak in the alignment plot [189].

The process of extraction of the principal frequency from the movies cap-

tured by the camera is as follows. First, a kymograph was generated from the image sequence. Second, the time varying intensity of the kymograph was recorded. Third, a FFT function was applied to the resulting gray scale intensity values to generate a frequency spectrum. This spectrum represented the principal frequencies of myotube contraction. In order to detect the displacement of the myotubes, quantum dots (QDs) (Qtracker 585 Cell labeling kit, Invitrogen, Carlsbad, CA) were loaded in the cell to create a good contrast so that a semi-automated approach could be used for quantification. Digital image correlation (DIC) was used to compute the displacement field of the cells and a routine was written in MATLAB R2009a (MathWorks, Natick, MA). Figure 4.5 shows the C2C12 myoblasts/myotubes loaded with QDs and the approach used for detecting the displacement. A modified approach inspired by Kamgoue et al. was used [190]. A series of image files was generated from the individual frames of each movie, each separated by 0.21 seconds. The image files displayed good contrast between the QDs of interest and the background noise. In order to simplify the detection algorithm, noise thresholding was performed; all pixels below the noise thresholding value were set to a pixel value of 0. The first frame from each movie was used as Image 1, while all subsequent frames were used as Image N, where N was the frame number. A rectangular region of interest (ROI) was carefully chosen around each QD to be interrogated in Image 1, including approximately 10 $\mu$m of surrounding pixels to encompass displacement for the entirety of the movie. A window *(Win 1)* inside this ROI was selected tightly around each QD, chosen to minimize the amount of non-QD pixels. The coordinates and intensity of each pixel in *Win 1* were recorded in the matrix $I_1(i, j)$. For each subsequent image, the same ROI was interrogated to locate the most similar subset to *Win 1*. This target subset was called Win N and was represented by the matrix $I_N(i + u_N, j + v_N)$, where $u_N$ and $v_N$ designate the desired displacement values to be extracted for Image N. *Win N* was located by sweeping the matrix $I_N(i + u^*, j + v^*)$ through the ROI in Image N; each $I_N^*$ describes a temporary window *Win N** of the same size and shape as *Win 1*. Due to the very good contrast between QD pixels and non-QD pixels, we were able to consistently locate the target *Win N* by selecting the *Win N** of maximum mean intensity in the ROI given by Equation 4.1

$$I_N(i + u_N, j + v_N) = maxmean(I_N(i + u^*, j + v^*))|(u^*, v^*) \tag{4.1}$$

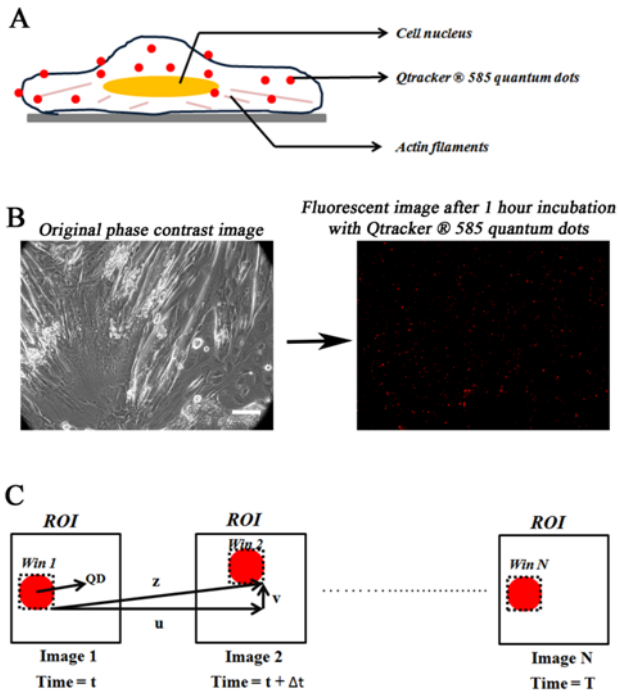


Figure 4.5: Technique used for the characterization of displacement of the myotubes after stimulating them with EPS. (A) Schematic of the cell loaded with with Qtracker 585 quantum dots (QDs) after 1 hour. (B) Phase contrast image of the control sample after 7 days in DM. (B) Digital image correlation (DIC) method used for quantifying the displacement of QDs and hence the myotube in two successive images taken at initial time ($t$) and time ($t + \Delta t$). $\Delta t$ is the frame rate of the camera and was around 0.21 s or 0.05 s. The x-component of displacement is represented by the vector $u$ while the y-component is shown by $v$. The net displacement of the QD is given by the vector $z$ which also shows the displacement of the myotubes (Scale bar = 100 $\mu$m).

The vectors $u_N$ and $v_N$ could then be correlated with the time value matching each frame N to construct the displacement versus time curves shown in Fig. 6.The ROI chosen in Image 1 must be chosen carefully to include the expected displacement for all frames in the movie sequence while minimizing selection of unwanted pixels (which can be either noise or adjacent QD not under interrogation). With proper selection of the ROI, we tested the automated displacement measurement method with several test sequences of images and determined the average error to be less than 1 pixel (around 0.285 $\mu$m).

### 4.2.7 Statistical analysis

Statistical analysis was performed using one-way ANOVA post-hoc Tukey-means comparison in OriginPro 8.5. All data values reported in the study are mean ± standard error of the mean (S.E.M).

## 4.3 Stress map analysis of the cell micro-islands

Finite element analysis (FEA) was used to create the stress patterns of the micro-patterned cell islands. A three-dimensional model for each type of cell island was created using COMSOL 4.1 (Palo Alto, CA). The two components used consist of a contractile layer and a passive layer as defined previously [106, 191]. The bottom of the passive layer was fixed and contractility of the cells was simulated by induction of a thermal strain on the top layer. Both the bottom (passive) and the top (contractile) layers were assumed as isotropic materials with Poisson's ratio of 0.499 and Young's modulus of 100 and 500 Pa respectively. The co-efficient of thermal expansion for the top layer was 0.05 K and its thermal conductivity was 10 $Wm^{-1}K^{-1}$. In order to simulate contraction, a temperature drop of 5 K was prescribed on the top contractile layer. The ratio of the height of the contractile layer to the passive layer was 5:1 and other dimensions were prescribed by the geometry of the micropatterned islands. The von Mises stresses at the bottom of the passive layer was reported. Thermal stress analysis was used as an analog to simulate the tractional stresses experienced by the cell. Meshes of different sizes (minimum mesh size varied from 0.4 - 8 $\mu$m) were used to confirm the convergence of the results.

Figure 4.6 shows the von Mises stress at the fixed side of the bottom passive layer for the three different geometries - linear (300 $\mu$m), circular (ID 200 $\mu$m, OD 360 $\mu$m) and hybrid (arc degree 30°). The predicted von Mises stress patterns from the FEA model matched well with previous reports on the equivalent principal stress of similar structures [106, 191]. The linear structure (line 300 $\mu$m) showed higher stresses at the edges than at the center and this stress value was maximized at the corners. Similarly, the torus (ID 200 $\mu$m, OD 360 $\mu$m) showed higher stress at the convex outer edge of the structure than at the concave inner edge. The stress distribution in the hybrid structure was at its maximum at the corners of the linear

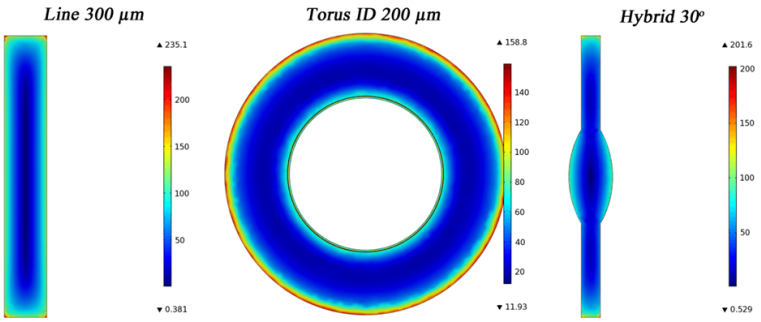


Figure 4.6: von Mises stress patterns of the three different types cell islands determined using FEA. The von Mises stress shown here are color-coded where red represents regions of maximum stress and blue represents the minimum stress. The maximum stresses are concentrated at the corners or the periphery of the structures independent of their shape.

portion while the circular portions showed higher stresses than the center of the structure. In general, the perimeter of the structures showed higher stresses than the inner regions.

It has been previously shown that the mechanical stress patterns in the micro-patterned structures corresponded to cellular growth and proliferation, meaning, higher growth and proliferation of the cell sheet was seen where mechanical stress patterns were high [106, 191]. The ratio of the stress between the convex outer edge to the concave inner edge for tori of different ID was constant at around 0.5. Since, the circumferential area was the least in the smaller ID torus (ID 40 $\mu$m), we see that even as early as 24 hours, the cells proliferated to form a complete circle rather remaining as a torus. During this time, the cells confined only to form a torus for larger ID torus (ID 200 $\mu$m) because of the larger area. However, with time (by day 7 in DM) even on the larger torus (ID 200 $\mu$m) some of the structures were filled up to form a circle rather than remaining a torus. As the torus ID 100 $\mu$m is intermediate between the ID 40 $\mu$m and ID 200 $\mu$m torus, the cellular conformity results for the ID 100 $\mu$m at 24 hours are also intermediate with some islands showing central closure reminiscent of the ID 40 $\mu$m, while other islands remain open like the ID 200 $\mu$m.

## 4.4 Fusion and maturation index of C2C12 cells

C2C12 myoblasts when deprived of serum undergo cell cycle arrest and start to fuse together to form multi-nucleated myotubes. Myotubes serve as the building blocks for skeletal muscle, thus understanding the differentiation process of C2C12 skeletal myoblasts *in vitro* has the potential to resolve mechanisms of the myogenic differentiation process *in vivo* as well. Figure 4.7 shows the fluorescent images of the cells present on the different patterns on days 1, 4 and 7 in DM; cells were cultured in GM for 24 hours and then switched to DM. As shown here, the myocyte differentiation increased as a function of time on all the substrates reaching a maximum by day 7 while nearly half of the toroid patterns showed very little to no differentiation even by day 7. Massive myotube detachment was seen on all substrates starting from 8-9 days in the DM, a result that has been reported previously [192, 193].

To quantify the differentiation of myotubes, the fusion index from the Immunofluorescent images was calculated by determining the number of nuclei in the MHC stained region (only regions with $> 2$ nuclei were used) to the total number of nuclei in the field of view. Figure 4.8A shows the fusion index of the C2C12 cells on hybrid patterns. The results show a progressive decrease in myotube differentiation starting with the hybrid 30° followed by hybrid 60° and hybrid 90°. Hybrid 30° ($45.38 \pm 2.57\%$) showed greater than 1.5 fold differentiation compared to hybrid 60° ($29.20 \pm 1.20\%$) and hybrid 90° ($25.71 \pm 2.62\%$). In contrast, there was no significant difference in the differentiation of C2C12 myotubes on the linear patterns of different widths Figure 4.8B. However, myotubes on the linear patterns showed a significant decrease in differentiation when compared to the control at $p < 0.01$. The large width line pattern (300 $\mu$m) was used to mimic the unpatterned control. Presumably, even thicker patterns are required so that the cells on these patterns start mimicking the properties of the cells on the unpatterned control. Similar results were observed for the circular geometry. There was no significant difference of differentiation between the toroids of different IDs; when compared to controls, all of the toroids showed a decrease in differentiation (Figure 4.8C, $p < 0.01$). Figure 4.8D summarizes the fusion index for all the different geometries by incorporating the highest for each type.

The results suggest that adding a small degree of circularity to a linear structure (hybrid 30° )enhances the differentiation of C2C12 myoblasts into

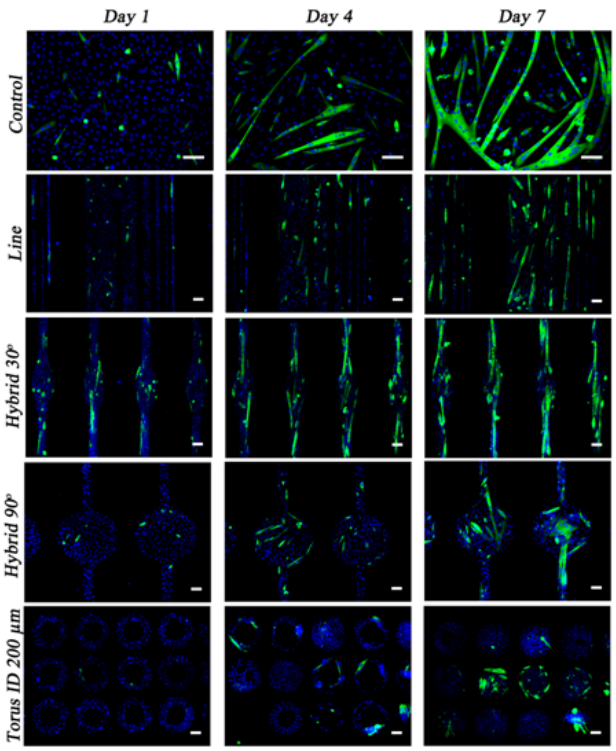


Figure 4.7: Fluorescent images of the C2C12 cells on the different patterns. Column 1 shows the C2C12 cells after one day, column 2 shows the cells after four days and column 3 shows the cells after seven days in the differentiation media. Row 1 shows the C2C12 cells present on the unpatterned (control) surface, row 2 shows them on the linear cell islands, row 3 and 4 shows the cells on hybrid patterns with different arc degrees (30° and 90°) and row 5 shows the cells on toroid cell islands. Cells were stained for anti-MHC (green) and nucleus (blue) and these were used for the calculation of the fusion index and the maturation index (% myotubes $>$ 5 nuclei) (Scale bar = 100 $\mu$m).

myotubes. This geometry showed the highest fusion index of all the different patterns used. The next highest fusion index was observed for the linear geometry while the circular geometry (torus) showed the lowest fusion index of all the patterns in this study.

The maturation index (% myotubes $>$ 5 nuclei) was also used as a parameter to evaluate the differentiation of C2C12 myotubes. The maturation index can also be used to quantify the size of the myotube, a higher maturation index represents a myotube which is larger in size [187]. The maturation index of the hybrid patterns is shown in Figure 4.9A. It can be seen that the hybrid 30° pattern, which showed highest fusion index, also shows the highest maturation index for the myotubes. The maturation index for the

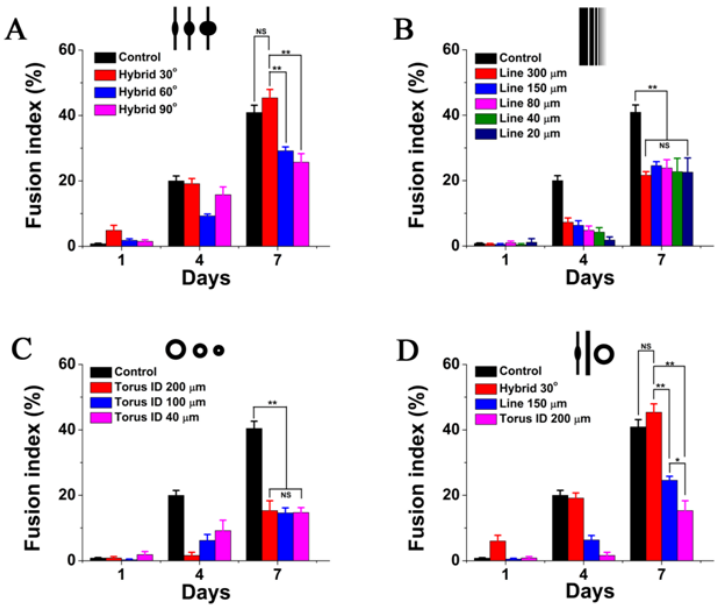


Figure 4.8: Quantification of the fusion index for the C2C12 cells on the different micro-patterned cell islands. Fusion index was calculated as the ratio of nuclei number in myocytes with two or more nuclei versus the total number of nuclei. (A) Hybrid patterns with different arc degrees (30° 60° and 90°), (B) Linear cell islands (line patterns) with different width (300 $\mu$m, 150 $\mu$m, 80 $\mu$m, 40 $\mu$m, and 20 $\mu$m), (C) Toroid cell islands (torus patterns) with different inner diameter (40 $\mu$m, 100 $\mu$m, and 200 $\mu$m). (D) The highest from each of the different cell islands are plotted together to show the geometry that maximized the fusion index of C2C12 cells - hybrid 30°. Significance $^{**}p < 0.01$, $^{*}p < 0.05$, and *NS = not significant*. Data is represented as mean ± S.E.M ($n = 10$ *patterns*).

hybrid 30° (73.09 ± 4.41%) pattern was statistically higher ($p < 0.05$) than that for the control (60.24 ± 2.19%), hybrid 60° (55.11 ± 3.83%) and hybrid 90° (46.71 ± 3.91%) ($p < 0.01$). Figure 4.9B shows the maturation index for the linear geometry with different widths. There was no statistically significant difference in the size of the myotubes on line patterns of different widths. Also, the toroid patterns showed similar results where no significant difference could be seen in the maturation index for tori of different inner diameter. However, each of them showed smaller maturation for the myotubes when compared to the control. Again, the hybrid 30° pattern emerges as the optimum geometry for myotube maturation showing higher maturation than either the linear or the circular geometry (Figure 4.9).

It was shown in Figure 4.8 B, C and Figure 4.9 B, C that the fusion and

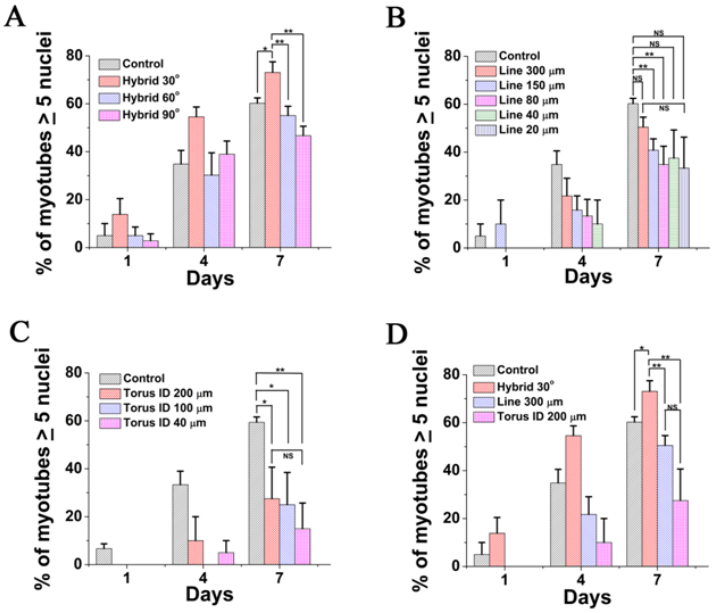


Figure 4.9: Quantification of the fusion index for the C2C12 cells on the different micro-patterned cell islands. Fusion index was calculated as the ratio of nuclei number in myocytes with two or more nuclei versus the total number of nuclei. (A) Hybrid patterns with different arc degrees (30°, 60°, and 90°). (B) Linear cell islands (line patterns) with different width (300 $\mu$m, 150 $\mu$m, 80 $\mu$m, 40 $\mu$m, and 20 $\mu$m), (C) Toroid cell islands (torus patterns) with different inner diameter (40 $\mu$m, 100 $\mu$m, and 200 $\mu$m). (D) The highest from each of the different cell islands are plotted together to show the geometry that maximized the fusion index of C2C12 cells - hybrid 30°. Significance $^{**}p < 0.01$, $^{*}p < 0.05$, and $NS$ = *not significant*. Data is represented as mean ± S.E.M ($n$ = *10 patterns*).

maturation indices were not statistically different for lines of different widths and tori of different IDs. However, within the same categories of geometric shapes, why we do not see different rates of fusion and maturation? As pointed out by Nelson et al., cellular signals like proliferation and differentiation emanate from the bulk tissue rather than the edges or length [106]. For example, they show that in their study there was a smaller proliferation along the long edge of the rectangle as compared to the square of the same edge length. Therefore, even though the stress values are different on the linear geometries (different width patterns) and circular geometries (tori of different IDs), the overall distribution in stress gradients is very similar on these structures. This leads to very similar fusion and maturation indices on linear (different width patterns) and circular (tori of different IDs) geome-

tries. Hence, the data suggests that it is not a particular stress value but the stress gradient (distribution of stress) in a structure that dictates the differentiation process.

## 4.5 Alignment of C2C12 myotubes

Controlling the alignment of cells is critical for any tissue engineered graft. *In vivo*, many cells/tissues like cardiac muscle [194], skeletal muscle [195], corneal tissue [196], vascular tissue [197], have a very high degree of alignment associated with them which in turn enhances their functionality. In particular, for skeletal and cardiac muscle, alignment of cells is extremely important in order to maximize the contractile power of the tissue. The alignment of myotubes on the micro-patterned cell islands was therefore investigated using two-dimensional FFT. For a detailed and excellent discussion on the technique the reader is recommended to look at Ayres et al [198, 189].

Figure 4.10 shows the alignment of MHC-positive myotubes on the different micro-patterns. The second column in the figure is the two-dimensional FFT of the image (or the red selection) which shows the distribution of pixels of different frequencies around the origin. Myotubes on the control (unpatterned) substrate shows no distinguishable peak in the 2D FFT alignment plot indicating that there is no alignment of myotubes on this substrate. This was further confirmed by looking at the angle of deviation of myotubes from the principal axis and only less than 20% myotubes showed 15° or less deviation. It has been shown previously that cells presenting less than 15° of deviation are considered aligned along the given axis [199]. As expected, myotubes on the linear patterns showed a very high degree of cell alignment. Myotubes on the line (width 80 $\mu$m) showed a very sharp narrow peak which is indicative of high degree of cell alignment. More than 90% of the myotubes showed less than 15° of deviation from the principal (long) axis of the linear geometry. However, as the width of the linear geometry was increased from 80 $\mu$m to 300 $\mu$m , a sharp decrease in the alignment of myotubes was seen. Less than 40% of the myotubes now showed 15° or less of cellular deviation. Also, the 2D FFT alignment plot is now much broader which indicates more than one axis of alignment. By quantifying the alignment of myotubes on the hybrid patterns, we see that hybrid 30° patterns (width of the linear por-

tion is about 100 $\mu$m) showed the highest fusion and maturation index for the myotubes also showed a very high degree of myotube alignment. Almost 90% of the myotubes showed 15° or less of deviation while 100% of the myotubes were within 30° of deviation from the principal axis of the geometry. The 2D FFT alignment plot also showed a narrow high peak indicating high degree of alignment for the myotubes. However, the alignment of myotubes for the hybrid 90°patterns (width of the linear portion is about 100 $\mu$m) was not very high. Less than 30% of the myotubes showed $< 15°$ of deviation from the principal axis of the geometry and the 2D FFT alignment plot did not show peaks.

Taken together, these results suggest that as the width of the linear portion in the geometry is increased, the degree of alignment goes down. Also, by adding a curvature to the linear geometry, the degree of alignment decreases. However, for small curvatures, the deviation is small as seen for the hybrid 30° pattern. As the arc degree of the curvature increases the alignment decreases substantially as seen for the hybrid 90° pattern.

Studies have shown the alignment of myotubes by modulating the surface topography for instance using grooves/ridges [124], by grinding the substrate with abrasives [125], by using UV-lithography to micro-pattern glass [126], and others [200, 201]. In this study, alignment of cells was achieved on different geometries by using $\mu$CP in contrast to creating wells/channels for guiding the cells in it. Alignment of cells in wells/channels is present because of the topography of the substrate while alignment of cells on micro contact patterned substrate is present because of the chemical patterns.

Chemical patterns differ from topographic patterns in the sense that topographic features do not limit the area of for cellular extension and hence the area of cell contact remains unrestricted [201]. Depending on the size of the channels, cell extension can follow "gap guidance" or "contact guidance". On the other hand, in the chemical patterns the area of cell contact is limited by the cell patterns and in general, the cells cannot cross the boundary between the adhesive and no-adhesive cell islands. Alignment of cells is extremely important for skeletal tissue engineering applications as in vivo the skeletal muscle is formed by highly aligned structure consisting of parallel arrays of multi-nucleated myotubes. This requires the remodeling of the actin cytoskeleton such that the actin filaments are now aligned parallel to the long (principal) axis of the micro-pattern which in turn can also affect

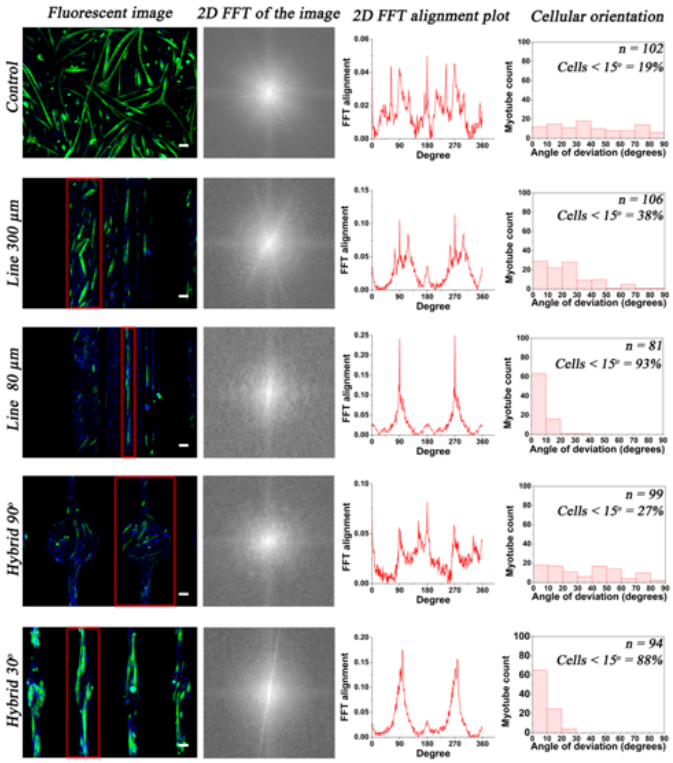


Figure 4.10: Quantification of alignment of C2C12 cells on the micropatterned cell islands. Column 2 shows the two-dimensional FFT of the image in the first column or the selection (red rectangle) in the image. (Scale bar = 100 $\mu$m).

the differentiation of myotubes.

Alignment of myotubes also imparts anisotropy to the skeletal muscle tissue so that the contractile power of the muscle is maximized. As expected, linear geometries with smaller line widths showed a high degree of alignment. However, the hybrid 30° geometry, which combined both linear and circular features together in a single geometry, also showed a very high degree of alignment. This combined with the fact that hybrid 30° also showed the highest fusion and maturation indices; it emerges as a promising geometry for studies involving other cell types like hMSCs, ESCs and induced pluripotent stem cells iPSCs where both differentiation and alignment of the cells/tissue is required.

## 4.6 Response of electrical pulse stimulation on mature myotubes

Muscles being an electrogenic tissue, their development are closely linked to their electrical activity. Therefore, it was interesting to look at the contraction of these cells using an EPS. First, the affect of frequency on the contraction of myotubes was investigated. The myotubes contracted at the rate at which a frequency pulse from the waveform generator was applied to them as seen in Figure 4.11A. The data suggests that it is possible to synchronize the frequency of contractions of myotubes to the electrical pulse frequency.

The displacement of myotubes under the application of an electric filed for cells on different patterns was quantified. Figure 4.11B shows the displacement profile of myotubes on the different patterns on day 7. Twitch responses of myotubes were observed at lower frequencies (1 - 10 Hz) while tetanic contractions were observed at higher frequencies ($\geq$ 30 Hz). It can be seen from this that the cells showed very uniform displacement under the application of the field. The displacement amplitude slightly increased from day 4 to day 7 for all the different patterns as can be seen in Figure 4.11C. The highest displacement was seen for the hybrid 30° pattern with the average being 1.24 $\pm$ 0.16 $\mu$m. The line pattern (width 300 $\mu$m) showed the second highest displacement which was 0.71 $\pm$ 0.09 $\mu$m followed by the torus (ID 200 $\mu$m) pattern which registered an average of 0.60 $\pm$ 0.09 $\mu$m displacement. Patterns with higher fusion/maturation index show higher displacements.

Myotubes or muscles are linear actuators where the biochemical energy from the cell culture medium is converted into mechanical motion by the actomyosin motors in the cell. As a result, these cells have become strong candidates for many biological micro-electromechanical systems (BioMEMS). There have been several examples of using cardiac and skeletal muscle cells for "lab on a chip" applications [202, 203, 204, 205]. For all contraction studies, the direction of the electrical field was parallel to the direction of the long axis (longitudinal direction) of the patterns as it has been shown previously that a smaller electrical energy is required when the electric field is parallel to the longitudinal axis of the myotubes compared to be perpendicular to it [193]. As shown in Figure 4.11, it is possible to synchronize the frequency

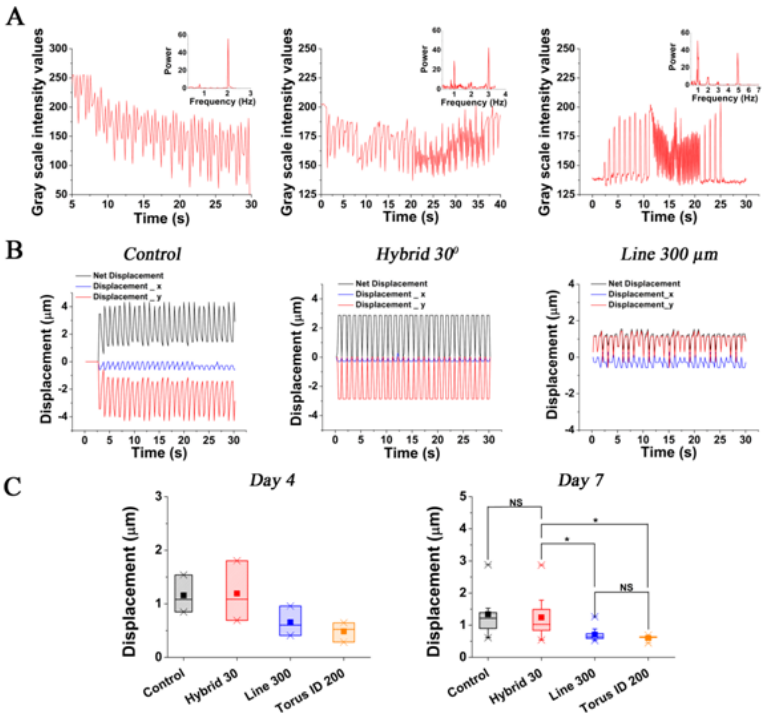


Figure 4.11: Quantification of the C2C12 myotubes using the EPS on the different micro-patterns. (A) Myotubes were stimulated at different frequencies using the EPS and their response was recorded *via* a kymograph. Inset shows the spectral density of the signal obtained from the kymograph by FFT. (B) Time course of maximum contractile displacement of the myotubes on the control, hybrid 30° and line patterns. (C) Box plots showing the average displacements of the patterns on day 4 ($n = 3$) and day 7 ($n = 5$ for the torus, $n = 7$ for line (300 $\mu$m) and $n = 13$ for control and hybrid 30° patterns). Significance, $^*p < 0.05$, and $NS = not\ significant$. Data is represented as mean ± S.E.M.

of contractions of myotubes to the electrical pulse frequency which can have several applications in the field of BioMEMS like using a tissue engineered system of myotubes as an artificial pump for "lab on a chip" applications.

## 4.7 Affect of density on the process of myogenesis

The same numbers of cells were seeded on each of the substrates (initial seeding density was the same on all patterns), but the outcome shows different cell densities for each pattern. This could be attributed to the different areas and different number of patterns on each chip. Messina et al., showed that

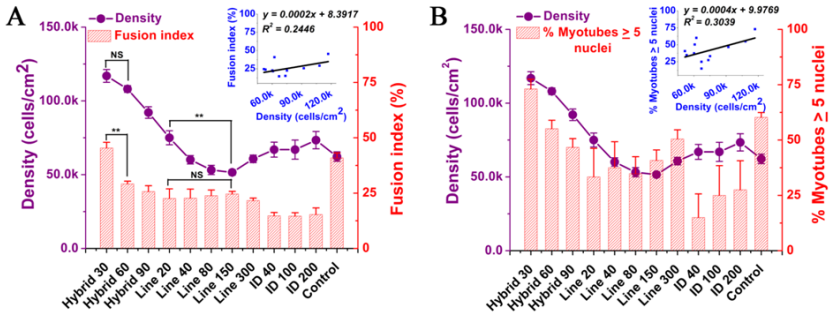


Figure 4.12: Influence of density on the differentiation of C2C12 myotubes on the different micro-patterns. (A) The fusion index and density of C2C12 myotubes on the various micro-patterned cell islands on day 7. The inset shows a scatter plot of the fusion index and the density of C2C12 myotubes. The Pearson's correlation coefficient (r) is 0.495 indicating a low association between the fusion index and the density of C2C12 myotubes for day 7. (B) The maturation index (% myotubes $>$ 5 nuclei) and density of C2C12 myotubes on the various micropatterned cell islands on day 7. The inset shows a scatter plot of the maturation index and the density of C2C12 myotubes. The Pearson's correlation coefficient (r) is 0.551 indicating a low association between the maturation index and the density of C2C12 myotubes for day 7. Significance $^{**}p < 0.01$, $^{*}p < 0.05$, and $NS = not\ significant$. Data is represented as mean $\pm$ S.E.M ($n = 10$ *patterns*).

myogenesis *in vitro* follows a phenomenon known as the "community effect" where the initial cell density of the myoblast plating is important. [206] When C2C12 myoblasts were seeded at low cell densities (LD, 500 cells/cm$^2$) compared to high cell densities (HD, 20000 cells/cm$^2$) they showed very different fusion indices where LD cultures showed less than 10% MHC positive nuclei while HD cultures showed more than 80% MHC positive nuclei after 72 hours in the DM.

Figure 4.12 shows the average cell density on the different patterns plotted together with the fusion index for day 7. Hybrid 30° pattern showed the highest average cell density and the highest fusion index. The inset for Figure 4.12A shows cell density plotted against the fusion index of cells. The Pearson's correlation coefficient is 0.495 which suggests that there is a very low level of associativity between fusion index and cell density. Even though the highest cell density showed the highest cell fusion, density cannot be the dominant factor because of these differences in the fusion indices are seen on the different patterns. For example, there is a statistically significant difference between the fusion index of the hybrid 30° and the hybrid 60° pattern

at $p < 0.01$. However, for the two same geometries, there is no significant difference in the density. In contrast, the linear geometries (20 $\mu$m versus 150 $\mu$m) show no significant difference in the fusion indices while there is a statistically significant difference in the densities between these two different structures. The same argument also holds true for Figure 4.12B where the cellular density and maturation index is plotted against the type of pattern while the inset shows them plotted against each other. The Pearson's correlation coefficient is 0.551 which means that there is low associativity between the two parameters - maturation index and cellular density. Figure 4.3 shows the density of myotubes on the various patterns as a function of time. Under our given experimental conditions it can be concluded that the effects of maturation index and fusion index on the different patterns are not likely to be attributed to the differences in densities on those patterns. Rather, the data suggests that other inherent mechanisms and cellular pathways exert a dominant influence on this fusion and maturation process for different micro-patterned geometries.

A very simple explanation why we see a greater differentiation activity on the hybrid 30° pattern is that it combines the best of the linear (high degree of myotube alignment) and circular (high density) geometries. But in order to get a more mechanistic understating of this process it is necessary to look at the molecular pathways and molecules that might be involved. However, it was very difficult in this study to point out a single molecule that might be responsible for up regulation of myogenesis on a particular geometry as there are 32 known molecules that are involved in mammalian process of myoblast fusion [207]. These can be broadly classified into three major types namely - membrane-associated proteins, intracellular molecules and extracellular/secreted molecules. It is well known know that there are four known muscle regulatory factors (MRFs) - MyoD, Myf-5, myogenin and MRF4 that are involved in vitro myogenesis [208, 209]. Since, MyoD and Myf-5 are "commitment" or "specification" factors, myogenin is a "differentiation" factor and MRF4 has both aspects, one or more of the 32 molecules involved in skeletal myogenesis targets these four MRFs at different stages of myogenesis leading to differences in differentiation on the different geometries.

After performing a thorough analysis of the different parameters important for the differentiation of C2C12 myoblasts which included - fusion index, maturation index, alignment of myotubes and electrical actuation (displace-

ment of myotubes), hybrid 30° pattern emerges as the optimum geometry in this study.

## 4.8 Conclusion

Protein micro patterning can be used to mimic, at a fundamental level, the *in vivo* architecture of the tissues and to study cellular differentiation *in vitro*. We conclude that geometrical cues influence differentiation process of C2C12 myoblasts. Hybrid structures with the smallest arc degree (hybrid 30°) showed the best results for all four differentiation parameters. The hybrid 30° pattern exhibits a ∼2-fold increase in the fusion index when compared to the line patterns and ∼3-fold increase when compared to the toroid pattern. The hybrid 30° also showed a higher maturation index compared to the line or the toroid patterns. In response to electrical field stimulation (20 V, 50 ms pulse, 1 Hz), mature myotubes on hybrid 30° patterns showed a ∼2-fold increase in cellular displacement when compared to myotubes on the line and torus patterns. The influence of C2C12 cell density on fusion and maturation indices was also tested, and the results suggest that density does not play a significant influence on cellular differentiation under these conditions. Therefore, by using $\mu$CP the micro-environmental cue of geometry was systematically studied. These results can have applications in tissue engineering of muscle cells and designing muscle cell bio-actuators.

# CHAPTER 5

# GRAPHENE PROMOTES MYOGENESIS OF C2C12 SKELETAL MUSCLE MYOBLASTS

## 5.1 Introduction

Graphene is an atomic layer thin sheet of $sp^2$-hybridized carbon atoms that are arranged in a unique 2D honeycomb structure. Graphene has intrigued researchers worldwide because of its unique physical (high specific surface area, 2630 $m^2$ $g^{-1}$), chemical (thermal conductivity, ~5000 K m $W^{-1}$), electrical (mobility of charge carriers, 200,000 $cm^2$ $V^{-1}$ $s^{-1}$), and mechanical (Young's modulus, 1100 GPa) properties [210, 211]. As a result of these unique properties, graphene and its derivatives have found applications in a variety of fields like nanoelectronics [212], composite materials [213], energy technology [214], sensors [215], and catalysis [216] to name a few [217]. However, the biomedical applications of graphene have yet not been fully explored. This chapter will therefore explore the potential of graphene as a novel substrate for muscle tissue engineering. Since, graphene is an allotrope of carbon; it can easily mimic the native cellular micro-environment in terms of its physical and chemical properties. Thus graphene becomes a novel candidate for 3D tissue engineering and regenerative medicine.

Section 5.2 will outline the scheme for transferring graphene films on silicon oxide substrates. Section 5.3 will show the fusion of C2C12 cells on silicon oxide/graphene chips. Section 5.4 will investigate the potential of Insulin-like growth factor (IGF-1) on the process of myogenesis. Section 5.5 will show the fusion of C2C12 cells on graphene chips with the media being supplemented with IGF-1. Section 5.6 will summarize the major findings of this chapter.

## 5.2 Transferring graphene films on silicon oxide chips

Graphene was grown by chemical vapor deposition (CVD) method on copper foil (99.8%, Alfa Aesar 0.001 inch using methane as a precursor gas. The growth parameters were $CH_4$:$H_2$:Ar=100:50:1000 sccm at 1000 °C, growth time 40 minutes, growth pressure 100 mTorr. The wet transfer using two PMMA resists as a supporting film was applied with a standard clean two process (20:1:1 $H_2O$:$H_2O_2$:HCl) step [218]. First, PMMA 495 A2 with 495000 g $mol^{-1}$ molecular weight, 2% dissolved in anisole, was spun on graphene/copper sample with 3000 rpm for 30 seconds and baked at 200 °C for 2 minutes and second PMMA 950 A4 with 950000 g $mol^{-1}$ dissolved in 4% of anisole, spun with 3000 rpm for 30 seconds and baked at 200 °C for 2 minutes. Copper foil was etched overnight in $FeCl_3$ Printed Circuit Copper Etchants 100 (Transene, CO INC). As a last step of the transfer process the graphene/PMMA film was deposited on the substrates: $SiO_2$ (285 nm)/Si (100) substrate. The PMMA film was lifted off with dichloromethane:methanol (1:1) solution for 50 minutes and the graphene film on substrate was annealed for 1 hour at 400 °C in $H_2$ (500 sccm) and Ar (500 sccm) atmosphere.

Quality of the graphene was studied by Raman spectroscopy. Raman measurements were performed using a Renishaw Raman/PL Micro-spectroscopy System with laser excitation wavelength 633 nm, a 50x long-distance objective, power 10% and the acquisition time was 30 seconds. The data were acquired in the range from 1200 $cm^{-1}$ to 3000 $cm^{-1}$.Structure morphology of graphene films was characterized with SEM an AFM techniques. SEM was performed with Hitachi S-4800 machine and AFM was done with Digital Instruments Dimension 3000 in a tapping mode. AFM scan size was $10\times10\mu m^2$. Figure 5.1 summarizes the quality characterization performed on the graphene used for the growth of C2C12 cells. Raman spectrum is given in the figure 5.1A for graphene transferred on $SiO_2$/Si (100) substrate. The characteristic graphene Raman peaks (D, G and 2D) are indicated. The graphene growth results in the monolayer coverage as it follows from the 2D peak shape (Lorentzian), 2D/G peak intensity ratio (≈3), G peak shift [219, 220, 221]. The inset to Figure 5.1A shows the SEM image of the graphene. The AFM image shows the surface morphology and is presented in 5.1B. Root mean square (RMS) roughness obtained from the AFM data is 5 nm for $10\times10$ $\mu m^2$ scan.

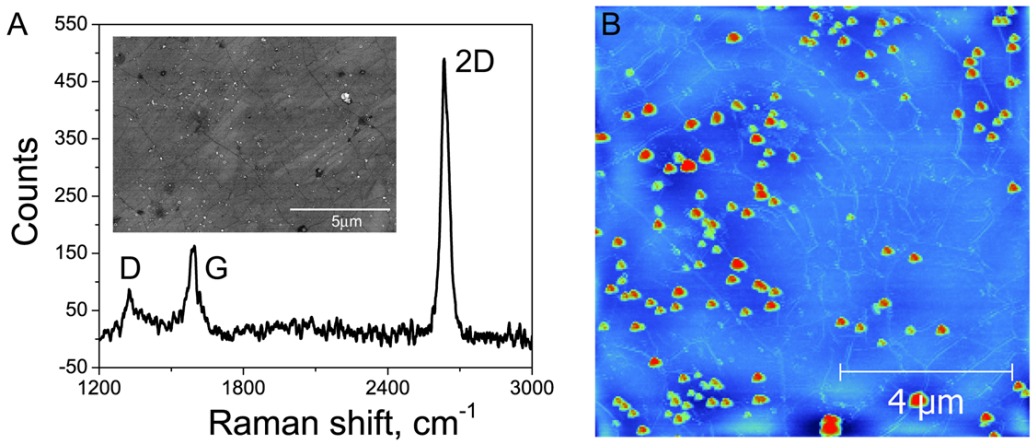


Figure 5.1: Characterization of graphene film on $SiO_2$ substrate. (A)Raman spectrum of graphene transferred on $SiO_2$/Si (100) substrate. The principal Raman peaks (D, G and 2D) are indicated. The inset shows the SEM image of the graphene surface. (B)AFM data for the graphene transferred on $SiO_2$/Si(100) substrate.

## 5.3 Graphene enhances the myogenesis of C2C12 cells

Skeletal myogenesis is a highly orchestrated terminal differentiation process in which the proliferating mono-nucleated myoblasts differentiate when deprived of serum and fuse together to form multi-nucleated myotubes [222, 223]. C2C12 cells are used as a model system to study different types of muscular dystrophies like Duchenne muscular dystrophy (DMD), Emery-Dreifuss muscular dustrophy (EDMD) and limb-girdle muscular dystrophy (LGMD) *in vitro* [224, 225]. Since, graphene can also be used a sensor, it therefore becomes very interesting to study the process of C2C12 myogenesis on graphene. To that end, the myogenic potential of C2C12 cells was investigated on graphene.

The graphene/$SiO_2$ chips fabricated in section 5.2 were first cleaned by incubating them in 70% ethanol for 4 hours after which they were rinsed thrice with DI water and twice with PBS. After this, these chips were placed in one of the wells of a 6 well plate. $\sim$1,000,000 C2C12 cells (passage number $< 10$) were then seeded in the well holding the chip. Thus leading to an initial cell seeding density of $\sim$1000 cells $mm^{-2}$ which is similar to the cell density used in [186]. The protocol for the culture of C2C12 cells is described in chapter 4 sub-section4.2.2. The regular cell culture media consisted of Dulbecco's modified Eagle's medium supplemented with 10% FBS (growth medium, GM).

To induce the differentiation of myoblasts into myotubes, C2C12 cells at 80-90% confluence were shifted to DMEM supplemented with 2% horse serum (differentiation medium, DM) and the medium was replaced every other day. All the time points in the figures refer to cells being present in the DM. Cells were cultured on these chips for four days and the fusion index, myotube area and cell density was investigated on these chips on day two, four for both the graphene and $SiO_2$ regions of the chip. Fusion index was calculated as the ratio of nuclei number in myocytes with two or more nuclei versus the total number of nuclei [187]. Immunofluorescence was done as per the protocol described in chapter 4 sub-section4.2.3. Briefly, the cells were first fixed with 4% PFA for 20 minutes, permeabilized with 0.2% Triton X-100 for 10 minutes and blocked with 1% BSA at room temperature. The cells were incubated with MF-20 overnight at 4 °C followed by incubation with fluorescein isothiocyanate (FITC) conjugated anti-mouse IgG and DAPI in dark at 37 °C. The stained cells were imaged with a fluorescent microscope and the images were quantified using ImageJ. The images obtained from the MHC and DAPI signals were pseudo-colored green and blue respectively. Figure 5.2 shows the fluorescent images of the cells over the period of four days and the parameters of fusion index, myotube area and cell density on both graphene and $SiO_2$ regions of the chip. It can be seen that the percentage of myotubes (green) increase as a function of time on both graphene and $SiO_2$. However, myotubes are mostly present on the graphene region of the chip with very little myotube formation on the $SiO_2$ region. Also, at the interface of $SiO_2$ and graphene the elongation of myotubes can be seen on day 4. The higher attachment of cells on graphene is solely based on the differences in the material properties of $SiO_2$ and graphene. The RMS roughness of graphene is $\sim$5 nm while the RMS roughness of $SiO_2$ is $\sim$0.4 nm [132]. This increase in the roughness provides a higher attachment area for the cells [226]. In addition, $SiO_2$ is very hydrophilic (contact angle = $30.4^\circ \pm 3.21^\circ$) while graphene has a contact angle of $79.71^\circ \pm 3.30^\circ$ making it slightly hydrophilic [132, 227]. The optimum contact angle for cell attachment is $\sim 64^\circ$ with a decrease in cell adhesion on very hydrophilic or very hydrophobic surfaces [226].These material properties promote higher C2C12 attachment on graphene over $SiO_2$ surfaces. Figure 5.2B shows the fusion index of C2C12 cells on graphene and $SiO_2$ surfaces. By day 4, graphene shows a fusion index of $21.52 \pm 1.64\%$ while only $9.30 \pm 2.50\%$ myotubes fuse on the $SiO_2$ surfaces and this is sta-

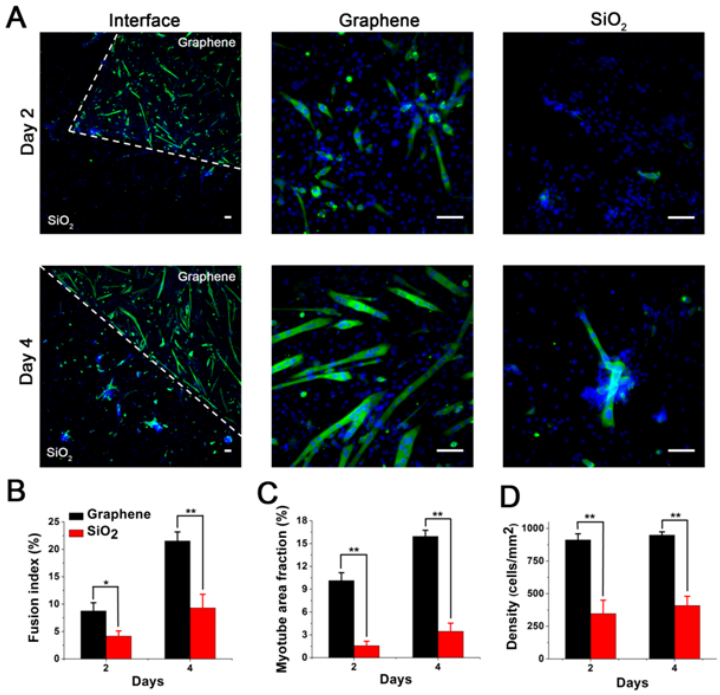


Figure 5.2: C2C12 cells on graphene/$SiO_2$ chips.(A)Fluorescent images of the C2C12 cells on graphene and $SiO_2$. Column 1 shows the cells on interface of graphene and $SiO_2$ parts of the chip for day 2 and 4. Column 2 shows the cells on graphene and column 3 shows the cells on $SiO_2$. Row 1 shows the C2C12 cells on day two while row 2 shows the cells on day four. Cells were stained for anti-MHC (green) and nucleus (blue) and these were used for the calculation of the fusion index. The dashed white bars in column 1 are used to separate the $SiO_2$ and graphene surfaces of the chip. (Scale bar = 100 $\mu$m)Quantification of (B)fusion index (C) myotube area fraction and (D) cell density, for the C2C12 cells on graphene and $SiO_2$. Significance $^{**}p < 0.01$ and $^{*}p < 0.05$. Data is represented as mean $\pm$ S.E.M ($n = 5$).

tistically significant at $p < 0.01$. Similar results are obtained for the myotube area fraction and the cell density where graphene out performs $SiO_2$ surface. Serum protein adsorption on the substrate plays a big role in the attachment properties of cells. Both graphene and derivatives of graphene have a high capacity of serum protein adsorption compared to $SiO_2$ [228]. Since, serum proteins contain a lot of ECM proteins like albumin and fibronectin [138], these proteins can get easily get adsorbed on the graphene surfaces. Also, the $\pi-$electron cloud in graphene can interact with the inner hydrophobic core of proteins enhancing cell attachment [228]. The higher density of these ECM proteins on graphene surfaces results in higher adhesion sites for the

cells which in turn results in higher cell density and attachment of cells on graphene. Higher C2C12 cell density can be verified from figure 5.2C where the graphene surface shows over twice the number of C2C12 cells than $SiO_2$ surface. "Community effect" is a well-known phenomenon in C2C12 myogenesis where higher initial cell density increases the fusion index of myotubes [206]. Thus most likely by higher initial C2C12 cell recruitment on graphene over $SiO_2$ surface, graphene enhances the process of C2C12 myogenesis.

## 5.4 Insulin-like growth factor as a promoter of C2C12 myogenesis

Skeletal muscle is a highly dynamic tissue that can change its phenotype in terms of mass and composition based on environmental cues like nutrition, exercise or starvation [229]. Two molecules namely IGF-1 and Growth and Differentiation Factor 8 (GDF8) (also known as myostatin) have been recognized to be key regulators in the control of skeletal muscle size [230]. IGF-1 has been recognized to be a positive regulator for muscle growth and it was shown that mice null for IGF-1 show large retardation in skeletal muscle mass [231, 232], while those over-expressing IGF-1 showed significant myofiber hypertrophy, increased protein synthesis and myoblast proliferation [233, 234]. On the other hand myostatin has been established as a negative regulator for muscle growth and studies have shown that mice null for the myostatin showed tremendous increase in muscle mass with some muscles increasing by as much as 200-300% [235, 236]. Therefore, in this study the influence of IGF-1 on C2C12 myoblasts was investigated to see its affect on graphene. Figure 5.3 summarizes the findings of this study. 1 ng $ml^{-1}$ of IGF-1 was added to the DM and while the control was the sample with just the DM. As expected, the samples treated with IGF-1 show higher percentage of myotubes by the end of five days as seen in figure 5.3A. Also, the IGF-1 treated samples show higher fusion index and cell density compared to the control. IGF-1 acts as an autocrine and paracrine factor and thereby up-regulates myoblast proliferation and myotube differentiation *via* a number of pathways [230]. As one of the pathways up-regulated by IGF-1 is mitogen-activated protein kinase (MAPK), which is responsible for cellular proliferation and division [230], higher cell densities were expected for the IGF-1 treated samples. This was

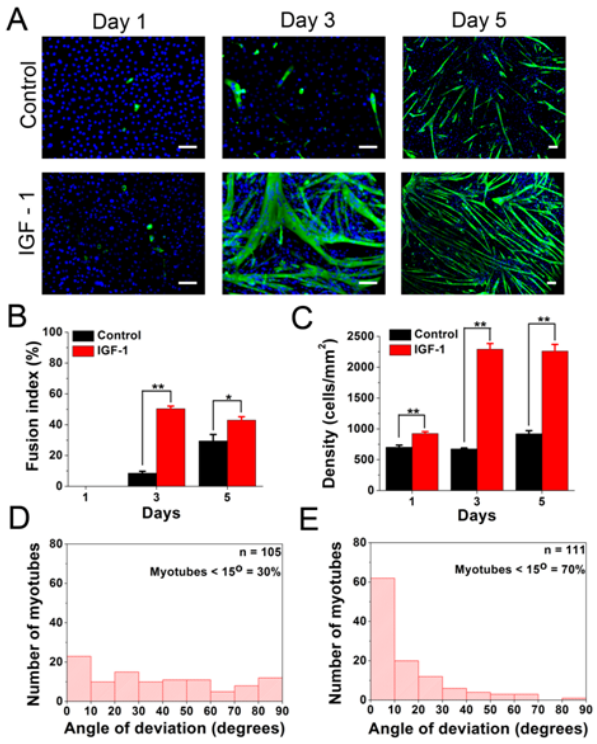


Figure 5.3: Affect of IGF-1 on C2C12 myogenesis. A) Fluorescent images of the C2C12 cells with and without IGF-1 (control). Column 1, 2, and 3 shows the cells on day 1, 3, and 5 on the control and the IGF-1 treated sample. Row 1 shows the cells on control and row 2 shows the cells on IGF-1 treated samples.(Scale bar = 100 $\mu$m) Quantification of (B)fusion index and (C) cell density on the control and IGF-1 treated samples. Significance $^{**}p < 0.01$ and $^{*}p < 0.05$. Data is represented as mean $\pm$ S.E.M ($n = 6$). Spontaneous alignment of C2C12 cells in the petri dishes on day 5 for the (D) control ($n = 105$) and (E) IGF-1 treated samples ($n = 111$).

verified from figure 5.3C, where the samples treated with IGF-1 shows more than twice the cell density versus the control sample by the end of five days. In addition, it was very interesting to see spontaneous myotube alignment on the IGF-1 treated samples by day 5. Myotubes on the control show no net alignment (figure 5.3D). However, localized regions on the IGF-1 treated samples show a net alignment as more than 70% of the myotubes show less than 15° of deviation from one common axis (figure 5.3E). It should be noted that this alignment is highly localized and myotubes in the entire petri dish do not show alignment along the same axis. However, in the field of view captured by the objective, most myotubes seem to align along one common axis. Thus by restricting the growth of cells in smaller patterns ($\sim$2$\times$2 mm$^2$)

regions, one can expect myotube alignment locally.

## 5.5 Graphene with insulin-like growth factor further enhances the myogenesis of C2C12 cells

C2C12 cells were then again seeded on graphene/$SiO_2$ chips. However, this time the DM was supplemented with 1 ng $ml^{-1}$ of IGF-1 and the same protocol as listed in section 5.3 of this chapter was repeated. Figure 5.4A shows the fluorescent images of C2C12 cells on the graphene and $SiO_2$ surface of the chip on days 2 and 4. Again, the graphene surface of the chip shows most of the myotubes with very little myotube formation on the $SiO_2$ surface. Figure grapheneIGFB, C, and D show the quantification for fusion index, myotube area fraction, and cell density on the graphene and $SiO_2$ surfaces of the chip. Graphene shows higher values for all the three parameters and the values are statistically significant at $p < 0.01$. By the end of 4 days, the fusion index on graphene is $\sim$2 larger than on $SiO_2$, the myotube area fraction on graphene is $\sim$4 larger than on $SiO_2$ while the density of C2C12 cells on graphene is $\sim$3 larger than on $SiO_2$. Thereby graphene emerges as an ideal surface for muscle tissue engineering. The higher differentiation on graphene could again be attributed to the surface properties of graphene like roughness, hydropathy, and the $\pi-$electron cloud which leads to higher cell attachment and thereby higher differentiation. Since, recently there have been few reports of graphene field-effect-transistors (grapheneFETs) [237, 238, 239], it would be very interesting to simultaneously use graphene for actuating and recording action potentials from these electrogenic C2C12 cells. Furthermore, a new breed of genetically engineered C2C12 cells, optogenetic C2C12 cells, have been recently reported [240]. These cells are genetically encoded with the light activated cation channel, Channelrhodopsin-2. Thus these cells can be activated by blue light of wavelength 473 nm. Future studies can also use grapheneFETs to record the action potentials from these optogenetic C2C12 cells and thus provide an insight about its molecular biology. Also, currently efforts are underway to put this graphene sheet in 3D PEGDA hydrogels and look at the differentiation of both regular C2C12 cells and mESCs. Previous studies have already showed the influence of carbon nanotube dimensions on the differentiation of hMSCs.

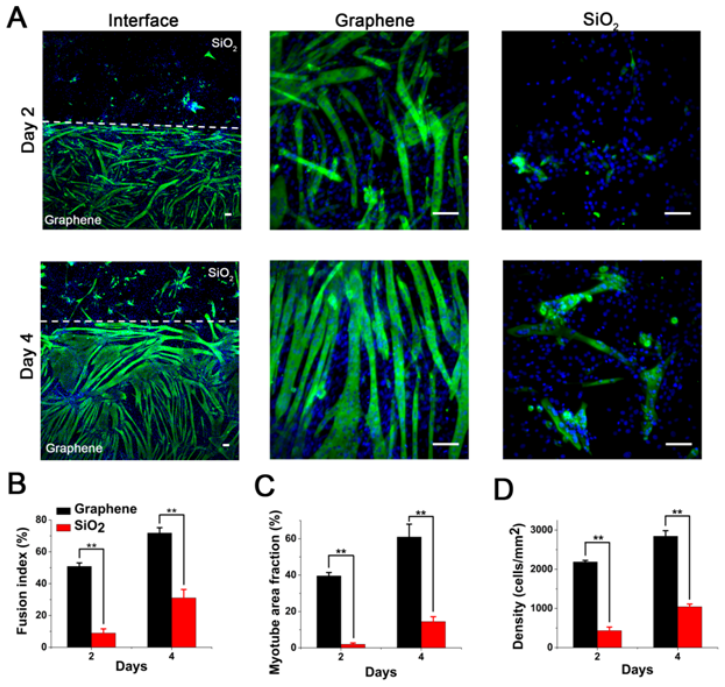


Figure 5.4: C2C12 cells on graphene/$SiO_2$ chips with IGF-1 supplemented DM.(A)Fluorescent images of the C2C12 cells on graphene and $SiO_2$. Column 1 shows the cells on interface of graphene and $SiO_2$ parts of the chip for day 2 and 4. Column 2 shows the cells on graphene and column 3 shows the cells on $SiO_2$. Row 1 shows the C2C12 cells on day two while row 2 shows the cells on day four. Cells were stained for anti-MHC (green) and nucleus (blue) and these were used for the calculation of the fusion index. The dashed white bars in column 1 are used to separate the $SiO_2$ and graphene surfaces of the chip. (Scale bar = 100 $\mu$m)Quantification of (B) Fusion index (C) Myotube area fraction and (D) Cell density, for the C2C12 cells on graphene and $SiO_2$. Significance $^{**}p < 0.01$ and $^{*}p < 0.05$. Data is represented as mean $\pm$ S.E.M $(n = 5)$.

## 5.6 Conclusion

The differentiation potential of C2C12 cells on graphene/$SiO_2$ chips was investigated in this study. More than two folds higher fusion index and myotube area fraction were recorded on graphene than the $SiO_2$ surface of the chip. Graphene enhances C2C12 attachment which in turn enhances the process of myogenesis of C2C12 cells. Thus material properties of graphene like, $\pi - \pi$ stacking, surface roughness, and its wettability make graphene an ideal substrate for muscle tissue engineering. Also, being organic in nature, graphene can easily mimic the native cellular micro-environment and hence

it becomes an interesting candidate for engineering 3D artificial tissues.

# CHAPTER 6

# THREE DIMENSIONAL PATTERNING OF EMBRYONIC STEM CELLS IN HYDROGELS

## 6.1 Introduction

In this chapter, the two different cues of geometry and stiffness are combined together to create 3D hydrogel scaffolds with micro-scale tissue architecture and physiologically relevant stiffnesses. Traditional encapsulation of cells in hydrogels distributes them in 3D. However, these methods typically lack spatial control of multi-cellular organization and do not allow for the possibility of cell-cell contacts as seen for the native tissue. Here, DEP is combined with SL apparatus to achieve controlled patterning of cells in 3D PEGDA hydrogel constructs. As a proof of concept, patterning and encapsulation of C2C12 skeletal muscle myoblasts and mESCs is shown in 3D hydrogels. In addition, using the same platform, patterning spheroids of mESCs and C2C12 cells is also demonstrated. Both cells and spheroids show good viability in the hydrogels after DEP. This robust and flexible *in vitro* platform can enable various applications in stem cell differentiation and tissue engineering by mimicking elements of the native 3D *in vivo* cellular micro-environment.

Section 6.2 will describe the phenomenon of DEP and the underlying physics behind it. Section 6.3 will briefly describe the SL apparatus. Section 6.4 will be the experimental section of this study and will show the process flow for achieving the controlled patterning of cells in 3D hydrogels. Also, the protocols used for imaging and analysis will be described. Section 6.5 will show the patterning of C2C12 cells and mESCs in physiologically relevant stiffness 3D hydrogels. Section 6.6 will describe the process of formation of 3D aggregates of mESCs and C2C12 muscle cells. Section 6.7 will also show the patterning for the aggregates of these cells in the hydrogels. Section 6.8 will summarize the findings of this chapter and how this platform can be used for controlling the fate of embryonic stem cells. The results presented

in this chapter have been published in [241, 242].

## 6.2 Dielectrophoresis

This section will describe the physics behind DEP, other major forces involved when a particle experiences DEP, and the simulations of electric fields to determine the relative DEP forces.

### 6.2.1 Physics

DEP force in the simplest form is the force exerted on the induced dipole moment of the particle by non-uniform electric fields. The electric field polarizes the particle and then depending on the orientation of the dipole relative to the electric field, the particle will either experience an attractive or a repulsive force. Since, a non-uniform field is applied, the particle moves as it responds to the direction of the greatest electric field gradient. The time-averaged DEP force $\langle F_{DEP}(t) \rangle$ for a spherical particle of radius $R$ suspended in an aqueous medium of dielectric permittivity $\varepsilon_m$is given by equation 6.1

$$\langle F_{DEP}(t) \rangle = 2\pi\varepsilon_m R^3 Re\{K(\omega)\}|\nabla E_{rms}^2| \tag{6.1}$$

where *K(ω)* is called the Clausius Mossotti (CM) factor and *Re* stands for the real part. This equation is a close approximation for the DEP forces and is valid for most situations [243]. However, regions where the spatial non-uniformity of the electric fields is very large like the electrode edges, this equation breaks down. In that case, other higher order terms are also necessary for completely describing the phenomenon of DEP [244]. The CM factor for a homogeneous solid is given by equation 6.2

$$K(\omega) = \frac{\varepsilon_p^* - \varepsilon_m^*}{\varepsilon_p^* + 2\varepsilon_m^*} \tag{6.2}$$

The subscript $p$ represents the particle and $m$ represents the fluid medium surrounding the particle. The asterisk represents a complex dielectric permittivity, $\varepsilon^* = \varepsilon_o\varepsilon_r + \sigma/2\pi f$ where $\varepsilon_o$ dielectric permittivity of vacuum ($8.85e^{-12}$ $Fm^{-1}$), $\sigma$ is the conductivity and $f$ is the frequency. The dielectric permittiv-

ity for polystyrene (PS) beads was $2.5\varepsilon_o$ and for the fluid was $80\varepsilon_o$ [245]. The real part of $K(\omega)$ is bounded between the values -0.5 $\leq K(\omega) \leq$ 1. Therefore, a particle will experience positive DEP (pDEP) if the CM factor is positive or the particle is more polarizable than suspended fluid. It will experience negative DEP (nDEP) if the medium is more polarizable than the particle. However, mammalian cells are much more complex than a homogeneous solid because of the presence of internal membranes and a nucleus. Therefore, the complex dielectric permittivity of a mammalian cell can be approximated by a spherical shell and is given by equation 6.3

$$\varepsilon_p^* = \varepsilon_m^* \left\{ \frac{(\frac{R}{R-d})^3 + 2(\frac{\varepsilon_i^* - \varepsilon_m^*}{\varepsilon_i^* + 2\varepsilon_m^*})}{(\frac{R}{R-d})^3 - (\frac{\varepsilon_i^* - \varepsilon_m^*}{\varepsilon_i^* + 2\varepsilon_m^*})} \right\} \tag{6.3}$$

Here, $d$ is the thickness of the cell membrane and subscript $i$ stands for the interior of the cell. The radius of both C2C12 and mESCs was measured to be 8 $\mu$m using the hemocytometer and the membrane thickness was found to be 8 nm [245]. The dielectric permittivity of the cell membrane was found to be $8\varepsilon_o$ and for the cell cytosol was found to be $50\varepsilon_o$ [245].

### 6.2.2 Other forces experienced by the particle

Other major forces acting on the spherical particle when it is suspended in the liquid medium are the fluid drag ($F_{drag}$), the buoyancy force ($F_{buoy}$) and the gravitational force ($F_{grav}$). [246] These forces are given by equations 6.4, 6.5,and 6.6 [246].

$$F_{drag} = 6\pi\eta RKv \tag{6.4}$$

where $\eta$ is the viscosity of the fluid medium, $K$ is the wall-correction factor and $v$ is the instantaneous cell velocity.

$$F_{buoy} = \rho_m V_p g \tag{6.5}$$

where $\rho_m$ is the density of the liquid medium, $V_p$ is the volume of the particle and $g$ is the gravitational constant.

$$F_{grav} = mg = \rho_p V_p g \tag{6.6}$$

where $\rho_p$ is the density of the particle and the volume of the particle $V_p$ is given by $V_p = 4/3\pi R^3$. These forces can be broken down in their respective x- and y-components as $F_{DEP_X}$, $F_{DEP_Y}$, $F_{drag_X}$, $F_{drag_Y}$, $F_{buoy}$, and $F_{grav}$. Doing a force decomposition and applying Newton's law of motion, equations 6.7 and 6.8 are obtained.

$$F_{DEP_X} - F_{drag_X} = m\frac{d^2x}{dt^2} \tag{6.7}$$

$$F_{DEP_Y} - F_{drag_Y} + F_{buoy} - F_{grav} = m\frac{d^2y}{dt^2} \tag{6.8}$$

where $m$ is the mass of the particle and $t$ is the time. Adding equations 6.1, 6.4, 6.5, 6.6, 6.7, and 6.8 equations 6.9 and 6.10 are obtained

$$2\pi\varepsilon_m R^3 Re\{K(\omega)\}\frac{\partial}{\partial x}|E^2| - 6\pi\eta R K_x\frac{dx}{dt} = m\frac{d^2x}{dt^2} \tag{6.9}$$

$$2\pi\varepsilon_m R^3 Re\{K(\omega)\}\frac{\partial}{\partial y}|E^2| - 6\pi\eta R K_y\frac{dy}{dt} + (\rho_m - \rho_p)V_p g = m\frac{d^2y}{dt^2} \tag{6.10}$$

By solving these two differential equations, the approximate location of the particle in the chamber can be obtained. It should be noted that these forces are dependent on a number of different parameters like chamber geometry, fluid viscosity, gap between the electrodes, etc. Therefore, for every particular case, these forces need to solved independently.

### 6.2.3 Simulations

Finite element analysis (FEA) was used to generate the distributions for the electric field and its gradient for a simple interdigitated electrode assembly. Since, the electrodes are much longer than their width, the system can be reduced to a 2D analysis and COMSOL 4.2a (Palo Alto, CA) was used for modeling. Electrical double layer, Van der Waals forces and electrothermal effects were neglected for these simulations. Current conduction across symmetry planes and the boundaries was assumed to be zero, thereby applying the Neumann boundary condition, $\partial\phi/\partial n = 0$. A constant potential $\phi =$ 10 V was prescribed at one of the electrode surface while the other was the ground. In addition, a periodic boundary condition was applied for the symmetry planes. Figure 6.1 shows the setup used for generation of electric field

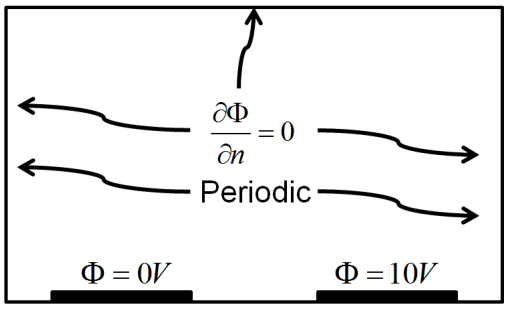


Figure 6.1: Setup for modeling the electric field distributions.

distributions.

Figure 6.2 shows the finite element model of the electric field distributions and the CM factor for PS beads. The highest electric field is present at the edges of the electrodes as evidenced by the high density of streamlines while the lowest is present right at the center of the individual electrodes. Thereby particles experiencing pDEP will be pulled to regions of electric field maxima while those which experience nDEP will be levitated above the center of the electrodes. Figure 6.2 B and C show the distribution of electric potential and electric field as a function of Z-height above the electrodes. As we move above the electrode, both the potential and electric field decreases. At 100 $\mu$m above the electrode, the electric field is only 23% of that at 5 $\mu$m above the electrode. Figure 6.2 D shows the real part of the CM, $K(\omega)$) factor for PS beads. Between the frequency range of 1-10 MHz which was used for patterning of cells in the two different polymers, PEGDA 700 and PEGDA 3400, the PS beads will experience nDEP and as a result be levitated above the center of the gold electrodes.

### 6.2.4 Uses of DEP

DEP has been widely used by researchers over the past few decades for manipulating biological entities. Researchers have shown particle separation using DEP in micro-fluidic devices [247], DEP based cell electroporation [248], patterning hepatocytes using DEP [249], selectively isolating dead cells from live ones using DEP [250], etc. DEP is advantageous for creating massively parallel cellular patterns as it is limited by the overall area of the underlying electrodes. This coupled to the fact that mammalian cells can withstand

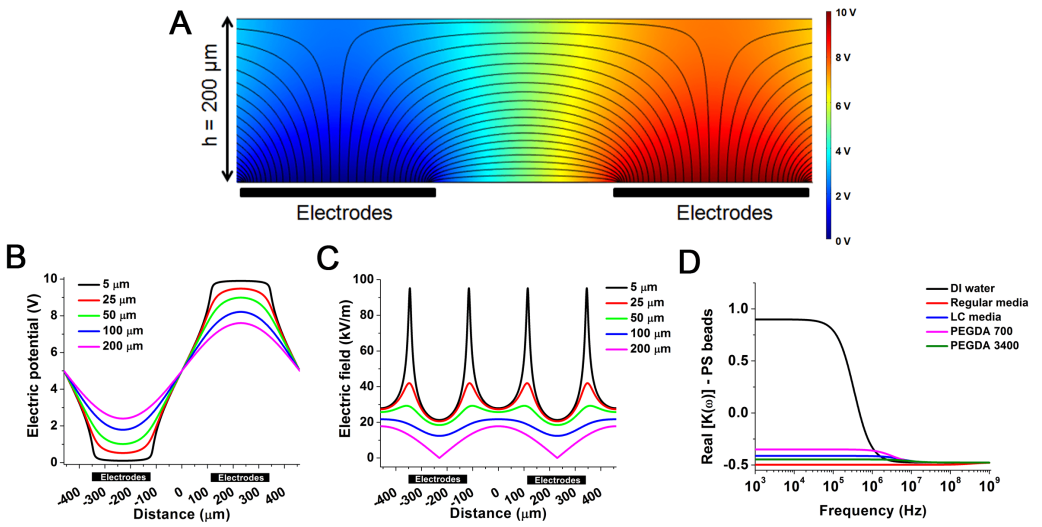


Figure 6.2: (A) Finite element model of the interdigitated Au electrodes. The streamlines show the gradient of electric field. Highest field gradients can be found at the edges of the electrodes shown by higher density of streamlines. (B, C) The electric potential and the electric field as a function of height above the electrodes. (D) Real part of the CM factor for PS beads in the different fluids used for DEP patterning. Between 1-10 MHz, PS beads always undergo nDEP for the two different polymers (PEGDA 700 and 3400) used in this study.

high frequency electrical signals for short bursts of time, DEP emerges as a very lucrative patterning technique for mammalian cells [251]. However, one of the limiting factors is that the DEP force is temporary and hence the cells are free to move around once the force is removed. Therefore, DEP needs to be combined with other immobilization techniques for long term patterned cell culture [252, 253, 254].

## 6.3 Stereolithography apparatus

SL is a solid free form (SFF) technique that was first introduced in the mid 1980s by 3D Systems to create prototypes prior to the production of different parts for the automotive, aerospace and other design industries [255]. It is a computer aided design (CAD) based tool used for additive manufacturing or rapid prototyping. The design of the structure for manufacturing can be developed using 3D computer drawing software or it can be acquired by imaging technologies like magnetic resonance imaging (MRI) [255]. After the

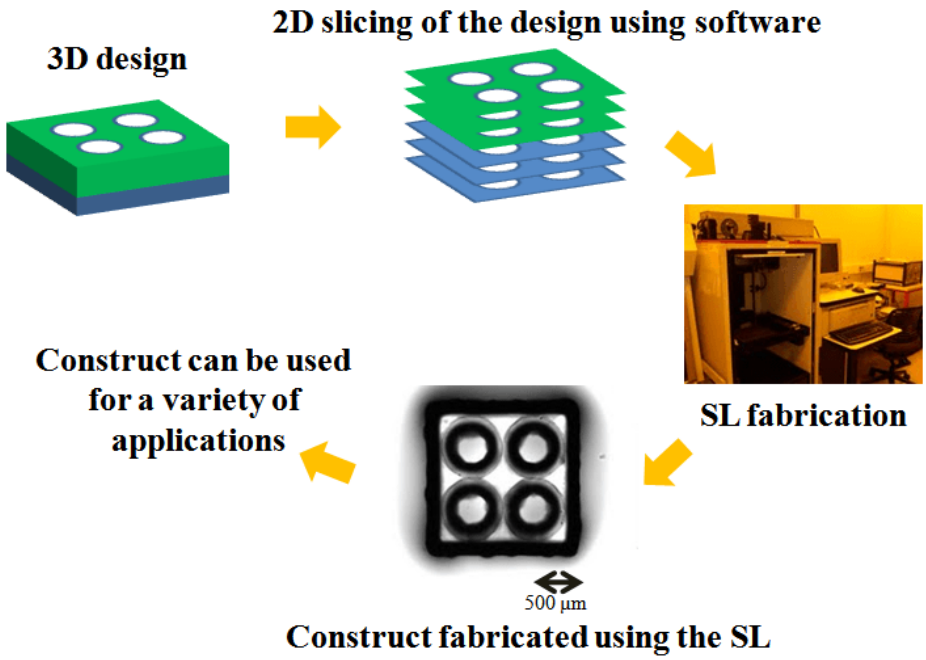


Figure 6.3: Overview of the process for fabricating structures using the SL (Figure adapted from Melchels et al. [255]).

design is developed, the structure is sliced in to a number of different layers (25-100 $\mu$m) by software and this data can then be passed to the SL machine for manufacturing [242]. Figure 6.3 shows the basic overview of the process that is used to make parts by SL. Many different types of resins can be used with the SL machine. For an acrylate resin system, usually a free radical is used as a catalyst. This radical is photochemically generated using a photoinitiator and then the acrylate polymer with the help of photoinitiator goes through different stages of addition like - initiation, propagation and termination [256]. Although, the exact kinetics of this polymerization reaction are quite complicated, much simpler equations have been developed to describe the fabrication of structures using Beer-Lambert's law. This law describes the exponential decay of light intensity as it passes through a medium and it can be used to generate a semi-empirical equation known as the "working curve" equation, which is absolutely fundamental to the SL machine [256].

$$C_d = D_p ln(\frac{E_{max}}{E_c}) \tag{6.11}$$

Equation 6.11 relates the thickness of the solidified layer ($C_d$, cure depth ($\mu$m)) to the maximum light irradiation $E_{max}$ (mJ cm$^2$). A semi-log plot of $C_d$ versus $E_{max}$ is a straight line and the slope of this line gives the penetration depth ($D_p$ ($\mu$m)) which is the depth at which the irradiance becomes $1/e$ (0.367) times that at the surface. The abscissa (x-intercept) of this line is the critical energy ($E_c$ (mJ cm$^2$)) or the energy required to convert the liquid polymer to a solid layer. Both the parameters, $D_p$ and $E_c$ are unique to a resin and are independent of the laser power of the SL machine. The $E_c$ of the resin however does depend on a variety of other factors like the concentration of the photopolymer, photoinitiator and the amount of dissolved oxygen. It should be noted that the working curve equation is only valid for a confined cure depth range $D_p < C_d < 4D_p$ [256]. If $C_d < D_p$ than the partially cured photopolymer is very weakly developed and if $C_d > 4D_p$ the working curve shows a super-logarithmic behavior [256]. After the two parameters for the resin are extracted from the working curve, structures can be fabricated using the SL and that resin system. For the current SL system, PEGDA polymer of different molecular weights ($M_w$) was used as the resin. PEGDA has been found to be biocompatible with mammalian cells and when polymerized, forms a hydrogel [257]. The stiffness of this hydrogel depends on the $M_w$ of the polymer and SL parameters.

Hydrogels have attracted much attention recently because of their use in a variety of biomedical applications such as drug delivery, wound management and tissue engineering [154, 155, 156, 157]. Many studies have used different techniques like solvent casting [158], freeze drying [159], gas foaming [160], electrospinning [161], and SL [87] for constructing the complex 3D architecture found in the body using hydrogels. Among these techniques, SL offers several unique advantages like multi-cell, multi-material fabrication and the capability to encapsulate cells during the process of structure fabrication [258]. Also, unlike other photo-polymerization techniques which require a physical mask, SL is a maskless CAD based rapid prototyping (RP) technology. Such merits of SL apparatus make it a great technology for tissue engineering applications and regenerative medicine [255]. However, micro-scale tissue organization, a hallmark of *in vivo* tissues, cannot be achieved by conventional SL apparatus due to limitations in the beam width. Commercially available lasers typically have beam widths in the range of few hundred microns, which is much larger than size of single cells [259]. Figure 6.4 shows

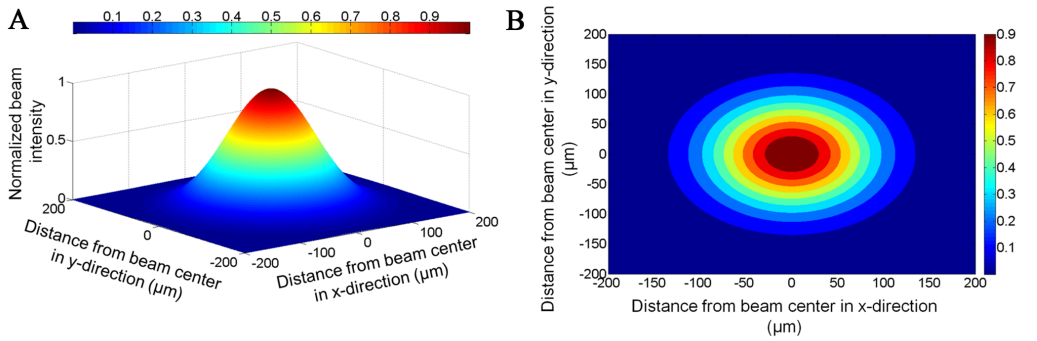


Figure 6.4: Gaussian beam of the laser in SLA 250/50 machine. (A) 3D Gaussian beam profile of the Helium Cadmium laser. (B) Two dimensional profile of the beam showing the intensity distribution in the x- and y-component

the Gaussian beam profile of the SLA 250/50 system that was used for this study. The wavelength ($\lambda$) of this laser system is 325 nm. From this 3D beam profile, it was found that the beam waist was 125 $\mu$m, thereby the diameter of the being 250 $\mu$m. This beam is however focused about 3 mm under the SL machine's stage. Therefore, the diameter of the beam at the surface of the stage where the polymerization happens is $\sim$255 $\mu$m, much bigger than the size of individual cells. Therefore, in order to achieve single cell patterning in 3D, SL apparatus has to be combined with another technology.

In this study, we combine the merits of SL apparatus and DEP together to create hydrogels of physiologically relevant stiffnesses with micro-scale organization as seen for *in vivo* tissues. We show the patterning and encapsulation of mESCs and C2C12 skeletal muscle myoblasts in the hydrogels. However, as cell clusters (spheroids of cells) of different sizes can also locally alter the cellular micro-environment via differential gene expression [109], we also show the patterning of mouse embryoid bodies (mEBs) and C2C12 spheroids in the hydrogels. Previous studies have only focused on patterning individual cells via DEP forces in hydrogels [245, 260]. This platform can thus be used to create hydrogels with micro-scale tissue architecture and enable applications in tissue engineering, regenerative medicine, and stem cell differentiation.

## 6.4 Experimental

This section will present the protocols used for patterning and encapsulating cells in 3D.

### 6.4.1 Cell culture

Murine-derived muscle cell line (C2C12 cells), was purchased from American Type Culture Collection (ATCC, Manassas, VA) and was cultured in Dulbecco's modified Eagle's medium (DMEM, Mediatech, Manassas, VA) supplemented with 10% FBS ( Atlanta Biologicals, Lawrenceville, GA) and 1% penicillin-streptomycin (Invitrogen, Carlsbad, CA) in standard cell culture conditions. W4129S6 mESCs (Taconic, Hudson, NY) were cultured in high glucose DMEM (Invitrogen, Carlsbad, CA) supplemented with 15% FBS, 1% penicillin-streptomycin, 1 mM sodium pyruvate, 2 mM glutamine, 100 $\mu$M non-essential amino acids, 10 ng ml$^{-1}$ of mouse Leukemia Inhibitory Factor (mLIF) and 100 $\mu$M of mono-thiogycerol (Sigma, St. Louis, MO) on 0.1% gelatin coated petri dishes in standard cell culture conditions. Unless otherwise mentioned, all products for the culture of mESCs were purchased from Stem Cell Technologies, Vancouver, BC, Canada.

### 6.4.2 Cell patterning in the polymer mixture and hydrogel fabrication

PEGDA 700 (Sigma, St. Louis, MO) and PEGDA 3400 (Laysan Bio, Arab, AL) polymers were mixed with 0.5% 4-(2-hydroxyethoxy) phenyl-(2-hydroxy-2-propyl) ketone (Irgacure 2959, Ciba) in a low conductivity media (LCM). Irgacure 2959 served as the photoinitiator for this hydrogel system. 10mM HEPES (Mediatech, Manassas, VA), 100 nM CaCl2 (Sigma, St. Louis, MO), 59 mM D-glucose (Sigma, St. Louis, MO) and 236 mM sucrose (Sigma, St. Louis, MO) were mixed in DI water to make the LCM [245]. Three parts of the polymer was added to one part of the cell mixture such that the final concentration of the cell-polymer solution was 10%, 15% and 20% respectively. 50-200 $\mu$L of this polymer-cell mixture was pipetted on the glass slide with gold (Au) micro-electrodes and was sandwiched by 18×18 mm coverslip. Sub-section 6.4.3 describes the process flow for fabricating

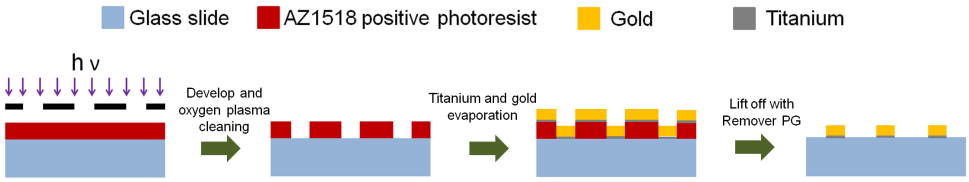


Figure 6.5: Process flow for the fabrication of the Au electrodes.

the Au electrodes. The waveform generator (Agilent, Santa Clara, CA) was turned on to provide 10 $V_{pp}$, 1-10 MHz sinusoid to achieve cell patterning. After the patterning, SL apparatus was used to polymerize the cell-polymer mixture to form the hydrogel.

### 6.4.3 Fabrication of the gold electrodes

Corning glass microscope slide (TedPella Inc, Redding, CA) was used as the substrate for electrode fabrication. Glass slides were first piranha cleaned for 10 minutes (1:1 $H_2O_2$-$H_2SO_4$) followed by a 1 minute of oxygen plasma treatment (500 mTorr, 300 W). AZ1518 photoresist (AZ Electronic Materials, Branchburg, NJ) was then spin coated to form a 2 $\mu$m layer. Photoresist was soft baked for 8 minutes at 110 °C and electrode features were exposed in the photoresist using an ultraviolet lamp and a high-resolution transparency mask (FineLine, Raleigh, NC). Exposed regions were then removed by developing the glass slide in MIF AZ300 (AZ Electronic Materials, Branchburg, NJ) for 2 minutes. After the second oxygen plasma treatment for 30 seconds (500 mTorr , 300 W), 50 Å of titanium (Ti) followed by 2000 Å of Au was deposited using e-beam evaporation (CHA SEC-600, CHA Industries, Fremont, CA). The glass slide was then immersed in 80 °C bath of remover PG (MicroChem, Newton, MA) for 1 hour to lift off undesired metal leaving patterned Au electrodes on the glass slide. Figure 6.5 shows the process flow for the fabrication of the gold electrodes.

### 6.4.4 Immunofluorescene microscopy and viability testing

In order to track the cells in the hydrogels after patterning and encapsulation, the cells were incubated with 1/1000 of cell tracker dyes (green or red,

| Liquid used for DEP patterning | Concentration [%] | $\sigma$ [mS m$^{-1}$] | $\eta$ [cP] |
|---|---|---|---|
| DI water | 100 | 0.105 | 1.04 |
| Cell culture medium | 100 | 1504 | 1.11 |
| LCM | 100 | 23.55 | 1.31 |
| PEGDA700 in LCM | 10 | 15.78 | 2.05 |
| | 15 | 13.16 | 2.62 |
| | 20 | 10.64 | 3.46 |
| PEGDA3400 in LCM | 10 | 36.9 | 3.69 |
| | 15 | 39.9 | 5.83 |
| | 20 | 41.2 | 9.97 |

Table 6.1: Electrical and viscous properties of the fluids.

(Invitrogen, Carlsbad, CA)) before mixing it with the polymer. Viability testing was done by employing the live/dead (Invitrogen, Carlsbad, CA) assay. The cells were incubated with 2 $\mu$M calcein AM (green, live) and 4 $\mu$M of ethidium homodimer (red, dead) for 15 minutes in phenol free DMEM. After 15 minutes, the hydrogels were washed twice in PBS ( Invitrogen, Carlsbad, CA) and immediately used for imaging. Green indicates that the cells are viable while red shows dead cells. ImageJ was used for counting the cells by taking their images in the respective channels. In order to check the viability of mEBs, the integrated density of EBs in the FITC (green, live) and the TRITC (red, dead) channel was found. The ratio of integrated density in the FITC to TRITC channel was reported as the viability of mEBs.

### 6.4.5 Characterization of DEP solution

The electrical conductivity of the different medium used for patterning the cells/spheroids of cells was measured by using an Orion 4 star conductivity meter (Thermo Electron Corporation, Waltham, MA). The viscosity of the solution was measured by using a DV II Pro Plus viscometer (Brookfield Engineering Laboratories, Middleboro, MA). Table 6.1 shows the electrical conductivity ($\sigma$) and viscosity ($\eta$) of DEP liquid used in this study and some standard solutions.

### 6.4.6 Statistical analysis

Statistical analysis was performed using two sample t-test in OriginPro 8.5. All data values reported in the study are mean ± standard deviation (SD).

### 6.4.7 Process for patterning mammalian cells in 3D hydrogels

Figure 6.6 shows the schematic of the overall process of simultaneous patterning and encapsulation of mammalian cells and PS beads on Au microelectrodes. The scheme for fabricating gold electrodes can be seen in figure 6.5. Cells and beads were first patterned by means of DEP forces to achieve spatial patterning. They were then encapsulated in the hydrogel by the SL apparatus. In order to achieve efficient DEP patterning, the DEP liquid medium needs to have low conductivity and low viscosity [243]. Low conductivity minimizes Joule heating while low viscosity decreases the drag force and patterning time. Table 6.1 shows the properties of the DEP liquid used in this study and some standard solutions. Albrecht et al., derived an equation which showed that the patterning time scales linearly with the viscosity of the medium. Therefore, lower the viscosity of the medium faster the patterning time [243]. Although, the viscosity of regular cell culture medium (RM) is low (1.11 cP), it has a relatively high electrical conductivity, 1504 mS $m^{-1}$. As a result, RM will cause excessive Joule heating which could be detrimental to the viability of cells [261]. Therefore, a different medium was used for patterning of cells and beads. This new medium had both low viscosity (1.31 cP) and low conductivity (23.55 mS $^{-1}$). It not only allowed efficient DEP patterning but also maintained very high cell viability (Figure 6.7). Two different $M_w$ PEGDA polymers, 700 and 3400, at three different concentrations (10%, 15% and 20%) were used to form hydrogels. The low conductivity medium (LCM) was used as the solvent for the polymers. By varying the $M_w$ and the concentration of the polymer, we were able to obtain hydrogels of physiologically relevant stiffnesses [87, 69, 262]. For both the polymers used in the study, the viscosity increases with an increase in the polymer concentration. As a result of this, the fastest patterning time ($\tau$) was achieved in 10% PEGDA 700 ($\tau < 10$ seconds), which is the lowest viscosity polymer. It took close to 240 seconds to pattern cells in 20% PEGDA 3400, the highest viscosity polymer. Also higher voltages were required to pattern

cells in this polymer. Unless otherwise specified, all the results presented in this study were obtained in 15% PEGDA 3400 ($\tau \sim 90$ seconds). mESCs show a good viability in LCM for holding time up 30 minutes (Figure 6.7). Given the patterning time of cells in the different solutions, multiple hydrogel constructs could be easily fabricated while maintaining good viability. As the same polymer solution was used for fabrication of multiple constructs, batch-to-batch variability in terms of material properties was eliminated. The size of the assembly that could be patterned using DEP is dependent on the area of electrodes, the spacing of electrodes, and the area that could be polymerized by the SL apparatus. It is independent of the liquid medium used for patterning. In this study, cells were patterned and encapsulated in a $10\times10$ mm area of the hydrogel. Thus this platform can be used for constructing very large arrays of micro-scale cellular patterns in three dimensions.

Figure 6.6B shows the real part of the CM, $K(\omega)$) factor for mammalian cells in the different liquid medium. It can be seen that for the polymers used in the study, the cells will experience both nDEP and pDEP depending on the frequency. Specifically, for PEGDA 3400, at frequencies lower than 0.12 MHz or at frequencies higher than 115 MHz, cells will experience nDEP. Between these frequency ranges, the cells experience pDEP. Since, it is well documented that patterning via pDEP is faster than nDEP, pDEP was used for patterning of cells [243]. Furthermore, CM factor which also determines the relative DEP force is also larger in the pDEP regime. Therefore, for PEGDA 700 and PEGDA 3400, a frequency range of 1-10 MHz was chosen. This maximized the CM factor and hence the relative DEP force experienced by the cells. At the same frequency range, the PS beads experienced nDEP (Figure 6.2D).

Mammalian cells have a large differential of ions between its interior and exterior leading to the development of a resting membrane potential. The maintenance of this resting membrane potential is of utmost importance for the proper functioning of the cellular activities. When an alternating sinusoidal electric field is applied to a cell, this new field gets superimposed to the resting membrane potential. If the resultant resulting membrane potential is sufficiently high, it might lead to an asymmetric breakdown of the cellular membrane causing cell death [263]. Irreversible cellular electroporation occurs at field strengths of 1-1.3 kV $cm^{-1}$ [264]. This means that a potential difference of approximately 1 V can be potentially lethal for a cell

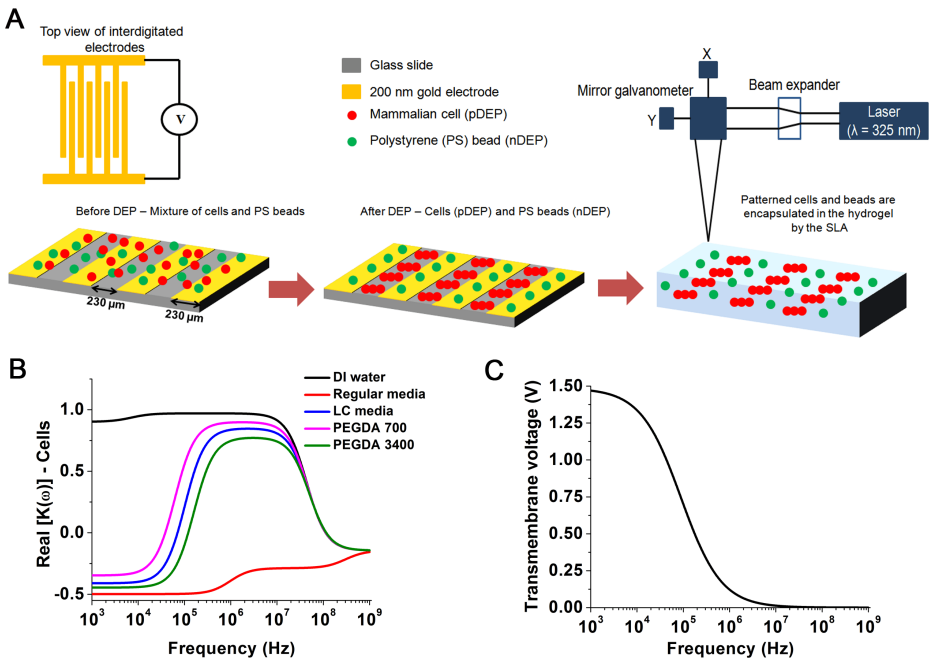


Figure 6.6: Fabrication of spatially patterned 3D hydrogel constructs. (A) Schematic showing the overall process of creating 3D spatially patterned hydrogel constructs. A mixture of cells and PS beads is first introduced on the glass slide with patterned gold electrodes. After this the electrodes are energized with a 10 $V_{pp}$ (3.535 $V_{rms}$) 1-10 MHz signal which leads to pDEP patterning of the cells and nDEP patterning of the PS beads. The SL apparatus then polymerizes the PEGDA polymer and patterned cells and beads get encapsulated in the 3D hydrogel. (B) Real part of the CM factor for mammalian cells in the different fluids used for DEP patterning. Between 1-10 MHz, mammalian cells always undergo pDEP for the two different polymers (PEGDA 700 and 3400) used in this study. (C) TMV of the cells as a function of applied frequency.

of diameter 10 $\mu$m. Figure 6.6C shows the transmembrane voltage (TMV) in the cell as a function of the applied electric field from 1 kHz to 1 GHz. For the frequency range used for patterning of cells in the polymers (1-10 MHz), the transmembrane voltage is around 0.12-0.013 V respectively. Since, this value is much smaller than the threshold voltage of 1 V, the cells will not undergo irreversible electroporation as a result of dielectrophoretic manipulation. Equation 6.12 was used to calculate the TMV across the cell. Here, $E$ is the external field in the liquid medium (123828 V $m^{-1}$) at a height of 3 $\mu$m above the electrode, $R$ is the radius of the cell (8 $\mu$m), $\omega$ is the angular frequency ($\omega = 2\pi f$ and f = $10^4$ - $10^9$), $C_m$ is the membrane capacitance per

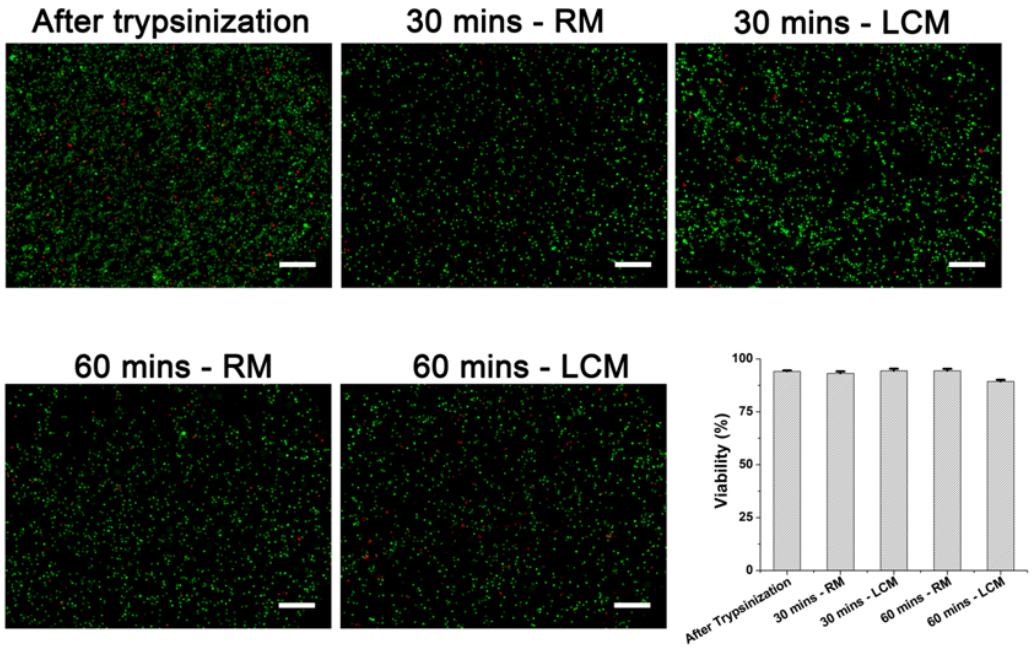


Figure 6.7: Live/dead assay showing the viability of mESCs after trypsinization, and after suspension in the LCM and RM for 30 and 60 minutes respectively ($n = 5$). There is no statistical difference in the viability of mESCs in LCM and RM at 30 minutes at $p < 0.05$.

unit area ($10^{-2}$ F $m^{-2}$) [263] and $\rho_i$ (1 Ω m) [263] and $\rho_a$ (42.46 Ω m) are the resistivity of the cell interior and the electrolyte respectively. Since, both the CM factor and the TMV are optimized between 1-10 MHz for the polymers, this range was chosen for patterning of cells *via* DEP.

$$TMV = \frac{1.5ER}{1 + i\omega RC_m(\rho_i + \frac{\rho_a}{2})} \tag{6.12}$$

## 6.5 Multi-cell patterning in three-dimensional hydrogels

Figures 6.8A-C shows the encapsulated C2C12 cells and mESCs in 15% and 20% PEGDA 700 hydrogels. Highly uniform arrays of cells and beads can be seen encapsulated in the hydrogel after polymerization. This indicates that DEP forces can be used for manipulating cells in the polymers. Before patterning the cells in the polymer, their viability was checked in the LCM. Figure 6.7 shows that mESCs show a high viability after being suspended

in a LCM for 30 minutes and this was not statistically different ($p < 0.05$) from that of the cells in RM. Figures 6.8A,B shows that C2C12 cells (red) undergo pDEP and PS beads (green) undergo nDEP at 10 MHz in 15% PEGDA 700. Figure 6.8C shows the same for mESCs (red) in 20% PEGDA 700. Lee et al., showed that incorporation of hydrophobic nanoparticles can introduce network defects in the hydrogel while minimally affecting its mechanical and viscous properties [265]. Therefore, controlling the position of hydrophobic PS beads *via* DEP forces can be used to create network defects at regular spatial locations in the hydrogel. This can improve the permeability of compounds through the hydrogel and thereby improve their viability.

Figures 6.8D-F shows the encapsulation of mESCs with two different colored dyes (green and red) in 15% PEGDA 3400. By encapsulation of multiple types of cells using conventional SL, the two different types of cells are generally present with minimal cell-cell contacts in the hydrogel (Figure 6.8D). While these co-culture studies can be very useful for studying paracrine signaling [258], cell-cell contacts which are responsible for fate decisions by embryonic stem cells cannot be studied using this approach [266]. However, as seen in figures 6.8E and F, DEP allows cell-cell contacts by formation of cellular pearl chains. These pearl chains can be used for studying the fate decisions by stem cells. Numerous studies have demonstrated the role of cellular co-culture for determining the fate of ESCs [267, 268]. This combined DEP-SL apparatus platform will enable the study of multiple cell interactions via cell-cell contacts in 3D and can open new doors in stem cell biology.

Figure 6.8G, H shows the image of a live/dead assay for mESCs with and without DEP on day 0 in 15% PEGDA 3400. It can be seen from these fluorescent images that most of the cells survive patterning *via* DEP and SLA encapsulation. Figure 6.8I quantifies the viability of cells with and without DEP. The cells which were aligned in the hydrogel with DEP show a viability of 91.79 $\pm$ 1.4% while those which were not subjected to DEP show a slightly higher viability of 94.27 $\pm$ 0.5%. Thus these studies show that our combined platform can be used for studying multi-cell interactions in 3D hydrogels while maintaining their viability.

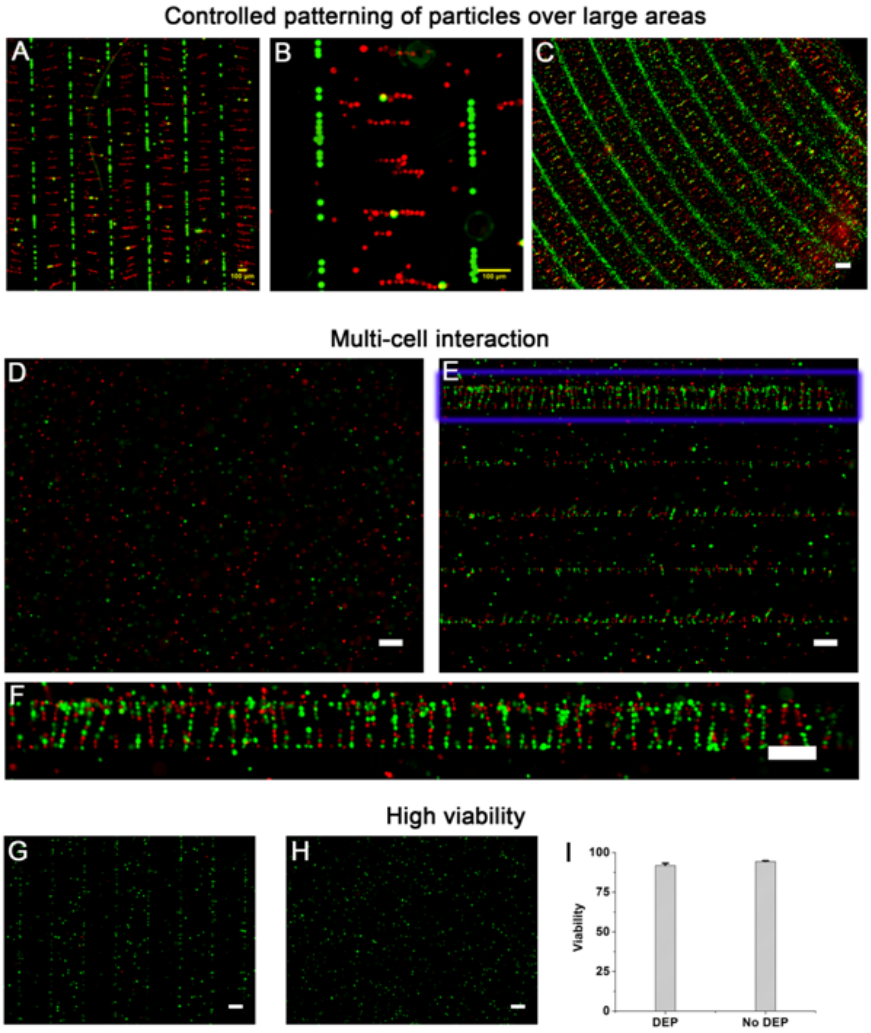


Figure 6.8: Multi-cell patterning and encapsulation in different stiffness hydrogels by DEP and SL. (A) C2C12 (red) cells (pDEP) and PS beads (green) (nDEP) in 15% PEGDA 700 (Scale bar = 100 $\mu$m) (B) Zoomed image of (A) (Scale bar = 100 $\mu$m) (C) mESCs (pDEP) and PS beads (green) (nDEP) in 20% PEGDA 700 (Scale bar = 200 $\mu$m) by using spiral electrodes. (D-F) mESCs with two different colored dyes (red and green) were encapsulated in 15% PEGDA 3400. (D) Without DEP (Scale bar = 100 $\mu$m). (E) With DEP (Scale bar = 100 $\mu$m). (F) Zoomed image of the highlighted blue box clearly showing cell-cell interactions in the hydrogel (Scale bar = 100 $\mu$m). (G-I) Demonstrates that high cell viability can be achieved using this platform. (G) Live/dead assay at day 0 with DEP (Scale bar = 100 $\mu$m). (H) Live/dead assay at day 0 without DEP (Scale bar = 100 $\mu$m). (I) Graph showing the viability of cells with and without DEP.

## 6.6 Formation of aggregates of embryonic stem cells

mEBs are 3D aggregates of mESCs and serve as an excellent model for studying the controlled differentiation of mESCs. As previously shown, the differentiation of cells in the EBs is extremely sensitive to a variety of factors including the size (density of cells in the EB) of the EB. Larger EBs ($\sim$ 450 $\mu$m) promote cardiogenesis while smaller EBs ($\sim$ 150 $\mu$m) promote endothelial differentiation [109]. Large number of uniform sized EBs were formed using AggreWell plates. Desired numbers of cells were seeded, centrifuged, and incubated in the plates. After 24 hours of incubation, highly uniform EBs were seen in the micro-wells of the plate. Figure 6.9A shows the different initial seeding densities of mESCs in the plates at 0 hours and the resultant EBs that formed after 24 hours in one of the microwells of the plate. Each of these plates contain anywhere from 9,600 to 28,200 micro-wells. Hence, a large number of uniformly sized EBs can be rapidly obtained. Figure 6.9B (i) is an SEM showing the uniformity of the EBs obtained from these plates. Figure 6.9B (ii) shows an individual EB while Figure 6.9B (iii) shows the close-up of an individual EB. These SEMs show that large number of highly uniform EBs can be obtained using AggreWell plates. Figure 6.9C shows the area of EBs as a function of the initial seeding density of the cells. Interestingly, the area of the EB does not double by doubling the initial cell seeding density. This suggests that the packing properties of cells in the EBs are a density dependent phenomenon. Figure 6.9D shows the theoretical and the measured volume of the EBs as a function of the initial seeding density of cells. It can be seen that the theoretical volume matches closely to the calculated volume of the EBs. The inset of the figure shows the radius of the EB as a function of the initial seeding density. Both the theoretical and measured radius show good match as well. A 250 cell EB measured 68 $\mu$m while this radius increased to only 110 $\mu$m by quadrupling the initial cell seeding density (2000 cells). Therefore, larger mEBs show a higher packing density which can be seen in Figure 6.9E. This could be possible because of differences in the E-cadherin expression in the EBs. Different levels in E-cadherin expression have been reported for EBs of different sizes and different time points [109]. 1000 cell EB shows the highest packing density of approximately 425,000 cells $mm^{-3}$. Also, the same EB shows the best packing efficiency which is the ratio of measured volume to the theoretical volume.

Future studies can explore the effect of packing density and packing efficiency on the differentiation potential of mEBs. In addition, to further understand the packing properties of the EBs, they can be labeled for E-cadherin which will show cell-cell contacts in the EBs [266].

Figure 6.10 shows the characterization of C2C12 spheroids. The assumptions made in order to calculate the theoretical volume of the spheroid (mEB) were as follows. The radius of the cell was measured to be 8 $\mu$m using the hemocytometer. The cell was assumed to be a perfect sphere and its volume was calculated to be $\sim$ 2214 $\mu m^3$. In order to find the volume of the EB, it was assumed that there are no voids in the EBs and hence by multiplying the number of cells in the EBs with the volume of each cell the theoretical volume was found. The measured volume of EB was calculated by finding the radius of the EB from ImageJ and by using the relation $V = 4/3\pi R^3$. The protocol for the formation of C2C12 spheroids was the same as that employed for formation of mEBs. Desired numbers of C2C12 cells were seeded in Aggrewell plates. For instance, if a 1000 cell spheroid was to be formed, 1.2 million C2C12 cells were seeded in one of the wells of the plate which contained 1200 micro-wells. Prior to seeding the cells in the wells, the plate was incubated with 2% Pluronic F127 to prevent the attachment of cells to the wells. After this, the plate was centrifuged and the cells were pulled to the bottom of the micro-well in the plate. The plate was incubated for 24 hours in the incubator and uniformly shaped C2C12 spheroids (or mEBs) were formed in most of the microwells of the plate. Mild pipetting was required to remove the spheroids from the wells. Figure 6.10 shows the characterization of C2C12 cell spheroids obtained from the Aggrewell plates. Figure 6.10A shows the area of the spheroids as a function of the number of cells in the spheroid. A 50 cell spheroid was measured to be slightly over 2600 $\mu m^2$ while a 1000 cell spheroid was roughly about 25000 $\mu m^2$. Therefore, increasing the initial seeding density by 20 times resulted in less than 10 times the increase in the area. Figure 6.10B shows the radius of the C2C12 cell spheroid as a function of the initial cell seeding density. The measured radius seems to follow a power law behavior with power being 2.76 (1/0.362) instead of the expected power of 3 (1/0.333). However, for the smaller spheroids (50, 100 cells) the measured radius is in good consistency with the theoretical radius.

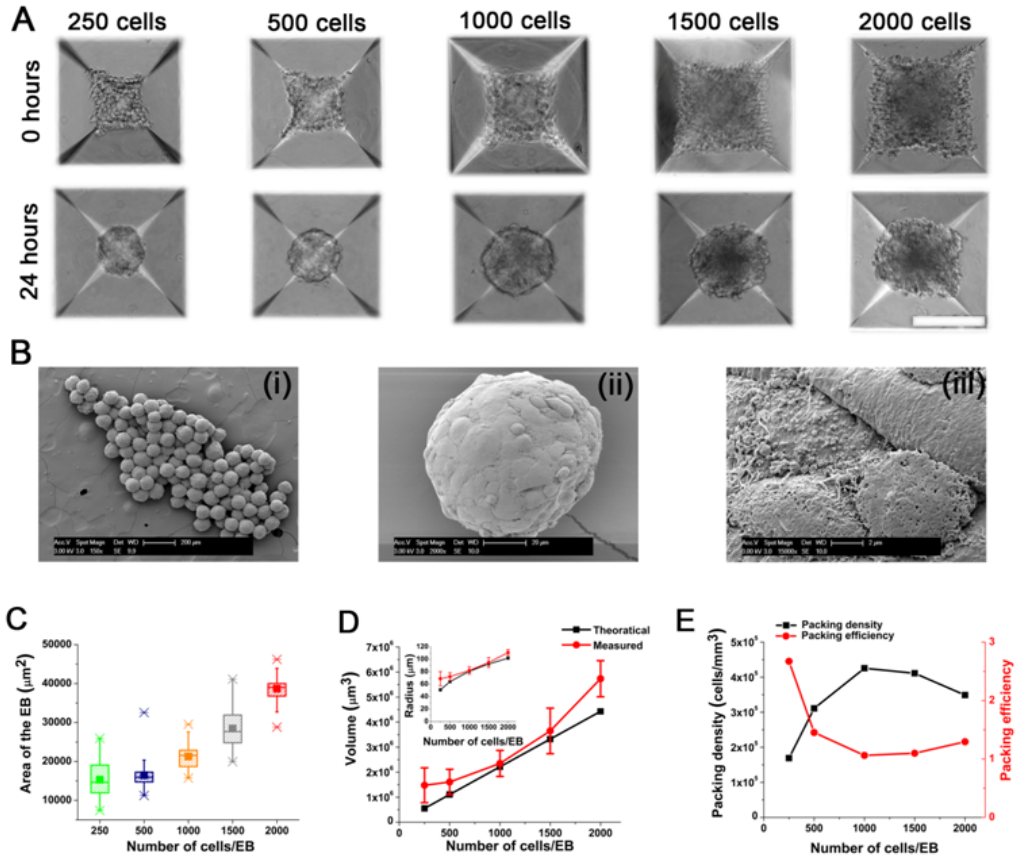


Figure 6.9: Characterization of EBs of mESCs. (A) Different densities of cells (250, 500, 1000, 1500, and 2000) seeded in AggreWell plates at 0 hours and after 24 hours (Scale bar = 200 $\mu$m). (B) SEMs of a 1000 cell mEBs at different resolution (i) Shows the uniformity of the EBs obtained from the AggreWell plates (Scale bar = 200 $\mu$m). (ii) An individual EB (Scale bar = 20 $\mu$m). (iii) Close up of the EB (Scale bar = 2 $\mu$m). (C) The area of the EBs as a function of the initial seeding density. (D) The volume of the EBs as a function of the initial seeding density. The inset shows the radius for the same. (E) Packing density and packing efficiency of the EBs as a function of the initial seeding density. Packing efficiency was calculated by dividing the actual volume by theoretical volume, $n > 50$ EBs for (C-E).

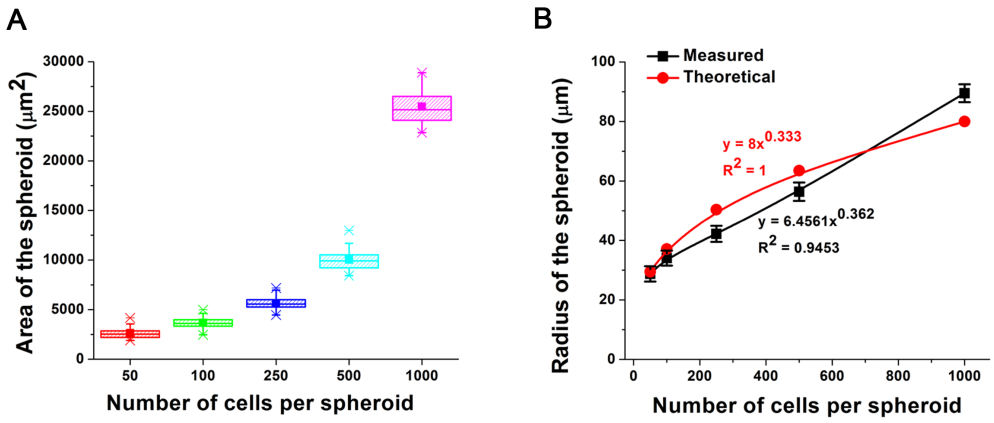


Figure 6.10: Characterization of C2C12 spheroids. (A) The area of the spheroid as a function of the initial cell seeding density. (B) The measured and the theoretical radius as a function of the initial cell seeding density ($n = 35$).

## 6.7 Patterning of aggregates of embryonic stem cells

After the successful formation of mEBs (or spheroids of C2C12 cells, for characterization of C2C12 spheroids, see Figure 6.10), the patterning and encapsulation of these cell clusters in the hydrogels is also shown. Figure 6.11i, ii, show the images of 500 cell C2C12 spheroids with and without DEP in 15% PEGDA 700 respectively. The spheroids have been labeled with a red colored cell tracker dye. For the convenience of the reader, approximate locations of the underlying electrodes (Figure 6.11i) for the DEP sample have been drawn. It can be seen that the spheroids of C2C12 cells undergo pDEP in 15% PEGDA 700 at 1 MHz. Most of the spheroids can be seen touching the edges of the electrodes (electric field maxima) and trying to form pearl chains, a characteristic of pDEP. Figure 6.12 shows the patterning of C2C12 spheroids via DEP in 15% PEGDA 700. Presence of multiple pearl chains of C2C12 spheroids can be clearly seen in these images further confirming that cell spheroids undergo pDEP. The inset of figure 6.11A shows the FFT of the raw grayscale image (without the electrodes) which was used to check the alignment of the spheroids [186, 198]. Figure 6.11B shows the FFT alignment plot for the spheroids encapsulated in 15% PEGDA 700 hydrogels. The FFT alignment plot shows a major peak at 180° (peak FFT = 0.103) for the sample which underwent DEP manipulation. Since FFT is a symmetric

function, two other peaks can also be seen at 0° and 360° respectively. The sample with no DEP shows two very small peaks at 90° and 270° (peak FFT = 0.031) with very small signal to noise ratio of 1.47. If a circular mask is applied to this image, peaks were also seen at 0°, 90°, 180°, 270°, and 360°. Therefore, this sample does not show a net alignment for the spheroids. In this study, all the alignment quantification has been performed without using a circular mask. The height and the overall shape of the peaks represent the degree of alignment in the original image. A high and narrow peak indicates a more uniform degree of alignment while a broad peak indicates that more than one axis of alignment may be present. A completely random alignment is shown by no discernible peak in the alignment plot or by the presence of peaks at multiple peaks 0°, 90°, 180°, 270°, and 360° in the same alignment plot [189]. Directional basis in a material develops at 0.05 units or higher [198, 189, 269]. Hence, DEP can be used to align spheroids of cells (cellular aggregates or clusters) in the hydrogels as well. This is the first study showing the patterning of spheroids in 3D hydrogels via DEP. Figure 6.11C shows the live/dead images of mEBs (500 cell spheroids of mESCs) in 15% PEGDA 3400 for days 1, 3 and 5. From these images, it can be seen that mEBs easily survive this combined process of DEP SL apparatus and show a good viability. Figure 6.11D show FFT alignment plots for the images shown in Figure 6.11C. These alignment plots show that mEBs that were subjected to DEP were patterned in the hydrogel as evidenced by the high, narrow peak and the corresponding high peak FFT values. The hydrogels that were not subjected DEP show more than one degree of alignment and relatively low peak FFT values, indicative of no net alignment. Figure 6.11E shows the viability of mEBs in the hydrogel. There is no statistical difference in viability for the samples that were subjected to DEP and no DEP for days 1 ($p = 0.703$), 3 ($p = 0.443$) and 5 ($p = 0.096$). Viability in this plot is the ratio of integrated density (area X mean gray value) of FITC (live cells) filter to TRITC (dead cells) filter. Even after five days in the hydrogel both the DEP and the no DEP sample show viability of over 1, indicating that there are more live cells than dead cells. Hence, the platform can be used for patterning mEBs in 3D hydrogels while maintaining their viability.

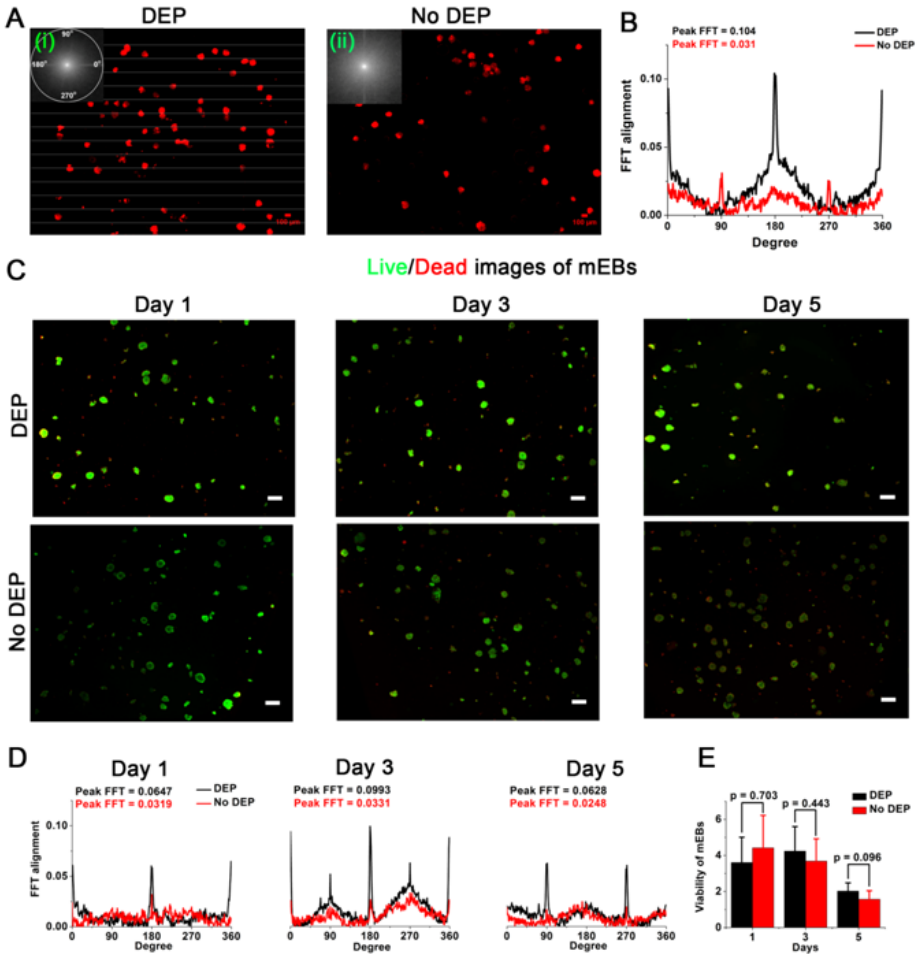


Figure 6.11: Alignment of C2C12 spheroids and mEBs in different hydrogels. (A) Alignment of 500 cell C2C12 spheroids in 15% PEGDA 700 labeled with red colored cell tracker dye. (i) Sample subjected to DEP. Approximate location of the electrodes is shown in the figure to show that the spheroids get pulled to the edges of the electrode, a hallmark of pDEP. (ii) No DEP sample. The inset of the plot shows the FFT of the corresponding images (Scale bar = 100 $\mu$m). (B) FFT alignment plot obtained from the FFT of the images. The alignment plot shows that the hydrogel sample subjected to DEP shows a net alignment. (C) Live/dead images of 500 cell mEBs in 15% PEGDA 3400 for days 1, 3 and 5 for both DEP and no DEP samples (Scale bar = 250 $\mu$m). (D) FFT alignment plots of the images in (C). The alignment plot shows that the hydrogel sample subjected to DEP shows a net alignment. (E) Viability of mEBs in the hydrogels ($n > 3$). An integrated density of 1 or higher means that there are more live cells than dead cells. There is no statistical difference in the viability of the mEBs for the DEP and the no DEP samples at $p < 0.05$.

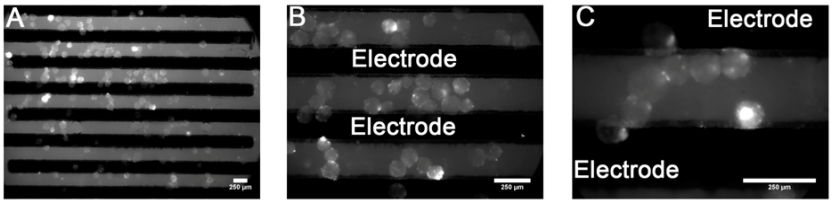


Figure 6.12: (A-C) 500 cell C2C12 spheroids at different magnification on interdigitated electrodes of a printed circuit board in 15% PEGDA 700 labeled with red colored cell tracker dye (Scale bar = 250 $\mu$m).

## 6.8 Conclusion

Controlling the assembly of cells in three dimensions is very important for engineering functional tissues, drug screening, probing cell-cell/cell-matrix interactions, and studying the emergent behavior of cellular systems. Although the current methods of cell encapsulation in hydrogels can distribute them in three dimensions, these methods typically lack spatial control of multi-cellular organization and do not allow for the possibility of cell-cell contacts as seen for the native tissue. Here, we showed the integration of DEP with SL apparatus for the spatial patterning and encapsulation of mESCs, C2C12 cells and their spheroids in different types of hydrogels has been shown and their viability after DEP has been confirmed. mESCs have the potential to differentiate into cells of the three germ layers - ectoderm, mesoderm and endoderm. However, controlling their differentiation to a particular lineage with high purity is extremely difficult because of the unknown cellular interactions with each other and their environment. DEP allows us to spatially organize the cells and their spheroids. Thus previously unknown cellular interactions can now be studied in a high throughput fashion. SL apparatus offers multi-cell, multi-material fabrication and allows for fabrication of a variety of physiologically relevant photolabile hydrogels. This combined platform thus takes us one step closer to mimicking the *in vivo* cellular micro-environment and can have applications in tissue engineering, regenerative medicine and stem cell differentiation.

# CHAPTER 7

# VIABILITY AND DIFFERENTIATION OF EMBRYONIC STEM CELLS IN 3D PEGDA HYDROGEL CONSTRUCTS

## 7.1 Introduction

ESCs have the potential to differentiate into any cell of the body and therefore hold the promise to revolutionize modern medicine[11]. However, controlling their differentiation to a particular lineage is very challenging because it is often difficult to recapitulate the myriad of bio-chemical and bio-physical cues of the growing embryo [20]. In this chapter, some preliminary results show the viability and differentiation of mESCs encapsulated in 3D PEGDA hydrogels polymerized by stereolithography (SL) are presented. Section 7.2 discusses the protocol used for running this study. Section 7.3 show the viability of mESCs and mouse embryoid bodies (mEBs) in 20% PEGDA hydrogels. Section 7.4 presents some preliminary data of mESC differentiation in 15% and 20% PEGDA 3400 hydrogels.

## 7.2 Experimental

W4129S6 mESCs were cultured in high glucose DMEM supplemented with 15% FBS, 1% penicillin-streptomycin, 1 mM sodium pyruvate, 2 mM glutamine, 100 $\mu$M non-essential amino acids, 10 ng ml$^{-1}$ of mouse Leukemia Inhibitory Factor (mLIF) and 100 $\mu$M of mono-thiogycerol on 0.1% gelatin coated petri dishes in standard cell culture conditions. PEGDA 3400 polymer was mixed with 0.5% 4-(2-hydroxyethoxy) phenyl-(2-hydroxy-2-propyl) ketone (Irgacure 2959, Ciba) in DMEM. Irgacure 2959 served as the photoinitiator for this hydrogel system. Three parts of the polymer was added to one part of the cell mixture such that the final concentration of the cell-polymer solution was 15% and 20% respectively. 250 $\mu$L of this polymer-cell mixture

was pipetted onto a glass bottom coverslip. The final concentration of cell in the polymer-cell mixture was $\sim 10 \times 10^6$ cells per mL. After polymerization *via* SL, the hydrogels were incubated in cell culture media and viability studies were performed at different time intervals. In addition, mEBs were also encapsulated in 20% PEGDA hydrogels using the above procedure. The protocol for mEB formation and its characterization is presented in 6, section 6.6. Two different size mEBs, 250 cells and 1500 cells were encapsulated in the same PEGDA hydrogels. For the differentiation studies, hydrogels were incubated in a media devoid of mLIF but with all the other factors present. mLIF is a pleiotropic cytokine which is extensively used for the maintenance of pluripotency [270] Therefore, by culturing the cells in a media with no mLIF allows them to spontaneously differentiate based on the cues of the micro-environment.

Viability testing was done by employing the live/dead assay. The cells were incubated with 2 $\mu$M calcein AM (green, live) and 4 $\mu$M of ethidium homodimer (red, dead) for 15 minutes in phenol free DMEM. After 15 minutes, the hydrogels were washed twice in PBS and immediately used for imaging. Green indicates that the cells are viable while red shows dead cells. Viability testing was employed after days 1, 5, 7, 10, and 14. ImageJ was used for counting the cells by taking their images in the respective channels. In order to check the viability of both mESCs and mEBs, the integrated density (area X mean gray value) in the FITC (green, live) and the TRITC (red, dead) channel was found. The ratio of integrated density in the FITC to TRITC channel was reported as the viability of mEBs.

Statistical analysis was performed using Mann-Whitney in OriginPro 8.5. Unless otherwise mentioned, the values reported are mean $\pm$ standard error of the mean (SEM) and the results were considered statistically significant when the $p$-value was less than 0.05 ($p < 0.05$)

## 7.3 Viability of mESCs and mEBs in PEGDA hydrogels

Figure 7.1 shows the viability of mESCs and mEBs in 20% PEGDA 3400 over the course of 14 days. It can be seen from figure 7.1A that on day 1, both the mESCs and mEBs show a very high viability as evidenced by the

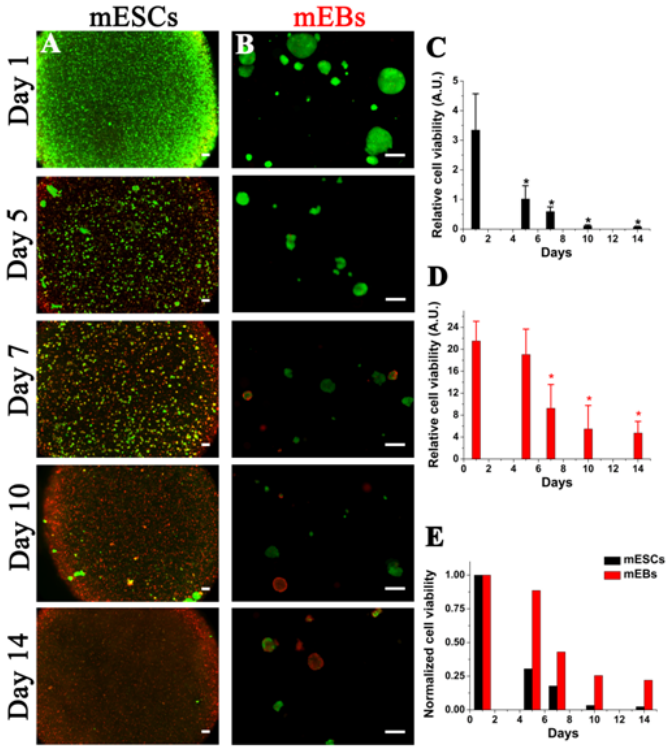


Figure 7.1: Viability of mESCs and mEBs in 20% PEGDA 3400 hydrogels. Live/dead assay showing the vaibility of (A) mESCs (B) mEBs over 14 days. Quantitative relative viability of (C) mESCs (D) mEBs over 14 days. (E) Normalized cell viability to day 1 of mESCs (black bar) and mEBs (red bar). Asterisks indicate statistical significance. At $p < 0.05$, the means are statistically different to day 1. Data show is the mean $\pm$ SEM ($n = 5$). Scale bar: 100 $\mu$m

live/dead assay. There are two sources of death when mammalian cells are encapsulated *via* SL apparatus.

- Initial cell death because of exposure to the UV laser of the SL apparatus.
- Death over the long-term because of the diffusion limitations inside the hydrogel.

However, the high day 1 viability for both mESCs and mEBs indicate that these cells can easily survive the UV laser of the SL apparatus. Thus it becomes possible to explore a variety of other biologically relevant photolabile polymers with mESCs and the SL apparatus. With time, there is an increase in the death of cells for both mESCs and mEBs as evidenced from figure

7.1A, B. By day 14, almost all the individual mESCs are dead. However, the same is not true for the mEBs. A significant portion of mEBs still survive the long-term encapsulation in PEGDA hydrogels. Figure 7.1C, D, and E show the quantitative viability plots for mESCs and mEBs in PEGDA 3400. It is clear that by the end of 14 days, ∼22% mEBs survive the long-term encapsulation while less than 2.5% of individual mESCs survive this process. It should be noted that no cell-adhesion molecules were tethered to the polymer backbone. By covalent attachment of cell-adhesive peptides like RGDS, this viability can be further increased dramatically [87]. Similar viability values have been reported for other cell types like fibroblasts, C2C12 cells, and PC12 cells previously [87, 258]. Thus this study showed that it is possible to achieve long-term mESC viability in 20% PEGDA hydrogels. However, it was very interesting to see that mEBs show almost 10 times higher viability than individual mESCs. A cell spheroid is a homogeneous structure, with cells even at the center of the sphere. These cells at the center will be more starved of nutrients than the individual mESCs. However, a higher percentage of these EBs are able to survive in the hydrogels over the course of 14 days. The reason for this anomalous behavior could be paracrine and autocrine signaling. The mEBs provide the cells a native 3D cellular micro-environment which is seen in a growing embryo. It is possible that by mimicking this 3D micro-environment even the cells at the center of the EB are able to survive in a diffusion limited environment possibly by lowering their metabolic demands. It will be very interesting to investigate the metabolic activities of cells in EB and individual cells in future studies.

Another very interesting phenomenon that was observed in this study was the formation of spontaneous EBs in hydrogels which were encapsulated with individual mESCs. It is known that the pore size of 20% PEGDA hydrogels is less than 10 nm [87]. Therefore, it is highly improbable that there is movement of cells from inside the hydrogels to the outside since the diameter of an individual mESC is ∼16 $\mu$m. Figure 7.2 shows the formation of spontaneous EBs in 20% PEGDA hydrogels. It can be seen that as early as day 3, individual mESCs spontaneously aggregate together to from spherical looking cell spheroids similar to EBs that were formed using the AggreWell plates. However, these spontaneous EBs do not have a fixed diameter rather a very wide range of 100 $\mu$m to few millimeters. It was confirmed *via* confocal microscopy that there was not a statistically different number of cells

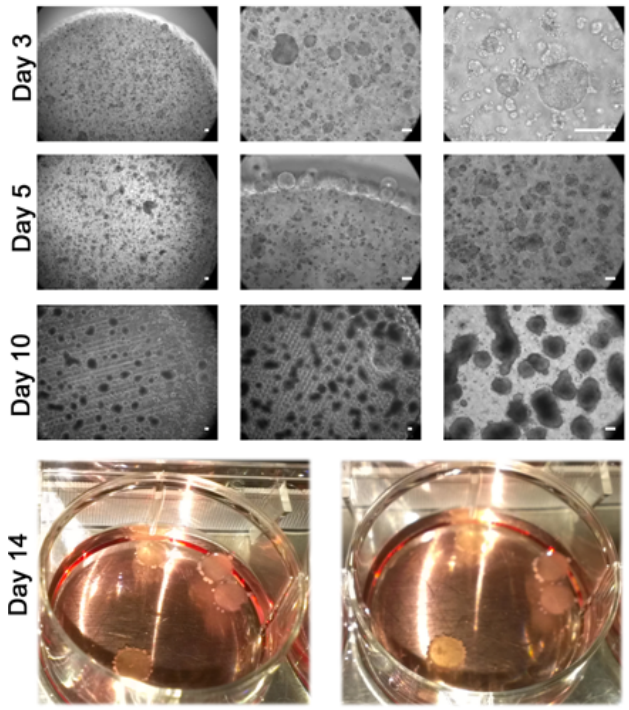


Figure 7.2: Images showing spontaneous EB formation in 20% PEGDA 3400. Row 1 corresponds to day 1, Row 2 corresponds to day 5, Row 3 corresponds to day 10. Scale bar = 100 $\mu$m. Row 4 shows images of hydrogel disks in 6-well plates showing the resultant EBs formed attached to the hydrogel disks. The diameter of each disk is 10 mm.

from day 1 to day 14 inside the hydrogels. So most likely these EBs form by the aggregation of cells on the surface of the hydrogels. However, this is still very interesting for two main reasons. Generally, EB formation is a precursor to differentiation of mESCs. Therefore, it is very possible that these mESC cell aggregates so formed could lead to differentiation of these cells to a different cell type. However, their differentiation potential was not explored yet and was the topic of research of some ongoing work. Another reason spontaneous EB formation is interesting because this phenomenon was not observed for other cell types like C2C12 cells, fibroblasts, PC 12 cells [87, 258]. However, further studies must be done to fully understand the basis of this phenomenon and the fate of these spontaneous EBs.

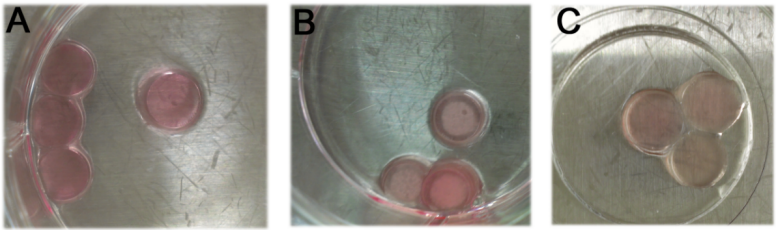


Figure 7.3: (A) mESCs encapsulated in 15% PEGDA 3400 hydrogel with mLIF on day 14. (B) mESCs encapsulated in 20% PEGDA 3400 hydrogel without mLIF on day 14. (C) C2C12 cells encapsulated in 20% PEGDA 3400 hydrogel in DMEM with mLIF on day 14. One hydrogel disk is 10 mm in diameter.

## 7.4 Differentiation of mESCs in PEGDA hydrogels

The previous studies were done with cells encapsulated in hydrogels and incubated in media with mLIF. As mLIF is responsible for maintaining the pluripotency of mESCs [270], studies were also run to see the affect of mLIF removal from the media. Individual mESCs were encapsulated in 20% and 15% PEGDA 3400 and incubated in DMEM wihout mLIF but all the other chemical factors mentioned in section 7.2. Cells encapsulated in 15% PEGDA 3400 showed a higher viability than the cells encapsulated in 20% PEGDA 3400. This is possibly because lowering the concentration of PEGDA increases the pore size in the hydrogel network which allows for better diffusion of chemicals in and out of the hydrogel [271, 272]. The Young's modulus (stiffness) of the hydrogel disks made by the SL apparatus was measured by using a mechanial testing system by compressing the disks at a constant rate of 1 mm $s^{-1}$ in the ambient. Stiffness was calculated using the slope of stress versus the strain curve within the first 10% of the strain. The stiffness of the 15% PEGDA 3400 hydrogel was measured to be 72.66 $\pm$ 4.07 kPa while the stiffness of 20% PEGDA 3400 hydrogel was measured as 397.48 $\pm$ 27.00 kPa. Thus the 20% hydrogel was significantly much stiffer than the 15% hydrogel. Figure 7.3 shows the images mESCs and C2C12 cells encapsulated in 15% and 20% PEGDA 3400 hydrogels on day 14. It can be seen from figure 7.3A that hydrogel disks with mESCs encapsulated in 15% PEGDA 3400 appears transparent and structurally similar to the disks obtained right after fabrication on day 0. However, figure 7.3B shows the hydrogel disks with mESCs encapsulated in 20% PEGDA 3400. All the 4

disks have changed their opacity and have become almost opaque at the center. Figure 7.3C shows C2C12 cells encapsulated in 20% PEGDA 3400 with mLIF. These disks again look transparent and similar to disks obtained in figurehydrogelDisksA. Since, 20% PEGDA 3400 is significantly much stiffer than 15% PEGDA 3400 and also since the cells were cultured without mLIF, it could be possible that the cells have differentiated to some cell type (possibly a type of bone cell) and the change in the hydrogel opacity could be just mineral deposition. It has been previously showed that hMSCs cultured on stiff substrates ($>$ 100 kPa) show markers of osteogenesis and promote bone differentiation [68]. In order to confirm mineral deposition, the hydrogel disks were incubated in a solution of 2% Alizarin red stain. Alizarin red is a calcium indicator and ubiquitously used for staining calcium deposition by osteoblasts [273]. Figure 7.4A, B shows the 20% PEGDA 3400 hydrogel disks on day 14 with encapsulated C2C12 cells. No major staining is visible in these disks. Figure 7.4C, D shows PEGDA 15% hydrogel disks on day 14 with mESCs in the absence of mLIF. Again, no major staining is visbile, although the spontaneously formed EBs can be clearly seen in these images in the hydrogel. Figure 7.4E, F shows 20% PEGDA 3400 hydrogel disks on day 14 with mESCS in the absence of mLIF. There is a very strong staining for Alizarin red in these disks. The center region of the disk has been stained very strongly for Alizarin red and almost appears black (dark red). This could possibily be calcium deposition by the mESCs in these stiff hydrogels. From these images it can be interpreted that the 20% PEGDA 3400 hydrogel disks which had mESCs encapsulated showed possible mineral deposition after the end of 14 days in culture. However, neither of the other two samples, 20% PEGDA 3400 with C2C12 cells or the 15% PEGDA 3400 showed any mineral deposition after this period. It should also be noted that here no osteogenic induction media has been used. The differentiation is solely based on the stiffness cues received from the micro-environment of the different stiffness hydrogels.

Furthermore, fluorescence microscopy also revealed mESC spreading on the 20% PEGDA 3400 hydrogels (without mLIF) as shown in figure 7.5A. These gels do not have any cell adhesive peptides anchored to it. It is well known that unmodified PEGDA does not allow cell spreading [274]. Therefore, this mESC spreading could be attributed to the deposition of some ECM proteins either by spontaneously formed EBs or by the cells themselves which allow

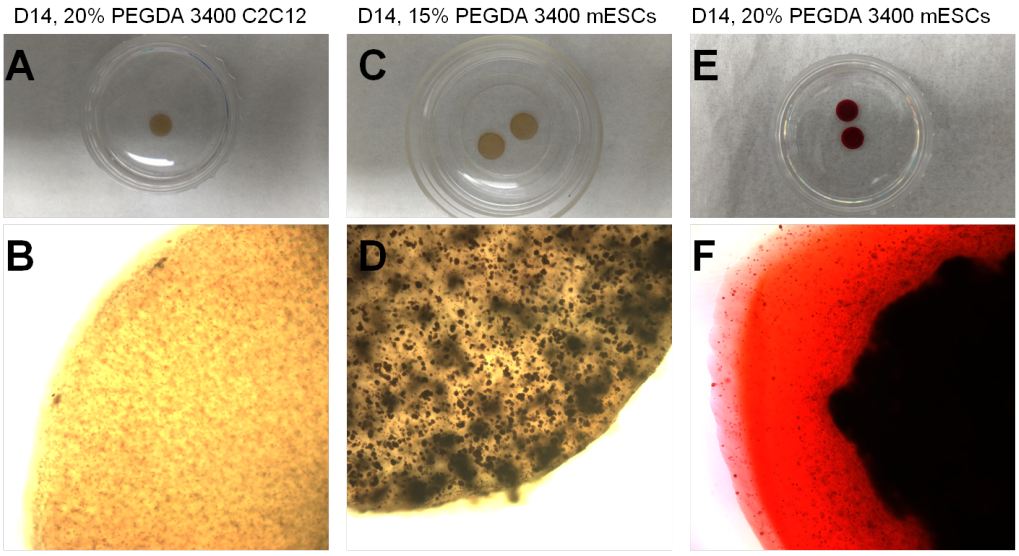


Figure 7.4: Alizarin red staining. (A, B) Day 14 20% PEGDA 3400 hydrogel disk with C2C12 cells. (C, D) Day 14 15% PEGDA 3400 hydrogel disk with mESCs without mLIF. (E, F) Day 14 20% PEGDA 3400 hydrogel disk with mESCs without mLIF. Each hydrogel disk has a diameter of 10 mm.

for the spreading of cells on it. This phenomenon was not observed on 15% PEGDA 3400 hydrogels (without mLIF) as can be seen in figure 7.5B. This again indicates that the micro-environmental cue of stiffness possibly leads to differentiation of mESCs in 20% PEGDA 3400 but not in 15% PEGDA 3400.

Energy Dispersive X-ray Fluorescence (ED-XRF) was also done on these hydrogel constructs. ED-XRF gives a finger print of the elements present

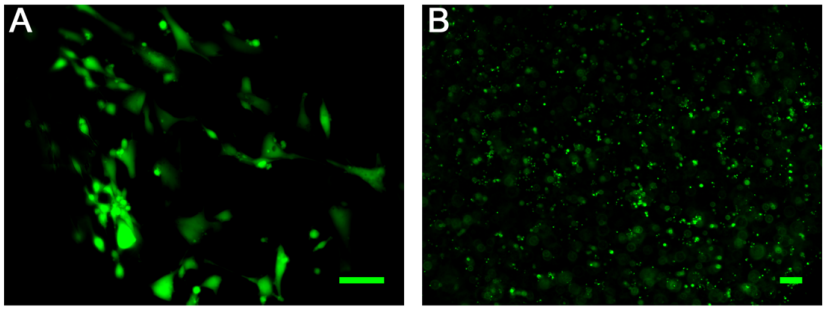


Figure 7.5: mESCs encapsulted in (A) 20% PEGDA 3400 (B) 15% PEGDA 3400 hydrogels on day 14 incubated in media without mLIF. Calcein AM stain clearly shows mESCs spread on 20% PEGDA 3400 hydrogels but not on 15% PEGDA 3400 hydrogels. Scale bar = 100 $\mu$m

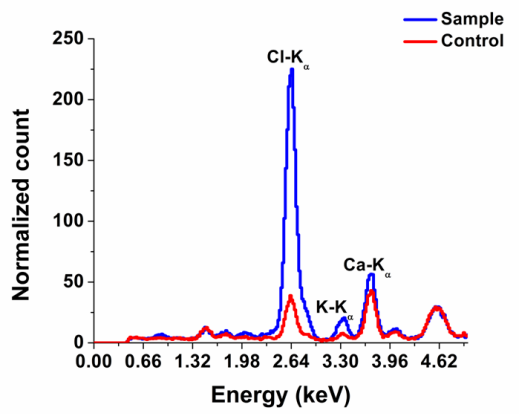


Figure 7.6: ED-XRF data showing higher level of Cl-K$_\alpha$, K-K$_\alpha$, and Ca-K$_\alpha$ peaks in 20 % PEGDA 3400 hydrogels with mESCs.

in the system. ED-XRF has major applications in geology, environmental remediation, and recycling. It was therefore used to see the presence of the different elements in the hydrogels. An added advantage of ED-XRF is that organic elements cannot be detected by conventional silicon based detectors as the fluorescence photons from these elements are too low in energy. So the results will not be overwhelmed by the organic nature of the hydrogels but will only detect peaks from higher elements. Figure 7.6 shows the ED-XRF data from 20% PEGDA 3400 hydrogel on day 14 with and without mESCs. It can be clearly seen that the hydrogel disks with mESCs show higher Cl-K$_\alpha$, K-K$_\alpha$, and Ca-K$_\alpha$ peaks compared to the control. It is known that the osteogenic tissue is made of 1/3 organic and 2/3 inorganic matter by weight. This inorganinc matter consists of 85% hydroxyapatite 10% calcium carbonate, minerals like fluoride, potassium, and magnesium [275]. Higher levels of peaks for calcium, potassium and chlorine indicate the presence of these inorganic matters. This is again an indication of differentiation of mESCs towards osteogenic lineage.

Much more in-depth studies like DNA micro-arrays, western-blotting, and immunofluorescent studies are required to confirm these findings. However, these preliminary studies give an indication of possible mESC differentiation to osteogenic lineage because of changes in the elasticity of the hydrogels.

## 7.5 Conclusion

In this study, mESCs and mEBs were encapsulated in different stiffness PEGDA 3400 hydrogels with and without mLIF. For the hydrogels encapsulated with mLIF, mEBs showed much higher viability then individual mESCs in 20% PEGDA 3400. Removal of mESCs possibly lead to mESC differentiation based on the stiffness of the hydrogels which was confirmed with Alizarin red stain, mESC spreading on unmodified PEGDA hydrogels, and ED-XRF data. Although, very preliminary, these studies showed that microenvironmental cues play a huge role in controlling the fate of mammalian cells. Future studies need to be done in order to fully understand this phenomenon. In all the differentiation studies, no induction media was used. Therefore, in future studies the hydrogels can be incubated in specific differentiation media to increase both the rate and efficiency of differentiation.

# CHAPTER 8

# FINAL REMARKS AND FUTURE WORK

## 8.1 Final Remarks

There is a big demand for organ replacement with the aging population of the world. Currently, the transplantation of vital organs like kidney, heart, liver, and lung is the only treatment for their end-stage failure. However, there is a huge shortage of viable, functional organs and on average 18 people die waiting for an organ transplant [1]. Various new technologies like stem cell based tissue engineering, xenotransplantation, and organogenesis all have the potential to replace or augment organ function. In addition to regenerative medicine, tissue engineered organs could also serve as an alternative to traditional drug discovery/screening [4]. Doing efficacy testing of drugs on physiologically relevant tissues could also significantly aid in reducing the timeline for drug discovery. These artificially engineered would serve as a complementary and not competing technology and it would have the potential to revolutionize both the fields of regenerative medicine and drug discovery. However, *in vivo* tissue receives a myriad of bio-physical and bio-chemical cues from its cellular micro-environment which are difficult to mimic for *in vitro* tissues. Furthermore, it is getting clear that these micro-environmental cues are responsible for controlling the fate of the cells. Therefore, a novel platform is needed which can mimic these complex *in vivo* cues simultaneously in the same scaffold so that it is possible to control the fate decision of cells *in vitro*. The aim of this dissertation was developing a platform which can be used to control the fate decision of mammalian cells, including ESCs.

Chapter 3 showed that by modulating the stiffness of the substrate, it is possible to control the cytoskeletal and physiological properties of the tissues. ECCMs showed the highest beating rate on the substrate which matched the

stiffness of cardiac tissue. Furthermore, highly aligned sarcomeric striations were observed on the substrate which had elasticity comparable to the native *in vivo* cardiac tissue. Chapter 4 used soft-lithography to constraint the growth of C2C12 cells in well-defined geometrical shapes. It was found that hybrid structures showed the highest myogenic potential for the C2C12 skeletal myoblasts. Thus by mimicking the *in vivo* morphology of the native tissue it was possible to achieve best degree of myotube formation which is a pre-cursor to muscle development. Later, the myogenic potential of C2C12 cells on graphene was also investigated in chapter 5. Being organic in nature, graphene was easily able to mimic the physical and chemical properties of the native tissue and therefore showed a high degree of myotube formation on its surface. All these previous studies were 2D cultures of cells. However, an engineered tissue which is capable of mimicking the native tissue should ideally be a 3D tissue. Therefore, the cues of stiffness and geometry were combined together in chapter 6 by merging SL and DEP in 3D. These two technologies were used to mimic the micro-scale architecture of the native 3D tissue in hydrogels which also matched the stiffness of *in vivo* tissues. Single cell patterning of mESCs over a large area was achieved by using this novel platform while maintaining its viability. In addition, embryoid bodies, pre-cursor to differentiation of mESCs were also patterned by using this technology and showed good viability. Finally, chapter 7 showed some preliminary results on the differentiation of mESCs towards the osteogenic lineage based on the cues of the micro-environment. This work showed that by controlling the properties of the micro-environment it was possible to control the fate decision of a variety of cell types like ECCMs, C2C12 cells and mESCs. Much work is still needed to fabricate a 3D functioning engineered tissue for drug screening/discovery or for *de novo* organ development. However, this dissertation developed a novel platform by independently investigating the micro-environmental cues of stiffness, geometry, and topography in 2D and them combining them in 3D. This platform could thus be used to control the fate of cells and open new doors in stem cell biology, drug discovery/screening, tissue engineering, and regenerative medicine.

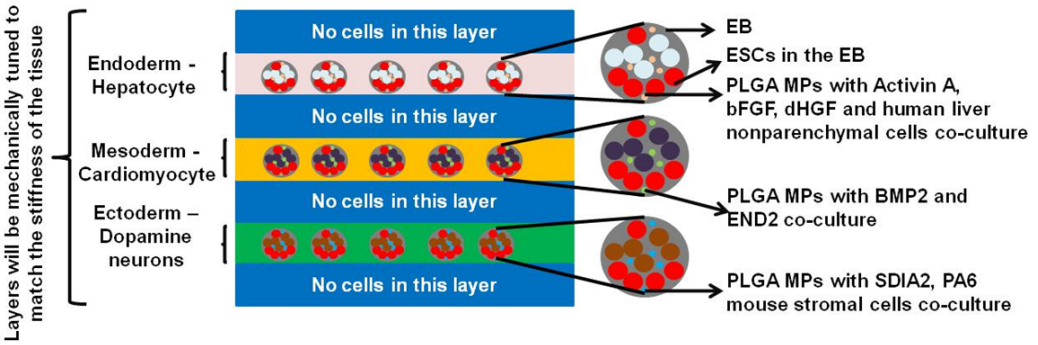


Figure 8.1: Heterogenic differentiation of ESCs into cells of three primary germ layers by a combination of co-culture and soluble factors.

## 8.2 Future work

In order to achieve a construct which can be used for screening of drugs, DEP can be combined with SL in a mechanically tuned, biodegrading 3D hydrogel with encapsulated ESCs and EBs. This hydrogel would consist of Oxidized Methacrylic Alginate (OMA) linked with cell adhesion peptides arginine-glycine-aspartate (RGD) and poly(ethylene glycol) methyl ether methacrylate (PEGMA). The $M_w$ of the hydrogel can be altered to modulate the stiffness of the hydrogel. Many soluble factors like basic fibroblast growth factor (bFGF), transforming growth factor $\beta 1$ (TGF-$\beta 1$), activin-A, bone morphogenic protein 4 (BMP-4), hepatocyte growth factor (HGF), epidermal growth factor (EGF), $\beta$ nerve growth factor ($\beta$NGF), and retinoic acid in different concentrations are known to direct the differentiation of stem cells into different lineages [276]. EBs with poly(lactic-co-glycolic acid) (PLGA)/gelatin microparticles (MPs) loaded with different soluble factors can be encapsulated in mechanically tuned hydrogels for a highly organized, homogenous and optimized differentiation of stem cells to different lineages. Figure 8.1 shows the envisioned hydrogel construct for differentiating the ESCs to ectoderm (dopamine neurons), mesoderm (cardiomyocyte) and endoderm (hepatocyte). The soluble factors that could be used for differentiation are 1) Ectoderm - (dopamine neurons - stromal-derived inducing activity (SDIA2) with PA6 stromal cell co-culture), Mesoderm - (Cardiomyocyte - BMP2 and END2 cells co-culture), 3) Endoderm - (Hepatocyte like cells - Activin A, bFGF, dHGF with liver nonparenchymal cells co-culture) [17].

Co-culture studies are useful since the factors released from one cell can act

on the other cell type to influence its function/phenotype. It has already been demonstrated that hESCs when cultured with visceral mouse endoderm cells (END2) leads to upto 25% differentiation into cardiomyocytes while without the END2 cells less than 1% cells are differentiated into cardiomyocytes [277, 267]. mESCs co-cultured with alginate bead-encapsulated notochords from chicken embryos in the presence of retinoic acid differentiated to motor neurons [278]. mESCs co-cultured with human liver parenchymal cells in the presence of Activin A, bFGF, dHGF differentiated to liver cells [268]. mESCs co-cultured with PA6 mouse stromal cells differentiated to dopaminergic neurons [279]. Similar studies could be performed in 3D with co-culturing hESCs with different types of cells to differentiate the cells into the three germ lineages. By controlling the positioning of the cells *via* DEP, the proposed platform will be better at controlling the spatio-temporal release of soluble factors. This added to the fact that the cells will be patterned in a 3D mechanically tuned scaffold could truly enhance the differentiation of ESCs. It would be possible to achieve a very homogenous population of a single cell-type which could then be used for drug screening or for development of a 3D tissue.

# REFERENCES


[1] "Donate the gift of life," 2012, U.S. Department of Health and Human Services. [Online]. Available: http://www.organdonor.gov/about/data.html

[2] S. A. Hunt and F. Haddad, "The changing face of heart transplantation," *Journal of the American College of Cardiology*, vol. 52, no. 8, pp. 587–598, 2008.

[3] P. W. Zandstra and A. Nagy, "Stem cell bioengineering," *Annual Review of Biomedical Engineering*, vol. 3, no. 1, pp. 275–305, 2001.

[4] F. S. Collins, "Reengineering translational science: The time is right," *Science Translational Medicine*, vol. 3, no. 90, p. 90cm17, 2011.

[5] B. M. Bolten and T. DeGregorio, "Trends in development cycles," *Nat Rev Drug Discov*, vol. 1, no. 5, pp. 335–336, 2002, 10.1038/nrd805.

[6] H. Geerts, "Of mice and men: Bridging the translational disconnect in cns drug discovery," *CNS Drugs*, vol. 23, no. 11, pp. 915–926 10.2165/11 310 890–000 000 000–00 000, 2009.

[7] S. M. Paul, D. S. Mytelka, C. T. Dunwiddie, C. C. Persinger, B. H. Munos, S. R. Lindborg, and A. L. Schacht, "How to improve r&d productivity: the pharmaceutical industry's grand challenge," *Nat Rev Drug Discov*, vol. 9, no. 3, pp. 203–214, 2010, 10.1038/nrd3078.

[8] B. Munos, "Lessons from 60 years of pharmaceutical innovation," *Nat Rev Drug Discov*, vol. 8, no. 12, pp. 959–968, 2009, 10.1038/nrd2961.

[9] M. de Jong and T. Maina, "Of mice and humans: Are they the same?implications in cancer translational research," *Journal of Nuclear Medicine*, vol. 51, no. 4, pp. 501–504, 2010.

[10] J. A. Thomson, J. Itskovitz-Eldor, S. S. Shapiro, M. A. Waknitz, J. J. Swiergiel, V. S. Marshall, and J. M. Jones, "Embryonic stem cell lines derived from human blastocysts," *Science*, vol. 282, no. 5391, pp. 1145–1147, 1998.

[11] D. E. Cohen and D. Melton, "Turning straw into gold: directing cell fate for regenerative medicine," *Nat Rev Genet*, vol. 12, no. 4, pp. 243–252, 2011, 10.1038/nrg2938.

[12] R. Young, "Control of the embryonic stem cell state," *Cell*, vol. 144, no. 6, pp. 940–954, 2011.

[13] D. Tosh and J. M. W. Slack, "How cells change their phenotype," *Nat Rev Mol Cell Biol*, vol. 3, no. 3, pp. 187–194, 2002, 10.1038/nrm761.

[14] A. D. Ebert and C. N. Svendsen, "Human stem cells and drug screening: opportunities and challenges," *Nat Rev Drug Discov*, vol. 9, no. 5, pp. 367–372, 2010, 10.1038/nrd3000.

[15] S. Levenberg, N. F. Huang, E. Lavik, A. B. Rogers, J. Itskovitz-Eldor, and R. Langer, "Differentiation of human embryonic stem cells on three-dimensional polymer scaffolds," *Proceedings of the National Academy of Sciences*, vol. 100, no. 22, pp. 12 741–12 746, 2003.

[16] L. H. Lee, R. Peerani, M. Ungrin, C. Joshi, E. Kumacheva, and P. Zandstra, "Micropatterning of human embryonic stem cells dissects the mesoderm and endoderm lineages," *Stem Cell Research*, vol. 2, no. 2, pp. 155–162, 2009.

[17] I. Klimanskaya, N. Rosenthal, and R. Lanza, "Derive and conquer: sourcing and differentiating stem cells for therapeutic applications," *Nat Rev Drug Discov*, vol. 7, no. 2, pp. 131–142, 2008, 10.1038/nrd2403.

[18] R. Peerani, K. Onishi, A. Mahdavi, E. Kumacheva, and P. W. Zandstra, "Manipulation of signaling thresholds in engineered stem cell niches? identifies design criteria for pluripotent stem cell screens," *PLoS ONE*, vol. 4, no. 7, p. e6438, 2009.

[19] R. Peerani, C. Bauwens, E. Kumacheva, and P. W. Zandstra, *Patterning Mouse and Human Embryonic Stem Cells Using Micro-contact Printing*, ser. Methods in Molecular Biology. Humana Press, 2009, vol. 482, pp. 21–33.

[20] A. J. Keung, K. E. Healy, S. Kumar, and D. V. Schaffer, "Biophysics and dynamics of natural and engineered stem cell microenvironments," *Wiley Interdisciplinary Reviews: Systems Biology and Medicine*, vol. 2, no. 1, pp. 49–64, 2010.

[21] A. J. Keung, S. Kumar, and D. V. Schaffer, "Presentation counts: Microenvironmental regulation of stem cells by biophysical and material cues," *Annual Review of Cell and Developmental Biology*, vol. 26, no. 1, pp. 533–556, 2010.

[22] R. L. Vacanti and J. P., "Tissue engineering," *Science*, vol. 260, pp. 920–926, 1993.

[23] F. Berthiaume, T. J. Maguire, and M. L. Yarmush, "Tissue engineering and regenerative medicine: History, progress, and challenges," *Annual Review of Chemical and Biomolecular Engineering*, vol. 2, no. 1, pp. 403–430, 2011.

[24] K. Takahashi, K. Tanabe, M. Ohnuki, M. Narita, T. Ichisaka, K. Tomoda, and S. Yamanaka, "Induction of pluripotent stem cells from adult human fibroblasts by defined factors," vol. 131, no. 5, pp. 861–872, 2007.

[25] A. J. Firestone and J. K. Chen, "Controlling destiny through chemistry: Small-molecule regulators of cell fate," *ACS Chemical Biology*, vol. 5, no. 1, pp. 15–34, 2009.

[26] P. Zorlutuna, N. Annabi, G. Camci-Unal, M. Nikkhah, J. M. Cha, J. W. Nichol, A. Manbachi, H. Bae, S. Chen, and A. Khademhosseini, "Microfabricated biomaterials for engineering 3d tissues," *Advanced Materials*, vol. 24, no. 14, pp. 1782–1804, 2012.

[27] Y. Haraguchi, T. Shimizu, M. Yamato, and T. Okano, "Concise review: Cell therapy and tissue engineering for cardiovascular disease," *Stem Cells Translational Medicine*, vol. 1, no. 2, pp. 136–141, 2012.

[28] H. C. Ott, T. S. Matthiesen, S.-K. Goh, L. D. Black, S. M. Kren, T. I. Netoff, and D. A. Taylor, "Perfusion-decellularized matrix: using nature's platform to engineer a bioartificial heart," *Nat Med*, vol. 14, no. 2, pp. 213–221, 2008, 10.1038/nm1684.

[29] T. H. Petersen, E. A. Calle, L. Zhao, E. J. Lee, L. Gui, M. B. Raredon, K. Gavrilov, T. Yi, Z. W. Zhuang, C. Breuer, E. Herzog, and L. E. Niklason, "Tissue-engineered lungs for in vivo implantation," *Science*, vol. 329, no. 5991, pp. 538–541, 2010.

[30] C. G. Williams, T. K. Kim, A. Taboas, A. Malik, P. Manson, and J. Elisseeff, "In vitro chondrogenesis of bone marrow-derived mesenchymal stem cells in a photopolymerizing hydrogel," *Tissue Engineering*, vol. 9, no. 4, pp. 679–688, 2003.

[31] M. M. Stevens, "Biomaterials for bone tissue engineering," *Materials Today*, vol. 11, no. 5, pp. 18–25, 2008.

[32] S. MacNeil, "Biomaterials for tissue engineering of skin," *Materials Today*, vol. 11, no. 5, pp. 26–35, 2008.

[33] "Burn incidence and treatment in the united states: 2011 fact sheet," 2011, American Burn Association. [Online]. Available: www.ameriburn.org/resources/factsheet.php

[34] R. V. Shevchenko, S. L. James, and S. E. James, "A review of tissue-engineered skin bioconstructs available for skin reconstruction," *Journal of the Royal Society Interface*, vol. 7, no. 43, pp. 229–258, 2010.

[35] W. Lee, J. C. Debasitis, V. K. Lee, J.-H. Lee, K. Fischer, K. Edminster, J.-K. Park, and S.-S. Yoo, "Multi-layered culture of human skin fibroblasts and keratinocytes through three-dimensional freeform fabrication," *Biomaterials*, vol. 30, no. 8, pp. 1587–1595, 2009.

[36] T. Eschenhagen, A. Eder, I. Vollert, and A. Hansen, "Physiological aspects of cardiac tissue engineering," *American Journal of Physiology - Heart and Circulatory Physiology*, vol. 303, no. 2, pp. H133–H143, 2012.

[37] "Report finds lung disease death rates increasing while cancer, heart disease and stroke death rates are decreasing," June 2008, American Lung Association. [Online]. Available: http://www.lung.org/press-room/press-releases/death-rates-decreasing.html

[38] A. G. R. M. A. M. T. P. M. Gordana Vunjak-Novakovic, Nina Tandon and M. Radisic., "Challenges in cardiac tissue engineering," *Tissue Engineering Part B: Reviews.*, vol. 16, no. 2, pp. 169–187, 2010.

[39] P. Anversa and J. Kajstura, "Ventricular myocytes are not terminally differentiated in the adult mammalian heart," *Circulation Research*, vol. 83, no. 1, pp. 1–14, 1998.

[40] A. Sachinidis, B. K. Fleischmann, E. Kolossov, M. Wartenberg, H. Sauer, and J. Hescheler, "Cardiac specific differentiation of mouse embryonic stem cells," *Cardiovascular Research*, vol. 58, no. 2, pp. 278–291, 2003.

[41] S. S. Y. Wong and H. S. Bernstein, "Cardiac regeneration using human embryonic stem cells: producing cells for future therapy," *Regenerative Medicine*, vol. 5, no. 5, pp. 763–775, 2010.

[42] D. Jing, A. Parikh, and E. S. Tzanakakis, "Cardiac cell generation from encapsulated embryonic stem cells in static and scalable culture systems," *Cell Transplantation*, vol. 19, no. 11, pp. 1397–1412, 2010.

[43] C. Mummery, D. Ward, C. E. Van Den Brink, S. D. Bird, P. A. Doevendans, T. Opthof, A. B. De La Riviere, L. Tertoolen, M. Van Der Heyden, and M. Pera, "Cardiomyocyte differentiation of mouse and human embryonic stem cells*," *Journal of Anatomy*, vol. 200, no. 3, pp. 233–242, 2002.

[44] X. L. I. R. G. B. D. Josowitz, Rebecca; Carvajal-Vergara, "Induced pluripotent stem cell-derived cardiomyocytes as models for genetic cardiovascular disorders," *Current Opinion in Cardiology*, vol. 26, pp. 223–229, 2011.

[45] P. Rana, B. Anson, S. Engle, and Y. Will, "Characterization of human-induced pluripotent stem cellderived cardiomyocytes: Bioenergetics and utilization in safety screening," *Toxicological Sciences*, vol. 130, no. 1, pp. 117–131, 2012.

[46] A. J. Engler, C. Carag-Krieger, C. P. Johnson, M. Raab, H.-Y. Tang, D. W. Speicher, J. W. Sanger, J. M. Sanger, and D. E. Discher, "Embryonic cardiomyocytes beat best on a matrix with heart-like elasticity: scar-like rigidity inhibits beating," *Journal of Cell Science*, vol. 121, no. 22, pp. 3794–3802, 2008.

[47] R. C. S. J. W. C. N. L. J. C. C. H. Craig K. Griffith, Cheryl Miller and S. C. George., "Diffusion limits of an in vitro thick prevascularized tissue," *Tissue Eng.*, vol. 11, pp. 257–266, 2005.

[48] B. P. Chan and K. W. Leong, "Scaffolding in tissue engineering: general approaches and tissue-specific considerations," *European Spine Journal*, vol. 17, no. 4, pp. 467–479, 2008.

[49] T. Shimizu, M. Yamato, Y. Isoi, T. Akutsu, T. Setomaru, K. Abe, A. Kikuchi, M. Umezu, and T. Okano, "Fabrication of pulsatile cardiac tissue grafts using a novel 3-dimensional cell sheet manipulation technique and temperature-responsive cell culture surfaces," *Circulation Research*, vol. 90, no. 3, pp. e40–e48, 2002.

[50] J. H. Jeong, V. Chan, C. Cha, P. Zorlutuna, C. Dyck, K. J. Hsia, R. Bashir, and H. Kong, "Living microvascular stamp for patterning of functional neovessels; orchestrated control of matrix property and geometry," *Advanced Materials*, vol. 24, no. 1, pp. 58–63, 2012.

[51] W. Bian and N. Bursac, "Engineered skeletal muscle tissue networks with controllable architecture," *Biomaterials*, vol. 30, no. 7, pp. 1401–1412, 2009.

[52] W. Bian, B. Liau, N. Badie, and N. Bursac, "Mesoscopic hydrogel molding to control the 3d geometry of bioartificial muscle tissues," *Nat. Protocols*, vol. 4, no. 10, pp. 1522–1534, 2009, 10.1038/nprot.2009.155.

[53] Y.-j. Lou and X.-g. Liang, "Embryonic stem cell application in drug discovery," *Acta Pharmacol Sin*, vol. 32, no. 2, pp. 152–159, 2011.

[54] S. Chen, M. Borowiak, J. L. Fox, R. Maehr, K. Osafune, L. Davidow, K. Lam, L. F. Peng, S. L. Schreiber, L. L. Rubin, and D. Melton, "A small molecule that directs differentiation of human escs into the pancreatic lineage," *Nat Chem Biol*, vol. 5, no. 4, pp. 258–265, 2009, 10.1038/nchembio.154.

[55] Y. Xu, Y. Shi, and S. Ding, "A chemical approach to stem-cell biology and regenerative medicine," *Nature*, vol. 453, no. 7193, pp. 338–344, 2008, 10.1038/nature07042.

[56] J. McNeish, M. Roach, J. Hambor, R. J. Mather, L. Weibley, J. Lazzaro, J. Gazard, J. Schwarz, R. Volkmann, D. Machacek, S. Stice, L. Zawadzke, C. O'Donnell, and R. Hurst, "High-throughput screening in embryonic stem cell-derived neurons identifies potentiators of -amino-3-hydroxyl-5-methyl-4-isoxazolepropionate-type glutamate receptors," *Journal of Biological Chemistry*, vol. 285, no. 22, pp. 17 209–17 217, 2010.

[57] I. Barbaric, P. J. Gokhale, M. Jones, A. Glen, D. Baker, and P. W. Andrews, "Novel regulators of stem cell fates identified by a multivariate phenotype screen of small compounds on human embryonic stem cell colonies," *Stem Cell Research*, vol. 5, no. 2, pp. 104–119, 2010.

[58] S. C. Desbordes, D. G. Placantonakis, A. Ciro, N. D. Socci, G. Lee, H. Djaballah, and L. Studer, "High-throughput screening assay for the identification of compounds regulating self-renewal and differentiation in human embryonic stem cells," *Cell stem cell*, vol. 2, no. 6, pp. 602–612, 2008.

[59] F. Zanella, J. B. Lorens, and W. Link, "High content screening: seeing is believing," *Trends in biotechnology*, vol. 28, no. 5, pp. 237–245, 2010.

[60] D. A. M. van Dartel, J. L. A. Pennings, L. J. J. de la Fonteyne, M. H. van Herwijnen, J. H. van Delft, F. J. van Schooten, and A. H. Piersma, "Monitoring developmental toxicity in the embryonic stem cell test using differential gene expression of differentiation-related genes," *Toxicological Sciences*, vol. 116, no. 1, pp. 130–139, 2010.

[61] D. A. M. van Dartel, J. L. A. Pennings, F. J. van Schooten, and A. H. Piersma, "Transcriptomics-based identification of developmental toxicants through their interference with cardiomyocyte differentiation of embryonic stem cells," *Toxicology and Applied Pharmacology*, vol. 243, no. 3, pp. 420–428, 2010.

[62] D. E. Jaalouk and J. Lammerding, "Mechanotransduction gone awry," *Nat Rev Mol Cell Biol*, vol. 10, no. 1, pp. 63–73, 2009, 10.1038/nrm2597.

[63] S. P. Barry, S. M. Davidson, and P. A. Townsend, "Molecular regulation of cardiac hypertrophy," *The International Journal of Biochemistry & Cell Biology*, vol. 40, no. 10, pp. 2023–2039, 2008.

[64] J. D. Humphries, P. Wang, C. Streuli, B. Geiger, M. J. Humphries, and C. Ballestrem, "Vinculin controls focal adhesion formation by direct interactions with talin and actin," *The Journal of Cell Biology*, vol. 179, no. 5, pp. 1043–1057, 2007.

[65] D. E. Ingber, "Cellular mechanotransduction: putting all the pieces together again," *The FASEB Journal*, vol. 20, no. 7, pp. 811–827, 2006.

[66] A. E. P. . M. A. Horton, "An historical perspective on cell mechanics," *Pfluegers Arch European Journal of Physiology*, vol. 456, pp. 3–12, 2008.

[67] S.-Y. Tee, A. R. Bausch, and P. A. Janmey, "The mechanical cell," *Current biology : CB*, vol. 19, no. 17, pp. R745–R748, 2009.

[68] A. J. Engler, S. Sen, H. L. Sweeney, and D. E. Discher, "Matrix elasticity directs stem cell lineage specification," *Cell*, vol. 126, no. 4, pp. 677–689, 2006.

[69] D. E. Discher, P. Janmey, and Y.-l. Wang, "Tissue cells feel and respond to the stiffness of their substrate," *Science*, vol. 310, no. 5751, pp. 1139–1143, 2005.

[70] Y. Cai and M. P. Sheetz, "Force propagation across cells: mechanical coherence of dynamic cytoskeletons," *Current Opinion in Cell Biology*, vol. 21, no. 1, pp. 47–50, 2009.

[71] P. C. Georges and P. A. Janmey, "Cell type-specific response to growth on soft materials," *Journal of Applied Physiology*, vol. 98, no. 4, pp. 1547–1553, 2005.

[72] D. S. Albert K. Harris, Patricia Wild, "Silicone rubber substrata: A new wrinkle in the study of cell locomotion," *Science*, vol. 208, pp. 177–179, 1980.

[73] P. W. Albert K. Harris, David Stopak, "Fibroblast traction as a mechanism for collagen morphogenesis." *Nature*, vol. 290, pp. 249–251, 1981.

[74] R. J. Pelham and Y.-l. Wang, "Cell locomotion and focal adhesions are regulated by substrateflexibility," *Proceedings of the National Academy of Sciences*, vol. 94, no. 25, pp. 13 661–13 665, 1997.

[75] Y.-L. Wang and R. J. Pelham Jr, *Preparation of a flexible, porous polyacrylamide substrate for mechanical studies of cultured cells.* Academic Press, 1998, vol. Volume 298, pp. 489–496.

[76] A. Gefen and S. S. Margulies, "Are in vivo and in situ brain tissues mechanically similar?" *Journal of Biomechanics*, vol. 37, no. 9, pp. 1339–1352, 2004.

[77] S. Diridollou, F. Patat, F. Gens, L. Vaillant, D. Black, J. M. Lagarde, Y. Gall, and M. Berson, "In vivo model of the mechanical properties of the human skin under suction," *Skin Research and Technology*, vol. 6, no. 4, pp. 214–221, 2000.

[78] A. J. Engler, M. A. Griffin, S. Sen, C. G. Bnnemann, H. L. Sweeney, and D. E. Discher, "Myotubes differentiate optimally on substrates with tissue-like stiffness: pathological implications for soft or stiff microenvironments," *The Journal of Cell Biology*, vol. 166, no. 6, pp. 877–887, 2004.

[79] G. E. L. V. P. S. K. M. C. X. R. C. S. M. Evans ND, Minelli C, "Substrate stiffness affects early differentiation events in embryonic stem cells." *European Cells and Materials*, vol. 18, pp. 1–14, 2009.

[80] T. Yeung, P. C. Georges, L. A. Flanagan, B. Marg, M. Ortiz, M. Funaki, N. Zahir, W. Ming, V. Weaver, and P. A. Janmey, "Effects of substrate stiffness on cell morphology, cytoskeletal structure, and adhesion," *Cell Motility and the Cytoskeleton*, vol. 60, no. 1, pp. 24–34, 2005.

[81] J. G. Jacot, A. D. McCulloch, and J. H. Omens, "Substrate stiffness affects the functional maturation of neonatal rat ventricular myocytes," *Biophysical Journal*, vol. 95, no. 7, pp. 3479–3487, 2008.

[82] B. Bhana, R. K. Iyer, W. L. K. Chen, R. Zhao, K. L. Sider, M. Likhitpanichkul, C. A. Simmons, and M. Radisic, "Influence of substrate stiffness on the phenotype of heart cells," *Biotechnology and Bioengineering*, vol. 105, no. 6, pp. 1148–1160, 2010.

[83] C.-M. Lo, H.-B. Wang, M. Dembo, and Y.-l. Wang, "Cell movement is guided by the rigidity of the substrate," *Biophysical Journal*, vol. 79, no. 1, pp. 144–152, 2000.

[84] E. M. Horn, M. Beaumont, X. Z. Shu, A. Harvey, G. D. Prestwich, K. M. Horn, A. R. Gibson, M. C. Preul, and A. Panitch, "Influence of cross-linked hyaluronic acid hydrogels on neurite outgrowth and recovery from spinal cord injury," *Journal of Neurosurgery: Spine*, vol. 6, no. 2, pp. 133–140, 2007.

[85] E. Hadjipanayi, V. Mudera, and R. A. Brown, "Close dependence of fibroblast proliferation on collagen scaffold matrix stiffness," *Journal of Tissue Engineering and Regenerative Medicine*, vol. 3, no. 2, pp. 77–84, 2009.

[86] J. Fu, Y.-K. Wang, M. T. Yang, R. A. Desai, X. Yu, Z. Liu, and C. S. Chen, "Mechanical regulation of cell function with geometrically modulated elastomeric substrates," *Nat Meth*, vol. 7, no. 9, pp. 733–736, 2010, 10.1038/nmeth.1487.

[87] V. Chan, P. Zorlutuna, J. H. Jeong, H. Kong, and R. Bashir, "Three-dimensional photopatterning of hydrogels using stereolithography for long-term cell encapsulation," *Lab on a Chip*, vol. 10, no. 16, pp. 2062–2070, 2010.

[88] S. Kidoaki and T. Matsuda, "Microelastic gradient gelatinous gels to induce cellular mechanotaxis," *Journal of Biotechnology*, vol. 133, no. 2, pp. 225–230, 2008.

[89] R. D. G. P. T. G. S. I. M. D. S. S. B. A. A. L. . B. G. Balaban NQ, Schwarz US, "Force and focal adhesion assembly: a close relationship studied using elastic micropatterned substrates," *Nature Cell Biology*, vol. 3, pp. 466–472, 2001.

[90] A. M. Ross, Z. Jiang, M. Bastmeyer, and J. Lahann, "Physical aspects of cell culture substrates: Topography, roughness, and elasticity," *Small*, pp. n/a–n/a, 2011.

[91] B. T. Houseman and M. Mrksich, "The microenvironment of immobilized arg-gly-asp peptides is an important determinant of cell adhesion," *Biomaterials*, vol. 22, no. 9, pp. 943–955, 2001.

[92] B. G. Keselowsky, D. M. Collard, and A. J. Garca, "Integrin binding specificity regulates biomaterial surface chemistry effects on cell differentiation," *Proceedings of the National Academy of Sciences*, vol. 102, no. 17, pp. 5953–5957, 2005.

[93] G. Kumar, C. K. Tison, K. Chatterjee, P. S. Pine, J. H. McDaniel, M. L. Salit, M. F. Young, and C. G. Simon Jr, "The determination of stem cell fate by 3d scaffold structures through the control of cell shape," *Biomaterials*, vol. 32, no. 35, pp. 9188–9196, 2011.

[94] W. Marshall, "Origins of cellular geometry," *BMC Biology*, vol. 9, no. 1, p. 57, 2011.

[95] V. M. Lauschke, C. D. Tsiairis, P. Francois, and A. Aulehla, "Scaling of embryonic patterning based on phase-gradient encoding," *Nature*, vol. advance online publication, 2012, 10.1038/nature11804.

[96] N. Barkai and B.-Z. Shilo, "Developmental biology: Segmentation within scale," *Nature*, vol. advance online publication, 2012, 10.1038/nature11849.

[97] M. T. Niessen, S. Iden, and C. M. Niessen, "The in vivo function of mammalian cell and tissue polarity regulators how to shape and maintain the epidermal barrier," *Journal of Cell Science*, vol. 125, no. 15, pp. 3501–3510, 2012.

[98] C. M. Bidan, K. P. Kommareddy, M. Rumpler, P. Kollmannsberger, P. Fratzl, and J. W. C. Dunlop, "Geometry as a factor for tissue growth: Towards shape optimization of tissue engineering scaffolds," *Advanced Healthcare Materials*, pp. n/a–n/a, 2012.

[99] D. E. Ingber and J. Folkman, "Mechanochemical switching between growth and differentiation during fibroblast growth factor-stimulated angiogenesis in vitro: role of extracellular matrix," *The Journal of Cell Biology*, vol. 109, no. 1, pp. 317–330, 1989.

[100] F. Re, A. Zanetti, M. Sironi, N. Polentarutti, L. Lanfrancone, E. Dejana, and F. Colotta, "Inhibition of anchorage-dependent cell spreading triggers apoptosis in cultured human endothelial cells," *The Journal of Cell Biology*, vol. 127, no. 2, pp. 537–546, 1994.

[101] A. Kumar and G. M. Whitesides, "Features of gold having micrometer to centimeter dimensions can be formed through a combination of stamping with an elastomeric stamp and an alkanethiol "ink" followed by chemical etching," *Applied Physics Letters*, vol. 63, no. 14, pp. 2002–2004, 1993.

[102] Y. Xia and G. M. Whitesides, "Soft lithography," *Angewandte Chemie International Edition*, vol. 37, no. 5, pp. 550–575, 1998.

[103] C. S. Chen, M. Mrksich, S. Huang, G. M. Whitesides, and D. E. Ingber, "Geometric control of cell life and death," *Science*, vol. 276, no. 5317, pp. 1425–1428, 1997.

[104] R. McBeath, D. M. Pirone, C. M. Nelson, K. Bhadriraju, and C. S. Chen, "Cell shape, cytoskeletal tension, and rhoa regulate stem cell lineage commitment," *Developmental Cell*, vol. 6, no. 4, pp. 483–495, 2004.

[105] N. D. Gallant, K. E. Michael, and A. J. Garcia, "Cell adhesion strengthening: Contributions of adhesive area, integrin binding, and focal adhesion assembly," *Mol. Biol. Cell*, vol. 16, no. 9, pp. 4329–4340, 2005.

[106] C. M. Nelson, R. P. Jean, J. L. Tan, W. F. Liu, N. J. Sniadecki, A. A. Spector, and C. S. Chen, "Emergent patterns of growth controlled by multicellular form and mechanics," *Proceedings of the National Academy of Sciences of the United States of America*, vol. 102, no. 33, pp. 11 594–11 599, 2005.

[107] S. A. Ruiz and C. S. Chen, "Emergence of patterned stem cell differentiation within multicellular structures," *Stem Cells*, vol. 26, no. 11, pp. 2921–2927, 2008.

[108] K. A. Kilian, B. Bugarija, B. T. Lahn, and M. Mrksich, "Geometric cues for directing the differentiation of mesenchymal stem cells," *Proceedings of the National Academy of Sciences*, 2010.

[109] Y.-S. Hwang, B. G. Chung, D. Ortmann, N. Hattori, H.-C. Moeller, and A. Khademhosseini, "Microwell-mediated control of embryoid body size regulates embryonic stem cell fate via differential expression of wnt5a and wnt11," *Proceedings of the National Academy of Sciences*, vol. 106, no. 40, pp. 16 978–16 983, 2009.

[110] K. Kushiro, S. Chang, and A. R. Asthagiri, "Reprogramming directional cell motility by tuning micropattern features and cellular signals," *Advanced Materials*, pp. n/a–n/a, 2010.

[111] G. Mahmud, C. J. Campbell, K. J. M. Bishop, Y. A. Komarova, O. Chaga, S. Soh, S. Huda, K. Kandere-Grzybowska, and B. A. Grzybowski, "Directing cell motions on micropatterned ratchets," *Nat Phys*, vol. 5, no. 8, pp. 606–612, 2009, 10.1038/nphys1306.

[112] E. Cimetta, S. Pizzato, S. Bollini, E. Serena, P. De Coppi, and N. Elvassore, "Production of arrays of cardiac and skeletal muscle myofibers by micropatterning techniques on a soft substrate," *Biomedical Microdevices*, vol. 11, no. 2, pp. 389–400, 2009.

[113] M. Flaibani, L. Boldrin, E. Cimetta, M. Piccoli, P. D. Coppi, and N. Elvassore, "Muscle differentiation and myotubes alignment is influenced by micropatterned surfaces and exogenous electrical stimulation," *Tissue Engineering Part A*, vol. 15, no. 9, pp. 2447–2457, 2009.

[114] C. Bettinger, R. Langer, and J. Borenstein, "Engineering substrate topography at the micro- and nanoscale to control cell function," *Angewandte Chemie International Edition*, vol. 48, no. 30, pp. 5406–5415, 2009.

[115] E. Pamua, V. De Cupere, Y. F. Dufrne, and P. G. Rouxhet, "Nanoscale organization of adsorbed collagen: Influence of substrate hydrophobicity and adsorption time," *Journal of Colloid and Interface Science*, vol. 271, no. 1, pp. 80–91, 2004.

[116] L. Bozec, G. van der Heijden, and M. Horton, "Collagen fibrils: Nanoscale ropes," *Biophysical Journal*, vol. 92, no. 1, pp. 70–75, 2007.

[117] H. Haga, C. Irahara, R. Kobayashi, T. Nakagaki, and K. Kawabata, "Collective movement of epithelial cells on a collagen gel substrate," *Biophysical Journal*, vol. 88, no. 3, pp. 2250–2256, 2005.

[118] P. Friedl, "Prespecification and plasticity: shifting mechanisms of cell migration," *Current Opinion in Cell Biology*, vol. 16, no. 1, pp. 14–23, 2004.

[119] E.-B. B. Peter Friedl, "T cell migration in three-dimensional extracellular matrix: Guidance by polarity and sensations," *Clinical and Developmental Immunology*, vol. 7, pp. 249–266, 2000.

[120] V. M. A. A. D. B. L. U. Yuan Fan, Qian Chen and S. Kumar, "Scanning probe recognition microscopy investigation of tissue scaffold properties," *International Journal of Nanomedicine*, vol. 2, no. 4, pp. 651–661, 2007.

[121] S. B. Carter, "Haptotaxis and the mechanism of cell motility," *Nature*, vol. 213, no. 5073, pp. 256–260, 1967, 10.1038/213256a0.

[122] M. Lampin, R. Warocquier-Clrout, C. Legris, M. Degrange, and M. F. Sigot-Luizard, "Correlation between substratum roughness and wettability, cell adhesion, and cell migration," *Journal of Biomedical Materials Research*, vol. 36, no. 1, pp. 99–108, 1997.

[123] D. D. Deligianni, N. D. Katsala, P. G. Koutsoukos, and Y. F. Missirlis, "Effect of surface roughness of hydroxyapatite on human bone marrow cell adhesion, proliferation, differentiation and detachment strength," *Biomaterials*, vol. 22, no. 1, pp. 87–96, 2000.

[124] P.-Y. Wang, H.-T. Yu, and W.-B. Tsai, "Modulation of alignment and differentiation of skeletal myoblasts by submicron ridges/grooves surface structure," *Biotechnology and Bioengineering*, vol. 106, no. 2, pp. 285–294, 2010.

[125] K. Shimizu, H. Fujita, and E. Nagamori, "Alignment of skeletal muscle myoblasts and myotubes using linear micropatterned surfaces ground with abrasives," *Biotechnology and Bioengineering*, vol. 103, no. 3, pp. 631–638, 2009.

[126] D. L. Yamamoto, R. I. Csikasz, Y. Li, G. Sharma, K. Hjort, R. Karlsson, and T. Bengtsson, "Myotube formation on micro-patterned glass: Intracellular organization and protein distribution in c2c12 skeletal muscle cells," *J. Histochem. Cytochem.*, vol. 56, no. 10, pp. 881–892, 2008.

[127] H. Jeon, H. Hidai, D. J. Hwang, and C. P. Grigoropoulos, "Fabrication of arbitrary polymer patterns for cell study by two-photon polymerization process," *Journal of Biomedical Materials Research Part A*, vol. 93A, no. 1, pp. 56–66, 2010.

[128] D.-H. Kim, C.-H. Seo, K. Han, K. W. Kwon, A. Levchenko, and K.-Y. Suh, "Guided cell migration on microtextured substrates with variable local density and anisotropy," *Advanced Functional Materials*, vol. 19, no. 10, pp. 1579–1586, 2009.

[129] J.-P. Kaiser, A. Reinmann, and A. Bruinink, "The effect of topographic characteristics on cell migration velocity," *Biomaterials*, vol. 27, no. 30, pp. 5230–5241, 2006.

[130] D.-H. Kim, P. P. Provenzano, C. L. Smith, and A. Levchenko, "Matrix nanotopography as a regulator of cell function," *The Journal of Cell Biology*, vol. 197, no. 3, pp. 351–360, 2012.

[131] A. I. Teixeira, G. A. Abrams, P. J. Bertics, C. J. Murphy, and P. F. Nealey, "Epithelial contact guidance on well-defined micro- and nanostructured substrates," *Journal of Cell Science*, vol. 116, no. 10, pp. 1881–1892, 2003.

[132] P. Bajaj, D. Akin, A. Gupta, D. Sherman, B. Shi, O. Auciello, and R. Bashir, "Ultrananocrystalline diamond film as an optimal cell interface for biomedical applications," *Biomedical Microdevices*, vol. 9, no. 6, pp. 787–794, 2007.

[133] L. Altomare, N. Gadegaard, L. Visai, M. C. Tanzi, and S. Far, "Biodegradable microgrooved polymeric surfaces obtained by photolithography for skeletal muscle cell orientation and myotube development," *Acta Biomaterialia*, vol. 6, no. 6, pp. 1948–1957, 2010.

[134] J. Gingras, R. M. Rioux, D. Cuvelier, N. A. Geisse, J. W. Lichtman, G. M. Whitesides, L. Mahadevan, and J. R. Sanes, "Controlling the orientation and synaptic differentiation of myotubes with micropatterned substrates," *Biophysical Journal*, vol. 97, no. 10, pp. 2771–2779, 2009.

[135] P.-Y. Wang, H. Thissen, and W.-B. Tsai, "The roles of rgd and grooved topography in the adhesion, morphology, and differentiation of c2c12 skeletal myoblasts," *Biotechnology and Bioengineering*, vol. 109, no. 8, pp. 2104–2115, 2012.

[136] W. Chen, L. G. Villa-Diaz, Y. Sun, S. Weng, J. K. Kim, R. H. W. Lam, L. Han, R. Fan, P. H. Krebsbach, and J. Fu, "Nanotopography influences adhesion, spreading, and self-renewal of human embryonic stem cells," *ACS Nano*, vol. 6, no. 5, pp. 4094–4103, 2012.

[137] M. F. R. H. L. M. L. E.-M. F. A. F. K. W. F. B. F. S. P. Lotte DAndrea Markert, Jette Lovmand and M. Duch., "Identification of distinct topographical surface microstructures favoring either undifferentiated expansion or differentiation of murine embryonic stem cells," *Stem Cells and Development*, vol. 18, pp. 1331–1342, 2009.

[138] S. Oh, K. S. Brammer, Y. S. J. Li, D. Teng, A. J. Engler, S. Chien, and S. Jin, "Stem cell fate dictated solely by altered nanotube dimension," *Proceedings of the National Academy of Sciences*, 2009.

[139] J. B. Recknor, D. S. Sakaguchi, and S. K. Mallapragada, "Directed growth and selective differentiation of neural progenitor cells on micropatterned polymer substrates," *Biomaterials*, vol. 27, no. 22, pp. 4098–4108, 2006.

[140] K.-N. Chua, C. Chai, P.-C. Lee, Y.-N. Tang, S. Ramakrishna, K. W. Leong, and H.-Q. Mao, "Surface-aminated electrospun nanofibers enhance adhesion and expansion of human umbilical cord blood hematopoietic stem/progenitor cells," *Biomaterials*, vol. 27, no. 36, pp. 6043–6051, 2006.

[141] A. M. P. Turner, N. Dowell, S. W. P. Turner, L. Kam, M. Isaacson, J. N. Turner, H. G. Craighead, and W. Shain, "Attachment of astroglial cells to microfabricated pillar arrays of different geometries," *Journal of Biomedical Materials Research*, vol. 51, no. 3, pp. 430–441, 2000.

[142] C. Xie, L. Hanson, W. Xie, Z. Lin, B. Cui, and Y. Cui, "Noninvasive neuron pinning with nanopillar arrays," *Nano Letters*, vol. 10, no. 10, pp. 4020–4024, 2010.

[143] M. Ghibaudo, L. Trichet, J. Le Digabel, A. Richert, P. Hersen, and B. Ladoux, "Substrate topography induces a crossover from 2d to 3d behavior in fibroblast migration," *Biophysical Journal*, vol. 97, no. 1, pp. 357–368, 2009.

[144] M. T. Frey, I. Y. Tsai, T. P. Russell, S. K. Hanks, and Y.-l. Wang, "Cellular responses to substrate topography: Role of myosin ii and focal adhesion kinase," *Biophysical Journal*, vol. 90, no. 10, pp. 3774–3782, 2006.

[145] F. Guilak, D. M. Cohen, B. T. Estes, J. M. Gimble, W. Liedtke, and C. S. Chen, "Control of stem cell fate by physical interactions with the extracellular matrix," *Cell stem cell*, vol. 5, no. 1, pp. 17–26, 2009.

[146] E. Cukierman, R. Pankov, D. R. Stevens, and K. M. Yamada, "Taking cell-matrix adhesions to the third dimension," *Science*, vol. 294, no. 5547, pp. 1708–1712, 2001.

[147] V. Weaver, O. Petersen, F. Wang, C. Larabell, P. Briand, C. Damsky, and M. Bissell, "Reversion of the malignant phenotype of human breast cells in three-dimensional culture and in vivo by integrin blocking antibodies," *The Journal of Cell Biology*, vol. 137, no. 1, pp. 231–245, 1997.

[148] F. Wang, R. K. Hansen, D. Radisky, T. Yoneda, M. H. Barcellos-Hoff, O. W. Petersen, E. A. Turley, and M. J. Bissell, "Phenotypic reversion or death of cancer cells by altering signaling pathways in three-dimensional contexts," *Journal of the National Cancer Institute*, vol. 94, no. 19, pp. 1494–1503, 2002.

[149] K.-J. N. N. Z. Y.-H. G.-J. C. J. W. W.-G. Z. Chun-Li Li, Tao Tian, "Survival advantages of multicellular spheroids vs. monolayers of hepg2 cells in vitro," *Oncology Reports*, vol. 20, pp. 1465–1471, 2008.

[150] M. D.-G. T. H. Tsiona Elkayam, Sigalit Amitay-Shaprut and S. Cohen, "Enhancing the drug metabolism activities of c3a a human hepatocyte cell line by tissue engineering within alginate scaffolds," *Tissue engineering*, vol. 12, pp. 1357–1368, 2006.

[151] H. Hosseinkhani, M. Hosseinkhani, and H. Kobayashi, "Design of tissue-engineered nanoscaffold through self-assembly of peptide amphiphile," *Journal of Bioactive and Compatible Polymers*, vol. 21, no. 4, pp. 277–296, 2006.

[152] J. L. Drury and D. J. Mooney, "Hydrogels for tissue engineering: scaffold design variables and applications," *Biomaterials*, vol. 24, no. 24, pp. 4337–4351, 2003.

[153] K. T. Nguyen and J. L. West, "Photopolymerizable hydrogels for tissue engineering applications," *Biomaterials*, vol. 23, no. 22, pp. 4307–4314, 2002.

[154] S. V. Vinogradov, T. K. Bronich, and A. V. Kabanov, "Nanosized cationic hydrogels for drug delivery: preparation, properties and interactions with cells," *Advanced Drug Delivery Reviews*, vol. 54, no. 1, pp. 135–147, 2002.

[155] T. A. Holland, J. K. V. Tessmar, Y. Tabata, and A. G. Mikos, "Transforming growth factor-1 release from oligo(poly(ethylene glycol) fumarate) hydrogels in conditions that model the cartilage wound healing environment," *Journal of Controlled Release*, vol. 94, no. 1, pp. 101–114, 2004.

[156] J. L. Ifkovits and J. A. Burdick, "Review: Photopolymerizable and degradable biomaterials for tissue engineering applications," *Tissue Engineering*, vol. 13, no. 10, pp. 2369–2385, 2007.

[157] L. E. Freed, G. C. Engelmayr, J. T. Borenstein, F. T. Moutos, and F. Guilak, "Tissue engineering: Advanced material strategies for tissue engineering scaffolds (adv. mater. 32-33/2009)," *Advanced Materials*, vol. 21, no. 32-33, pp. n/a–n/a, 2009.

[158] Z. G. Tang, R. A. Black, J. M. Curran, J. A. Hunt, N. P. Rhodes, and D. F. Williams, "Surface properties and biocompatibility of solvent-cast poly[-caprolactone] films," *Biomaterials*, vol. 25, no. 19, pp. 4741–4748, 2004.

[159] P. Basile, T. Dadali, J. Jacobson, S. Hasslund, M. Ulrich-Vinther, K. Soballe, Y. Nishio, M. H. Drissi, H. N. Langstein, D. J. Mitten, R. J. O'Keefe, E. M. Schwarz, and H. A. Awad, "Freeze-dried tendon allografts as tissue-engineering scaffolds for gdf5 gene delivery," *Mol Ther*, vol. 16, no. 3, pp. 466–473, 2008.

[160] L. D. Harris, B.-S. Kim, and D. J. Mooney, "Open pore biodegradable matrices formed with gas foaming," *Journal of Biomedical Materials Research*, vol. 42, no. 3, pp. 396–402, 1998.

[161] T. J. Sill and H. A. von Recum, "Electrospinning: Applications in drug delivery and tissue engineering," *Biomaterials*, vol. 29, no. 13, pp. 1989–2006, 2008.

[162] C. Y. Tay, M. Pal, H. Yu, W. S. Leong, N. S. Tan, K. W. Ng, S. Venkatraman, F. Boey, D. T. Leong, and L. P. Tan, "Bio-inspired micropatterned platform to steer stem cell differentiation," *Small*, vol. 7, no. 10, pp. 1416–1421, 2011.

[163] P. Bajaj, X. Tang, T. A. Saif, and R. Bashir, "Stiffness of the substrate influences the phenotype of embryonic chicken cardiac myocytes," *Journal of Biomedical Materials Research Part A*, vol. 95A, no. 4, pp. 1261–1269, 2010.

[164] X. Tang, P. Bajaj, R. Bashir, and T. A. Saif, "How far cardiac cells can see each other mechanically," *Soft Matter*, vol. 7, no. 13, pp. 6151–6158, 2011.

[165] T. Boudou, J. Ohayon, C. Picart, and P. Tracqui, "An extended relationship for the characterization of young's modulus and poisson's ratio of tunable polyacrylamide gels," *Biorheology*, vol. 43, no. 6, pp. 721–728, 2006.

[166] K. J. Vesna Damljanovic, B. Christoffer Lagerholm, "Bulk and micropatterned conjugation of extracellular matrix proteins to characterized polyacrylamide substrates for cell mechanotransduction assays," *BioTechniques*, vol. 39, p. 847851, 2005.

[167] A. J. Engler, L. Richert, J. Y. Wong, C. Picart, and D. E. Discher, "Surface probe measurements of the elasticity of sectioned tissue, thin gels and polyelectrolyte multilayer films: Correlations between substrate stiffness and cell adhesion," *Surface Science*, vol. 570, no. 12, pp. 142–154, 2004.

[168] V. Hamburger and H. L. Hamilton, "A series of normal stages in the development of the chick embryo," *Developmental Dynamics*, vol. 195, no. 4, pp. 231–272, 1992.

[169] P. J. R. S. J. Abramoff, M.D.; Magalhes, "Image processing with imagej," *Biophotonics international*, vol. 11, pp. 36–42, 2004.

[170] M. G. Mrquez, M. del Carmen Fernndez-Tome, N. O. Favale, L. G. Pescio, and N. B. Sterin-Speziale, "Bradykinin modulates focal adhesions and induces stress fiber remodeling in renal papillary collecting duct cells," *American Journal of Physiology - Renal Physiology*, vol. 294, no. 3, pp. F603–F613, 2008.

[171] P. Kohl, P. Camelliti, F. L. Burton, and G. L. Smith, "Electrical coupling of fibroblasts and myocytes: relevance for cardiac propagation," *Journal of Electrocardiology*, vol. 38, no. 4, Supplement, pp. 45–50, 2005.

[172] T. Yeung, P. C. Georges, L. A. Flanagan, B. Marg, M. Ortiz, M. Funaki, N. Zahir, W. Ming, V. Weaver, and P. A. Janmey, "Effects of substrate stiffness on cell morphology, cytoskeletal structure, and adhesion," *Cell Motility and the Cytoskeleton*, vol. 60, no. 1, pp. 24–34, 2005.

[173] F. B. HARARY I, "In vitro studies on single beating rat heart cells. i. growth and organization." *Experimental Cell Research*, vol. 29, pp. 451–465, 1963.

[174] A. Engler, L. Bacakova, C. Newman, A. Hategan, M. Griffin, and D. Discher, "Substrate compliance versus ligand density in cell on gel responses," *Biophysical Journal*, vol. 86, no. 1, pp. 617–628, 2004.

[175] E. A. Cavalcanti-Adam, A. Micoulet, J. Blmmel, J. Auernheimer, H. Kessler, and J. P. Spatz, "Lateral spacing of integrin ligands influences cell spreading and focal adhesion assembly," *European Journal of Cell Biology*, vol. 85, no. 34, pp. 219–224, 2006.

[176] W.-h. Guo, M. T. Frey, N. A. Burnham, and Y.-l. Wang, "Substrate rigidity regulates the formation and maintenance of tissues," *Biophysical Journal*, vol. 90, no. 6, pp. 2213–2220, 2006.

[177] S.-w. Lee and J. J. Otto, "Vinculin and talin: Kinetics of entry and exit from the cytoskeletal pool," *Cell Motility and the Cytoskeleton*, vol. 36, no. 2, pp. 101–111, 1997.

[178] K. Burridge and M. Chrzanowska-Wodnicka, "Focal adhesions, contractility, and signaling," *Annual Review of Cell and Developmental Biology*, vol. 12, no. 1, pp. 463–519, 1996.

[179] M. Chrzanowska-Wodnicka and K. Burridge, "Rho-stimulated contractility drives the formation of stress fibers and focal adhesions," *The Journal of Cell Biology*, vol. 133, no. 6, pp. 1403–1415, 1996.

[180] R. Zaidel-Bar, C. Ballestrem, Z. Kam, and B. Geiger, "Early molecular events in the assembly of matrix adhesions at the leading edge of migrating cells," *Journal of Cell Science*, vol. 116, no. 22, pp. 4605–4613, 2003.

[181] K. A. Beningo, M. Dembo, I. Kaverina, J. V. Small, and Y.-l. Wang, "Nascent focal adhesions are responsible for the generation of strong propulsive forces in migrating fibroblasts," *The Journal of Cell Biology*, vol. 153, no. 4, pp. 881–888, 2001.

[182] S. J. S. J. Dabiri GA, Turnacioglu KK, "Myofibrillogenesis visualized in living embryonic cardiomyocytes." *Proc Natl Acad Sci USA*, vol. 94, pp. 9493–9498, 1997.

[183] A. A. Dlugosz, P. B. Antin, V. T. Nachmias, and H. Holtzer, "The relationship between stress fiber-like structures and nascent myofibrils in cultured cardiac myocytes," *The Journal of Cell Biology*, vol. 99, no. 6, pp. 2268–2278, 1984.

[184] S. Yang and M. T. A. Saif, "Force response and actin remodeling (agglomeration) in fibroblasts due to lateral indentation," *Acta Biomaterialia*, vol. 3, no. 1, pp. 77–87, 2007.

[185] S. Yang and T. Saif, "Micromachined force sensors for the study of cell mechanics," *Review of Scientific Instruments*, vol. 76, no. 4, p. 044301, 2005.

[186] P. Bajaj, B. Reddy, L. Millet, C. Wei, P. Zorlutuna, G. Bao, and R. Bashir, "Patterning the differentiation of c2c12 skeletal myoblasts," *Integrative Biology*, vol. 3, no. 9, pp. 897–909, 2011.

[187] Y. Sun, Y. Ge, J. Drnevich, Y. Zhao, M. Band, and J. Chen, "Mammalian target of rapamycin regulates mirna-1 and follistatin in skeletal myogenesis," *The Journal of Cell Biology*, vol. 189, no. 7, pp. 1157–1169, 2010.

[188] R. B. Mario Marotta and A. M. Gmez-Foix1, "Design and performance of an electrical stimulator for long-term contraction of cultured muscle cells," *Biotechniques*, 2004.

[189] H. M. J. R. B.-G. L. B. S. C. H. CHANTAL E. AYRES, B. SHEKHAR JHA and D. G. SIMPSON, "Measuring fiber alignment in electrospun scaffolds: a users guide to the 2d fast fourier transform approach," *J. Biomater. Sci. Polymer Edn*, vol. 19, pp. 603–621, 2008.

[190] A. Kamgou, J. Ohayon, Y. Usson, L. Riou, and P. Tracqui, "Quantification of cardiomyocyte contraction based on image correlation analysis," *Cytometry Part A*, vol. 75A, no. 4, pp. 298–308, 2009.

[191] B. Li, F. Li, K. M. Puskar, and J. H. C. Wang, "Spatial patterning of cell proliferation and differentiation depends on mechanical stress magnitude," *Journal of Biomechanics*, vol. 42, no. 11, pp. 1622–1627, 2009.

[192] S. Cooper, A. Maxwell, E. Kizana, M. Ghoddusi, E. Hardeman, I. Alexander, D. Allen, and K. North, "C2c12 co-culture on a fibroblast substratum enables sustained survival of contractile, highly differentiated myotubes with peripheral nuclei and adult fast myosin expression," *Cell Motility and the Cytoskeleton*, vol. 58, no. 3, pp. 200–211, 2004.

[193] K.-i. Yamasaki, H. Hayashi, K. Nishiyama, H. Kobayashi, S. Uto, H. Kondo, S. Hashimoto, and T. Fujisato, "Control of myotube contraction using electrical pulse stimulation for bio-actuator," *Journal of Artificial Organs*, vol. 12, no. 2, pp. 131–137, 2009.

[194] C.-Y. Chung, H. Bien, and E. Entcheva, "The role of cardiac tissue alignment in modulating electrical function," *Journal of Cardiovascular Electrophysiology*, vol. 18, no. 12, pp. 1323–1329, 2007.

[195] Y. Zhao, "Investigating electrical field-affected skeletal myogenesis using a microfabricated electrode array," *Sensors and Actuators A: Physical*, vol. 154, no. 2, pp. 281–287, 2009.

[196] R. A. Crabb, E. P. Chau, M. C. Evans, V. H. Barocas, and A. Hubel, "Biomechanical and microstructural characteristics of a collagen film-based corneal stroma equivalent," *Tissue Engineering*, vol. 12, no. 6, pp. 1565–1575, 2006.

[197] P. Bajaj, D. Khang, and T. J. Webster, "Control of spatial cell attachment on carbon nanofiber patterns on polycarbonate urethane," *International Journal of Nanomedicine*, vol. 1, no. 3, pp. 361–365, 2006, 246ZX Times Cited:2 Cited References Count:16.

[198] C. Ayres, G. L. Bowlin, S. C. Henderson, L. Taylor, J. Shultz, J. Alexander, T. A. Telemeco, and D. G. Simpson, "Modulation of anisotropy in electrospun tissue-engineering scaffolds: Analysis of fiber alignment by the fast fourier transform," *Biomaterials*, vol. 27, no. 32, pp. 5524–5534, 2006.

[199] A. S. Crouch, D. Miller, K. J. Luebke, and W. Hu, "Correlation of anisotropic cell behaviors with topographic aspect ratio," *Biomaterials*, vol. 30, no. 8, pp. 1560–1567, 2009.

[200] T. M. Patz, A. Doraiswamy, R. J. Narayan, R. Modi, and D. B. Chrisey, "Two-dimensional differential adherence and alignment of c2c12 myoblasts," *Materials Science and Engineering: B*, vol. 123, no. 3, pp. 242–247, 2005.

[201] J. L. Charest, A. J. Garca, and W. P. King, "Myoblast alignment and differentiation on cell culture substrates with microscale topography and model chemistries," *Biomaterials*, vol. 28, no. 13, pp. 2202–2210, 2007.

[202] A. W. Feinberg, A. Feigel, S. S. Shevkoplyas, S. Sheehy, G. M. Whitesides, and K. K. Parker, "Muscular thin films for building actuators and powering devices," *Science*, vol. 317, no. 5843, pp. 1366–1370, 2007.

[203] Y. Tanaka, K. Morishima, T. Shimizu, A. Kikuchi, M. Yamato, T. Okano, and T. Kitamori, "An actuated pump on-chip powered by cultured cardiomyocytes," *Lab on a Chip*, vol. 6, no. 3, pp. 362–368, 2006.

[204] Y. Tanaka, K. Morishima, T. Shimizu, A. Kikuchi, M. Yamato, T. Okano, and T. Kitamori, "Demonstration of a pdms-based bio-microactuator using cultured cardiomyocytes to drive polymer micropillars," *Lab on a Chip*, vol. 6, no. 2, pp. 230–235, 2006.

[205] H. Herr and R. Dennis, "A swimming robot actuated by living muscle tissue," *Journal of NeuroEngineering and Rehabilitation*, vol. 1, no. 1, p. 6, 2004.

[206] G. Messina, C. Blasi, S. A. La Rocca, M. Pompili, A. Calconi, and M. Grossi, "p27kip1 acts downstream of n-cadherin-mediated cell adhesion to promote myogenesis beyond cell cycle regulation," *Mol. Biol. Cell*, vol. 16, no. 3, pp. 1469–1480, 2005.

[207] K. M. J. Pavlath and G. K., "Molecular control of mammalian myoblast fusion," 2008.

[208] N. Yoshida, S. Yoshida, K. Koishi, K. Masuda, and Y. Nabeshima, "Cell heterogeneity upon myogenic differentiation: down-regulation of myod and myf-5 generates 'reserve cells'," *J Cell Sci*, vol. 111, no. 6, pp. 769–779, 1998.

[209] M. Kitzmann and A. Fernandez, "Crosstalk between cell cycle regulators and the myogenic factor myod in skeletal myoblasts," *Cellular and Molecular Life Sciences*, vol. 58, no. 4, pp. 571–579, 2001.

[210] H. Jiang, "Chemical preparation of graphene-based nanomaterials and their applications in chemical and biological sensors," *Small*, vol. 7, no. 17, pp. 2413–2427, 2011.

[211] S. Guo and S. Dong, "Graphene nanosheet: synthesis, molecular engineering, thin film, hybrids, and energy and analytical applications," *Chemical Society Reviews*, vol. 40, no. 5, pp. 2644–2672, 2011.

[212] T. S. M. Q. M. A. C. J. A. C. Y. Xuan, Y. Q. Wu and P. D. Ye, "Atomic-layer-deposited nanostructures for graphene-based nanoelectronics," *Appl. Phys. Lett.*, vol. 92, pp. 013 101–013 103, 2008.

[213] X. Yang, Y. Tu, L. Li, S. Shang, and X.-m. Tao, "Well-dispersed chitosan/graphene oxide nanocomposites," *ACS Applied Materials & Interfaces*, vol. 2, no. 6, pp. 1707–1713, 2010.

[214] C. Liu, S. Alwarappan, Z. Chen, X. Kong, and C.-Z. Li, "Membraneless enzymatic biofuel cells based on graphene nanosheets," *Biosensors and Bioelectronics*, vol. 25, no. 7, pp. 1829–1833, 2010.

[215] C.-H. Lu, H.-H. Yang, C.-L. Zhu, X. Chen, and G.-N. Chen, "A graphene platform for sensing biomolecules," *Angewandte Chemie International Edition*, vol. 48, no. 26, pp. 4785–4787, 2009.

[216] L. Qu, Y. Liu, J.-B. Baek, and L. Dai, "Nitrogen-doped graphene as efficient metal-free electrocatalyst for oxygen reduction in fuel cells," *ACS Nano*, vol. 4, no. 3, pp. 1321–1326, 2010.

[217] M. L. Z. Z. He Shen, Liming Zhang, "Biomedical applications of graphene," *Theranostics*, vol. 2, no. 3, pp. 283–294, 2012.

[218] X. Liang, B. A. Sperling, I. Calizo, G. Cheng, C. A. Hacker, Q. Zhang, Y. Obeng, K. Yan, H. Peng, Q. Li, X. Zhu, H. Yuan, A. R. Hight Walker, Z. Liu, L.-m. Peng, and C. A. Richter, "Toward clean and crackless transfer of graphene," *ACS Nano*, vol. 5, pp. 9144–9153, 2011.

[219] A. C. Ferrari, J. C. Meyer, V. Scardaci, C. Casiraghi, M. Lazzeri, F. Mauri, S. Piscanec, D. Jiang, K. S. Novoselov, S. Roth, and A. K. Geim, "Raman spectrum of graphene and graphene layers," *Phys. Rev. Lett.*, vol. 97, p. 187401, 2006.

[220] A. Gupta, G. Chen, P. Joshi, S. Tadigadapa, and Eklund, "Raman scattering from high-frequency phonons in supported n-graphene layer films," *Nano Letters*, vol. 6, pp. 2667–2673, 2006.

[221] D. R. Lenski and M. S. Fuhrer, "Raman and optical characterization of multilayer turbostratic graphene grown via chemical vapor deposition," *Journal of Applied Physics*, vol. 110, p. 013720, 2011.

[222] I. Delgado, X. Huang, S. Jones, L. Zhang, R. Hatcher, B. Gao, and P. Zhang, "Dynamic gene expression during the onset of myoblast differentiation in vitro," *Genomics*, vol. 82, no. 2, pp. 109–121, 2003.

[223] M. Kitzmann, G. Carnac, M. Vandromme, M. Primig, N. J. Lamb, and A. Fernandez, "The muscle regulatory factors myod and myf-5 undergo distinct cell cyclespecific expression in muscle cells," *The Journal of Cell Biology*, vol. 142, no. 6, pp. 1447–1459, 1998.

[224] A. Fanzani, E. Stoppani, L. Gualandi, R. Giuliani, F. Galbiati, S. Rossi, A. Fra, A. Preti, and S. Marchesini, "Phenotypic behavior of c2c12 myoblasts upon expression of the dystrophy-related caveolin-3 p104l and tft mutants," *FEBS Letters*, vol. 581, no. 26, pp. 5099–5104, 2007.

[225] C. Favreau, E. Delbarre, J.-C. Courvalin, and B. Buendia, "Differentiation of c2c12 myoblasts expressing lamin a mutated at a site responsible for emery-dreifuss muscular dystrophy is improved by inhibition of the mek-erk pathway and stimulation of the pi3-kinase pathway," *Experimental Cell Research*, vol. 314, no. 6, pp. 1392–1405, 2008.

[226] D. P. Dowling, I. S. Miller, M. Ardhaoui, and W. M. Gallagher, "Effect of surface wettability and topography on the adhesion of osteosarcoma cells on plasma-modified polystyrene," *Journal of Biomaterials Applications*, vol. 26, no. 3, pp. 327–347, 2011.

[227] H. E. Nguessan, A. Leh, P. Cox, P. Bahadur, R. Tadmor, P. Patra, R. Vajtai, P. M. Ajayan, and P. Wasnik, "Water tribology on graphene," *Nat Commun*, vol. 3, p. 1242, 2012, 10.1038/ncomms2247.

[228] W. C. Lee, C. H. Y. X. Lim, H. Shi, L. A. L. Tang, Y. Wang, C. T. Lim, and K. P. Loh, "Origin of enhanced stem cell growth and differentiation on graphene and graphene oxide," *ACS Nano*, vol. 5, no. 9, pp. 7334–7341, 2011.

[229] A. Matsakas and K. Patel, "Skeletal muscle fibre plasticity in response to selected environmental and physiological stimuli," *Histology and Histopathology*, vol. 24, no. 5, pp. 611–629, 2009, 417ZG Times Cited:7 Cited References Count:111.

[230] A. Otto and K. Patel, "Signalling and the control of skeletal muscle size," *Experimental Cell Research*, vol. 316, no. 18, pp. 3059–3066, 2010.

[231] J.-P. Liu, J. Baker, A. S. Perkins, E. J. Robertson, and A. Efstratiadis, "Mice carrying null mutations of the genes encoding insulin-like growth factor i (igf-1) and type 1 igf receptor (igf1r)," *Cell*, vol. 75, no. 1, pp. 59–72, 1993.

[232] J. Baker, J. P. Liu, E. J. Robertson, and A. Efstratiadis, "Role of insulin-like growth-factors in embryonic and postnatal-growth," *Cell*, vol. 75, no. 1, pp. 73–82, 1993, mb667 Times Cited:1274 Cited References Count:82.

[233] M. E. Coleman, F. DeMayo, K. C. Yin, H. M. Lee, R. Geske, C. Montgomery, and R. J. Schwartz, "Myogenic vector expression of insulin-like growth factor i stimulates muscle cell differentiation and myofiber hypertrophy in transgenic mice," *Journal of Biological Chemistry*, vol. 270, no. 20, pp. 12 109–12 116, 1995.

[234] E. R. Barton-Davis, D. I. Shoturma, A. Musaro, N. Rosenthal, and H. L. Sweeney, "Viral mediated expression of insulin-like growth factor i blocks the aging-related loss of skeletal muscle function," *Proceedings of the National Academy of Sciences of the United States of America*, vol. 95, no. 26, pp. 15 603–15 607, 1998.

[235] S.-J. Lee and A. C. McPherron, "Regulation of myostatin activity and muscle growth," *Proceedings of the National Academy of Sciences of the United States of America*, vol. 98, no. 16, pp. 9306–9311, 2001.

[236] A. C. McPherron, A. M. Lawler, and S.-J. Lee, "Regulation of skeletal muscle mass in mice by a new tgf-p superfamily member," *Nature*, vol. 387, no. 6628, pp. 83–90, 1997, 10.1038/387083a0.

[237] T. Cohen-Karni, Q. Qing, Q. Li, Y. Fang, and C. M. Lieber, "Graphene and nanowire transistors for cellular interfaces and electrical recording," *Nano Letters*, vol. 10, no. 3, pp. 1098–1102, 2010.

[238] M. Dankerl, M. V. Hauf, A. Lippert, L. H. Hess, S. Birner, I. D. Sharp, A. Mahmood, P. Mallet, J.-Y. Veuillen, M. Stutzmann, and J. A. Garrido, "Graphene solution-gated field-effect transistor array for sensing applications," *Advanced Functional Materials*, vol. 20, no. 18, pp. 3117–3124, 2010.

[239] L. H. Hess, M. Jansen, V. Maybeck, M. V. Hauf, M. Seifert, M. Stutzmann, I. D. Sharp, A. Offenhusser, and J. A. Garrido, "Graphene transistor arrays for recording action potentials from electrogenic cells," *Advanced Materials*, vol. 23, no. 43, pp. 5045–5049, 2011.

[240] M. S. Sakar, D. Neal, T. Boudou, M. A. Borochin, Y. Li, R. Weiss, R. D. Kamm, C. S. Chen, and H. H. Asada, "Formation and optogenetic control of engineered 3d skeletal muscle bioactuators," *Lab on a Chip*, vol. 12, no. 23, pp. 4976–4985, 2012.

[241] P. Bajaj, D. Marchwiany, C. Duarte, and R. Bashir, "Patterned three-dimensional encapsulation of embryonic stem cells using dielectrophoresis and stereolithography," *Advanced Healthcare Materials*, pp. n/a–n/a, 2012.

[242] P. Bajaj, V. Chan, J. H. Jeong, P. Zorlutuna, H. Kong, and R. Bashir, "3-d biofabrication using stereolithography for biology and medicine," in *Engineering in Medicine and Biology Society (EMBC), 2012 Annual International Conference of the IEEE*, 28 2012-sept. 1 2012, pp. 6805 –6808.

[243] D. R. Albrecht, R. L. Sah, and S. N. Bhatia, "Geometric and material determinants of patterning efficiency by dielectrophoresis," *Biophysical Journal*, vol. 87, no. 4, pp. 2131–2147, 2004.

[244] J. Voldman, R. A. Braff, M. Toner, M. L. Gray, and M. A. Schmidt, "Holding forces of single-particle dielectrophoretic traps," *Biophysical Journal*, vol. 80, no. 1, pp. 531–542, 2001.

[245] D. R. Albrecht, G. H. Underhill, T. B. Wassermann, R. L. Sah, and S. N. Bhatia, "Probing the role of multicellular organization in three-dimensional microenvironments," *Nat Meth*, vol. 3, no. 5, pp. 369–375, 2006, 10.1038/nmeth873.

[246] C. H. Kua, Y. C. Lam, I. Rodriguez, C. Yang, and K. Youcef-Toumi, "Cell motion model for moving dielectrophoresis," *Analytical Chemistry*, vol. 80, no. 14, pp. 5454–5461, 2008.

[247] S. Choi and J.-K. Park, "Microfluidic system for dielectrophoretic separation based on a trapezoidal electrode array," *Lab on a Chip*, vol. 5, no. 10, pp. 1161–1167, 2005.

[248] H. Lu, M. A. Schmidt, and K. F. Jensen, "A microfluidic electroporation device for cell lysis," *Lab on a Chip*, vol. 5, no. 1, pp. 23–29, 2005.

[249] C.-T. Ho, R.-Z. Lin, W.-Y. Chang, H.-Y. Chang, and C.-H. Liu, "Rapid heterogeneous liver-cell on-chip patterning via the enhanced field-induced dielectrophoresis trap," *Lab on a Chip*, vol. 6, no. 6, pp. 724–734, 2006.

[250] H. Shafiee, M. B. Sano, E. A. Henslee, J. L. Caldwell, and R. V. Davalos, "Selective isolation of live/dead cells using contactless dielectrophoresis (cdep)," *Lab on a Chip*, vol. 10, no. 4, pp. 438–445, 2010.

[251] H. Glasser and G. Fuhr, "Cultivation of cells under strong ac-electric fielddifferentiation between heating and trans-membrane potential effects," *Bioelectrochemistry and Bioenergetics*, vol. 47, no. 2, pp. 301–310, 1998.

[252] R.-Z. Lin, C.-T. Ho, C.-H. Liu, and H.-Y. Chang, "Dielectrophoresis based-cell patterning for tissue engineering," *Biotechnology Journal*, vol. 1, no. 9, pp. 949–957, 2006.

[253] D. R. Albrecht, V. L. Tsang, R. L. Sah, and S. N. Bhatia, "Photo- and electropatterning of hydrogel-encapsulated living cell arrays," *Lab on a Chip*, vol. 5, no. 1, pp. 111–118, 2005.

[254] D. R. Albrecht, G. H. Underhill, A. Mendelson, and S. N. Bhatia, "Multiphase electropatterning of cells and biomaterials," *Lab on a Chip*, vol. 7, no. 6, pp. 702–709, 2007.

[255] F. P. W. Melchels, J. Feijen, and D. W. Grijpma, "A review on stereolithography and its applications in biomedical engineering," *Biomaterials*, vol. 31, no. 24, pp. 6121–6130, 2010.

[256] P. F. Jacobs, *Rapid Prototyping & Manufacturing Fundamentals of Stereolithography*, D. T. Reid, Ed. Society of Manufacturing Engineers; 1st edition, 1992.

[257] B. D. Fairbanks, M. P. Schwartz, C. N. Bowman, and K. S. Anseth, "Photoinitiated polymerization of peg-diacrylate with lithium phenyl-2,4,6-trimethylbenzoylphosphinate: polymerization rate and cytocompatibility," *Biomaterials*, vol. 30, no. 35, pp. 6702–6707, 2009.

[258] H. K. Pinar Zorlutuna, Jae Hyun Jeong and R. Bashir, "Stereolithography-based hydrogel micro-environments for examining cellular interactions," *Advanced Functional Materials*, 2011.

[259] F. P. W. Melchels, J. Feijen, and D. W. Grijpma, "A poly(d,l-lactide) resin for the preparation of tissue engineering scaffolds by stereolithography," *Biomaterials*, vol. 30, no. 23-24, pp. 3801–3809, 2009.

[260] J. Ramon-Azcon, S. Ahadian, R. Obregon, G. Camci-Unal, S. Ostrovidov, V. Hosseini, H. Kaji, K. Ino, H. Shiku, A. Khademhosseini, and T. Matsue, "Gelatin methacrylate as a promising hydrogel for 3d microscale organization and proliferation of dielectrophoretically patterned cells," *Lab on a Chip*, vol. 12, no. 16, pp. 2959–2969, 2012.

[261] S. V. Puttaswamy, S. Sivashankar, R.-J. Chen, C.-K. Chin, H.-Y. Chang, and C. H. Liu, "Enhanced cell viability and cell adhesion using low conductivity medium for negative dielectrophoretic cell patterning," *Biotechnology Journal*, vol. 5, no. 10, pp. 1005–1015, 2010.

[262] J. P. Mazzoccoli, D. L. Feke, H. Baskaran, and P. N. Pintauro, "Mechanical and cell viability properties of crosslinked low- and high-molecular weight poly(ethylene glycol) diacrylate blends," *Journal of Biomedical Materials Research Part A*, vol. 93A, no. 2, pp. 558–566, 2010.

[263] C. Grosse and H. P. Schwan, "Cellular membrane potentials induced by alternating fields," *Biophysical Journal*, vol. 63, no. 6, pp. 1632–1642, 1992.

[264] P. Ellappan and R. Sundararajan, "A simulation study of the electrical model of a biological cell," *Journal of Electrostatics*, vol. 63, no. 34, pp. 297–307, 2005.

[265] W. Lee, N.-J. Cho, A. Xiong, J. S. Glenn, and C. W. Frank, "Hydrophobic nanoparticles improve permeability of cell-encapsulating poly(ethylene glycol) hydrogels while maintaining patternability," *Proceedings of the National Academy of Sciences*, vol. 107, no. 48, pp. 20 709–20 714, 2010.

[266] F. Soncin, L. Mohamet, D. Eckardt, S. Ritson, A. M. Eastham, N. Bobola, A. Russell, S. Davies, R. Kemler, C. L. R. Merry, and C. M. Ward, "Abrogation of e-cadherin-mediated cellcell contact in mouse embryonic stem cells results in reversible lif-independent self-renewal," *Stem Cells*, vol. 27, no. 9, pp. 2069–2080, 2009.

[267] R. Passier, D. W.-v. Oostwaard, J. Snapper, J. Kloots, R. J. Hassink, E. Kuijk, B. Roelen, A. B. de la Riviere, and C. Mummery, "Increased cardiomyocyte differentiation from human embryonic stem cells in serum-free cultures," *Stem Cells*, vol. 23, no. 6, pp. 772–780, 2005.

[268] A. Soto-Gutierrez, N. Navarro-Alvarez, D. Zhao, J. D. Rivas-Carrillo, J. Lebkowski, N. Tanaka, I. J. Fox, and N. Kobayashi, "Differentiation of mouse embryonic stem cells to hepatocyte-like cells by co-culture with human liver nonparenchymal cell lines," *Nat. Protocols*, vol. 2, no. 2, pp. 347–356, 2007, 10.1038/nprot.2007.18.

[269] C. E. Ayres, G. L. Bowlin, R. Pizinger, L. T. Taylor, C. A. Keen, and D. G. Simpson, "Incremental changes in anisotropy induce incremental changes in the material properties of electrospun scaffolds," *Acta Biomaterialia*, vol. 3, no. 5, pp. 651–661, 2007.

[270] Z. He, J.-j. Li, C.-h. Zhen, L.-y. Feng, and X.-y. Ding, "Effect of leukemia inhibitory factor on embryonic stem cell differentiation: implications for supporting neuronal differentiation," *Acta Pharmacol Sin*, vol. 27, no. 1, pp. 80–90, 2006.

[271] B. V. Slaughter, S. S. Khurshid, O. Z. Fisher, A. Khademhosseini, and N. A. Peppas, "Hydrogels in regenerative medicine," *Advanced Materials*, vol. 21, no. 32-33, pp. 3307–3329, 2009.

[272] N. A. Peppas, Y. Huang, M. Torres-Lugo, J. H. Ward, and J. Zhang, "Physicochemical foundations and structural design of hydrogels in medicine and biology," *Annual Review of Biomedical Engineering*, vol. 2, no. 1, pp. 9–29, 2000.

[273] S. K. M. Y. U.-i. C. N. K. Y. T. Y. H. Y. A. K. N. T. K. Toru Akune, Shinsuke Ohba and H. Kawaguchi, "Ppar ? insufficiency enhances osteogenesis through osteoblast formation from bone marrow progenitors," *The Journal of Clinical Investigation*, vol. 113, pp. 846–855, 2004.

[274] J. S. Stephens-Altus, P. Sundelacruz, M. L. Rowland, and J. L. West, "Development of bioactive photocrosslinkable fibrous hydrogels," *Journal of Biomedical Materials Research Part A*, vol. 98A, no. 2, pp. 167–176, 2011.

[275] K. S. Saladin, *Anatomy & Physiology: The Unity of Form and Function*. Mcgraw-Hill College, 2006.

[276] M. Schuldiner, O. Yanuka, J. Itskovitz-Eldor, D. A. Melton, and N. Benvenisty, "Effects of eight growth factors on the differentiation of cells derived from human embryonic stem cells," *Proceedings of the National Academy of Sciences*, vol. 97, no. 21, pp. 11 307–11 312, 2000.

[277] C. L. Mummery, D. Ward, and R. Passier, *Differentiation of Human Embryonic Stem Cells to Cardiomyocytes by Coculture with Endoderm in Serum-Free Medium*. John Wiley & Sons, Inc., 2007.

[278] M. Anjomshoa, K. Karbalaie, M. Mardani, S. Razavi, S. Tanhaei, M. H. Nasr-Esfahani, and H. Baharvand, "Generation of motor neurons by coculture of retinoic acid-pretreated embryonic stem cells with chicken notochords," *Stem Cells and Development*, vol. 18, no. 2, pp. 259–268, 2009.

[279] A. S. Correia, S. V. Anisimov, L. Roybon, J.-Y. Li, and P. Brundin, "Fibroblast growth factor-20 increases the yield of midbrain dopaminergic neurons derived from human embryonic stem cells," *Frontiers in Neuroanatomy*, vol. 1, 2007.